Optical Characterisation of CVD Diamond

Charles, David

Awarding institution:
King's College London

Optical Characterisation of CVD Diamond

David R. Charles

Department of Physics

King's College London

A thesis submitted for the degree of Doctor of Philosophy

in the University of London

September 2008

Abstract

Synthetic single-crystal diamonds grown by microwave-assisted chemical vapour deposition have been investigated using optical spectroscopy. Absorption, photoluminescence and cathodoluminescence have been utilised to obtain optical spectra of the diamonds in the ultraviolet, visible and infrared regions, in order to characterise point defects present in the crystals. Temperature dependence measurements, isotopic substitution and thermal annealing have been used to characterise the atomic constituents of defects. Application of a uniaxial stress to oriented samples has allowed the symmetries of a number of point defects to be determined; in particular, defect centres with zero-phonon lines (ZPLs) at 466.6 nm (2.657 eV), 467.2 nm (2.654 eV), 496.8 nm (2.495 eV), 532.7 nm (2.327 eV) and 562.5 nm (2.204 eV) have been determined to have rhombic I, rhombic I, rhombic I, monoclinic I and monoclinic I or rhombic I symmetries, respectively.

The 466.6, 496.8 and 562.5 nm ZPLs demonstrate a preferential orientation along the <110> crystallographic axes, which is potentially characteristic of the growth process. Atomic configurations are proposed for these centres. The 467.2 nm transition is proposed as originating from an atomically perturbed version of the 466.6 nm centre. A calibration factor for the silicon-vacancy defect centre (with ZPL at 736.8 nm (1.682 eV)) has been determined. Studies of nitrogen-15 doped samples have unambiguously confirmed the direct involvement of nitrogen in a number of new and previously investigated ZPLs.

Chapter one introduces the project and outlines the objectives. Chapter two introduces the basic relevant theoretical background. Chapter three details the experimental methods utilised. Chapter four is concerned with the general optical characterisation of single-crystal CVD diamonds. Chapter five presents data on the preferentially oriented centres. Chapter six discusses a number of other defect centres investigated and some further characterisations. Chapter seven concludes the work and discusses suggestions for future investigation.

Acknowledgments

I will forever be indebted to Professor Alan Collins, who welcomed me as his student shortly after I had graduated from my undergraduate degree. He has guided me through the past four years with unfailing patience, ever-willing to assist me with experimental and theoretical work, and freely imparting his knowledge of diamonds and understanding of physics; I consider it an honour to have studied under, and worked alongside him.

I am grateful to the Diamond Trading Company for providing a fully funded studentship for the duration of my Ph.D., which has made all of this possible. I am pleased to have been an undergraduate student at King's College London, and to have continued my studies in physics at a postgraduate level here.

I am also grateful to Professor Gordon Davies, whose ready assistance, and clear explanation of the various theoretical concepts has helped me to characterise these point defects. Additionally, I am grateful to Professor Alison Mainwood for many helpful comments and support over the years.

I thank Bill Luckhurst for his continual willingness to fix things after my frequent experimental blunders in the lab. Furthermore, many support staff have facilitated a smooth four years at King's, and to them all I am grateful.

My postgraduate time at King's would not have been as enjoyable as it was, if it were not for the 1A-team: Bozo, Caz and Kriti. After three years of spontaneously breaking out in song, random self-mumblings, and frequent cursing at computers, it is reassuring to know that I'm not the only one who is, as Bozo would put it, "not normal".

There are many people at King's with whom it has been a pleasure to share a department (and occasionally, office), go to lunch, and socialise; in no particular order: Ferhat, Ben, Zoya, Paula, Will, Chiara, James, Claudio, and Eugene (for soiling my desk with such regularity); Richard and Frances, with whom I also did my undergraduate study; and finally, Nic and Tom, with whom, along with Kriti, I spent many evenings, either in the Lyceum, or, if we were

feeling adventurous, the George. I am delighted to have met Emily and treasure the time we have spent together.

Finally, the largest part of my gratitude is owed to my parents, who have made me the person I am, unfalteringly supported me, and endlessly loved me. This work is dedicated to you – thank you for everything.

Publications and presentations

"*Characterisation of high-quality thick single-crystal diamond grown by CVD with a low nitrogen addition*"
Diamond and Related Materials, **15**, 1700–1707, 2006
A. Tallaire, A.T. Collins, D. Charles, J. Achard, R. Sussmann, A. Gicquel, M.E. Newton, A.M. Edmonds, R.J. Cruddace

"*Optical spectroscopy of the 736.8 nm silicon centre in single-crystal CVD diamond studied with the application of uniaxial stress*"
Presentation at the De Beers 58th Diamond Conference, 2007
David Charles, Alan T Collins, Gordon Davies, Philip Martineau

"*Defects in single-crystal CVD diamond studied using optical spectroscopy with the application of uniaxial stress*"
Poster at the GIA Gemmological Research Conference, 2006
David Charles, Alan T Collins, Gordon Davies, Philip Martineau

"*Optical centres in single-crystal CVD diamond studied using cathodoluminescence spectroscopy with the application of uniaxial stress*"
Presentation at the De Beers 57th Diamond Conference, 2006
David Charles, Alan T Collins, Gordon Davies, Philip Martineau

"*The 533 nm centre in single-crystal CVD diamond*"
Poster at the De Beers 56th Diamond Conference, 2005
David Charles, Alan T Collins, Philip Martineau

Contents

Abstract **2**

Acknowledgments **3**

Publications and presentations **5**

Contents **6**

List of tables **9**

List of figures **12**

1. Introduction and objectives **24**

2. Theoretical background **30**

2.1 Some physical properties of diamond . . . 30

2.1.1 Lattice physics 30

2.1.2 Interaction of light with the diamond lattice . 36

2.1.3 Defects 43

2.2 Optical properties of defects 53

2.2.1 Lattice vibrations and electronic transitions . 53

2.2.2 The zero-phonon line 62

2.2.2.1 Shape of the zero-phonon line . . 62

2.2.2.2 Temperature dependence . . . 67

2.2.2.3 Isotopic substitution . . . 71

2.3 Summary of the major optically active point defects . 75

2.4 Treatment of diamond 78

2.4.1 Irradiation 78

2.4.2 Thermal annealing 80

2.5 Uniaxial stress 84

3. Equipment and methods 88
3.1 Absorption spectroscopy 88
3.2 Photoluminescence spectroscopy 93
3.3 Cathodoluminescence spectroscopy 96
3.4 Spectroscopic considerations 100
3.5 Temperature dependence measurements 103
3.6 Other characterisation techniques 104

4. General characterisation of single-crystal CVD diamond . 107
4.1 Introduction 107
4.2 Samples studied 113
4.3 Common optical spectrum features of the CVD diamonds studied 117
4.4 Cathodoluminescence of DeB #1 131
4.5 Cathodoluminescence of Ap4 139

5. Preferentially oriented defects 143
5.1 Introduction 143
5.2 Results 150
5.2.1 Uniaxial stress measurements 150
5.2.2 Temperature dependence 160
5.2.3 Nitrogen isotope dependences 171
5.3 Discussion 173

6. Investigation of other defects 178
6.1 The 467.2 nm ZPL 178
6.1.1 Introduction 178
6.1.2 Results 179
6.1.2.1 Uniaxial stress measurements . . 179
6.1.2.2 Identification of the vibronic band . 182
6.1.2.3 Temperature dependence . . . 185
6.1.3 Discussion 187
6.2 The 510.3 nm ZPL 189

6.2.1 Introduction 189
6.2.2 Temperature dependence 190
6.3 The 532.7 nm ZPL 193
6.3.1 Introduction 193
6.3.2 Results 197
6.3.2.1 Uniaxial stress measurements . . 197
6.3.2.2 Identification of the vibronic band . 201
6.3.2.3 Temperature and nitrogen isotope dependence 205
6.3.3 Discussion 208
6.4 The 736.8 nm ZPL – the silicon-vacancy . . . 209
6.4.1 Introduction 209
6.4.2 Results 215
6.4.2.1 Annealing behaviour . . . 215
6.4.2.2 Liquid helium temperature absorption . 218
6.4.2.3 Uniaxial stress measurements . . 224
6.4.3 Discussion 230
6.5 Nitrogen-isotope-induced energy shifts of various ZPLs . 231

7. Conclusions and further work 235

8. References 237

List of tables

1.1	Type classification of diamond.	26
2.2.1	Variation of the coefficient of lattice expansion of diamond with temperature, after Slack and Bartram (1975). Error in α estimated to be ± 15 %.	70
2.3.1	Some properties of the major optically active defect centres in diamond. Defects can be observed in absorption (A), cathodoluminescence (CL) or photoluminescence (PL). 'V' means vacancy, 'N' means nitrogen, 'C' means carbon, 'Si' means silicon. Superscript 0, -, and + correspond to the charge state of the defect.	76
4.2.1	Some properties of the CVD samples studied. N_s means substitutional nitrogen, measured in parts per billion (ppb). *NM* means not measured. *ILC* means immeasurably low concentration.	114
4.2.2	Some properties of the HPHT samples studied.	114
4.3.1	Statistically averaged peak wavelength, energy and FWHM of the ZPLs studied in this work.	119
4.3.2	Summary of observed features in the cathodoluminescence spectra of the single-crystal CVD diamonds studied in this work. Error in measurements of ± 0.025 nm, ± 0.108 meV. 'N' means nitrogen, 'C_I' means interstitial carbon, 'V' means vacancy, 'u' means un-measurable, 'Z' means ZPL, 'b' means band. Features highlighted in grey indicate a structured group of lines. Features highlighted in blue have been investigated in this work.	124
4.3.3	Summary of all observed features in the UV-visible absorption spectra of the single-crystal CVD diamonds studied in this work. Error in measurements of ± 0.025 nm, ± 0.108 meV. 'N_s' means substitutional nitrogen, 'N' means nitrogen, 'V' means vacancy, 'u' means un-measurable, 'Z' means ZPL, 'b' means	125

band. The feature highlighted in blue has been investigated in this work. The features highlighted in yellow have only been observed in a brown colouration in sample DeB #1 (see section 4.4)

4.3.4 List of the wavelength, energy and normalised intensity of each line in the series between ~ 455 and 485 nm in the single-crystal CVD diamonds studied in this work. 127

5.2.1 Comparison of theoretical and observed ZPL intensities for the preferentially oriented centres, showing <110> anisotropies. 151

5.2.2 The effects upon the ZPL of a defect centre with rhombic I symmetry undergoing an A ↔ B transition, as observed in absorption or luminescence spectroscopy. The 'A' parameters show how the energy of the ZPL components vary under each stress direction, i.e. parallel to the [001], [111] or [110] orientations. The ratios show the relative intensities of the observed components at high stress. After Mohammed *et al* (1982). 152

5.2.3 Calculated values of the stress-splitting parameters for the preferentially oriented centres. The first set for the 562.5 nm centre are those for the fit to a monoclinic I symmetry, and the second for a rhombic I symmetry. The values are in meV GPa^{-1} with an error of ± 0.30 meV GPa^{-1}. 153

5.2.4 The effects upon the ZPL of a defect centre with monoclinic I symmetry undergoing an A'' ↔ A' transition, as observed in absorption or luminescence spectroscopy. The 'A' parameters show how the energy of the ZPL components vary under each stress direction, i.e. parallel to the [001], [111] or [110] orientations. The ratios show the relative intensities of the observed components at high stress. After Mohammed *et al* (1982). 157

6.1.1 Comparison of the stress-parameters for the defects centres with ZPL at 466.6 and 467.2 nm. Stress-parameter values are in meV GPa^{-1}; errors have been omitted for clarity – see the appropriate 188

sections for values.

6.5.1 ZPL energy shifts of various centres in nitrogen-15 doped samples. Values are the differences between the ZPL energies measured in the nitrogen-15 doped samples and the undoped samples. 233

7.1 Summary of the properties the ZPLs investigated in this work. Italicised properties are tentative. 236

List of figures

1.1	Schematic of a microwave cavity resonator used for CVD diamond growth (after Benndorf *et al* (1996)).	28
2.1.1	Phonon dispersion relation for a monatomic infinite linear chain of atoms, as in equation 2.1.1.	32
2.1.2	Lattice absorption of high-purity, type IIa CVD diamond at 77 K.	36
2.1.3	Upper limit of the absorption window of a type IIa natural diamond at room temperature.	37
2.1.4	Typical cathodoluminescence spectrum from an as-grown single-crystal CVD diamond.	38
2.1.5	Schematic depiction of the shell model of an atomic lattice, after Elliot and Gibson (1976). Grey-filled circles represent nuclei, and dashed circles represent electron spheres. See text for details.	39
2.1.6	Lattice absorption bands of silicon, at various temperatures, after Collins and Fan (1954).	41
2.1.7	Near-infrared absorption of a high nitrogen concentration natural type IaB diamond at 300 K.	42
2.1.8	Schematic representations of two types of extended crystallographic defect. In (a), a monatomic simple square lattice, with atoms represented by grey-filled circles, shows a line dislocation, where the fifth column of atoms extending upwards from bottom terminates after four lattice sites; the lattice deforms and continues upwards. In (b), a simple two-dimensional representation of grain boundaries (red lines) separating growth sectors of different orientations (represented by shading direction).	43
2.1.9	Calculated strain field of a [110] dislocation in silicon [Gattinoni (2007)]. Dark blue regions indicate compressive strain, dark red regions indicate expansive strain.	45

2.1.10	Cathodoluminescence spectra of a single-crystal CVD diamond, in a highly dislocated region of the sample. Main spectrum shows the 429 nm (2.89 eV) dislocation-related luminescence band. Inset shows a high resolution spectrum of the 532.7 nm (2.327 eV) ZPL from the same region of the sample; note the splitting of the ZPL.	46
2.1.11	Schematic representation of some basic types of point defect in a two-dimensional, simple square lattice. Grey-filled circles represent the atoms comprising the regular lattice. The dotted, unfilled circle represents a vacancy. The shaded circle embedded between lattice sites represents a self-interstitial. The large blue circle represents an impurity atom. Note the deformations of the local lattice regions in response to the presence of the defects.	47
2.1.12	Figure 1 from Mita (1996). Demonstrates the change in absorption spectra of a synthetic type Ib diamond after neutron irradiation (concentration values inset). Spectrum (b) shows the reduction in intensity of the 637 nm ZPL (the $(N\text{-}V)^-$), and the presence of the 575 nm ($(N\text{-}V)^0$)and 594 nm ZPLs after heavy irradiation. This is due to a lowering of the Fermi level causing charge transfer from the $(N\text{-}V)^-$, leaving neutral (N-V) centres.	50
2.2.1	Demonstrative configurational coordinate diagram: a schematic representation of the vibrational potentials of a defect. See text for details.	53
2.2.2	Schematic diagrams showing electronic transitions between energy states of a defect. See text for details.	59
2.2.3	Example fit of a quadratic function to the coefficient of lattice expansion data, in order to interpolate between data points: $\alpha(T) = (1.221\times10^{-11})T^2 - (3.332\times10^{-10})T$.	70
2.4.1	Generalised relationship between activation energy and annealing temperature.	83
3.1.1	Schematic diagrams of the experimental equipment used in	91

this work. a) Schematic representation (plan view) of the visible region absorption spectrometer. b) Representation of the copper sample holder, with indium to embed the sample. c) Representation of the cryostat used to hold the cold-finger and copper sample holder. See text for further details of all diagrams.

3.2.1 Schematic diagram of the photoluminescence spectrometer system used in this work (side view). 95

3.3.1 Schematic diagram of the cathodoluminescence spectrometer system used in this work (plan view). 99

3.4.1 Calibration of the CL spectrometer's monochromator using calibration lines across the range of the monochromator. Shows the variation of the measured calibration lines in the spectra compared to the known literature values; hence showing the drift of the monochromator. Uncertainty in the measured values is ± 0.025 Å. 100

3.4.2 Inline calibration of a cathodoluminescence system schematic (plan view). 101

4.1.1 Typical cathodoluminescence spectrum of a single-crystal CVD diamond. See text for explanation of the highlighted features. 110

4.3.1 Cathodoluminescence spectrum of the optical features characteristic of single-crystal CVD diamond in the visible range. See text for label details. 117

4.3.2 Cathodoluminescence spectra of ZPLs A and B (466.6 and 467.2 nm, respectively) in four single-crystal CVD samples. The upper spectrum is from a sample grown by the University of Paris XIII, the lower ones recorded from samples grown by Element Six. Note the non-constant relative intensities. Spectra have been displaced and scaled for clarity. 119

4.3.3 High resolution cathodoluminescence scans over line E, the 532.7 nm ZPL. a) the peak shows minimal splitting. b) the 121

peak demonstrates the often observed shoulder.

4.3.4 Spectra of the 737 nm doublet (at liquid nitrogen temperature) in an irradiated and annealed single-crystal CVD diamond grown with silicon in the gas phase; spectra recorded in a) absorption, and b) cathodoluminescence. 122

4.3.5 Typical photoluminescence spectrum of a single-crystal CVD diamond, excited using a 325 nm HeCd laser, showing weak luminescence from a number of the ZPLs observed in the CL spectra. 126

4.3.6 Cathodoluminescence spectra of two samples of single-crystal CVD diamond grown by Element Six, showing the 637 nm (1.945 eV) centre, along with the 575 nm (2.156 eV) centre. 126

4.3.7 Cathodoluminescence spectrum of the series of weak sharp lines between ~ 455 and 485 nm, observed in the single-crystal CVD diamonds studied in this work. The two intense ZPLs present are the 466.6 and 467.2 nm lines. 127

4.3.8 Figure 4.3.8 – Comparison of the energies of the most intense transitions in the 2.56 to 2.71 eV range with the calculated energies as determined by the DAPR model simulation. The dotted line shows a 1:1 ratio with the observed transition energies, in order to highlight the scatter found at higher energy. 130

4.4.1 A schematic diagram of the DeB #1 sample. 131

4.4.2 Absorption spectrum of the DeB #1 sample, recorded with the sample at liquid nitrogen temperature. 132

4.4.3 Absorption spectra of the DeB #1 sample, at liquid nitrogen temperature. The blue spectrum is the absorption measured through the clear region of the sample. The pink spectrum is the absorption measured through the brown region of the sample. 133

4.4.4 Comparative composite cathodoluminescence spectra of the clear (blue, upper spectrum), and brown (pink, lower 134

spectrum) sides of sample DeB #1. Spectra have been displaced and scaled for clarity – relative intensities should not be inferred from this spectrum.

4.4.5 Cathodoluminescence spectra of the clear (blue, upper spectrum) and brown (pink, lower spectrum) sides of sample DeB #1. Spectra have been displaced for clarity. These are not composite plots; hence relative intensities may be inferred. 135

4.4.6 Comparative CL spectra showing how a generated Gaussian peak (orange spectrum, superimposed on the lowest, black spectrum – the unmodified CL spectrum of the brown side of DeB #1), can produce a modified spectrum (pink, middle) which appears qualitatively similar to the CL spectrum of the clear side (blue, upper spectrum). Spectra have been displaced vertically for clarity. 136

4.4.7 Cathodoluminescence spectrum of the brown side of sample DeB #1. 137

4.4.8 Cathodoluminescence spectrum of sample DeB #1. 138

4.5.1 Cathodoluminescence spectrum of sample Ap4 139

4.5.2 Cathodoluminescence spectrum of sample Ap4, showing the 574.8 nm ZPL and vibronic band. 140

4.5.3 Cathodoluminescence spectrum of sample Ap4, showing broad-band luminescence at ~ 387 nm (~ 3.2 eV). 141

4.5.4 Cathodoluminescence spectrum of sample Ap4, showing the 389 nm (3.188 eV) and 441 nm (2.808) eV centres. 141

5.1.1 Cathodoluminescence spectrum of a single-crystal CVD diamond. Defect centres with zero-phonon lines highlighted in red show preferential orientation. 144

5.1.2 Variation across six single-crystal CVD diamonds of the ratio of integrated intensities (in CL) of each of the three ZPLs with respect to the other two. a) is for the 466.6 nm ZPL, and b) is for the 496.8 nm ZPL. 144

5.1.3 a) Representation of the crystallographic axes of an oriented 146

CVD diamond sample. b) Schematic representation of the sample chamber of the cathodoluminescence spectrometer, modified for the incorporation of a uniaxial stress system: the electron-beam (dashed line) is incident on the sample. Luminescence follows the paths indicated through a converging lens and a polariser (thick black line) into the monochromator (not shown). The crystal is initially oriented with its <001> axis parallel to the arrow. The polariser can be aligned parallel to the arrow, or rotated by $\pi / 2$ into the page, to align parallel to a <110> axis.

5.1.4 Cathodoluminescence spectra of single-crystal CVD diamond oriented with <001> axis vertical; electron beam incident on a <110> face. In a) the upper (blue) spectrum shows the luminescence observed when polarised perpendicular to the <001> direction, i.e. along the <110> direction; the lower (pink) spectrum shows the luminescence observed when the luminescence is polarised parallel to the <001> axis. Note the missing ZPLs at 466.6 and 496.8 nm in the lower spectrum. The spectra in b) have the same experimental parameters as in a). Note the missing ZPL at 562.5 nm in the lower spectrum. 147

5.2.1 Uniaxial stress splitting data for the 466.6 nm (2.656 eV) centre in cathodoluminescence, showing change in energy of ZPL components as a function of applied stress. Data points are experimental results, lines are calculated from the fit to a rhombic I symmetry. a) ZPL under <001> compression (**S**); crosses are for electric vector of luminescence $\mathbf{E} \parallel \mathbf{S}$; unfilled circles are for $\mathbf{E} \perp \mathbf{S}$. b) ZPL under <111> compression; crosses are for $\mathbf{E} \parallel \mathbf{S}$; unfilled circles are for $\mathbf{E} \perp \mathbf{S}$. c) ZPL under [110] compression; crosses are for $\mathbf{E} \parallel \mathbf{S}$ when viewing along; unfilled circles are for $\mathbf{E} \perp \mathbf{S}$ when viewing along [001], filled circles for $\mathbf{E} \perp \mathbf{S}$ when viewing along $[1\,\bar{1}\,0]$. Stick diagrams show 153

relative intensities of stress-split ZPL components at maximum recorded stress, with vertical lines above the horizontal line representing **E**$\parallel$**S**, and vertical lines below representing **E**$\perp$**S**.

5.2.2 Uniaxial stress splitting data for the 496.8 nm (2.495 eV) centre in cathodoluminescence, showing change in energy of ZPL components as a function of applied stress. Data points are experimental results, lines are calculated from the fit to a rhombic I symmetry. a) ZPL under <001> compression (**S**). b) ZPL under <111> compression. c) ZPL under [110] compression. Data point notation as in 5.2.1. Stick diagrams show relative intensities of stress-split ZPL components at maximum recorded stress, with vertical lines above the horizontal line representing **E**$\parallel$**S**, and vertical lines below representing **E**$\perp$**S**. 155

5.2.3 Uniaxial stress splitting data for the 562.5 nm (2.204 eV) centre in cathodoluminescence, showing change in energy of ZPL components as a function of applied stress. Data points are experimental results, lines are calculated from the fit to a rhombic I symmetry. a) ZPL under <001> compression (**S**). b) ZPL under <111> compression. c) ZPL under [110] compression. Data point notation as in 5.2.1. Stick diagrams show relative intensities of stress-split ZPL components at maximum recorded stress, with vertical lines above the horizontal line representing **E**$\parallel$**S**, and vertical lines below representing **E**$\perp$**S**. 158

5.2.4 Temperature dependence measurements of the 466.6 nm (2.657 eV) ZPL in CVD diamond, recorded in cathodoluminescence. a) shows variation of integrated intensity of the peak with temperature, b) that for the peak energy, and c) that for the FWHM. Data points in all figures are the measured data. Lines through the data are the theoretical fits, see text for details. 160

5.2.5 Temperature dependence measurements of the 496.8 nm (2.495 eV) ZPL in CVD diamond, recorded in cathodoluminescence. a) shows variation of integrated intensity of the peak with temperature, b) that for the peak energy, and c) that for the FWHM. Data points in all figures are the measured data. Lines through the data are the theoretical fits, see text for details. 161

5.2.6 Temperature dependence measurements of the 562.5 nm (2.204 eV) ZPL in CVD diamond, recorded in cathodoluminescence. a) shows variation of integrated intensity of the peak with temperature, b) that for the peak energy, and c) that for the FWHM. Data points in all figures are the measured data. Lines through the data are the theoretical fits, see text for details. 163

5.2.7 Temperature dependence of the peak energy of the 575 nm (2.156 eV) centre in CVD diamond, measured in cathodoluminescence. Data points show measured values, lines show theoretical fits – see text for details. 167

5.3.1 a) Schematic diagram of a rhombic I configured molecule, showing the V-X-V configuration. b) Schematic diagram of a monoclinic I configured molecule. 176

6.1.1 Uniaxial stress splitting data for the 467.2 nm (2.653 eV) centre in cathodoluminescence, showing change in energy of ZPL components as a function of applied stress. Data points are experimental results, lines are calculated from the fit to a rhombic I symmetry. a) ZPL under <001> compression (**S**); crosses are for electric vector of luminescence $\mathbf{E} \parallel \mathbf{S}$; unfilled circles are for $\mathbf{E} \perp \mathbf{S}$. b) ZPL under <111> compression; crosses are for $\mathbf{E} \parallel \mathbf{S}$; unfilled circles are for $\mathbf{E} \perp \mathbf{S}$. c) ZPL under [110] compression; crosses are for $\mathbf{E} \parallel \mathbf{S}$ when viewing along; unfilled circles are for $\mathbf{E} \perp \mathbf{S}$ when viewing along [001], filled circles for $\mathbf{E} \perp \mathbf{S}$ when viewing along $[1\,\bar{1}\,0]$. Stick diagrams show 180

relative intensities of stress-split ZPL components at maximum recorded stress, with vertical lines above the horizontal line representing **E**$\parallel$**S**, and vertical lines below representing **E**$\perp$**S**.

6.1.2 Cathodoluminescence spectrum of two single-crystal CVD diamond samples, demonstrating the variation of the 467.2 nm ZPL intensity with that of the band centred at ~ 480 nm. 182

6.1.3 Huang-Rhys factor of the 467.2 nm ZPL and band at ~ 480 nm, over a number of samples. Full line is the average of the values. 183

6.1.4 Cathodoluminescence spectrum of the 467.2 nm (2.653 eV) ZPL and associated band at 480.7 nm (2.579 eV). Dashed blue line is the assumed background luminescence function, full red line is a Gaussian fitted to the experimental spectrum, centred at 2.579 eV with a FWHM of 18 meV. 184

6.1.5 Temperature dependence of the peak energy of the 467.2 nm (2.653 eV) ZPL in CVD diamond, recorded in cathodoluminescence. See text for details. 186

6.2.1 Temperature dependence measurements of the 510.3 nm (2.429 eV) ZPL in CVD diamond, recorded in cathodoluminescence. a) shows variation of integrated intensity of the peak with temperature, b) that for the peak energy, and c) that for the FWHM. Data points in all figures are the measured data. Lines through the data are the theoretical fits, see text for details. 190

6.3.1 Uniaxial stress splitting data for the 532.7 nm (2.327 eV) centre in cathodoluminescence, showing change in energy of ZPL components as a function of applied stress. Data points are experimental results, lines are calculated from the fit to a rhombic I symmetry. a) ZPL under <001> compression (**S**); crosses are for electric vector of luminescence **E**$\parallel$**S**; unfilled circles are for **E**$\perp$**S**. b) ZPL under <111> compression; crosses are for **E**$\parallel$**S**; unfilled 198

circles are for **E⊥S**. c) ZPL under [110] compression; crosses are for **E∥S** when viewing along; unfilled circles are for **E⊥S** when viewing along [001], filled circles for **E⊥S** when viewing along [$1\bar{1}0$]. Stick diagrams show relative intensities of stress-split ZPL components at maximum recorded stress, with vertical lines above the horizontal line representing **E∥S**, and vertical lines below representing **E⊥S**.

6.3.2 Typical cathodoluminescence spectrum of a single-crystal CVD diamond, showing the 532.7 nm ZPL and the weak band at ~ 549 nm; a) broad scan of the local region, b) the ZPL and band, corrected for background luminescence. 201

6.3.3 Intensity ratio of the band at ~ 549 nm to the 532.7 nm ZPL, measured over six samples. Data points are recorded data, full line is the average ratio. 203

6.3.4 Temperature dependence measurements of the 532.7 nm (2.327 eV) ZPL in CVD diamond, recorded in cathodoluminescence. a) shows variation of integrated intensity of the peak with temperature, and b) that for the peak energy. Line through the peak energy data is the theoretical fit, see text for details. 205

6.4.1 Integrated intensities of the GR1 and 737 nm ZPLs after each annealing stage (data points). Lines show the theoretical change in absorption after each stage (see text). Data and fit for the 737 nm doublet are scaled by a factor of ten for clarity. 216

6.4.2 Comparison of absorption of the 1.6827 eV centre at liquid nitrogen temperature (77 K, dotted spectrum) and at liquid helium temperature (less than 40 K, full line spectrum, displaced vertically). 219

6.4.3 Absorption spectra of the 1.6827 eV centre at liquid helium temperature in a natural abundance silicon-28 sample, after irradiation and annealing (lower spectrum, scaled by a 220

factor of three), and a silicon-29 enriched sample (upper spectrum). Spectra are displaced vertically for clarity. Peak labels as Clark *et al* (1995).

6.4.4 Absorption spectrum of the 1.6827 eV centre at liquid helium temperature in a natural abundance silicon-28 sample, after irradiation and annealing (lower spectrum), and a generated absorption spectrum using bi-Lorentzians (upper spectrum). Spectra have been displaced vertically for clarity. 222

6.4.5 Absorption spectrum of the 1.6827 eV centre at liquid helium temperature in a silicon-29 enriched sample (lower spectrum), and a generated absorption spectrum using bi-Lorentzians (upper spectrum). Spectra have been displaced vertically for clarity. 222

6.4.6 Generated spectrum for the Si-29 enriched 1.6827 eV absorption system. The lower bi-Lorentzian peaks show the component transitions, and the upper spectrum shows the convolution of these. See text for identification of component patterns. Peak labels as Clark *et al* (1995). 223

6.4.7 Uniaxial stress splitting data for the 736.8 nm (1.682 eV) centre in absorption, at LNT, showing change in energy of ZPL components as a function of applied stress. Data points are experimental results, lines are guides (not theoretical fits). a) ZPL under <001> compression (**S**); crosses are for electric vector of luminescence $\mathbf{E} \parallel \mathbf{S}$; unfilled circles are for $\mathbf{E} \perp \mathbf{S}$. b) ZPL under <111> compression; crosses are for $\mathbf{E} \parallel \mathbf{S}$; unfilled circles are for $\mathbf{E} \perp \mathbf{S}$. c) ZPL under [110] compression; crosses are for $\mathbf{E} \parallel \mathbf{S}$ when viewing along; unfilled circles are for $\mathbf{E} \perp \mathbf{S}$ when viewing along [001], filled circles for $\mathbf{E} \perp \mathbf{S}$ when viewing along $[1\,\bar{1}\,0]$. 225

6.4.8 Variation of relative intensity of the components of the 737 nm doublet, as a function of stress. 227

6.4.9 Uniaxial stress effects on the 736.8 nm (1.682 eV) doublet 228

at liquid helium temperature, under [001] compression (data taken in absorption). a) Splitting pattern observed for stress from 0 GPa (top spectrum) to 1.4 GPa (lower spectrum) (not a linear selection of stresses). b) Change in energy of the components as a function of stress. Crosses are for electric vector, **E** parallel to the stress direction, **S**; open circles are for E$\perp$**S**. Lines are guides (not theoretical fits).

Chapter 1

Introduction and objectives

This thesis is a report of optical characterisations of point defects in single-crystal diamonds synthesised by microwave-assisted chemical vapour deposition (CVD). Optical spectroscopy of point defects in diamond is a well established field, which has its origins in experiments investigating the potential of diamond as a radiation detector. Systematic studies of natural diamonds proved fruitful in advancing the understanding of point defects in crystalline solids. The innovation of diamond synthesis by the high pressure high temperature (HPHT) technique in the 1950s brought enormous advantages to diamond researchers, as this material allowed much greater control over the investigation of defects than in natural samples. Importantly, it created the opportunity for greater industrial exploitation of the outstanding properties of diamond.

The studies of natural and HPHT synthetic samples has yielded great scientific achievements, such as a thorough understanding of the vacancy in diamond, the kinetics of thermal annealing of radiation damage products, and the first lattice-isotope substitution measurements of a solid. Insights into the properties of point defects have led to a better understanding of macroscopic effects in diamond, such as observed colour, thermal conductivity and electrical mobility. This has created the opportunity to utilise the material in a wide range of industrial and technological fields.

The innovation in the 1980s of using of chemical vapour deposition (CVD) to grow diamond offered extensive control over the growth process, including the ability to dope the synthetic diamonds with a variety of impurity species. The early material was polycrystalline, which resulted in reduced optical quality via the introduction of strain within the lattice. Recent developments of the CVD process in the early 2000s have allowed high-quality, large, single-

crystal samples to be grown, and have created a wealth of possible new uses for the material. It has been found that the quality of the diamonds synthesised by this new method is comparable to that of the best natural diamonds. However, relatively little research has been published on the optical characterisations of point defects in this material. Therefore, the motivation for the present work has been the need for detailed optical data.

There are ultimately two purposes for studying the point defects of diamond: the first is that diamond is an ideal material to investigate fundamental physical theories about the nature of the solid state, due to its regular lattice structure, wide optical transparency, and chemical and temperature hardness; the second reason is that the microscopic properties of a solid – the point defects – contribute to the macroscopic properties, which effect the potential scientific and industrial uses.

Previous researchers have extensively investigated point defects in *polycrystalline* CVD diamonds, and whilst many of those defects are present in single-crystal CVD samples, a large number of optical spectrum features of single-crystal samples appear to be unique to the material, and hence potentially the growth method. Most of these have not been explicitly reported previously, and none have been investigated in depth. The objective then, has been two-fold: first to comprehensively document the features of the optical spectra of a range of untreated single-crystal CVD diamonds; and second to perform detailed characterisations of as many as possible of the point defects in the material.

The detailed characterisation has been to determine the symmetry, nitrogen dependence and vibronic properties of the defects. This information, along with additional data, such as the effects of impurity elements on defect concentrations, allows for plausible atomic models of defects to be formulated. This is important because the presence of defects can have beneficial or detrimental effects on application of the material, depending on the use. The properties of certain defects may be crucial for particular applications (such as boron doping to obtain semi-conducting diamond, or nitrogen-vacancy centres used for single-photon sources; or in a related field – doping of silicon to produce p- and n-type material for use in computer chips), and so a comprehensive understanding of defects in a solid material is essential.

It is shown in this work that a group of point defects observable spectroscopically in the visible-light region, appear to be characteristic of the growth process. Two of the other centres investigated – the silicon-vacancy and the 532.7 nm line – are well-known defects in diamond and have been studied previously, although their symmetries had not been determined experimentally. The 532.7 nm line is considered particularly significant as an identifier of synthetic diamond.

As mentioned above, it is the presence of point defects in the lattice which creates much of the interesting physics of diamonds. Impurities play a large role in this, primarily nitrogen, as it is readily incorporated into the lattice. Early research found that natural diamonds could be separated into two types: those containing aggregated nitrogen impurities, and those which didn't. This categorisation has been sub-divided further as understanding of the nature of the defects developed. Table 1.1 shows the accepted classification of diamond.

Type		Characteristic impurity
Ia		Contains aggregated nitrogen in the A- and B-forms
	IaA	Contains primarily A-form nitrogen
	IaB	Contains primarily B-form nitrogen
Ib		Contains single-substitutional, paramagnetic nitrogen impurities
IIa		Contains very low single-nitrogen concentrations
IIb		Negligible nitrogen concentrations. Contains boron impurities

Table 1.1 – Type classification of diamond.

Approximately 98% of all natural diamonds are of type Ia. The high-quality single-crystal CVD diamonds currently available are of type IIa, showing nitrogen concentrations in the range of ten to a few hundred ppb. As such, it is useful to be able to characterise this material, which is at the higher end of the impurity-related quality scale.

HPHT synthesis of diamond takes place in a press where a capsule of graphite and a metal solvent-catalyst are mixed. A pressure of around 55000

atmospheres is applied and an electric current passed through the graphite / metal mixture in order to heat it to around 1400˚C. The graphite dissolves into the molten metal and diamond crystals nucleate. Transition metals, such as nickel and cobalt are often used as the solvent-catalyst. An inadvertent consequence of this is that the metals can often form impurity centres in the diamond crystals obtained.

An alternative growth technique, still using HPHT is the temperature gradient method, where a layer of graphite or other carbon source is sandwiched between solvent-catalyst layers. In this case a layer of graphite around the growth capsule is heated, after the application of pressure, and hence a temperature gradient is created between the carbon source and the outer graphite; this stimulates the nucleation of diamond crystals. The diamonds produced by HPHT synthesis are single-crystals, but are usually of small dimensions (of the order of a few cubic millimetres or less).

CVD synthesis of diamond can take place in a number of different ways, although microwave plasma is one of the dominant techniques. This is where a gas mixture is pumped through a microwave cavity resonator (see figure 1.1). The mixture is typically > 90% hydrogen and a few percent of methane. A substrate is at the base of the cavity. The microwave energy creates a plasma through dissociation of the gas constituents, and simultaneously heats the substrate to around 800˚C. The dissociated carbon forms diamond nucleation points on the substrate. If a non-diamond substrate is used, then polycrystalline diamonds are formed; if the synthesis is homoepitaxial, then single-crystal diamonds are created. These are the types of samples studied in this work. They are commonly synthesised with dimensions of a few cubic millimetres. Impurity doping of the synthesised samples is possible by including gas-phase chemical species; this can result in deliberate incorporation of, for example, nitrogen, silicon and boron.

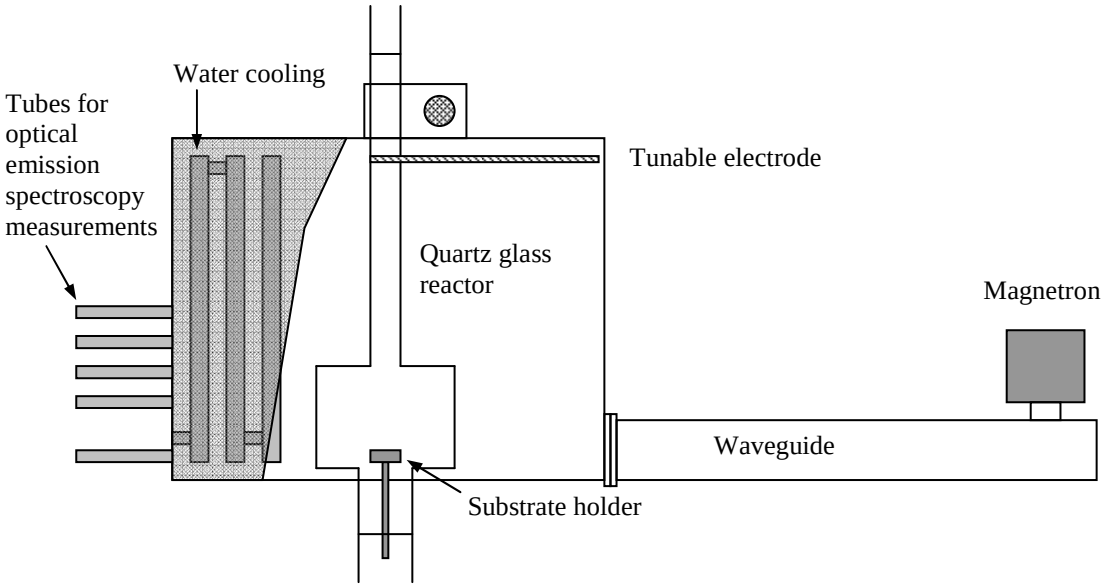

Figure 1.1 – Schematic of a microwave cavity resonator used for CVD diamond growth (after Benndorf *et al* (1996)).

The growth of diamond during CVD is understood to proceed by the interaction of reactive hydrogen: the surface of the substrate / homoepitaxial diamond is saturated by hydrogen, which is dynamically exchanged with gas-phase hydrogen. Occasionally a methane species is deposited, which allows the formation of tetrahedrally bonded carbon at the surface. Any graphitic carbon forms are etched away by hydrogen, allowing exclusive development of diamond.

The presence of gas-phase species other than hydrogen and methane can directly affect the growth process. The incorporation of oxygen is considered to form OH species which more effectively etch graphitic carbon; whilst the presence of nitrogen has been found to increase the growth rate and crystalline quality of the samples. As mentioned above, gas-phase chemical species, whilst affecting the growth process of the material, can also become incorporated into the material, forming complexes which would not otherwise be observed. This can be utilised for analysis and performance of the material, such as non-abundant isotope doping to investigate impurity presence in defects.

The CVD process is relatively cheap, compared to the market cost of obtaining reasonably sized natural diamonds for technical purposes. Diamond

can now readily be used for such applications as laser windows, heat-spreaders, p-type semiconductors, radiation detectors and many more inventive uses.

This work develops the relevant background theory in chapter two, followed in chapter three by details of the experimental techniques used. Chapter four presents results of general characterisations of the material, and chapter five reports the discovery of preferentially oriented defects. Chapter six discusses the investigations into the other defect centres studied, and finally chapter seven draws together the conclusions of the research, along with suggestions for further related investigations.

Chapter 2

Theoretical background

2.1 Some physical properties of diamond

2.1.1 Lattice physics

The bonding of many atoms to form a regular lattice results in observable effects which do not have trivial origins. An understanding of the physics of solids can provide extraordinary insights into properties of crystals via spectroscopic methods; insights which an optical microscope cannot achieve.

The analysis of the complex nature of a solid can be simplified by considering the high symmetry of the system, along with simplifying treatments of the nuclei and electrons. These approaches can provide accurate descriptions of the system and often present surprising implications.

The starting point, perhaps, and one of the most important physical effects is the role played by vibrations of the lattice. Many features of the absorption and luminescence spectra of crystals are explained by considering the vibrations of the lattice, and the periodic nature of the electric potential within the crystal. These give rise to the phenomena of phonons, valence and conduction bands, and the band gap. The following simplified discussion can be found in more detail in many standard solid state textbooks. This work primarily uses Elliot and Gibson (1976) and Kittel (1986).

The atoms within a diamond lattice are connected by covalent bonds, and in a classical description may be considered to form chains of masses bonded by springs. At low temperatures, it is possible to model the motion of the nuclei as performing normal modes of harmonic oscillation. This can be justified as

follows. The simplifying assumption may be used, that the motion of heavy nuclei may be treated independently of that of the light electrons. The potential energy of interaction, *V*, between nuclei varies with distance, and around the equilibrium bonding separation, can be considered to be parabolic. The force acting upon each nucleus is then linear with distance, *R*, as $-\partial V/\partial R$. The oscillations of the masses (nuclei) can then be treated harmonically, and at low energies the motion of each mass is independent and has a characteristic frequency, i.e. normal modes of vibration.

The motion of one mass will be transmitted via the springs to its neighbours, so vibrations may propagate through the lattice. Each unit cell of the lattice will have a distinct amplitude and phase, and hence normal modes of vibration will persist throughout the lattice with characteristic frequencies. This is analogous to a wave, and a wavevector, *K*, may be assigned. Each vibrational mode can have its energy quantised, with energy levels at $\left(n+\frac{1}{2}\right)\hbar\omega$, where ω is the angular frequency of the mode, and *n*, the occupation number, will be either a positive integer or zero. The consequence of this, as is well known in quantum mechanics, is that even when there are no oscillations, i.e. $n=0$, there is a zero-point motion, with an associated energy known as the zero-point energy. These quantised lattice vibrations are called phonons, as an analogy with the quanta of electromagnetic radiation, photons. Furthermore, if one mode of oscillation is in the *n*th state, it is said that there are *n* phonons of that mode. If there is a transition of energy state by a phonon, i.e. a change of occupation number by, for example, *n* to (*n*+1), or (*n*-1), it is said that a phonon has been created or destroyed, respectively.

Solutions of the equations of motion for a system such as masses connected by springs, with associated spring constants, e.g. $F=M\ddot{x}$, can be found, and are known as phonon dispersion relations. It is found that for a monatomic linear chain, i.e. with one atom in the primitive cell, the frequency of a mode of vibration, ω, will be

$$\omega^2=\left(\frac{2C}{M}\right)(1-\cos(Ka)), \qquad \text{or} \qquad \omega(K)=2\left(\frac{C}{M}\right)^{\frac{1}{2}}\sin\left(\frac{1}{2}Ka\right), \qquad 2.1.1$$

where C is a constant related to the spring force constant, M is the mass of an atom, and a is the lattice constant. Plotting this ω as a function of K produces figure 2.1.1. Certain interesting physical consequences can be drawn from this result. The function repeats every $\frac{2\pi}{a}$, over the range $\frac{-\pi}{a}$ to $\frac{+\pi}{a}$, which is the same region as the Brillouin zone – the regions where the wavevectors of lattice vibrations have valid values. Furthermore, due to the translational symmetry of the system, the wavefunctions of particles within the system, such as electrons, are periodic and only defined over the Brillouin zone. When K is small, $\sin(\frac{1}{2}Ka) \rightarrow \frac{1}{2}Ka$, so the frequencies are linear in K. At the edge of the Brillouin zone, when $K = \frac{\pi}{a}$ (and when $\lambda = 2a$), the maximum frequency is found, i.e. no waves of higher frequency can propagate.

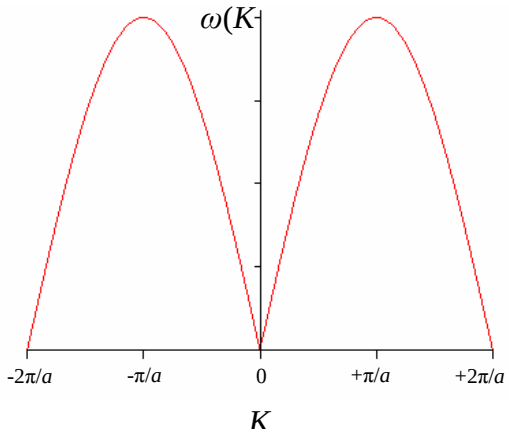

Figure 2.1.1 – Phonon dispersion relation for a monatomic infinite linear chain of atoms, as in equation 2.1.1.

If the primitive cell of the lattice were to have two atoms, such as in diamond, the dispersion relation will have two solutions, each of which is identified as a branch in the ω vs. K plot. The lower frequency branch is known as the *acoustic branch* because the displacements of the atoms in this mode of vibration are similar to that of sounds waves (longitudinal). The higher frequency branch is known as the *optic branch*, because in these vibrational modes, the two

atoms in the primitive cell are displaced in opposite directions; this, if the atoms were of opposite charge, would produce oscillating dipoles and hence electromagnetic radiation would be able to couple to these modes of vibration. More generally, for a three-dimensional lattice, it has been shown that for a primitive cell with n atoms, the dispersion relation has $3n$ branches: 3 acoustical branches and $(3n - 3)$ optical branches.

With the physics of lattice vibrations in mind, the electronic aspects of a crystal lattice can be approached. Describing the behaviour of electrons in covalently bonded crystals is a problem which can be eased by considering the translational symmetry of the system. Before approaching this problem, first consider what happens to the electronic wavefunctions of independent atoms when bonding.

When an atom is independent of other atoms and potentials, its electrons occupy discrete, quantised energy levels, as described by the solutions (i.e. wavefunctions) of the atom's Schrödinger equation. As two similar atoms approach one another their electron wavefunctions begin to overlap; the energy levels of the electrons of both atoms will be perturbed such that no two electrons in the molecule occupy the same energy state. If this were not so, the total wavefunction of the system of electrons, which is the product of each single electron wavefunction, would equal zero (i.e. the Pauli Exclusion Principle). In a many-atom system, this subtle shifting of energy states produces almost continuous regions of valid levels, which can be seen as bands.

Within a crystal, the electronic behaviour will reflect the structure; a first approximation to this is to treat the electrons as non-interacting bodies moving through a potential which is an average of the potential of all the other valence electrons, the core electrons and the nuclei. This is known as the independent electron model. Whilst it ignores the interaction of the valence electrons, it provides a good first approximation. There are two ways of approaching this: the first is to consider the electrons as attached to the nuclei, and the wavefunctions split over these; the second is to consider the electrons as nearly free particles, existing with plane-wave distributions and moving in a periodic potential caused by the nuclei. Thus, the wavefunction (known as a Bloch function) of electron i, with wavevector k, can be expressed as

$$\psi_{ik} = (N\Omega)^{1/2}\, U_{ik}(r) \exp(ik \cdot r), \qquad 2.1.2$$

where N is the number of unit cells, Ω is the volume of the unit cell, r is the position vector, and U_{ik} is the periodic potential due to the nuclei, and describes the unit cell and its atomic properties. The plane-wave function describes the behaviour of the electron across the crystal.

The approach which emphasises the plane wave part of equation 2.1.2 is called the nearly free electron model. The valid solutions of this model, when a small atomic potential is applied, correspond to the range over which the Brillouin zone exists. The approach which emphasises the atomic nature of equation 2.3 is known as the tight-binding approximation, the results of which qualitatively produce band characteristics, such as distortions of degenerate band structures due to relativistic coupling of the spin and orbital motion of the electrons (spin-orbit coupling).

It can be seen that the electron wavefunctions take the form of running waves and obey periodic boundary conditions defined by integer multiples of $\frac{\pm 2\pi}{a}$, where a is the lattice constant. This condition is comparable to that for phonons, above, in an infinite linear chain model of the lattice. Within the periodic boundary conditions, i.e. between, not at, the integer multiples of $\frac{\pm 2\pi}{a}$, the wavefunctions are within the allowed Brillouin zones. At the condition of Bragg reflection of the waves, i.e. at the integer multiples of $\frac{\pm 2\pi}{a}$, the Schrödinger equation has no wavelike solutions: instead, the wavefunctions become the sums of two standing waves, denoted by $\psi(+)$ and $\psi(-)$. For $\psi(+)$, the probability density has maxima at the ion cores, and minima equidistant between them. For $\psi(-)$, the probability density has maxima equidistant between the ion cores, and minima at them.

The band structure of crystal lattices can now be explained as consisting of two major bands known as the valence and conduction bands, with a band gap between them. The valence electrons of the lattice atoms have wavefunctions valid within the valence band, and for any electron to take part in electrical conduction, its wavefunction must be made valid within the conduction band.

The band gap is a forbidden zone for valence electrons due to Bragg reflection causing non-wavelike Schrödinger equation solutions. However, around point defects the electric potential field is distorted (see section 2.1.3), therefore the wavefunctions are not limited by Bragg reflection and may be valid within the band gap.

Band structure helps to explain the classification of metals (i.e. conductors), semiconductors, and insulators: conductors have an overlapping valence and conduction band, making conduction efficient; insulators have a band gap which is too large for electrons to be thermally excited into the conduction band; semiconductors have a band gap which is smaller than an insulator's, so that electrons can undergo thermal excitation into the conduction band at high enough temperatures.

At low energies, the band energy states will be filled sequentially until the valence electrons of the system are exhausted. The highest energy state which is filled at low temperature is called the Fermi level; this is useful to know, for if an impurity atom is present in a crystal, and the number of electrons in the unit cell changes, then the Fermi level will move towards the conduction or valence band. This is an important phenomenon in the observation of certain defects, for example, the neutral and negatively charged nitrogen-vacancy [Mita (1996)]; for further discussion, see Collins (2002), and section 2.1.3.

2.1.2 Interaction of light with the diamond lattice

Theoretically perfect diamond is transparent to photons with energies up to ~ 5.5 eV. This is because the crystal is composed isotropically of covalently bonded carbon atoms, with a homogeneous electric charge distribution. This leaves no electric dipole moments with coupling energies in the above range. There is an exception to this, however: vibrations of the lattice can induce electric dipoles over the range 165 to 495 meV (see figure 2.1.2). This is known as lattice or phonon absorption.

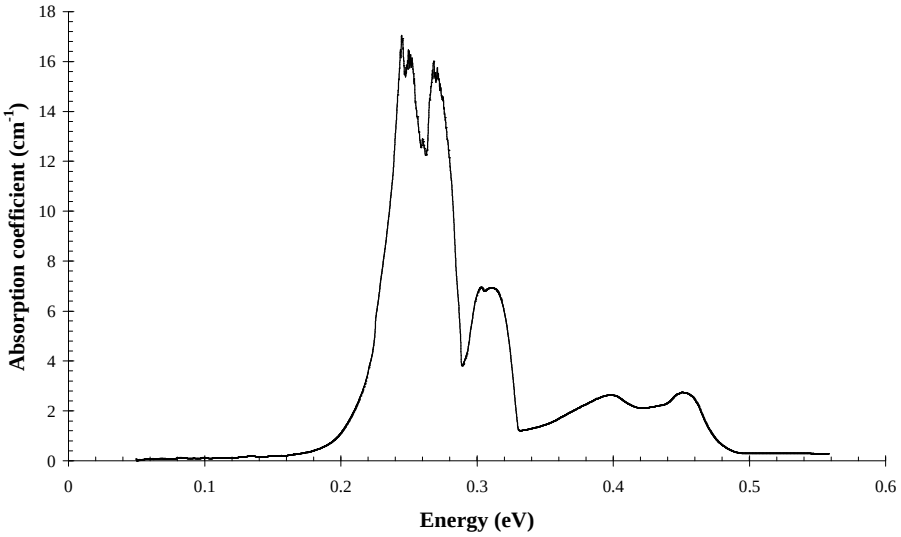

Figure 2.1.2 – Lattice absorption of high-purity, type IIa CVD diamond at 77 K [this work].

The upper energy limit of the diamond transparency window, at 5.48 eV (at 300 K) [Zaitsev (2001)], is the energy at which the valence electrons are excited across the band gap and into the conduction band. This is observed as a sharp cut-off in the absorption spectrum, where beyond this point, the absorption of photons is very intense (figure 2.1.3).

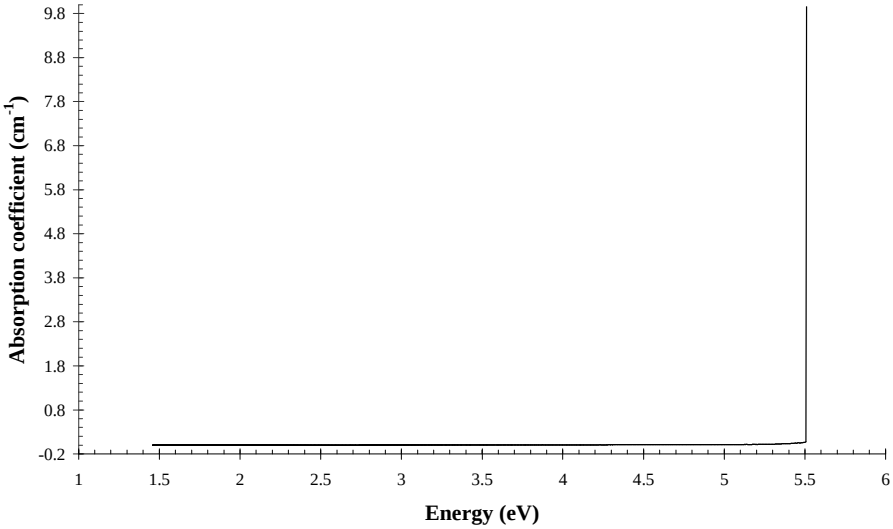

Figure 2.1.3 – Upper limit of the absorption window of a type IIa natural diamond at room temperature [this work].

Perfect diamond would display an absorption spectrum as described above – featureless except for the intrinsic absorption. In reality, however, defects within the crystal can produce optically observable effects such as electronic transitions with energies below 5.5 eV, which can be seen in absorption and emission spectra (for example, figure 2.1.4). The various types of defects found in diamond, and their effects, are discussed in section 2.1.3. It is useful to understand how some of the defects come to produce the effects observed; of primary interest in this work are point defects (atomic-sized defects) – what happens when they make transitions to excited states, and when they subsequently relax. This will be discussed in section 2.2, and will be useful for an understanding of the data presented in later chapters.

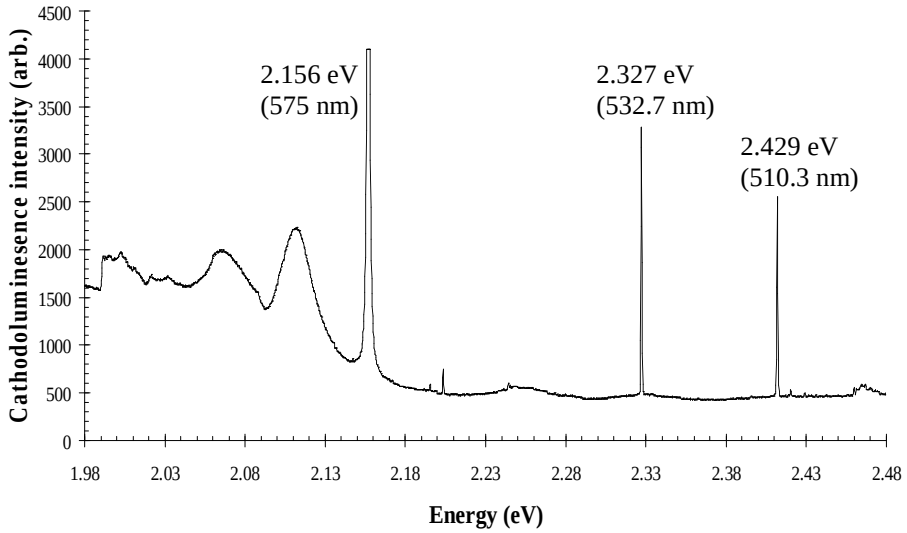

Figure 2.1.4 – Typical cathodoluminescence spectrum from an as-grown single-crystal CVD diamond.

A theoretically pure, homopolar, isotropic covalently bonded crystal, such as diamond or silicon, would have no electric dipoles present at low enough temperature for the nuclei to be considered stationary, as the electric charge density would be homogeneously distributed due to the symmetry of the lattice.

As discussed in section 2.1.1, however, even at low temperatures thermal energy causes vibrations of the nuclei, creating phonons. These can distort the electric charge distribution allowing photons to couple to the lattice. This phenomenon can be understood by considering the electric dipole moments created by the vibrating lattice. Additionally, some simplifying assumptions, known as the shell model, can be used to help provide a qualitative physical description: under this model, the nuclei in the lattice can be treated as masses bonded by springs to each neighbour. Each nucleus can be considered to have a hollow sphere of electrons bound to it by springs. Each sphere of electrons is also bound to the electron sphere of its neighbouring nucleus by springs, so that the lattice can be seen as something like that of figure 2.1.5 [Elliot and Gibson (1976)]. The assumption is made that the nuclei are heavy relative to the electron spheres, and that the electrons respond harmonically and instantaneously to the motion of the nuclei via the springs.

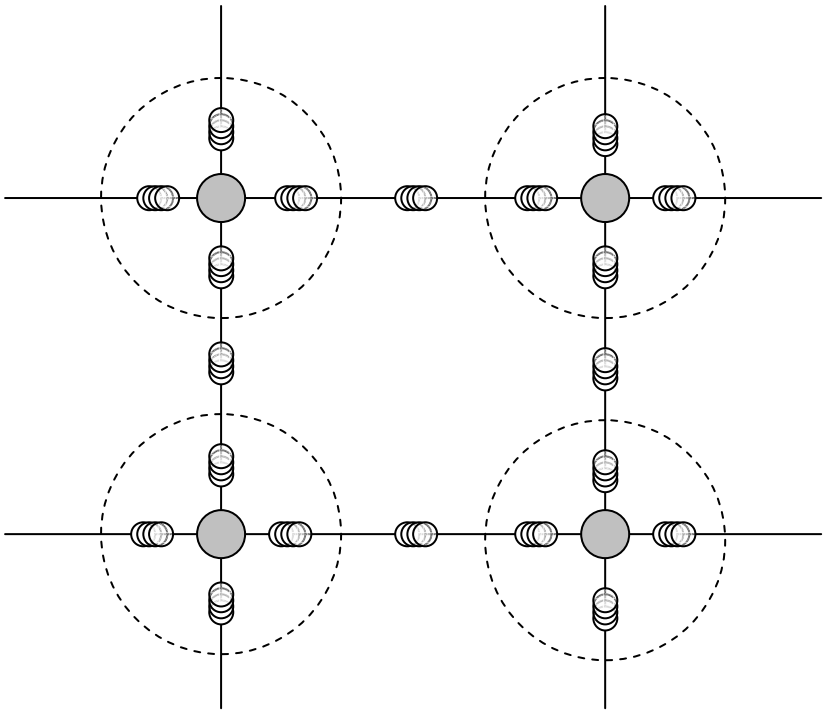

Figure 2.1.5 – Schematic depiction of the shell model of an atomic lattice, after Elliot and Gibson (1976). Grey-filled circles represent nuclei, and dashed circles represent electron spheres. See text for details.

First, consider the presence of one phonon in a hypothetically perfect diamond lattice: it can be seen via the shell model that this produces a displacement of the electron spheres. However, the charge distribution is merely translated homogeneously with the movement of the nuclei. More quantitatively, the expansion of the dipole moments for a model diamond-like lattice shows that there are multiple orders of moment, and that the coefficients of these are not all independent due to symmetry considerations, i.e. some coefficients can be grouped according to symmetry operations. It is found that the first order dipole moments vanish due to the inversion and translation invariance of the unit cell of diamond [Lax and Burstein (1955)]. This means that one phonon alone cannot create electric dipoles associated with the lattice.

Next, if two phonons are present, the interaction between them can result in anharmonic oscillations of neighbouring electron spheres, causing inhomogeneous charge distributions and hence electric dipoles. The mechanism can be seen as one phonon momentarily inducing a charge by displacing the electron spheres. Whilst this would normally then translate homogeneously, as

mentioned above, if a second phonon is present it can “catch” the disturbed charge and cause the electron spheres to oscillate, thus creating a dipole moment. In terms of the dipole moment expansion, this is found by examining the second order moments [Lax and Burstein (1955)]: this can be summarised compactly as $M = x_{t'} C x_t$, where M is the electric dipole moment that is created when the mode x_t induces a charge C, which is subsequently set to vibrate in the mode $x_{t'}$.

It would be reasonable to expect that if there can be two phonons interacting to produce dipole moments associated with the lattice then there could be interactions involving three or more. Indeed, diamond shows phonon absorption bands over the region 330 to 495 meV, where three phonons would be expected to interact (165 meV being the maximum phonon energy in diamond). These can be considered to occur from third order moments. Silicon shows absorption due to two and three phonons, and also appears to display absorption due to fourth order moments [Litvinov et al (2000)]. Higher order phonon absorption in diamond and silicon may not be observed as the multiple phonons could reduce to combinations of two, three and four phonon interactions.

As may be expected, the combination of modes involved can be many and complex. It is found that selection rules constrain the dipole moments to certain modes – the two phonons involved cannot originate from the same branch. Furthermore, the second order moments lead to phonon transitions, i.e. the creation and destruction of two phonons (the first order moments produce single phonon transitions, but these go to zero due to symmetry reasons, as above). This produces two bands in the lattice absorption spectrum: a summation band, and a difference band, of the two phonons involved in the interaction. For example the induced second order dipole moment corresponding to a transverse optical and transverse acoustic (TO + TA) phonon interaction can be observed in figure 2.1.6 as the most intense absorption peak close to 600 cm^{-1}. Assignments for each peak in the phonon absorption spectra of diamond and silicon can be made, see for example Yu and Cardona (2001).

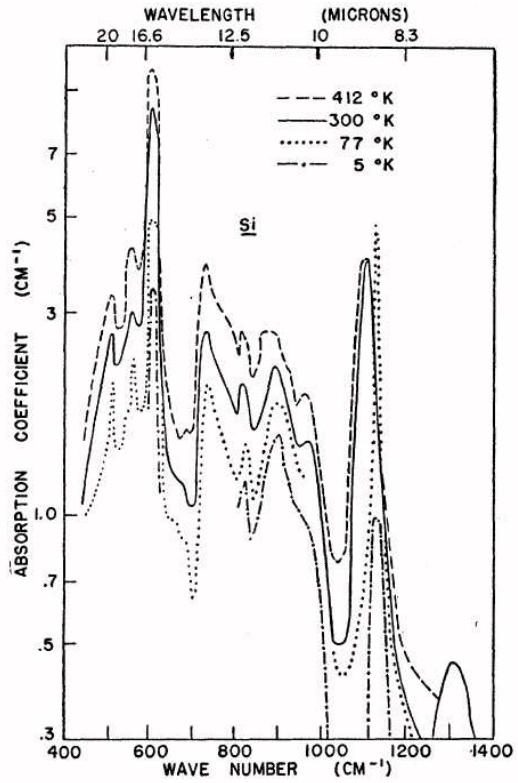

Figure 2.1.6 – Lattice absorption bands of silicon, at various temperatures, after Collins and Fan (1954).

The lattice absorption spectra of diamond and silicon can be seen in figures 2.1.2 and 2.1.6, respectively. These figures show the two and three phonon absorption regions. The sample used to measure the absorption in figure 2.1.2 is a high-purity CVD synthesised diamond, of type IIa, and it can be seen that the one-phonon region (below 165 meV) is free from absorption features, as predicted. Diamonds of type Ia, containing aggregated nitrogen impurities, show absorption features in what is then called the defect-induced one-phonon region. This is because, in terms of the shell model, the electric charge distribution around a defect may be different to that around its local lattice region, so one phonon alone can perturb the electron spheres enough to induce electric dipoles localised at the defect. This is demonstrated in figure 2.1.7, the absorption spectrum of a high nitrogen concentration natural type IaB diamond.

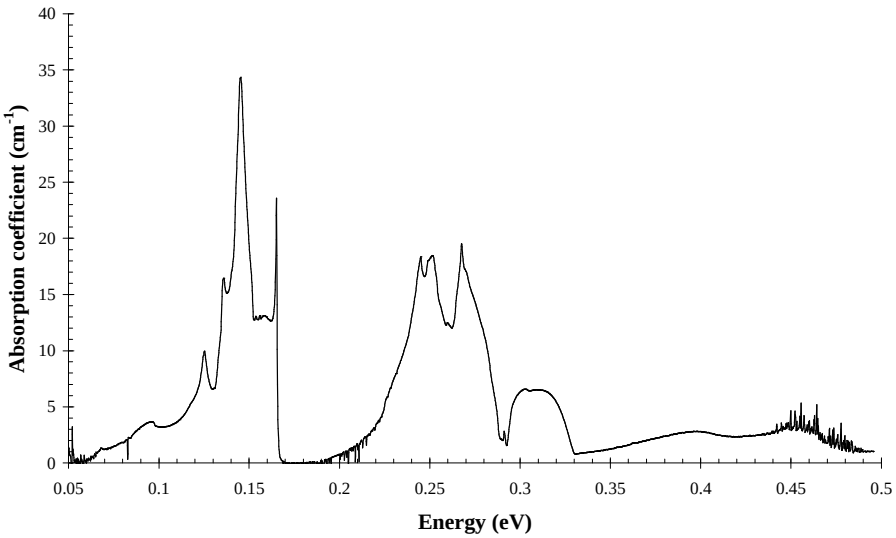

Figure 2.1.7 – Near-infrared absorption of a high nitrogen concentration natural type IaB diamond at 300 K. Nitrogen concentration estimated as ~ 1300 ppm.

Finally, it is worth noting the effects of temperature on the lattice absorption. Collins and Fan (1954) investigated this in silicon (figure 2.1.6), germanium and diamond and found that the absorption intensity is a function of the average displacement of the nuclei. Whilst this relationship holds in general, Lax and Burstein (1955) proposed that at temperatures well below the Debye temperature, $k_B T \ll \hbar\omega_{max}$ (where k_B is the Boltzmann constant, T is the temperature and $\hbar\omega_{max}$ is the maximum phonon energy), the average phonon occupation number becomes much less than one. This means that at these temperatures there are no phonons present in the lattice, and it is only upon examination of the crystal by absorption spectroscopy that phonons are created – by the absorption of photons. The mechanism for this can be understood as the presence of the photon's oscillating electric field inducing a small perturbation in the electron spheres as it passes through the lattice, which changes the charge distribution and creates dipoles. These in turn perturb the nuclei and create further phonons, accentuating the dipole creation effect (see, for example Pankove (1971) and Yu and Cardona (2001)).

2.1.3 Defects

Crystallographic defects are departures from the uniformity of the perfect crystal lattice. These can be grouped into two main categories: extended defects, and localised defects. Extended defects are structural changes in the lattice which can extend over many orders of magnitude of atomic spacings in one, two and three dimensions. Examples of one-dimensional defects are dislocations, where a plane of atoms terminates before the edge of the crystal is reached; and screw dislocations, where the lattice is helically rotated around a dislocation. An example of a two-dimensional defect is a grain boundary, where differently oriented growth sectors meet. An example of a three dimensional defect is an inclusion, where intrinsic (comprised of the constituents of the lattice) or extrinsic (i.e. impurities) point defects precipitate into three dimensional structures. Figure 2.1.8 schematically demonstrates some of these.

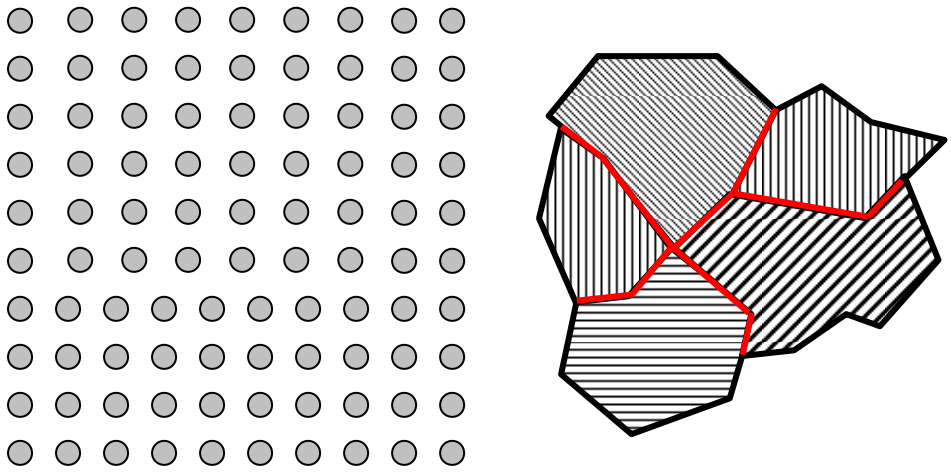

(a) (b)

Figure 2.1.8 – Schematic representations of two types of extended crystallographic defect. In (a), a monatomic simple square lattice, with atoms represented by grey-filled circles, shows a line dislocation, where the fifth column of atoms extending upwards from bottom terminates after four lattice sites; the lattice deforms and continues upwards. In (b), a simple two-dimensional representation of grain boundaries (red lines) separating growth sectors of different orientations (represented by shading direction).

Extended defects can have a range of effects on the properties of crystals, which can be particularly acute for diamond. Structural changes destroy the translational symmetry of the lattice. They also disturb the otherwise uniform electronic charge distribution of a perfect diamond lattice. Immediate consequences of these two effects are changes in the thermal conductivity and electrical mobility, due to phonon and carrier scattering [Isberg *et al* (2002)]. CVD synthesised single-crystal diamond (of type IIa) has been found to have thermal conductivity and electrical mobility of > 2000 W mK^{-1} and 4500 cm^2 V^{-1} (for electrons), respectively.

Structural defects also present a number of implications for the optical properties of diamond. Different growth sectors in synthetic HPHT diamond often result in inhomogeneous optical absorption and luminescence, due to preferential defect incorporation in sectors of differing orientation. Burns *et al* (1990), Collins and Dahwich (2003), and Blank *et al* (2007) have studied defect incorporation in HPHT synthesised diamond; it was found that some defects are more readily incorporated in sectors with certain orientations, such as single-substitutional nitrogen being favourably incorporated in {111} regions. Single-crystal CVD synthesised diamond does not involve differently oriented growth sectors; however, it will be seen in chapter five that preferential incorporation of defects is possible due to the growth process.

Dislocations present strain fields (see figure 2.1.9 for example) in the lattice which can affect the electronic charge distribution around point (localised) defects and hence broaden observed zero-phonon transitions to a Gaussian shape [Stoneham (1969), and see section 2.2.2.1]. The strain fields introduced by dislocations can also split zero-phonon lines (ZPLs); this is demonstrated in figure 2.1.10 [data from this work], where the intense broad-band luminescence centred at ~ 429 nm (~ 2.89 eV) indicates the presence of dislocations in this region of the sample [Yamamoto *et al* (1984)]. Inset in figure 2.1.10 is a high resolution scan of the ZPL at 532.7 nm (2.327 eV), recorded from this dislocated region of the sample; in regions of the sample which do not show dislocation luminescence this centre is usually unsplit. The magnitude of the splitting of the ZPL implies ~ 0.75 ± 0.25 GPa of internal stress acting on the defect (estimated

using uniaxial stress data for the defect (see section 6.3.2.1)). See section 4.1 for further discussion of dislocation related luminescence.

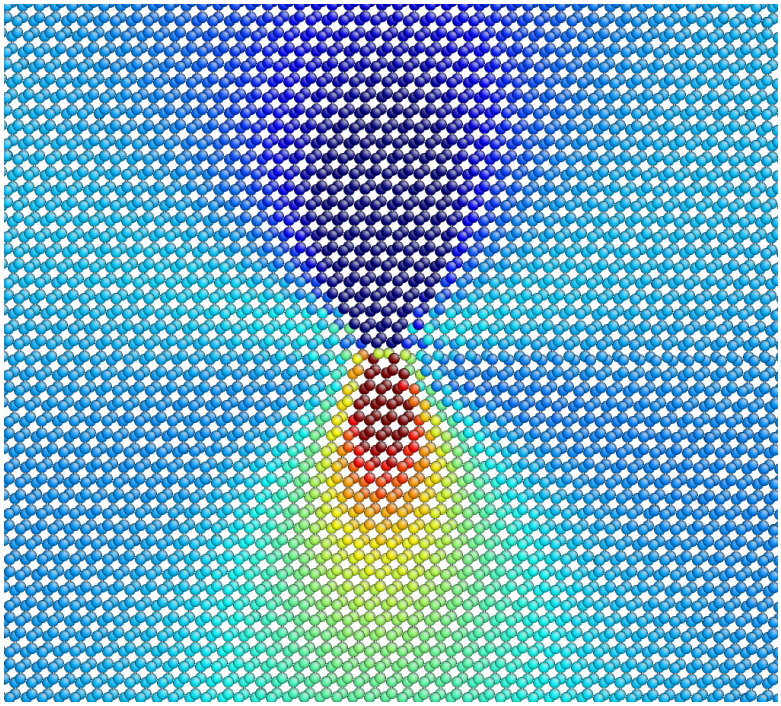

Figure 2.1.9 – Calculated strain field of a [110] dislocation in silicon [Gattinoni (2007)]. Dark blue regions indicate compressive strain, dark red regions indicate expansive strain.

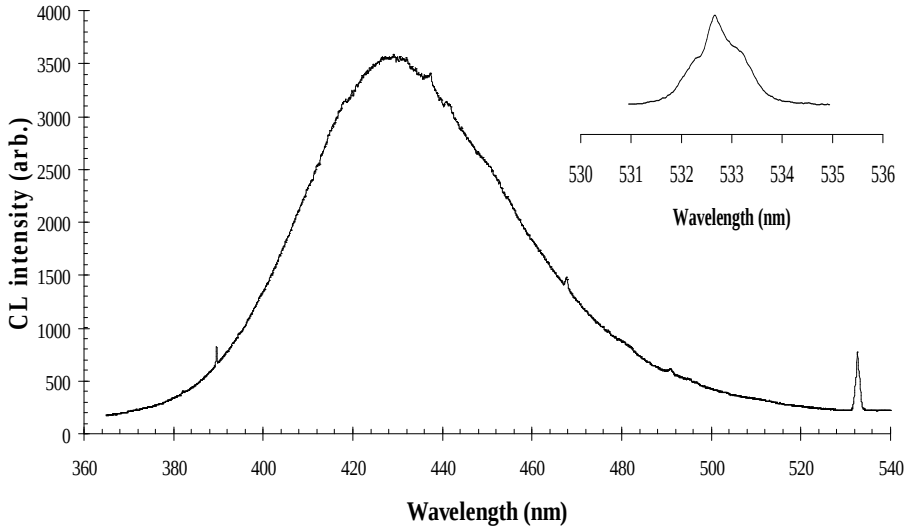

Figure 2.1.10 – Cathodoluminescence spectra of a single-crystal CVD diamond, in a highly dislocated region of the sample. Main spectrum shows the 429 nm (2.89 eV) dislocation-related luminescence band. Inset shows a high resolution spectrum of the 532.7 nm (2.327 eV) ZPL from the same region of the sample; note the splitting of the ZPL. An estimate of the magnitude of the stress inducing the splitting is given in the body text.

A few further effects of extended defects are plastic deformations introducing optical absorption bands in the visible region, which vividly affects the colour of a diamond, by giving a brown or pink colouration (see Field (1992), and Raal (1958)); and heavy dislocation densities (above 10^{10} cm^{-2}) changing the energy separation of the indirect band gap from ~ 5.5 eV to ~ 4.13 eV (see Zaitsev (2001)).

Localised, or point defects in regular crystals are highly localised variations in the perfect lattice, usually of the order of a few atomic spacings. In diamond, these variations occur in three main forms: vacancies, interstitials and substitutions. A vacancy is where an atom is missing from a regular lattice site. An interstitial is where an atom is present in the lattice between the regular lattice sites. This can be along a bond between two lattice sites, or in another region of lattice space. An interstitial atom which is of the same species as the host lattice is called a self-interstitial. A substitution is where an impurity atom replaces an atom of the host lattice at a regular lattice site. These main types of point defects can exist independently, but can often be found in combinations, which are known as complexes. All types of point defects are also referred to as *defect*

centres, or simply *centres*. Figure 2.1.11 schematically demonstrates some typical point defects in a lattice.

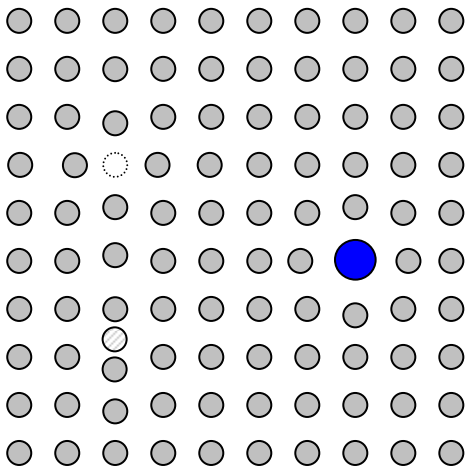

Figure 2.1.11 – Schematic representation of some basic types of point defect in a two-dimensional, simple square lattice. Grey-filled circles represent the atoms comprising the regular lattice. The dotted, unfilled circle represents a vacancy. The shaded circle embedded between lattice sites represents a self-interstitial. The large blue circle represents an impurity atom. Note the deformations of the local lattice regions in response to the presence of the defects.

As can be expected from the high symmetry of a crystal lattice, point defects usually fit into a symmetry group, in that choosing one spatial position within the centre, and then performing certain symmetry operations around that position, leaves the defect unchanged. This assigns a point group to a defect centre, depending on which operations satisfy the condition of invariance; this is an important step in understanding the atomic structure of a centre. A powerful experimental method of determining the symmetry of a defect is inspecting how the zero-phonon line (ZPL, the purely electronic transition) of a defect changes under the application of a uniaxial stress. This method is utilised extensively in this work to determine the symmetry of a number of ZPLs observed in the cathodoluminescence of single-crystal CVD diamond – see section 2.5 for a discussion of the theory, and later chapters for the experimental results.

Point defects disturb the periodicity of the regular lattice, and can disturb the otherwise uniform electronic charge distribution. Consequently, similar to the effects of extended defects, the thermal conductivity and electrical mobility of

the lattice can be impaired due to phonon and carrier scattering [Isberg *et al* (2002)]. Point defects can also deform the local lattice, which introduces strains. Strain fields can affect the electronic transitions of neighbouring defects [Stoneham (1969), Davies (1970), (1971)], by modifying the vibrational frequencies (i.e. force constants) of the local lattice.

Defect centres make significant contributions to the optical absorption and emission spectra of diamond. Whilst perfect diamond would ordinarily be transparent to photons (section 2.1.2), point defects can present a deformed electronic potential. The electronic wavefunctions of defects are then not limited by Bragg reflection and their energy states can exist in the band gap; within the lattice the defects provide electric dipoles to which photons of the appropriate frequency can couple. The absorption of photons of the appropriate frequency at a defect centre can cause the electrons of that centre to be promoted to an excited state. This produces two components in the optical absorption spectrum, which are characteristic of the absorbing centre, and also of its environment: the purely electronic transition, or zero-phonon line (ZPL); and the electronic transitions to vibrational energy levels in the excited state (the vibronic band), where phonons are created during the transition. The relaxation of a defect centre so that its electrons return to lower energy states, or more usually, the ground state, results in photons being emitted which correspond to the transition energy, thus the luminescence spectrum shows a ZPL; and phonon-assisted relaxation where photons *and* phonons are emitted from the centre (and hence a vibronic band is observed). These properties, along with the ones mentioned in the following paragraph, will be discussed in greater detail in section 2.2.

The extent of the modification to the optical absorption spectrum, i.e. changing the observed colour of the diamond, depends upon the properties of the particular absorbing centres. Some defect centres may absorb light strongly, potentially over extended energy ranges (i.e. phonon-assisted absorption), whilst other defect centres may absorb only weakly, or not at all. These features can be considered as follows: strong absorption at a centre is due to a high concentration of centres (as the integrated intensity of absorption of a ZPL is proportional to the concentration of the defect producing that ZPL), a high oscillator strength, i.e. the efficiency of electronic transition between energy states (see, for example, Birks (1970)), and / or a high Huang-Rhys factor (the natural logarithm

of the ratio of phonon-assisted transitions to zero-phonon transitions); a wide energy range of absorption of a particular point defect corresponds to photon absorption in the vibronic band region, where the electrons of the defect are excited to vibrational energy levels; weak or zero absorption at a centre can be due to a low concentration of absorbing centres, a low oscillator strength, or simply that the defect possesses no electric dipoles in the appropriate frequency range, i.e. an optically inactive centre. It is, of course, possible that there are defect centres present in the lattice which are optically inactive, and may only be detected by other techniques, such as electron paramagnetic resonance (EPR) (see section 3.6 for further discussion of EPR).

Changes in the optical emission spectrum due to defects correspond to similar phenomena as above, except that the integrated intensity of luminescence is not necessarily proportional to the concentration of centres (see section 3.2). However, there are important differences between luminescence and absorption measurements. First, some defects are optically active in absorption but not in luminescence measurements (for example, the 594 nm centre [Davies and Nazare (1980)]). Second, the vibronic band of defect centres usually appears different in luminescence than absorption; this is due to vibronic coupling, and sometimes, Jahn-Teller effects (e.g. the H3 centre; see Davies (1981) for further discussion of this phenomenon). Despite the less quantitative nature of luminescence than absorption measurements, it is important to utilise both methods in order to characterise point defects.

Particular defect centres can be present in concentrations ranging from a few parts per billion (ppb) to hundreds of parts per million (ppm; in diamond one ppm is 1.76×10^{17} cm^{-3}). For example, in the single-crystal CVD diamonds studied in this work, the neutral single-substitutional nitrogen concentration, $[N_S^0]$, is of the order of a few hundred ppb (see section 4.2). Similar, but high-purity material grown by Element Six displays extremely high carrier mobilities [Isberg *et al* (2002)]. Conversely, synthetic HPHT type Ib samples can show $[N_S^0]$ of several tens of ppm [Harlow (1998)]. It is the cumulative contribution of many defect centres of one type – for example, a vacancy, or substitutional nitrogen atom – which produce the observed optical absorption or luminescence. This cumulative effect is demonstrated in the shapes of the ZPLs [Stoneham

(1969)]: in diamond, the observed ZPL of a type of centre will be inhomogeneously broadened, where the transition energy of each centre of that type is slightly perturbed, depending upon the local environment in which each centre is present. This will be discussed further in section 2.2.2.1.

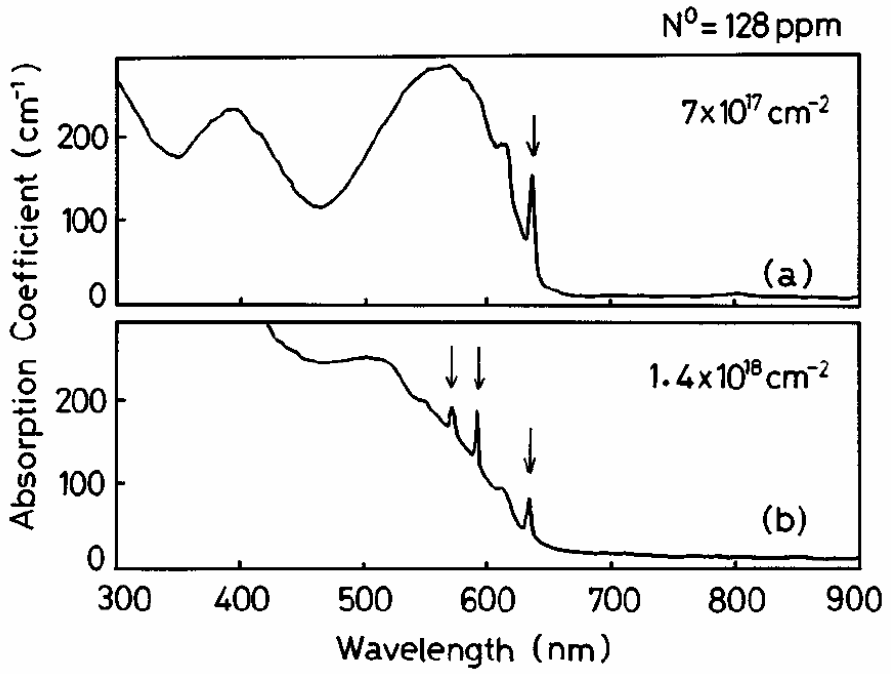

Figure 2.1.12 – Figure 1 from Mita (1996). Demonstrates the change in absorption spectra of a synthetic type Ib diamond after neutron irradiation (concentration values inset). Spectrum (b) shows the reduction in intensity of the 637 nm ZPL (the $(N\text{-}V)^-$), and the presence of the 575 nm ($(N\text{-}V)^0$)and 594 nm ZPLs after heavy irradiation. This is due to a lowering of the Fermi level causing charge transfer from the $(N\text{-}V)^-$, leaving neutral (N-V) centres.

In diamond, point defects can exist in multiple charge states, even within a single sample. Notable examples include the vacancy, with neutral charge state (GR1) ZPL at 741 nm (1.673 eV) [Davies (1974b), Clark and Walker (1973)] and negative charge state (ND1) ZPL at 393 nm (3.150 eV) [Davies (1977)]; the nitrogen-vacancy, with neutral charge state ZPL at 575 nm (2.156 eV) and negative charge state ZPL at 637 nm (1.945 eV) [Mita (1996)] (see figure 2.1.12). A defect charge state can potentially be determined optically by photochromism. This is where, under exposure to light in the frequency range of a centre's ZPL and vibronic band (if present), the absorption intensity of the

centre may change, assuming that the centre possesses the photochromic mechanism, of course. The process generally takes a number of hours, and is reversible in a similar amount of time, by leaving the sample in the dark, or heating it. The change in intensity can be an increase or decrease, depending on the properties of the defect and the mechanism. There are presently two proposed mechanisms, which occur separately in different defects: first, that charge at the centre is transferred to a local acceptor defect; second that the centre undergoes a lattice distortion causing a change in symmetry, and hence a change in electronic energy levels and transition energies.

An example of the first mechanism are the negative (ND1) and neutrally (GR1) charged vacancies, where exposing the ND1 centre to light at its absorbing frequency (393 nm, 3.150 eV) causes its absorption intensity to decrease, and the intensity of the GR1 absorption to increase; as the ND1 centres ionise and effectively create GR1 centres [Dyer and du Preez (1965)]. An example of the second mechanism is the 2.367 eV centre (~ 524 nm), where upon illumination with the appropriate frequency its absorption intensity reduces to less than 10 % of its original value; simultaneously, an absorbing centre at 1.979 eV (~ 626 nm) increases in intensity [Collins and Rafique (1979)].

Many author's identification of charge states of defects via photochromism often assumed that the defect's equilibrium charge states, prior to photochromism studies, were due to the Fermi level in the crystal – as defined by the concentration of donor atoms, i.e. $[N_S^0]$ (see, for example, Mita *et al* (1990)). Collins (2002), however, has shown that the standard mechanism for the Fermi level varying with the donor concentration, as in silicon and germanium, is not valid in diamond. This is because the nitrogen donor in diamond is only very weakly ionised at room temperature, unlike the donors and acceptors in other semiconductors. Hence, it is shown that the Fermi level in diamond must be calculated using expressions for the carrier freeze-out region, and that the level varies very little for nitrogen concentrations of 10^{17} to 10^{19} cm^{-3} (0.6 to 60 ppm). Collins thus proceeds to demonstrate how the equilibrium charge states of defects within diamond are due to their distance from a donor.

An appropriate defect example for this work is the nitrogen-vacancy complex in diamond: this where a vacancy is trapped at a substitutional nitrogen

impurity [Davies and Hamer (1976), Collins and Lawson (1989)]. The centre is found in most nitrogen-containing diamonds. It is found in untreated samples, and can also be created in nitrogen-rich samples by irradiating with electrons or ions to produce vacancies, and then annealing the sample to cause migration and capture of the vacancies at single-nitrogen defects.

The symmetry of the complex is trigonal, i.e. a tetrahedrally bonded substitutional nitrogen atom but with one of the four bonds elongated and a vacancy in place of the carbon at end of this bond. The nitrogen-vacancy bond is extended by a factor of approximately 1.88 relative to the nitrogen-carbon bonds of the centre [Butorac (2008)].

The defect has been found to exist in one of two charge states: neutral and negative. The $(N\text{-}V)^0$ has a zero-phonon transition energy of 2.156 eV (575 nm), and the $(N\text{-}V)^-$ has a ZPL at 1.945 eV (637 nm). The concentration of the negative form is determined by the concentration of single-substitutional nitrogen present in the sample, which acts a donor. The two forms are also photochromic (see above).

The nitrogen-vacancy is a dominant optically-active defect in synthetic diamond – the ZPL and vibronic band of the negative charge state is frequently observed in HPHT synthesised samples, using PL, CL and absorption spectra. Both charge states can be seen in CVD synthesised samples using PL, although only the $(N\text{-}V)^0$ is seen using CL (the CL at 1.945 eV in section 4.4 is most likely due to self-induced PL from the CL of the 2.156 eV ZPL and band). Absorption spectra of CVD diamond does not usually show the ZPLs of either charge state; however they have been detected in a sample used in this work (section 4.4).

A summary of many of the well-understood defect centres in diamond is presented in section 2.3.

2.2 Optical properties of defects

2.2.1 Lattice vibrations and electronic transitions

In section 2.1.3 it was discussed how point defects present a range of effects upon the properties of crystals. This is particularly evident in the optical properties of diamond, where the intrinsic photon absorption of the lattice is limited to a relatively short region, which leaves optical transparency over a wide energy range, allowing electronic transitions associated with point defects to be easily observed spectroscopically. It was briefly mentioned that a particular defect can display a signature absorption or luminescence feature in the optical spectra, generally consisting of two components: an intense, narrow peak, known as the zero-phonon line (ZPL); and a broad band feature, known as the vibronic band. These features will be quantitatively defined below. First, it will be of much assistance to utilise a configurational coordinate diagram. Figure 2.2.1 shows a demonstrative configurational coordinate diagram, the features of which will be expounded in the following text.

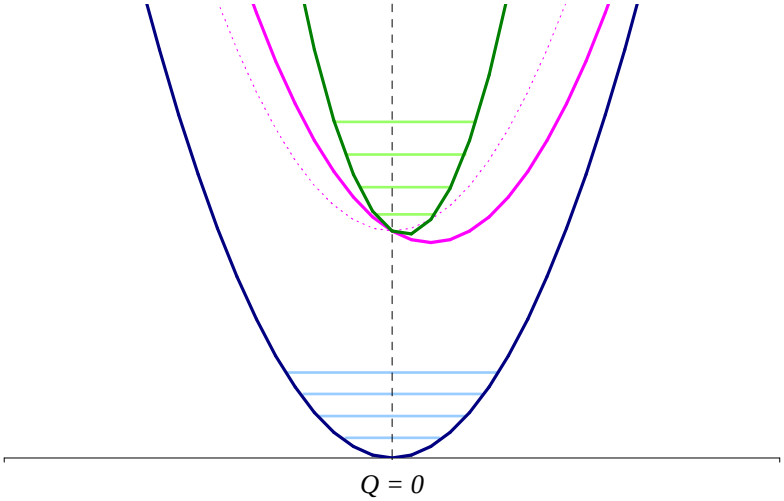

Figure 2.2.1 – Demonstrative configurational coordinate diagram: a schematic representation of the vibrational potentials of a defect. See text for details.

A point defect in a crystal bears some comparison to an isolated molecule, in that it has distinct electronic ground and excited states; it posses vibrational modes, although, usually in diamond, no rotational modes. The vibrational modes are defined by the bonding of the defect to the lattice, with the vibrational cut-off frequency matching that of the lattice (165 meV, 1332 cm^{-1} for diamond). The defect can potentially vibrate at higher frequencies than the lattice, these being called local modes, or local vibrational modes (LVMs).

Each electronic state of a point defect is represented by a vibrational potential, which is populated with equispaced, quantised vibrational energy levels corresponding to the modes of vibration at the defect (similar to the vibrational energy levels discussed in section 2.1.1). The vibrational potentials depend upon the Coulomb interaction of the nuclei and electrons of the defect and lattice, and hence the atomic separation. It is here that the configurational diagram can be invoked, where each electronic energy state of a defect can be represented by a potential well, the energy of each of which is a function of the defect's nuclear configuration, i.e. the positions of the nuclei within the defect relative to an origin, which for a one-dimensional system could be a separation distance, and can be generalised to higher dimensions. The origin is often defined as the equilibrium bonding position of the nuclei in the ground electronic state, where the potential energy is minimised. In a simplified picture, the ground electronic state of defect could be represented by the blue (lowest) parabola in figure 2.2.1, where energy increases on the vertical axis, and Q is the configurational coordinate along the horizontal axis.

In different electronic states, the equilibrium bonding position of the defect can be different. It can be seen that the properties of a defect centre depend on both the electronic and vibrational contributions, along with the interaction between them. This concept is referred to variously in the literature, for obvious reasons, as electron-phonon, electron-lattice, or vibronic (from vibrational-electronic) interactions or coupling.

The essence of vibronic coupling is that a change in electron wavefunction distribution at a defect can affect the vibrational modes, and that a change in the vibrational modes can affect the electronic distribution. The origin of the interaction is the mutual Coulomb attraction between the electrons and

nuclei: a point defect covalently bonded to the lattice has overlapping electronic wavefunctions with its neighbours. Under equilibrium conditions, it will bond at an equilibrium separation, where the potential energy of interaction is minimised. The nuclei can be modelled as masses joined by springs, which perform oscillations within this potential. If the distribution of the electronic wavefunction changes between the bonded nuclei by excitation of the electrons of a defect to an excited state, then the equilibrium bonding separation will change, the interaction potential will change, and hence the frequencies and modes of oscillation of the nuclei will be affected (different modes of vibration may take place, potentially creating phonons). So it can be seen that a change in the bonding of a defect to the lattice can affect the vibrational modes.

A change in electronic wavefunction distribution at a defect can be induced by the optical excitation of its electrons to excited states; it can be equally induced by a relaxation from an excited energy state. Furthermore, a number of other mechanisms can cause changes to the vibrational modes and electronic distribution at a defect, such as temperature, which through expansion or contraction of the lattice changes the equilibrium bonding separation and hence the electronic wavefunction overlap; isotopic changes of impurity defects, which affect the vibrational frequencies and hence electronic interaction; strain in the lattice or applied stress (hydrostatic, i.e. uniform in all dimensions, or uniaxial), which changes the bonding separation and therefore the electronic wavefunction overlap.

These effects can be observed in optical spectra of diamond (and most regular crystals), and manifest themselves in changes in the zero-phonon line and the vibronic bands of point defects. The zero-phonon lines can undergo shifts in energy, changes in shape, and even splitting due to lifting of electronic degeneracies. These effects will be discussed in the coming sections, as they are all encountered in this work.

The details of vibronic interactions will now be explored. It must first be stated that the Born-Oppenheimer (BO) approximation will be utilised. To summarise this: the qualitative manifestation of the BO approximation is that the light electrons can be considered to move instantaneously compared with the movement of the heavy nuclei. Mathematically this means that the wavefunctions involving electronic and vibrational contributions can be

separated into the product of the variables of the respective parts (this will be clarified by example later).

What is required is a quantitative description of how the electrons of a defect interact with the lattice to produce a change in the vibrational potential (the interaction potential). This discussion of vibronic coupling follows that of Davies (1981). It is appropriate to describe the initial vibrational potential of a defect in its ground electronic state, before any change in electron wavefunction takes place as

$$V_g = \frac{1}{2} m\omega^2 Q^2 . \qquad 2.2.1$$

Here, a vibrational potential is defined for a particular, single, dominant vibrational mode at the defect: m is the mass of the mode (for example, at a vacancy in diamond, the carbons are vibrating, hence m is the mass of a carbon atom), ω is the vibrational frequency of the mode, and Q is the configurational coordinate.

Now, if the defect were to be excited such that its valence electrons occupy a different orbital, at energy E above the ground electronic state, their electronic wavefunction distribution changes, and the equilibrium bonding separation of the nuclei changes. This can be described by a shift in the nuclear coordinates, and for simplicity here, a linear shift, aQ, will be applied. So in the excited state, the vibrational potential can be described as

$$\begin{aligned} V_e &= E + \frac{1}{2} m\omega^2 Q^2 + aQ \\ &\equiv E + \frac{1}{2} m\omega^2 \left(Q + \frac{a}{m\omega^2} \right)^2 - \frac{a^2}{2m\omega^2} . \end{aligned} \qquad 2.2.2$$

In terms of the configurational diagram, if there were not a change in Q, i.e. simply an increase in energy E, the excited state would be represented by the dotted pink parabola in figure 2.2.1. However, including a change in nuclear coordinates produces an excited state as represented by the full-line pink parabola in figure 2.2.1: this “corrected” excited state potential is shifted along the Q-axis, and is now slightly lower in energy than the potential without a shift

in Q. This reduction in energy is the motivation for the change in nuclear positions upon excitation of the defect. Quantitatively, equation 2.2.1.2 yields the energy reduction,

$$E_R = \frac{a^2}{2m\omega^2}, \tag{2.2.3}$$

and new equilibrium position of the vibrations,

$$Q_0 = \frac{-a}{m\omega^2}. \tag{2.2.4}$$

As suggested above, if the bonding has changed, then the vibrational frequencies will probably also have changed, as the strength of bonding to the lattice will probably have changed. In the configurational diagram model, the energy levels of the vibrational modes are equispaced within the potential wells, thus a change in frequency of a mode is caused by a change in *shape* of the potential. This can be found by including a quadratic shift in nuclear coordinates, bQ^2, upon excitation of the defect. The excited state vibrational potential is now

$$\begin{aligned} V_e' &= E + \frac{1}{2}m\omega^2 Q^2 + aQ + bQ^2 \\ &\equiv E + \left(\frac{1}{2}m\omega^2 + b\right)\left(Q + \frac{a}{m\omega^2 + b}\right)^2 - \frac{a^2}{2m\omega^2 + 4b}. \end{aligned} \tag{2.2.5}$$

Plotting a representative version of this new vibrational potential on the configurational diagram of figure 2.2.1 produces the green potential, where it is clear that the sides of the parabola have become steeper, relative to the ground state potential; this has changed the energies of the vibrational energy levels, when taking the bottom of this excited state potential as a relative zero. From equation 2.2.5, the vibrational frequency of the dominant mode (previously ω) is now

$$\Omega = \left(\omega^2 + \frac{2b}{m}\right)^{\frac{1}{2}}. \tag{2.2.6}$$

With the properties of the vibrational coupling established, it is now possible to explore how these contribute to the observed vibrational spectra. The first component of the absorption or luminescence spectra of a point defect is the zero-phonon line. This is composed of all of the transitions between the ground and excited, or sometimes excited and excited, states which do not involve a change in vibrational quantum number (the “red” transition in figure 2.2.2). A transition between electronic energy states requires the absorption or emission of a photon, the energy of which is

$$h\nu_0 = E + \frac{1}{2}\sum_i \left(\hbar\omega_{ei} - \hbar\omega_{gi}\right), \qquad 2.2.7$$

where E is the energy separation of the electronic states, and the summation is over the changes in energy of each pair of vibrational levels bearing the same vibrational quantum number, i, in each electronic state. This sum would be zero if the ground and excited state potentials had the same shape. More properties of the ZPL will be discussed in section 2.2.2.

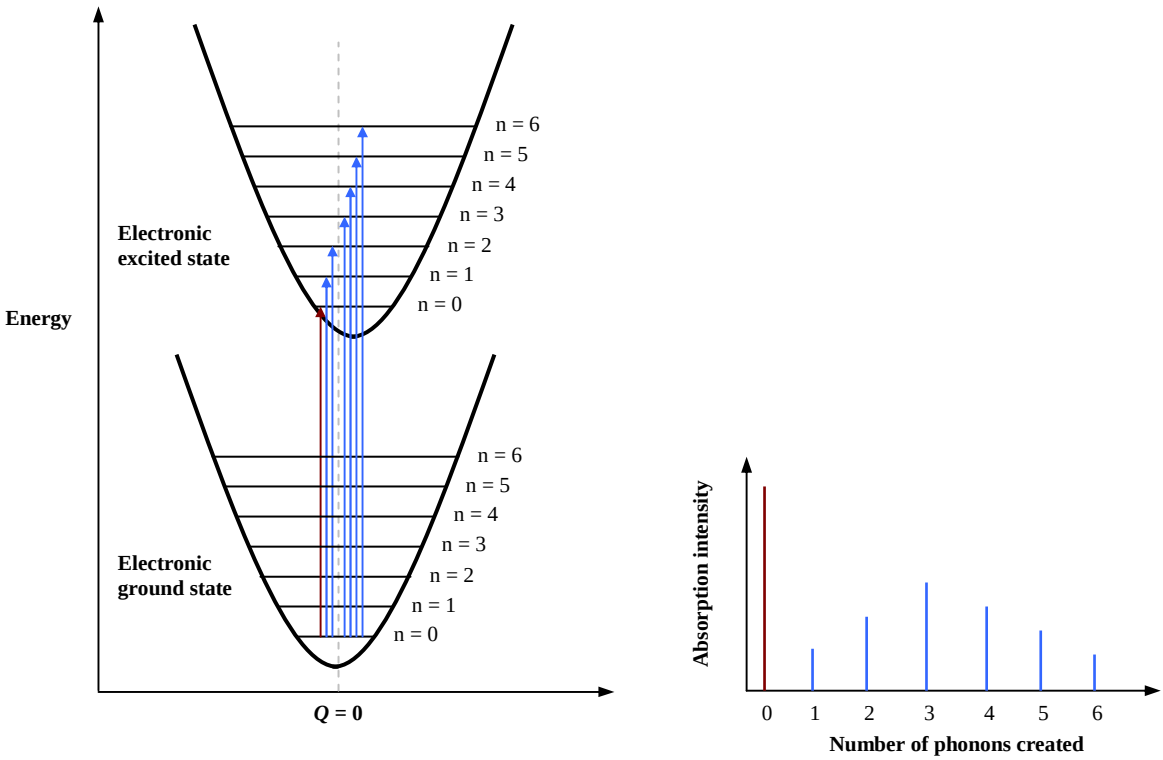

Figure 2.2.2 – Schematic diagrams showing electronic transitions between energy states of a defect. See text for details.

The second component of the absorption or luminescence spectra of a point defect is the vibronic band. This is composed of transitions between electronic energy states where the vibrational quantum number changes (the "blue" transitions in figure 2.2.2). Again, transitions between electronic energy states require the absorption or emission of a photon, however, additionally, the change of vibrational quantum number creates phonons: as electrons are excited to, or relax to vibrational levels, the corresponding modes of vibration are initiated, creating phonons in the lattice. These transitions are often called phonon-assisted. Non-radiative transitions can, of course, take place within an electronic state, where electrons are excited, or relax, within the vibrational potential, exclusively creating phonons. Ideally, the energy of vibronic transitions would be discrete, as in figure 2.2.2.

The vibronic wavefunction of a defect can be written as

$$\psi(r,Q) = \varphi_g(r)\,\chi_0(Q), \qquad 2.2.8$$

where $\varphi_g(r)$ is the ground electronic state wavefunction, and $\chi_0(Q)$ is vibrational wavefunction, or harmonic oscillator, in the lowest vibrational level, 0. A simplification is made here that the electronic wavefunction is independent of Q, as non-degenerate electronic states in equilibrium will be sufficiently spaced in energy as to be non-interacting under nuclear vibrations. However, in reality there may be slight interaction, and under the application of uniaxial stress, interaction can occur (see section 2.5). This simplification will not be explored more in this section; see Davies (1981) for further discussion.

The probability of optical transitions between two vibronic states, which for present purposes will be from the lowest level of the ground state (as in equation 2.2.8) to the *n*th vibrational level of the excited electronic state, is proportional to the square of

$$\iint \varphi_e^{\,*}(r)\,\chi_n^{\,*}(Q-Q_0)\,D\,\varphi_g(r)\,\chi_0(Q)\,dr\,dQ\,, \qquad 2.2.9$$

where an asterisk indicates complex conjugation, and D represents the electric-dipole operator. Note that the excited state vibrational wavefunction is in terms of the adjusted nuclear coordinates, $Q - Q_0$. Factorising equation 2.2.9 into the electronic and vibrational parts yields

$$\int \varphi_e^{\,*}(r)\,D\,\varphi_g(r)dr \int \chi_n^{\,*}(Q-Q_0)\,\chi_0(Q)dQ\,. \qquad 2.2.10$$

The electronic part can, in principle, be estimated from the radiative decay time of the transition, and the vibrational part is the overlap integral of the harmonic wavefunctions, M_{0n}. So, the vibronic band will consist of a series of discrete energy transitions, equally spaced in the optical spectrum as a function of phonon number, n:

$$h\nu_{0n} = E - E_R + n\hbar\omega. \qquad 2.2.11$$

The intensity of each transition is defined by the solution to the vibrational part of equation 2.2.10, and takes the form of a Poisson distribution,

$$\left|M_{0n}\right|^2 = \frac{S^n \exp(-S)}{n!}, \qquad 2.2.12$$

the argument, S, known as the Huang-Rhys factor, is the measure of how much of the total transition probability at the centre lies in the ZPL. This can be found from the experimental spectrum by measuring the ratio of the integrated intensity of the vibronic band to the integrated intensity of the ZPL, and taking the natural logarithm of this. Quantitatively, the Huang-Rhys factor can be expressed as

$$S = \frac{a^2}{2m\hbar\omega^3} \equiv \frac{E_R}{\hbar\omega}, \qquad 2.2.13$$

where the vibronic band shape defined by this S, is for single-mode coupling at the centre, characterised by the frequency of the mode, ω, the corresponding mode mass, m, and the induced lattice distortion, a. Single-mode coupling at centres in diamond is rare, and even then, the vibronic band transitions are not discrete in energy, but broadened in a similar manner that the zero-phonon line is not a discrete transition. Multiple-mode coupling is more common than single-mode, where the above expressions can be easily generalised (see Davies (1981)). The observed vibronic band then becomes the convolution of the many modes at the centre. Often, in diamond, vibronic bands are observed which show couplings to a few dominant (usually highly symmetric) phonons in the allowed energy region (0 to 165 meV). So to generate a matching vibronic band, the one-phonon band spectrum would have to be generated using equation 2.2.1.12, and following the generalised equations for multiple-mode coupling, a convolution of the many modes would be required.

The above quantitative discussion has been limited to defect centres with non-degenerate electronic energy states which couple to totally symmetry vibrations. This is because degenerate states would not have their degeneracy lifted by symmetric vibrations at the centre (see section 2.5 for the group theoretical explanation of this).

2.2.2 The zero-phonon line

2.2.2.1 Shape of the zero-phonon line

As briefly discussed in section 2.2.1, the zero-phonon line (ZPL) of a point defect is defined as the sum of all the electronic transitions between the ground and excited states which do not involve a change in vibrational quantum number; no phonons are involved in the transitions. It can be defined as

$$h\nu_0 = E + \frac{1}{2}\sum_i \left(\hbar\omega_{ei} - \hbar\omega_{gi}\right), \qquad 2.2.14$$

where E is the energy separation of the electronic states, and the summation is over the changes in energy of each pair of vibrational levels bearing the same vibrational quantum number, i, in each electronic state. This sum would be zero if the ground and excited state potentials had the same shape.

The ZPL will look the same in optical absorption and luminescence measurements. According to the above definition, the ZPL would theoretically appear as a discrete absorption or luminescence event, with a well-defined energy. In practice, however, the ZPL of a defect is observed as a peak with a definite width (in the CVD diamond studied in this work the ZPL full widths at half maximum height (FWHM) were found to be in the range 0.5 to 1.5 meV (see section 4.3)). There are a number of contributions to this broadening from a discrete transition: the lifetimes of the energy states of the transition; thermally-induced broadening; and strain affecting the defect. These will be discussed below. Additionally, the resolution of the spectrometer can artificially broaden a peak, so it must be ensured that the effective slit width is much less than the half-width of the peak observed, in order to obtain an accurate measurement of the peak.

The finite lifetimes of energy states of a defect will cause a broadening of the zero-phonon transition, as the defect will remain in any given excited state for a finite time, which is characteristic of that state, until there is a change in the expectation value of the state (i.e. the energy-time formulation of the Heisenberg

uncertainty principle). In diamond, many defect centres are found experimentally to have radiative lifetimes of the order of tens of nanoseconds, with non-radiative lifetimes (transitions between vibrational levels within electronic states) being of the order of 10^{-2} ps (see Zaitsev (2000) for examples). A radiative lifetime of τ = 10 ns translates into an observed spectroscopic transition with FWHM, Γ, of

$$\Gamma = \frac{h}{\tau \mathrm{e}} \approx 4.1\times10^{-4}\ \mathrm{meV}, \qquad 2.2.15$$

where *h* is Planck's constant and e is the electronic charge. Thus it can be seen that lifetime broadening contributes minimally to the broadening of a ZPL.

Thermal broadening produces very evident changes in the observed ZPL, and is discussed in section 2.2.2.2. However, even at temperatures below liquid nitrogen temperature (~ 77 K), the ZPL is seen to have a very definite width, which expands with increasing temperature. It is clear then that to identify the thermal broadening contribution to the linewidth, the initial shape of the line must be first subtracted. The question then, of the low temperature ZPL shape, remains; it has been shown to be answered by considering the strains of the local environment of the point defect.

Stoneham (1969) approached this issue by considering that there are two types of broadening of zero-phonon transitions in a lattice: homogeneous, where all of the defect centres of one type in the lattice produce transitions which possess the same peak energy and width, the width being defined by the lifetime of the states, as above; and inhomogeneous, where each defect centre of one type produces a transition with a slightly perturbed peak energy, yet similar widths – although the width of each transition is appreciably less than that of the observed ZPL. The perturbations originate from the local environment in which each centre exists, and are caused by random strains in the lattice from neighbouring defects, and also potentially from electric fields.

In a real diamond crystal, where defects are common throughout the lattice, it is likely that the broadening will primarily be inhomogeneous, with small homogeneous contributions. Furthermore, because diamond is a homopolar crystal, there are no random electric fields (other than those from defects), and so

the inhomogeneous perturbations will originate predominantly from the strains in the local lattice environment of a defect.

Stoneham utilised the *statistical* method to evaluate the issue. This involves three assumptions: first, the transition energy of the defect centre is linear in the local strain. This means that the lineshape ($\hbar\omega$ distribution) can be calculated explicitly by calculating the distribution of the strain; second, the contribution to the broadening by the defect centres causing it, add linearly; third, the defect centres causing the broadening are uncorrelated with each other.

Davies (1970) identified that the perturbation to electronic transitions between non-degenerate states of defect centres in diamond is linear in the applied strain. This satisfies the first approximation of the statistical method, making it a suitable approach to analysing zero-phonon transitions in diamond.

The statistical method yields a number of important and experimentally useful results. Stoneham derived the general zero-phonon lineshape for a general, uncorrelated defect distribution (as yet undefined as extended or point defects):

$$I(\varepsilon)=\frac{1}{2\pi}\int_{-\infty}^{\infty}\exp(ix\varepsilon)\exp(-\rho J(x))\,dx\,, \qquad 2.2.16$$

where ε is the strain, ρ is the defect density, and x is a variable with no physical significance. It is acceptable to express the lineshape I as a function of the strain because of the first approximation of the statistical method. $J(x)$ is defined as

$$J(x)=\int p(z)[1-\exp(-ix\varepsilon(z))]\,dz\,, \qquad 2.2.17$$

where $p(z)$ is the probability of a particular defect configuration. The limit of the observed lineshapes is found, by moment analysis, to tend to Gaussian; however, they rarely are so, due to odd-parity moment integrals vanishing, causing asymmetries in the moments.

Two distinct practical results follow from these expressions. First, if the local lattice of the optically active defect centre under study is populated by dislocations, then the $p(z)$ function will cause the observed lineshape to be Gaussian. Second, if the local lattice is populated by point defects, then the $p(z)$ function will cause the observed lineshape to be Lorentzian.

These important results were expanded by Davies (1970), where it was shown that for natural diamonds, the most common lineshape for zero-phonon transitions lies between Gaussian and Lorentzian: the bi-Lorentzian, with intensity function

$$I(\nu) = \frac{\alpha}{\left(\beta + (\nu - \nu_0)^2\right)^2}, \qquad 2.2.18$$

where α scales the entire function, ν_0 is the peak position and β determines the width of the peak. The β parameter is related to the FWHM, Γ, by

$$\beta = \left(\frac{\Gamma}{C}\right)^2, \qquad 2.2.19$$

where $C = 2\sqrt{(\sqrt{2} - 1)}$.

Whilst dislocations can vary slightly in structure and nature, there is greater variation in point defects within a lattice. Different species of point defects will affect the observed lineshapes of optically active defect centres, via the strains they introduce, by a simple convolution of the resulting intensity distributions that would occur separately. This comes from the second approximation of the statistical method, that the contribution of defect centres adds linearly. This is observed in practice in the many asymmetrical ZPLs seen in diamond.

These results are important in an experimental sense, particularly for this work, in that performing a fit to a zero-phonon line is not simply a peak-fitting exercise to obtain position and width information, but is in fact an investigation of the local environment in which that defect centre resides. The method of peak fitting used in this work is to perform a least-squares fit to the experimental data with a Pearson VII function, by varying the *p* factor. A *p* factor of one produces a Lorentzian shape, $p = 2$ produces the bi-Lorentzian shape, and $p \rightarrow \infty$ produces a Gaussian shape. The Pearson VII function is [Pearson (1916)]

$$I(\nu)=\frac{1}{\left(1+4\left(2^{1/p}-1\right)\left(\frac{(\nu_0-\nu)}{\Gamma}\right)^2\right)^p}. \qquad 2.2.20$$

2.2.2.2 Temperature dependence

The zero-phonon line is highly temperature dependent, in terms of its intensity, peak energy, and width. In a hypothetical diamond system with a point defect undergoing single-mode, totally symmetry vibrational coupling, only the lowest vibrational level of the ground electronic state is populated at zero Kelvin. With increasing temperature, the vibrational levels are occupied according to the Bose-Einstein population term

$$n(\omega,T)=\frac{1}{\left(1-\exp\left(\frac{\hbar\omega}{k_B T}\right)\right)}, \qquad 2.2.21$$

where ω is the frequency of the single-mode phonon coupling at the centre, $\hbar$ is the reduced Planck's constant, k_B is the Boltzmann constant, and T is the temperature. As the temperature increases and the first vibrational level of the ground state becomes occupied, the intensity of the ZPL will vary depending on the ratio of the zeroth and first solutions to the overlap integrals of the harmonic wavefunction, M_{00} and M_{11} (section 2.2.1) [Davies (1981)]. If $|M_{11}|^2 / |M_{00}|^2 < 1$, the ZPL intensity will decrease; if $|M_{11}|^2 / |M_{00}|^2 = 1$, the ZPL intensity will be independent of temperature; if $|M_{11}|^2 / |M_{00}|^2 > 1$, the ZPL intensity will increase. These ratios are inherently dependent upon the Huang-Rhys factor of the defect centre.

Generally, the zero-phonon intensity, $I_0(T)$, will decrease with increasing temperature, according to

$$I_0(T)\propto \exp\left[-\int_0^{\omega_m} I_1(\omega)(2n(\omega,T)+1)d\omega\right], \qquad 2.2.22$$

where the integral is over the full range of phonon frequencies in diamond (0 to ω_m = 165 meV), and $I_1(\omega)$ is the one-phonon vibronic band, which is defined, again, by the solution of the overlap integral of the harmonic wavefunction (equation 2.2.10 of section 2.2.1),

$$\int I_n(\omega)d\omega = |M_{0n}|^2 = \frac{S^n \exp(-S)}{n!}. \qquad 2.2.23$$

Variations of ZPL intensity are independent of the type of vibronic coupling at the defect, i.e. linear or quadratic. However, changes in the peak energy and linewidth require quadratic contributions to the coupling (see section 2.2.1): under the condition that the propagation of long-wavelength lattice modes are unaffected by a particular defect, then the quadratic strains at the centre become proportional to the linear strains, and can become evident in the zero-phonon line upon variation of temperature (see Davies (1981) for further discussion).

Strictly, the contribution to the shift of a ZPL's peak energy with temperature comes from the lattice-coupling induced shift *and* the thermal expansion of the lattice, as a change in lattice constant changes the energy of the band gap, and also the energy of the electronic states at a defect; this effect is small yet non-negligible. Thus, the peak energy of a ZPL at a given temperature, T, is

$$h\nu(T) = h\nu_0 + \upsilon(T) + L(T), \qquad 2.2.24$$

where $h\nu_0$ is the zero-phonon energy at zero Kelvin (equation 2.2.14 of section 2.2.2.1), $\upsilon(T)$ is the lattice-coupling contribution, given by

$$\upsilon(T) = c\int_0^{\omega_m} \omega^2 I_1(\omega) n(\omega,T) d\omega, \qquad 2.2.25$$

where c is a constant; this expression comes from the change in vibrational frequencies with temperature at the centre (see section 2.2.2.3 for further discussion). $L(T)$ is the lattice expansion contribution, given by

$$L(T) = A(c_{11} + 2c_{12})\int_0^T \alpha(T) dT\ , \qquad 2.2.26$$

where A is the shift rate of the ZPL under hydrostatic pressure (can be interpreted for uniaxial stress data), c_{11} and c_{12} are the elastic moduli of the perfect lattice, and $\alpha(T)$ is the coefficient of volume expansion of diamond. For reference, the values of the elastic moduli of diamond are c_{11} = 1079 ± 5 GPa, c_{12} = 124 ± 5 GPa, c_{44} = 578 ± 2 GPa [McSkimmin and Andreatch (1972)]. The coefficient of volume expansion of diamond is [Krishnan (1946)]

$$\alpha(T) = \frac{\gamma x_0 C_v}{V_0}, \qquad 2.2.27$$

where γ is the Grüneisen constant of diamond (γ = 1.1 for temperatures below 300 K), x_0 is the compressibility of diamond, C_v is the specific heat capacity of diamond, and V_0 is the atomic volume of a carbon atom. Krishnan's approach was to measure the change in lattice spacing as a function of temperature, via x-ray diffraction. Slack and Bartram (1975) have noted that it is satisfactory to use (for cubic crystals) the length, l, of one side of the crystal as a function of temperature, as the deviation between lattice spacing and crystal length as a function of temperature is only significant at high temperatures. Thus, Slack and Bartram define the coefficient of lattice expansion as

$$\alpha(T) = \frac{d(\ln l)}{dT}. \qquad 2.2.28$$

Data for $\alpha(T)$ are fairly coarse in resolution in the available published work, but are summarised in table 2.2.1. In practice it would be appropriate to define a suitable function to fit to the data, of a similar form to the variation of $\alpha(T)$ in Krishnan's work, in order to interpolate between the data points (see, for example, figure 2.2.3).

Temperature (K)	α (× 10^{-6} K^{-1})
0	0.00
100	0.00
200	0.45
300	1.05
400	1.79

Table 2.2.1 – Variation of the coefficient of lattice expansion of diamond with temperature, after Slack and Bartram (1975). Error in α estimated to be ± 15 %.

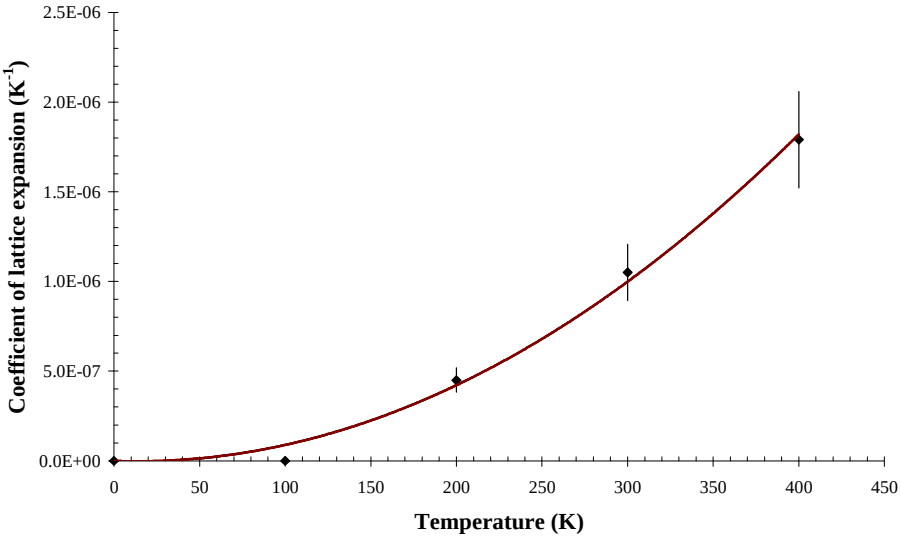

Figure 2.2.3 – Example fit of a quadratic function to the coefficient of lattice expansion data, in order to interpolate between data points: $\alpha(T) = (1.221\times10^{-11})T^2 - (3.332\times10^{-10})T$.

The full width at half of the maximum height (FWHM), Γ, of a ZPL at a given temperature is

$$\Gamma(T) = d\int_0^{\omega_m} \omega^2 I_1(\omega) n(\omega,T)\left(n(\omega,T)+1\right)d\omega, \qquad 2.2.29$$

where d is a constant. This is also a result of quadratic phonon-coupling at the defect. The true low-temperature width of a ZPL is determined by the strain environment in which the defect exists (see the previous section). Zero-phonon lineshapes change minimally below approximately 80 K [Davies (1970)]; at temperatures above this, the contribution of thermal broadening needs to be accounted for.

2.2.2.3 Isotopic substitution

Isotopic substitution in a crystal is a powerful method of obtaining information about point defects within the crystal. For this to be effective, control over the growth process is crucial. In diamond, both high pressure high temperature (HPHT) and chemical vapour deposition (CVD) synthesis can incorporate elemental isotopes other than the most naturally abundant. For example, samples can be grown using carbon-13 rather than carbon-12, which is known as host lattice substitution. Additionally, both synthesis methods can include minor element isotopes, commonly nitrogen-15, boron-10, deuterium, and silicon isotopes – the natural abundance counterparts of which are the dominant impurity elements in diamond.

Isotopic substitution of the host lattice manifests itself in changes in the energy of zero-phonon lines (ZPLs), vibronic bands, and local vibrational modes (LVMs) of point defects. Information is revealed about the vibrations taking place at the defect, analysis of which can identify the type of atoms vibrating, the type of bonding, and the vibrational modes taking place.

Impurity element isotopic substitution can be evident in energy changes of vibronic bands and LVMs (see, for example, Woods and Collins (1982), Collins *et al* (1987), Collins and Woods (1987), Collins *et al* (1988), Collins and Lawson (1989), Collins *et al* (1993)). Changes in energy of ZPLs due to isotopic effects may be observed if careful spectroscopic measurements are made: a ZPL will undergo a shift in energy if the defect centre producing the ZPL involves an impurity element which has been isotopically substituted. The origin of the shift is the change in vibrational frequencies at the centre, due to the change in nuclear mass; the ZPL is a transition between vibrational energy levels of the defect,

$$h\nu_0 = E + \frac{1}{2}\sum_i \left(\hbar\omega_{ei} - \hbar\omega_{gi}\right), \qquad 2.2.30$$

where $h\nu_0$ is the ZPL energy, E is the energy separation of the electronic states, and the summation is over the changes in energy of each pair of vibrational levels bearing the same vibrational quantum number, i, in each electronic state.

Hence a change in vibrational frequencies causes a change in zero-point energy, thus changing the transition energy.

In host lattice isotopic substitution, the origin of the total shift in energy of the ZPL is threefold [Collins *et al* (1988)]; the same contributions are valid for impurity element isotopic substitution, however, some can be discounted as discussed below. This is relevant to the present work as it is the effects of impurity element (nitrogen-15), rather than host lattice isotopic substitution that have been investigated.

The first contribution, known as the "static" shift, is the isotope-induced change in volume of the lattice, which comes from the change in zero-point energy of the vibrational modes of the lattice. Given the low concentrations of nitrogen impurities in this type of material (single-substitutional nitrogen is of the order of a few hundred ppb), the effect of N-15 on the vibrational modes of the lattice is negligible.

The second contribution, the "dynamic" shift, is the isotope-induced change in zero-point energy of the electronic states of the transition. The effect of nitrogen-15 on the vibrational modes at the centre will be non-negligible, as the vibrating masses at the centre will have different frequencies; hence the zero-point energy of the electronic states will be affected, and so the dynamic aspect of the shift makes a significant contribution to the observed shift. The same effect will occur from host lattice isotope substitution. Following Collins *et al* (1988), an excitation of the electrons of a defect centre will change the vibrational frequencies in the ground and excited state of the centre; the function $g(\omega)d\omega$ can be used to represent the change in vibrational frequencies in the ground state between ω to $\omega + d\omega$. The change in zero-phonon energy is then

$$\Delta h\nu = \frac{1}{2}\left(\int_0^{\omega_m} g_{15} d\omega - \int_0^{\omega_m} g_{14} d\omega \right), \qquad 2.2.31$$

where g_n is the change in vibrational frequencies at the centre involving isotope ^{n}N. The integrals are over the entire frequency range of the defect (ω_m), i.e. all lattice modes and the local vibrational modes (LVMs). The effect upon the lattice modes can be determined from the temperature dependence of the energy of the ZPL, as

$$\Delta h\nu(T) = \int_0^{\omega_m} g(\omega) n(\omega,T)\, d\omega, \qquad 2.2.32$$

where $n(\omega,T)$ is the Bose-Einstein population term (equation 2.2.21 of section 2.2.2.2). This expression can be evaluated as in equation 2.2.25 of section 2.2.2.2, for $g(\omega)$ may be approximated to $c\ \omega^m\ I(\omega)$, where c is a constant, $I(\omega)$ is the one-phonon sideband, as defined by equation equation 2.2.23 of section 2.2.2.2, and the index m = 1, 2 or 3 accounts for the extent of quadratic lattice coupling at the centre, and provides upper and lower limits on the shift.

The LVM contribution can be significant, as the local modes are unique to the atomic constituents of the defect, and so will be highly sensitive to a change in nuclear mass. However, the defects studied in this work do not show any LVM transitions, and so this contribution can be discounted.

The final contribution to the observed shift arises if the uniaxial stress analysis reveals non-linear splitting of the zero-phonon components. Non-linear splitting comes from an interaction of the electronic states during applied stress, and is due to either a Jahn-Teller or pseudo-Jahn-Teller effect at the centre. This can be accounted for in the isotope-induced shift by recalculating the stress analysis fitting of the experimental data (see Collins *et al* (1988) for further discussion of this). This effect is not observed in the uniaxial stress data of the ZPLs measured for isotope shifts in this work, and so this contribution will be zero.

Thus, for nitrogen isotope substitution in diamond, the sole origin of the change in energy of the ZPL is the dynamic shift, the change in vibrational frequencies at the defect centre. The change in frequencies in the ground and excited state can be estimated from the temperature dependent shift of the ZPL; however, this does not explicitly incorporate the change in mass of the vibrating components of the centre. Davies (1983) has shown that for an *impurity* atom, the change in vibrational frequencies due to a change in mass at a centre is not given simply by the square root of the ratio of the isotope masses, as might be expected. A computer simulation of a linear chain of n carbon atoms, with a single nitrogen impurity, shows that for a change in nuclear mass of the nitrogen, the vibrational frequencies change by

$$\frac{\omega_1}{\omega_2} = 1 - \frac{(m_1 - m_1)}{2nm}, \qquad 2.2.33$$

where ω_1 and ω_2 are the frequencies of the system with a nitrogen-14 and nitrogen-15 impurity respectively, m_1 and m_2 are the masses of nitrogen-14 and nitrogen-15 atoms respectively and m is the mass of a carbon-12 atom. Using this as the fractional change in frequencies at the centre, the energy shift can be defined as (from equation 2.2.30**)**

$$h\nu_0^1 - h\nu_0^2 = \frac{1}{2}\left(\frac{m_2 - m_1}{2nm}\right)\sum_i (h\omega_{ei} - h\omega_{ei}), \qquad 2.2.34$$

where $h\nu_0^1$ and $h\nu_0^2$ are the ZPL peak energies of the defect with nitrogen-14 and nitrogen-15, respectively. The summation can be found from the temperature dependent shift of the ZPL, and if this is to lower energies, then the sum will be negative, and hence the isotope shift of a ZPL will be positive, i.e. to higher energy.

The magnitude of the shift is determined, in part, by the number of vibrating atoms, *n*. Davies (1983) points out that the vibronic bands of defects in diamond do not show sharp structure, and hence the phonons involved must be closely spaced in energy. Davies utilises the Lax-Hu-Narayanamurti theorem, which states that a phonon cannot decay into a set of phonons each of whose phase velocity is higher than that of the initial phonon [Lax *et al* (1981)]; thus, as the energy spacing of the phonons will be less than the width of the ZPL, then the 165 meV phonon range in diamond must be spanned by phonons of 2 meV spacing or less. Therefore at least 80 atoms will be required. As a guide to the magnitude of the shift expected for a nitrogen-15 impurity substitution, Davies uses the N3 centre as an example, where the calculated shift is of the order of ~ 0.1 meV.

2.3 Summary of the major optically active point defects

In general, a narrow (FWHM ~ 0.5 to 2.0 meV) transition line observed in the optical absorption or luminescence spectra of a diamond is the zero-phonon line (ZPL) of a point defect within the crystal. There can be exceptions, of course, where some narrow transitions are local vibrational mode (LVM) transitions of a defect. Around 500 ZPLs from optically active defect centres have been observed in the optical spectra of diamond [Zaitsev (2001)], of which only a few have had the defects producing them confidently identified (see, for example, Collins (1999)).

Some types of defect centres are only present in (and hence characteristic of) certain diamond types, such as the A centre (a pair of substitutional nitrogen atoms) which characterises the IaA type; whereas other types of defect are present across a number of diamond types, such as the vacancy. The defects incorporated from a particular growth process (for synthetic diamonds) or from specific regions of the world (for natural diamonds), can help to identify a sample's origins [Collins (1999)].

Single-crystal diamonds synthesised by chemical vapour deposition (CVD) show a number of narrow transitions in the optical absorption and luminescence spectra over the range 0.165 to 5.480 eV, some of which are well-understood centres which also exist in other types of diamond. However, some cathodoluminescence transitions, particularly in the region 2 to 3 eV, appear to be unique to CVD synthesised diamond, yet haven't had the defects producing them characterised until now. The data and analyses presented in chapters five and six identify the symmetries and nitrogen dependencies of some of the major ZPLs unique to CVD diamond.

Table 2.3.1 presents a summary of some of the major, well-understood optically active defect centres in observed in natural, HPHT and synthetic CVD diamond. This compilation of information about these defects lists the atomic models (if known) and where possible, provides enough information to identify the defect in an optical spectrum – the transition energies, Huang-Rhys factor (vibronic band to ZPL ratio), dominant phonon energies (peak energies in the

band) and LVM energies (if present). Comprehensive data and discussion for these and other centres can be found in, for example, Zaitsev (2001), Iakoubovskii and Stesmans (2002a), Collins (1999). Some of the lines produced by radiation damage (including annealing) may also be seen in CVD diamond. ZPLs associated with defects unique to single-crystal CVD diamond are discussed in chapter four.

Transition energy	Found in diamond types	Observed in untreated CVD samples?	Optical method observed under	Properties
4.583 eV (270.5 nm)	Ib, IIa, IIb	Y	A (in CVD after irr. & ann.), CL (in CVD in untreated samples), PL	A pair of carbon atoms in a <100> split interstitial (the **5RL** centre). Rhombic-I symmetry. Huang-Rhys factor of 1.6. LVMs at 175, 193 and 237 meV in CL, 167 and 202 meV in absorption. Collins and Spear (1986), Collins (1999).
3.188 eV (388.9 nm)	All	Y	A (excl. CVD), CL, PL	A substitutional nitrogen and interstitial carbon complex (the 3.188 eV centre). Can be produced by irradiation. Couples to 75 and 165 meV phonons. Huang-Rhys factor of 1.82. LVM structure between 2.99 and 3.02 eV. Collins and Lawson (1989).
3.150 eV (393.6 nm)	Ia, Ib, IIa	N	A	V^-, the negatively charged vacancy (**ND1**). T_d symmetry. Couples to 76 to 80 meV phonons. Huang-Rhys factor of 3.18. Shows J-T effect under uniaxial stress. Davies (1977).
2.985 eV (415.3 nm)	Ia	N	A, CL, PL	$(N_3\text{-}V)^0$, the **N3** centre. Trigonal symmetry. Couples to 93 and 165 meV phonons. Huang-Rhys factor of 3.45. Woods (1986).
2.807 eV (441.6 nm)	Ib, IIa	N	A, CL	A substitutional nitrogen and interstitial carbon complex (the 2.807 eV centre). Naturally occurring in CVD diamond. Can be produced by irradiation. Collins and Lawson (1989).
2.543 eV (487.5 nm)	Ia, IIa	N	A	$(V\text{-}V)^0$, the neutral di-vacancy (**TH5**). Twitchen *et al* (1999a).
2.463 eV (503.2 nm)	IaA	N	A, CL, PL	$(N\text{-}V\text{-}N)^0$, the neutral di-nitrogen-vacancy (**H3**). C_{2v} symmetry. Couples to 41 and 152 meV phonons. Huang-Rhys factor of 3. Davies *et al* (1976).
2.462 eV (503.6 nm)	All	N	A, CL, PL	$(V\text{-}C\text{-}C\text{-}V)^0$, the **3H** centre, an irradiation product. C_{2v} symmetry. Couples to 67 meV phonons. Huang-Rhys factor of 0.8. Davies (1974b).

2.156 eV (575.0 nm)	All	Y	A (excl. CVD) CL, PL	$(N\text{-}V)^0$, the neutral nitrogen-vacancy. Naturally occurring in CVD diamond. Trigonal symmetry. Couples to 46 meV phonons. Huang-Rhys factor of 3.3. Shows dynamic J-T effect under uniaxial stress. Collins and Lawson (1989), Mita (1996).
1.945 eV (637.4 nm)	All	Y	A (excl. CVD), PL	$(N\text{-}V)^-$, the negatively charged nitrogen-vacancy. C_{3v} symmetry. Couples to 65 meV phonons. Huang-Rhys factor of 3.65. Davies and Hammer (1976), Mita (1996).
1.685 eV (735.8 nm)	All	N	A	The singly-split self-interstitial (**R2**). Hunt *et al* (2000).
1.682 eV (737.1 nm)	CVD and Si-doped HPHT	N	A, CL, PL	(Si-V), the silicon-vacancy centre. Possibly D_{3d} symmetry. Couples to 33 meV phonons. Huang-Rhys factor of 0.24. See section 6.4.1 for a literature review of this centre.
1.673 eV (741.0 nm)	All	N	A, CL, PL	V^0, the neutral vacancy (**GR1**). T_d symmetry. Couples to 41 and 96 meV phonons in absorption, and 36 meV phonons in luminescence. Huang-Rhys factor of 3.7. Shows dynamic J-T effect under uniaxial stress. Excited state transitions between 2.88 and 3.01 eV. Lowther (1978), Davies (1979c), Collins (1978b).
1.257 eV (986.3 nm)	Mixed type Ia/Ib	N	A, PL	$(N\text{-}V\text{-}N)^-$, the negatively charged di-nitrogen-vacancy (**H2**). Rhombic-I symmetry. Couples to 70 meV phonons. Huang-Rhys factor of 4. LVM at 167 meV. Mita *et al* (1990), (1993).

Table 2.3.1 – Some properties of the major optically active defect centres in natural, HPHT and synthetic CVD diamond. Defects can be observed in absorption (A), cathodoluminescence (CL) or photoluminescence (PL). 'V' means vacancy, 'N' means nitrogen, 'C' means carbon, 'Si' means silicon. Superscript 0, -, and + correspond to the charge state of the defect.

2.4 Treatment of diamond

2.4.1 Irradiation

The covalent bonding between carbon atoms in the diamond lattice results in extreme macroscopic hardness. It is also the reason for the lack of vacancy mobility at room temperature, and the radiation hardness of the lattice; electrons incident on the diamond lattice require kinetic energies of greater than ~ 150 keV before lattice damage will be observed [Wotherspoon *et al* (2002), Koike *et al* (1992)].

The diamond lattice is susceptible to radiation damage by sufficiently energetic electrons, photons, nucleons, ions and other exotic particles. The nature of the damage caused is the creation of vacancies, interstitials and related complexes [Clark *et al* (1956a), Dyer and du Preez (1965)]; the purpose of which is to create defects for studying scientifically (e.g. Clark *et al* (1956b), Davies (1974b), Steeds *et al* (1999)), changing the observed colour of the diamond [e.g. Collins (1982)], or the use of ion-implantation to insert non-native impurities into the sample for scientific and technological purposes [Zaitsev (2000)]. Often, irradiation of a sample is followed by the annealing of it, in order to investigate the creation and evolution of defects. Such an approach is used in this work to study the silicon-vacancy defect (section 6.4).

The mechanism of radiation damage in diamond can be mostly intuitively, although Campbell *et al* (2002) have shown that most of the lattice damage is caused by knock-on atoms, rather than the incident particles. Their findings will now be briefly reviewed.

A sufficiently energetic electron incident on a diamond sample will transfer energy to electrons within the lattice. The lattice electrons could be ionised from the atoms, entering the conduction band, or being ejected from the sample; a number of non-lattice damaging mechanisms involving the excited electrons can then take place (see section 3.3). The primary electron follows a

scattered trajectory through the lattice transferring energy to the electrons, emitting x-rays through scattering, until finally exhausting its kinetic energy.

Lattice damage will occur when the energy of the primary electron is greater than a threshold energy (which is lattice-orientation dependent [Koike *et al* (1992), and see Collins and Dahwich (2003)]). The energy transferred to the lattice electrons by the primary electron causes the lattice atom to be displaced, creating an interstitial and a vacancy. There is the possibility of these recombining if the separation is not large enough, or the irradiate takes place with the sample held at a sufficient temperature. The concentration of A-form nitrogen has been found to be important in post-irradiation recombination of vacancies and self-interstitials [Kiflawi *et al* (2006)]. The strain fields of A-form nitrogen traps the radiation products, preventing them from recombining; the higher the concentration of A-form nitrogen, the higher the concentration of the vacancies and self-interstitials.

The displaced atom can cause a cascade of further atomic displacements as it is displaced; this can result in clusters or chains of interstitials and vacancies which may not be spectroscopically or EPR observable, yet may act as electron traps [Campbell *et al* (2002)]. This is a similar result to the damage caused by ion-implantation, where nuclear-nuclear interaction causes lattice damage cascades. Damage caused by photon (gamma ray) irradiation is primarily due to the transfer of energy to lattice electrons, in the manner described above.

2.4.2 Thermal annealing

Heating a crystal can alter its optical properties by the modification, creation or destruction of defects. It can be used to investigate the evolution of defects (see, e.g. Chrenko *et al* (1977), Davies (1972)) and their kinetic properties, such as the thermal activation energy; and help to repair radiation damage through migration of vacancies and self-interstitials. The mechanisms of defect annealing are dependent upon the properties of the defects in consideration, and the properties of the crystal. A brief introduction of the topic, first with a general discussion, then quantification, follows.

A crystal can be seen as a lattice of atoms in potential wells, where the migration of one requires the input of energy to overcome the potential barriers (representing the energy required to make and break bonds). The presence of a point defect within a crystal affects the bond energies and spatial locations of its neighbouring nuclei; different point defects affect the properties of the crystal in their vicinity differently. When regarding thermal annealing, three broad groups of point defect can be considered: individual vacancies, defects consisting of individual atoms in interstitial or substitutional positions, and complexes.

Vacancies can migrate through the lattice, annihilate with self-interstitials, or combine with other defects to form complexes (see, for example, Davies *et al* (1992)). An interstitial or substitutional defect can become mobile within the crystal and has to navigate through the lattice without a gap into which to transfer. These defects can potentially combine with other defects to form complexes, depending upon the properties of both defects involved (for example, the aggregation of single-substitutional nitrogen in diamond [Evans and Qi (1982)]).

Point defect complexes *could* undergo migration within the lattice; however, considering that a large amount of energy would be required to break many bonds, and given the properties of a particular complex, it may be found that dissociation of the complex will occur during high temperature annealing (for example, the H4 centre in diamond [Collins *et al* (2005)]).

The energy required to mobilise a defect is not necessarily proportional to the complexity of the defect: the energy barriers to the migration are dependent on the chemical bonding of the defect in the lattice. For example, the vacancy has an activation energy of 2.3 ± 0.3 eV [Davies *et al* (1992), Lawson *et al* (1992b)], whereas that for the split-<001> self-interstitial is 1.6 ± 0.2 eV [Hunt *et al* (2000), Twitchen *et al* (1999b)].

The quantitative example of the annealing of a crystal containing vacancies and traps can be considered. Annihilation of vacancies with interstitials will first be discussed, followed by the kinetics of vacancy migration and trapping at centres. The split-<001> interstitial in diamond has a LVM at 1.859 eV. In type Ia diamond, annealing at ~ 400ºC destroys this peak and reduces the intensity of the GR1 absorption by ~ 25% [Kiflawi *et al* (2007)]. In type Ia diamond no H3 or H4 absorption is produced by this annealing, showing that the vacancy is not mobile at this temperature. The reduction in the absorption associated with the interstitial is therefore believed to be due to the interstitial becoming mobile at this temperature.

Heating a crystal imparts energy to the lattice atoms. The migration of a vacancy within the lattice takes place by the transition of lattice atoms into the site of the vacancy; because this will only happen when the neighbouring lattice atoms possess enough energy to overcome the potential barrier, an activation energy, E, can be said to be required for migration. This is true for the migration of all defects. The average time taken (in seconds) for a lattice atom to jump into a vacancy site, τ, can be expressed as [Mott and Gurney (1940)],

$$\tau = \nu^{-1} e^{\frac{E}{kT}}, \qquad 2.4.1$$

where, ν is the lattice frequency, T is the temperature (in Kelvin), and k is the Boltzmann constant. For the case of the vacancy within the trapping region of an interstitial (above), the average time decreases as the vacancy approaches the interstitial, because the energy barrier decreases due to the deformation of the lattice. It should be noted here, that the activation energy, E, of a particular defect, whilst apparently characteristic of the defect, depends upon the

environment in which it is; hence the description of a barrier / activation energy reduction in the above example.

The possibilities then, for a mobilised vacancy, are that it wanders through the lattice in a random-walk manner, eventually annihilating with a self-interstitial, becoming caught at traps (such as defects or dislocations), or reaching the crystal surface. The kinetics of the migration and trapping of a vacancy in a lattice are generally first-order: at a given temperature, the concentration of vacancies is a function of time (following Collins (1998)):

$$N_t = N_0 \exp\left(\frac{-t}{\tau}\right), \qquad 2.4.2$$

where N_t is the concentration of vacancies at time t, and N_0 is the initial concentration. $1/\tau$ is the migration rate of the defect, which is equivalent to the probability, P, of a vacancy being caught at a trap:

$$P = \left(\frac{\nu}{n_j}\right) \exp\left(\frac{-E}{kT}\right), \qquad 2.4.3$$

where, n_j is the average number of jumps made before the vacancy is caught; for a simple cubic lattice, this can be defined as $n_j = 1/C$, where C is the concentration of traps.

In diamond, it has been shown [Davies *et al* (1992)] that the concentration and type of defects (traps), determine the vacancy migration kinetics; and hence the defect constitution after annealing: for diamonds with high concentrations of nitrogen-related defects (type I), the annealing kinetics follow first-order; but for type IIa diamonds, where the concentration of traps is low, the vacancies form di-vacancies under annealing, following second-order kinetics. The activation energy of the neutral vacancy in diamond has been measured as 2.3 ± 0.3 eV [Davies *et al* (1992), Lawson *et al* (1992b)], regardless of the diamond type.

The rate of migration of a particular defect, $1/\tau$, with activation energy, E, is generalised by equation 2.4.1. The relationship between activation energy and annealing temperature, in diamond, has been plotted in figure 2.4.1. This shows

the temperature at which a defect with a given activation energy (or vice versa) will make a guaranteed lattice jump (i.e. when $1/\tau = 1$).

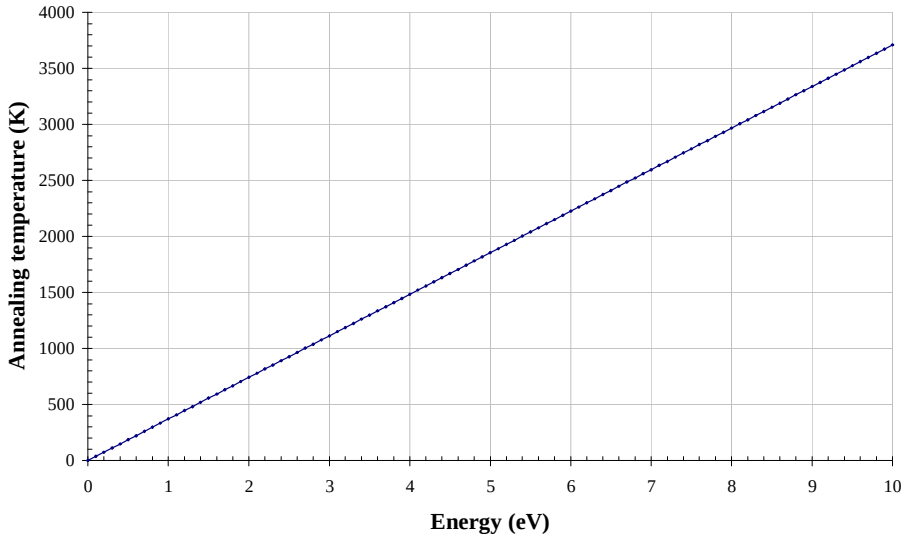

Figure 2.4.1 – Generalised relationship between activation energy and annealing temperature.

Thermal annealing usually takes place using a furnace consisting of a cylindrical ceramic tube with a heating element wrapped around; the temperature maintained by an electronic controller. In order to avoid graphitisation of diamond surfaces above 500˚C, the sample is often placed into an evacuated quartz tube, or alternatively an inert gas, such as argon, is continuously passed through the tube. Prior to annealing, removing surface contaminants by cleaning the sample often takes place; boiling in an appropriate acid solution (e.g. concentrated nitric-, sulphuric-, for a few minutes is common.

The annealing can take place as a unique event, or a series of anneals can be made, with monitoring of the changes after each stage. For a series, either the annealing time can be kept constant, with the temperature varying at each stage (isochronal), or the temperature can be constant with the length of time increasing at each stage (isothermal). The two approaches probe different aspects of defect kinetics, although both can yield activation energies.

2.5 Uniaxial stress

Determining the symmetry of a point defect is an important part of its characterisation. Knowledge of the symmetry constrains the atomic configuration, which, when combined with information about the atomic constituents, can lead to an atomic model of the centre.

The symmetry of a point defect can be determined by uniaxial stress spectroscopy. This is the use of optical spectroscopy on a crystal whilst it is compressed along its major crystallographic axes. The compression produces spectroscopically observable effect on the electronic transitions of the defects. Analysis of how a ZPL behaves under stress can yield the symmetry of the point defect it originates from.

The principle of uniaxial stress spectroscopy was established by Kaplyanskii (1964a, b), where the effects of crystallographic compression were considered, utilising group theory as applied to crystals and degenerate perturbation theory. The theoretical results of stress on the ZPL of a variety of defect symmetries were tabulated. It was found that point defects fell into two types, those which demonstrated stress-responses due to orientational degeneracy, and those demonstrating that due to orientational and electronic degeneracy. The only case in which defects show stress-responses exclusively due to electronic degeneracy is when the symmetry is the same as that of the lattice (for diamond, tetrahedral), and the electronic orbitals are degenerate; this will be explained below. Kaplyanskii's work treated most, but not all of the possible defect symmetries in cubic crystals. The outstanding symmetries have been discussed by other authors: Hughes and Runciman (1967) and Davies and Nazaré (1980).

In general, there are two types of stress-response – those when an electronic state of the defect couples with a vibrational state; and those where this doesn't happen. The former, a Jahn-Teller effect, is more complicated, and will be discussed later. The latter is discussed first.

Stress-responses due to orientational degeneracy arise from the isotropy of defect distribution within the crystal. Each defect of a particular type within

the crystal has a preferred dipole orientation, although, assuming isotropy, the many defects of that type are randomly oriented within the lattice, and hence the electric dipole is randomly oriented. The net effect is that when viewing along any lattice direction while the crystal is unperturbed, the absorption or luminescence of the centre will be equivalent to any other direction. The application of a stress along one of the principle, inequivalent crystal axes causes a compressive strain along the axis, which perturbs the energy of the electronic states of all of the defects which lie along that axis. The perturbation arises from the change of electronic wavefunction overlap due to covalent bonding. Considering that the observed shape of the zero-phonon line is the contribution of the ZPLs of many centres of the same type, in different strain environments (section 2.2.2.1), then it is clear that if all of the ZPLs of the centres in one orientation are perturbed, the ZPL will appear to split into two (or more, depending on symmetry) components.

Defects which possess electronically degenerate energy levels can have the degeneracy lifted by an external stress. The compression of the lattice deforms the symmetry of the defect and, as such, only defects with certain symmetries can have the degeneracy removed. The lifting of electronic degeneracy of a defect by stress can be best understood by considering group-theoretical arguments [Joshi (1973)]: consider the stress-induced perturbation V to the unstressed Hamiltonian, H_0, of the defect:

$$H' = H_0 + V, \qquad 2.5.1$$

where H' is the Hamiltonian of the stress-perturbed defect. The eigenfunctions of H_0, of which there are l_α, can be grouped by degeneracy into invariant subsets; these form the irreducible representation of the group G of symmetry operations on H_0. Each subset corresponds to a degenerate energy level of the defect, with an energy given by the eigenvalue E_α. Now consider the eigenfunctions of H', i.e. when the defect's symmetry is perturbed; there are still l_α eigenfunctions, but they belong to the group K (which is a subgroup of G), and are reducible. The subsets of the eigenfunctions which form K correspond to energy levels with necessarily different eigenvalues than those of the unstressed Hamiltonian, and

hence the degenerate energy levels of the unstressed defect appear to split under a symmetry perturbation.

The symmetry class of a given point defect in a crystal must be a subgroup of the lattice group, as the rotational and reflection symmetry is constrained by the lattice. The diamond lattice is of the cubic class O_h, and has the subgroups (in order of decreasing symmetry) tetragonal, trigonal, rhombic I and II, and monoclinic I and II. See Kaplyanskii (1964a, b) for further discussion of the symmetry groups in diamond.

Stress-induced strains on point defects are small in diamond, which means that the perturbation of the energy levels of a defect under lattice compression is linearly proportional to the stress [Davies (1970)]. The perturbation, V, to the unstressed Hamiltonian, H_0, of a defect is

$$\Delta V = \sum_{ij} A_{ij}\, \sigma_{ij} \quad , \qquad 2.5.2$$

where A_{ij} are the electronic operators and σ_{ij} the stress tensor, where the subscripts for both are over the cube axes [100], [010] and [001]. The stress tensor components are found by considering the projection of the stress along the chosen stress axes on to the cube axes [Hughes and Runciman (1967)]:

$$\sigma_{ij} = P \cdot Cos(p,i) \cdot Cos(p,j)\,, \qquad 2.5.3$$

where P is the magnitude of the stress, p is the stress vector, and (p,i) is the angle between p and the axis i. The basis functions of the full cubic symmetry, O_h, are known [Hughes and Runciman (1967)], and in order to inspect a particular symmetry within a cubic lattice, they should be reduced to the point group in question. This can be achieved by consulting the appropriate character tables to determine the irreducible representation, as discussed in detail by Hughes and Runciman (1967). The result is that the secular matrix for the centre with the given symmetry is obtained. This describes the perturbation to the energy levels of the centre, and should be treated according the inequivalent stresses to be applied to the centre. This can be demonstrated by considering the secular matrix obtained for a centre with tetragonal symmetry:

$$\begin{bmatrix} \alpha+\beta & \gamma \\ \gamma & \alpha-\beta \end{bmatrix}, \qquad 2.5.4$$

with

$$\begin{aligned} \alpha &= A_1\sigma_{zz} + A_2\left(\sigma_{xx}+\sigma_{yy}\right) \\ \beta &= B\left(\sigma_{xx}-\sigma_{yy}\right) \\ \gamma &= C\sigma_{xy}, \end{aligned} \qquad 2.5.5$$

where the constants A_1, A_2, B and C correspond to the electronic operators. The eigenvalues of the secular matrix are:

$$\Delta = \alpha \pm \left(\beta^2+\gamma^2\right)^{\frac{1}{2}}. \qquad 2.5.6$$

Finally, calculating the stress tensor elements for each of the inequivalent stress directions, and substituting into equation 2.5.6, yields the perturbation to the energy levels, i.e. the shift-rate expressions as tabulated in Mohammed *et al* (1982), and shown in table 5.2.2 of section 5.2.1. In order to assign each expression for the perturbation to a stress-split component, the polarisation of the transition must be considered (see Runciman (1965)).

If a Jahn-Teller or pseudo Jahn-Teller effect takes place at the centre, the electronic energy states can overlap, causing wavefunction mixing, which needs to be accounted for in the secular matrix. The observable result of this is non-linear shift-rates of the stress-split components, which qualitatively result from Coulomb repulsion of the energy states. This phenomenon has been thoroughly treated by Davies (1981), and see Davies (1979b).

Chapter 3

Equipment and methods

3.1 Absorption spectroscopy

Absorption spectroscopy is a simple yet powerful method of investigating point defects in crystals, particularly diamond. As diamond is transparent to photons with energy below the band gap energy (excluding the lattice-absorption regions), any absorption features are those due to defects within the crystal.

Photons incident on the crystal will be absorbed by a defect centre if the energies of the photons lie within the vibronic absorption band of that centre, assuming that the concentration of that species, or oscillator strength, is high enough. The mechanism of absorption at a defect centre is the incident photon coupling to the centre's electric dipole, exciting the electrons of the centre to higher energy states. These can be purely electronic transitions, or transitions to vibrational levels, as discussed in section 2.2.1.

Absorption spectroscopy is a quantitative technique, in that the integrated intensity of an absorption feature is proportional to the concentration of the defect producing that absorption feature. Light incident at the surface of a sample will pass through the sample, with a fraction of the total initial intensity absorbed by absorbing features, until the remaining fraction emerges at the exit face of the sample. Strictly, in polished, highly parallel samples, a portion of the light will reflect at the internal side of the exit face, and again at the internal side of the incident face, performing multiple passes of the path length of the sample. An absorption spectrum is generated by first recording a background spectrum, I_0, where there is no sample in place; then recording a transmission spectrum, I_t, where the sample is in place, and calculating the ratio of the two:

$$A = \log_{10}\left(\frac{I_0}{I_t}\right), \qquad 4.1.1$$

where A is the "absorbance" of the sample. The logarithm here is included because the software of many spectrometers outputs absorbance in this form. To quantify the absorbance, the path length of the light, i.e. the thickness of the sample, must be considered: the transmitted intensity, I_t, of the light can be expressed using a decaying exponential to describe how the light is absorbed by the sample. The quantified absorption, the absorption coefficient, μ, is given by,

$$\begin{aligned} I_t &= I_0 \exp(-\mu t), \\ \mu &= \frac{1}{t}\ln\left(\frac{I_0}{I_t}\right), \end{aligned} \qquad 4.1.2$$

where μ is in cm^{-1} and t is the thickness of the sample in cm. Incorporating equation 4.1.1 gives

$$\mu = \frac{A\ln(10)}{t}. \qquad 4.1.3$$

Absorption spectra of the diamonds studied in this work were recorded using four different spectrometers. Visible region (~ 400 – 750 nm) measurements were made on a custom spectrometer (see figure 3.1.1a). In this system, the sample is embedded in indium within a central hole of a copper sample holder, such that the incident light can pass through the sample (figure 3.1.1b). The copper holder is attached via screws to the end of a "cold-finger" which suspends liquid nitrogen in glass above the sample; thermal conduction takes place via the copper end of the cold-finger, and copper sample mount. The cold-finger is placed inside an evacuated glass cryostat with quartz windows which allows light transmission through the sample (figure 3.1.1c), without condensation of air onto the (cold) sample.

Light from a stabilised tungsten lamp is focussed by a spherical mirror through the sample. Transmitted light is collected by a second spherical mirror

and focussed (through filters if necessary) into a SPEX 1702, 0.75 m, Czerny-Turner grating monochromator. Light exiting the monochromator is detected by an EMI 9558Q photomultiplier, with electrical signals sent to a computer for data collection. The monochromator has entrance and exit slits which can vary between 0 and 3 mm, with an interval of 2 ± 1 μm. The monochromator has a diffraction grating with 1200 grooves mm^{-1}, blazed at a wavelength of 500 nm. The positions of all optical components of the system are finely adjustable in three dimensions, to allow optimisation of the signal.

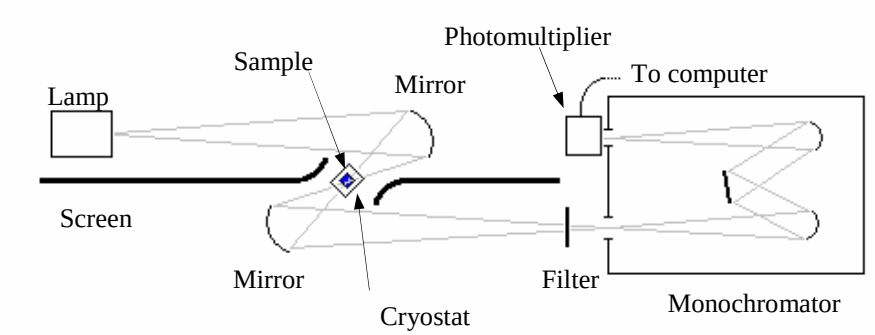

a)

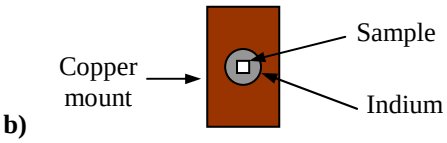

b)

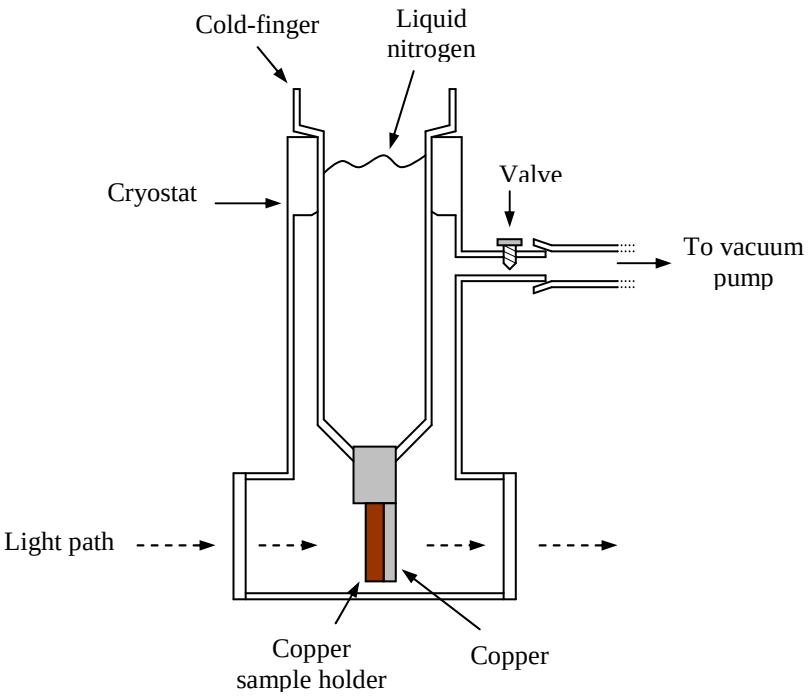

c)

Figure 3.1.1 – Schematic diagrams of the experimental equipment used in this work. a) Schematic representation (plan view) of the visible region absorption spectrometer. b) Representation of the copper sample holder, with indium to embed the sample. c) Representation of the cryostat used to hold the cold-finger and copper sample holder. See text for further details of all diagrams.

Visible to UV region absorption measurements were made using a PerkinElmer Lambda 800 UV-Vis spectrometer, which can record absorption

spectra over the range 200 to 900 nm. Liquid nitrogen temperature measurements using this spectrometer were made by using a cryostat similar to the one described above (figure 3.1.1c). The Lambda 800 is a double-beam system, which allows measurement of a background spectrum, I_0, simultaneously with the transmission spectrum, I_t. An additional background spectrum of the cryostat without the sample in place was recorded before each sample measurement. This style of spectrometer uses a diffraction grating to split the primary beam into the desired wavelength range prior to the light being incident on the sample.

Infra-red region measurements were made using a PerkinElmer Spectrum GX FTIR spectrometer and a Bruker IFS 66 spectrometer. The Fourier Transform system is based on a Michelson Interferometer. It is advantageous to use this, as recording an entire spectrum over the desired frequency range is fast, which means that many scans can be made in a reasonable amount of time, allowing signal averaging to reduce spectral noise. The PerkinElmer GX spectrometer has a maximum resolution of 0.1 cm^{-1}, and could measure over the near- and mid-infra-red regions (~ 12000 to 400 cm^{-1}). The Bruker is similar, except that it can support the incorporation of a liquid helium temperature flow-cryostat and uniaxial stress cell. The systems were only used for a small proportion of the experiments and so will be discussed in the section on liquid helium temperature measurements of the silicon-vacancy centre.

3.2 Photoluminescence spectroscopy

Photoluminescence (PL) is the use of optical excitation (often a laser) to excite optically-active defect centres in a crystal, causing them to produce characteristic luminescence. Laser energies above or below the band gap energy can be used to excite defect centres. Above band gap energy photons will produce similar luminescence to that of cathodoluminescence, as the excitation mechanism is the generation of electron-hole pairs due to electrons being ionised from the valence band.

Below band gap PL uses photons of discrete energy which can excite one or more defects, if the energy of excitation lies within the vibronic absorption band energy range of a defect. As the absorption bands of many defects can extend over many multiples of the maximum phonon range in diamond, and many defects' absorption bands can overlap, a single excitation energy can excite many optical centres.

The mechanism of luminescence production is the coupling of the incident photons to the electric dipole of a defect centre's electron, causing it to excite to a higher energy state of the centre. After a characteristic time, the electron will relax to lower energy states, releasing photons and phonons via transitions between electronic states and cascades through vibrational levels (see section 2.2.1).

Below band gap PL has the advantage of being able to excite defect centres directly, i.e. without intermediate steps as in CL and above band gap PL. Additionally, the ability to polarise the incident photon beam allows investigation of any possible polarisation of defect centres [Kaplyanskii (1964a,b)]. A disadvantage of PL is that defect centres with low concentrations, or low oscillator strengths, cannot efficiently absorb the energy of the beam, resulting in weak or negligible luminescence.

PL is at best only a semi-quantitative technique: the number of photons emitted by the centre is not necessarily proportional to the number of photons used to excite the centre. Whilst each centre will have a particular efficiency of luminescence, the lack of proportionality is due to a number of reasons: there

may be an unknown amount of self-absorption; there may be non-radiative decay processes; the concentration of A-form nitrogen in the sample can quench the luminescence [Davies and Crossfield (1973)]. The technique can be described as semi-quantitative though (provided non-radiative processes are not dominant), as excitation of any crystal with a laser will produce a Raman scattered luminescence line (at 1332 cm^{-1} in diamond). The intensity of the line will be approximately proportional to the power of the laser light incident on the crystal; hence comparing the integrated intensity of the entire ZPL and vibronic band of the defect being studied with that of the Raman line allows a certain amount of quantification.

The system used to measure photoluminescence in this work was a custom setup (figure 3.2.1). A sample is embedded in indium within a copper mount (as for the absorption spectrometer (section 3.1)), which is attached to the end of a cold-finger which can hold liquid nitrogen to cool the sample. This is placed inside an evacuated sample chamber. Laser light passes through a filter, and is focused on to the sample by a lens. The laser beam and photoluminescence emerge from the sample and continue along the spectrometer axis to a second lens, which focuses the photoluminescence through a filter (if necessary) into the monochromator. The laser beam is aligned slightly off-axis, so that it does not enter the monochromator. The lenses can be finely adjusted in three dimensions to optimise the signal. The monochromator used is a SPEX 1701, 0.75 m Czerny-Turner grating monochromator, with 1200 grooves mm^{-1}, blazed at 500 nm. The monochromator has entrance and exit slits which can vary between 0 and 3 mm, with an interval of 2 ± 1 μm.

An alternative setup can be to use mirrors to align the laser beam on to the sample perpendicularly to the spectrometer axis. This can help minimise any scattering of the laser signal into the monochromator.

Two lasers were used in this work: the first was an Ar^+, continuous wave, 514.5 nm laser, which could run up to 3 W, but was usually run at 1 W, with 30 A current. The second was a He-Cd, continuous wave, 325 nm laser, running at a fixed 25 mW. These lasers require filters to exclusively transmit the primary frequency beam; a Wratten 18B filter was used for the He-Cd laser, and a holographic notch filter was used for the Ar^+ laser.

Typical operating parameters for experiments using the PL spectrometer in this work are as follows: liquid nitrogen temperature (~ 77 K), monochromator slits of 60 to 300 μm, reading interval of 0.2 to 5 cm^{-1}, and 100 to 2000 signal readings at each wavelength interval, from which an average is found in order to reduce noise.

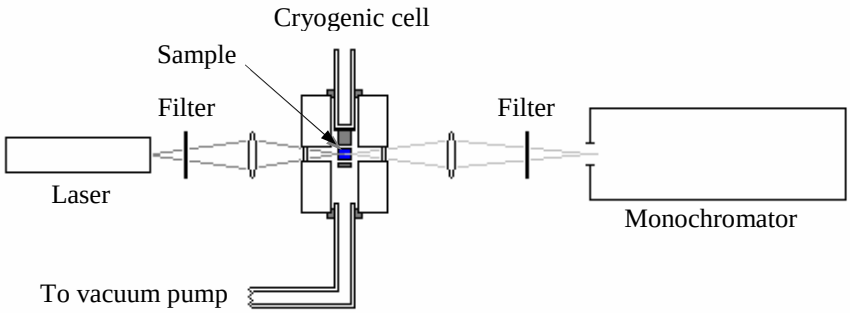

Figure 3.2.1 – Schematic diagram of the photoluminescence spectrometer system used in this work (side view).

3.3 Cathodoluminescence spectroscopy

The information in this section is taken from a number of sources [Yacobi and Holt (1986), Leamy (1982), Davies (1999) and Collins (1992)]. Cathodoluminescence is the generation of luminescence from a sample using an incident electron-beam. Electrons are accelerated towards a sample and incident on the surface; the primary electrons follow a scattered trajectory through the material, interacting with the lattice nuclei and valence electrons, imparting kinetic energy into the sample. Energy is transferred primarily to the valence electrons of the lattice, as they are lighter than the nuclei. This process results in a number of detectable signals: backscattered electrons, x-rays from the scattered primary electrons, secondary (Auger) electrons, and photons with energies in the UV, visible and infrared regions.

As the accelerating energy of the incident electrons is generally much greater than the energy gap of the material, a valence electron excited by a primary electron is promoted directly to the conduction band, leaving a hole in the valence band; this electron-hole pair is not bound (a free-exciton), and so free to travel through the lattice. An electron excited to the conduction band can undergo one of two processes: it can relax through the band states, releasing phonons (and possibly photons) until it reaches the conduction band minimum; or, the energy of excitation can be transferred to another conduction band electron, exciting it further and then either ejecting it from the sample (the Auger effect) or relaxing within the conduction band with the emission of phonons (and possibly photons).

Relaxation of the excited electron from the conduction band produces the observed cathodoluminescence. There are a number of mechanisms, which belong to two broad types: intrinsic, and extrinsic. Intrinsic transitions are characteristic of the material being studied: the excited electron transitions across the minimum energy gap of the material, from the most probably filled states of the conduction band minimum to the most probably unfilled states of the valence band maximum. The recombination of the electron and a hole results in the emission of a photon, and, if the band gap is indirect (as for diamond), the

emission of a momentum-conserving phonon. The energy of the phonon corresponds to the conduction band minima from which the electron transitioned; hence luminescence lines from free-exciton recombination can be observed with energies, $h\nu$, just below the band gap energy, E_g, according to

$$h\nu = E_g - E_x - \hbar\omega, \qquad 4.3.1$$

where E_x is the binding energy of the exciton, and $\hbar\omega$ is the energy of the phonon. The observation of free-exciton recombination luminescence requires that there are few other traps via which the free-excitons may recombine; because of this, the observation, and strength, of free-exciton recombination luminescence is a mark of the purity of a sample.

Extrinsic transitions are those which involve transitions from, to, or within defects energy states. These represent the radiative and non-radiative traps for the free-excitons. The roaming free-excitons can partially recombine to become bound-excitons; if the bound-exciton recombines at a defect, the energy of recombination can be transferred to the defect, exciting the electrons of the centre, which upon relaxation, can emit photons and phonons, characteristic of the centre. Cathodoluminescence can efficiently generate luminescence from point defects with very low concentrations (as low as ~ 10^{12} cm^{-3} [A. T. Collins, personal communication (2009)]); this is because defect centres in diamond generally have short luminescence decay times (typically of the order of a few tens of nanoseconds).

Along with general point defects, free-excitons generated by electron-beam excitation can be caught at donor and acceptor impurities which are located on nearby lattice sites; recombination releases a photon with energy which is a function of the spacing between the donor-acceptor pair. This produces the band-A luminescence (see Collins (1992) and Iakoubovskii and Stesmans (2002a) for further discussion).

Cathodoluminescence is suitable for the investigation of the properties of diamond as the carbon lattice is resistant to radiation damage from incident electrons with energies below ~ 150 keV [Wotherspoon *et al* (2002), Koike *et al* (1992)]. Typical accelerating energies are of the order of tens of keV, with beam currents of ~ 5 to 10 μA. The incident diameter produced is system dependent; in

the custom system used in this work, it is a few hundred micrometers. The electrons penetrate the sample and typically generate electron-hole (e-h) pairs, at a rate of ~ 10^{23} pairs per cm^3 per second [Collins (1992)]. The region of the sample which luminesces is at a depth of 0.010 to 0.018 × $V^{1.825}$ μm, where V is the beam voltage, in keV [Davies (1979a)]; for example a voltage of 40 keV produces a depth of ~ 8 to 15 μm. Due to scattering of the incident electrons within the crystal, the energy deposition is in an approximately spherical volume at approximately six tenths of this depth. Hence, cathodoluminescence is a useful tool to probe the near-surface region of a sample.

Cathodoluminescence spectroscopy is not a quantitative technique, as the intensity of luminescence from a point defect is dependent upon a number of unknown or ambiguous factors, such as the concentration of unknown non-radiative traps, and hence the efficiency of luminescence production at the centre. However, it *is* valid to measure the relative intensity of components in a single CL spectrum, and compare that to similar measurements in other parts of the same sample or in other samples, in order to determine if there is any kind of relationship between the components – such as if they originate at the same defect.

The cathodoluminescence spectrometer used in this work is shown schematically in figure 3.3.1. The system is custom made. An electron beam is generated by applying a voltage across a tungsten filament. The electrons are accelerated through an evacuated chamber towards the diamond sample. The beam direction and focus can be controlled via electromagnets. The beam passes through a hole in a spherical mirror and is incident on the sample; cathodoluminescence is emitted from the excited face of the sample, collected by the spherical mirror, and focused beyond the sample and cold-finger, through a window into a monochromator. The entire chamber is evacuated to below 10^{-5} Torr.

The sample is embedded in indium in the central hole of a copper mount, similar to the mount described for absorption measurements (section 3.1); however the central hole in this copper plate has a depth of half the thickness of the plate (rather than passing completely through). The copper mount is attached to the end of a cold finger which can contain liquid nitrogen, with thermal conduction taking place through the metal end of the cold-finger and the copper

mount. The position of the cold-finger can be adjusted in three dimensions using screws. Often the excitation face of the sample is masked using colloidal graphite, with an aperture etched in the desired region of the sample; this can serve two purposes, first to measure CL from particular regions of a sample, and second to avoid charging of the face of large area samples, which can result in beam deflection.

Cathodoluminescence is focused into a SPEX 1500, 0.75 m, Czerny-Turner grating monochromator. Light exiting the monochromator is detected by a Hamamatsu R636 photomultiplier, with electrical signals sent to a computer for data collection. The monochromator has entrance and exit slits which can vary between 0 and 3 mm, with an interval of 2 ± 1 μm. The monochromator has a diffraction grating with 1200 grooves mm^{-1}, blazed at a wavelength of 500 nm.

Typical operating parameters for experiments using the CL spectrometer in this work are as follows: accelerating voltage of 40 keV, beam current of 6 to 10 μA, liquid nitrogen temperature (~ 77 K); monochromator slit width of 40 to 200 μm, reading interval of 0.1 to 2.5 Å, and speed of 0.2 to 2 intervals s^{-1}.

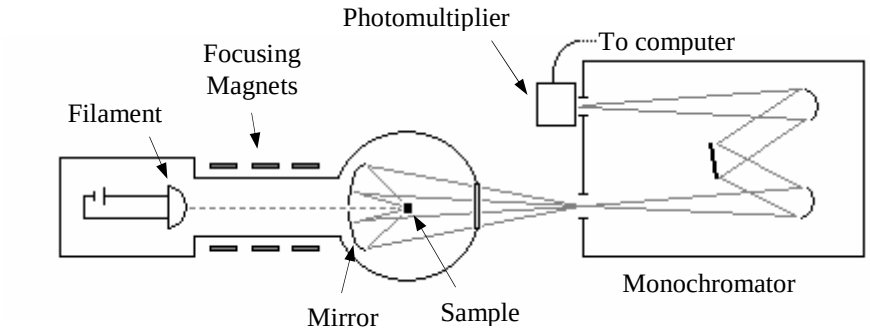

Figure 3.3.1 – Schematic diagram of the cathodoluminescence spectrometer system used in this work (plan view).

3.4 Spectroscopic considerations

Supplemental to the details of the spectroscopic systems described in the previous sections, there are a number of considerations to make in experimental spectroscopy.

In any monochromator, the accuracy of the drive mechanism may deteriorate over time, due to, among other things, slip of the thread mechanism which drives the rotation of the grating. Calibration of the monochromator may be performed by using a vapour lamp placed at the entrance slits of the detector. A spectrum of the known discrete transition energies of the lamp can be recorded across the range of the monochromator, and the measured peak energies of the emission lines can be compared to the standard emission energy values for the lamp. A plot of the displacement from the exact values may then be made, with a trend line fitted to the data. This function can be used to correct recorded experimental data. Figure 3.4.1 shows the data and function used to calibrate the CL spectrometer's monochromator.

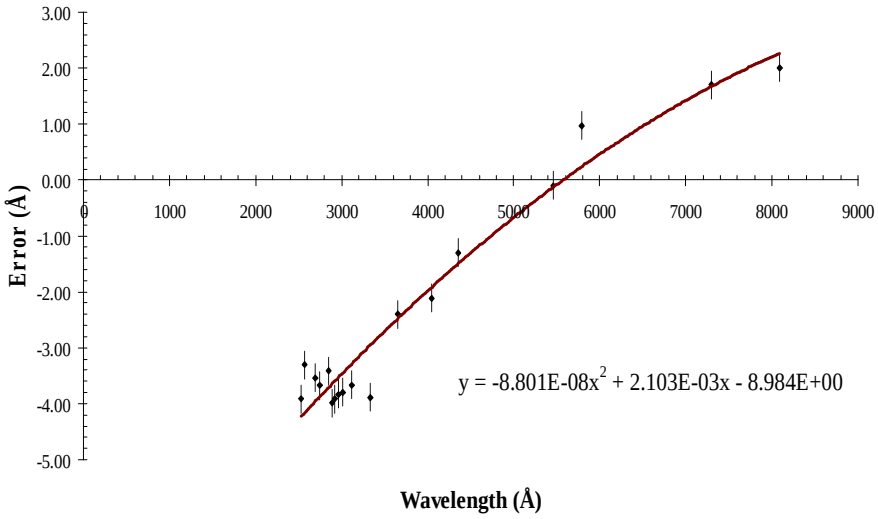

Figure 3.4.1 – Calibration of the CL spectrometer's monochromator using calibration lines across the range of the monochromator. Shows the variation of the measured calibration lines in the spectra compared to the known literature values; hence showing the drift of the monochromator. Uncertainty in the measured values is ± 0.025 Å.

It is often useful to know the precise peak energy of a zero-phonon transition, and this can be achieved using a similar method as above. A calibration lamp, with a known transition energy similar to that of the ZPL of interest, is placed in the configuration shown in figure 3.4.2 (as an example for the cathodoluminescence equipment; similar setups can be used in PL and absorption systems). This includes a beam splitter in the position shown. This setup allows both the ZPL and calibration line to be recorded in one spectral measurement. As the energy of the calibration line is known accurately, the energy of the ZPL can be corrected for the drift of the spectrometer, giving an accurate value for the energy of the ZPL. This inline calibration technique has been used in this work to measure the shifts (if any) of the ZPLs with nitrogen isotope substitution (small shifts of ~ 0.1 meV are anticipated (see section 2.2.2.3), and hence accurate readings are required).

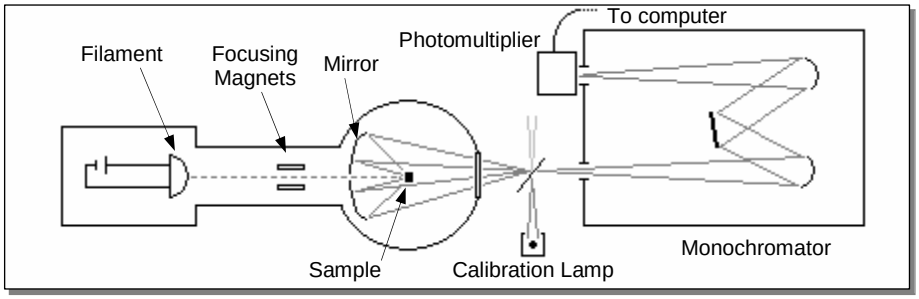

Figure 3.4.2 – Inline calibration of a cathodoluminescence system schematic (plan view).

The diffraction grating of the monochromators used in this work is of interest. Diffraction gratings have a band-pass and blaze wavelength: the wavelength regions of interest in this work are within the band-pass of the grating, and the blaze wavelength of all of the gratings is 500 nm, which, fortunately is around the region of interest for the ZPLs in this work (~ 450 to 600 nm). Thus extra considerations do not need to be made for these features.

In a number of cases, the luminescence from the sample is polarised before it enters the monochromator. This is important because the diffraction grating is ruled in the vertical direction. This means that any luminescence

polarised parallel to the grating orientation will be preferentially diffracted, and that polarised perpendicular will be less efficiently diffracted; this varies with wavelength, particularly near the blaze wavelength. To check the degree of polarisation of the grating, a stabilised tungsten lamp can be focused into the monochromator, with a polariser before the entrance slits. A scan over a spectral region can be performed in both polarisations, and the ratio found. For example, the monochromator of the photoluminescence system has a $\perp$: $\parallel$ ratio of approximately 1 : 0.6. Thus, in order to genuinely compare the intensity ratio of the data in both polarisations, the data of the less efficient polarisation should be scaled to match that of the preferential polarisation.

This effect can be problematic in situations where the signal intensity is weak, such as in uniaxial stress measurements, where applying high stresses causes the ZPL to decrease in intensity, yet broaden (the integrated intensity remains constant). Hence a weak luminescence signal may be difficult to detect in the non-preferential grating polarisation. Furthermore, polarisers (which ideally reduce the intensity by 50%, but in practice the reduction can be greater than this) and filters can reduce the luminescence intensity.

The use of long integration times and signal averaging (see section 3.2) can minimise the noise of the spectrum and help to better resolve the ZPL components; this does however mean longer time spent on each scan, which ideally should be avoided due to the risk of drift in the applied stress. Additionally, placing a de-polariser after the polariser used to select the luminescence orientation will redistribute the electric vector in all orientations; this will minimise the effect of the preferential grating orientation – at the expense of a slight loss of overall signal intensity, however.

3.5 Temperature dependence measurements

Investigation of the temperature dependence of the energy, intensity and shape of zero-phonon transitions in diamond forms an important part of the characterisation of defect centres producing the transitions (see section 2.2.2.2). Temperature dependence measurements of the ZPLs studied in this work were performed in cathodoluminescence, as no absorption by the centres was detected. Modifications to the CL spectrometer were made to achieve this.

The process of obtaining a ZPL measurement at a number of different temperatures was to cool the sample to liquid nitrogen temperature, and then record a spectrum at regular temperature intervals as the sample temperature increased to room temperature. The initial liquid nitrogen was allowed to completely evaporate, and the sample was allowed to reach equilibrium with room temperature via thermal conduction of the (now empty) cold-finger; no external heating mechanism was employed.

A thermocouple was attached to the copper plate in which the sample is mounted, and was calibrated to room temperature. The calibration was checked by cooling the sample to liquid nitrogen temperature – the error in temperature measurement was ± 5 K. Spectral data were recorded by the PC, as in the standard setup. When reading luminescence signal data from the photomultiplier, the software also read from the thermocouple, so that the output for a single spectrum consisted of three columns of data: the wavelength, the luminescence signal intensity, and the temperature at each data point.

An important requirement of temperature dependence measurements of ZPLs is that the time required to perform one scan of the ZPL is sufficiently short that the temperature variation during the scan is minimal. This is so that temperature-induced ZPL variations are minimised; a genuine ZPL can be recorded. Recording a high resolution spectrum over a localised region around any given ZPL took typically 30 to 60 s; the temperature variation over this time period was ~ 1 to 4 K, with the upper end of this spread seen at higher temperatures. Thus significant temperature-induced changes in the ZPL were not encountered during scan time.

3.6 Other characterisation techniques

This section will briefly review some of the other main techniques used to characterise diamond: electron paramagnetic resonance, Raman spectroscopy and SIMS.

Point defects in diamond which posses an unpaired electron can be studied using electron paramagnetic resonance (EPR). This is a powerful technique which allows determination of a number of properties of a chemical species such as the electronic structure and spin states, orientational properties, and information about the local environment of the species.

The effect comes from the splitting of degenerate electronic energy levels in the presence of a magnetic field. An unpaired electron's magnetic moment will align parallel or antiparallel to the direction of the field, i.e. populating one of the split energy states. If the electron is in the lower energy state (parallel to the field), absorption of electromagnetic radiation of the appropriate frequency will cause the electron to excite to the other state; it will subsequently relax. In many-body systems, the electrons will predominantly be in the lower energy state (due to Maxwell-Boltzmann statistics), and hence a net absorption of energy can occur. A particular system, e.g. a paramagnetic point defect in diamond, will have a characteristic resonance which is dependent on the intrinsic properties of the system, and the environment in which the system exists.

The local environment affects the magnetic moment of the unpaired electron by the influence of local magnetic fields. This results in changes of the resonant absorption spectrum of the system which are characteristic of the environment. Additionally, the magnetic moment of the electron can interact with the nuclear spins of nearby nuclei, which allows transitions to additional energy states to be valid, causing extra lines in the absorption spectra.

EPR is frequently used to study point defects in diamond, such as nitrogen-related centres (e.g. Newton and Baker (1991)), and transition metal centres (e.g. Nadolinny *et al* (1997)). It is advantageous because it is quantitative: the concentration of absorbing centres can be determined. Additionally, a particularly useful feature of EPR is the ability to determine the

symmetry of a centre: the magnetic moment of the unpaired electron, and the hyperfine coupling of local nuclei, are not necessarily the same in all orientations, and hence the symmetry of a defect can hypothetically be determined.

Probing the crystalline quality of a material can be achieved via Raman spectroscopy. This is where monochromatic photons incident on a sample are inelastically scattered by phonons, resulting in a measurable spectrum which is characteristic of the properties of the material. The spectrum generally consists of a peak with intensity, energy and width parameters determined by the Raman cross-section of the material, the crystalline quality, internal strains, temperature and the experimental set up (e.g. the power of the laser).

For diamond, a narrow peak at 1332 cm^{-1} is observed, with widths of 2 to 2.5 cm^{-1} in natural diamonds. Recent measurements of single-crystal CVD samples found widths of ~ 1.65 cm^{-1} [Tallaire *et al* (2006)]; earlier synthetic material showed widths of 1.7 to 14 cm^{-1} [Bachmann and Wiechert (1992)]. The peak position in diamond is relatively insensitive to temperature below about 300 K, yet shifts to lower energy by ~ 15 cm^{-1} at temperatures up to 1000 K.

The presence of non-diamond regions in a diamond sample introduces additional features in the Raman spectrum. Graphite can show two peaks at 1580 and 1357 cm^{-1}, with widths greater than that of the diamond peak. Increasing crystallographic disorder broadens the peaks and biases the intensity ratio of the peaks to the "disorder" peak at 1357 cm^{-1}.

Raman spectroscopy allows a non-destructive and experimentally simple way of determining the crystalline quality of a synthesised diamond, and is widely used. This very brief review of Raman spectroscopy followed [Bachmann and Wiechert (1992)].

Determination of the elemental composition of many solids, including diamond, can be determined using secondary ion mass spectrometry (SIMS). The technique is particularly suitable for diamond as it can detect material constituents with concentrations as low a 10^{14} cm^{-3} for particular impurities; although the sensitivity is impurity dependent.

SIMS is a destructive technique in which a primary ion beam is focused on the surface, ejecting secondary ions. These can be detected by separating the ions according to their charge to mass ratio, via electric and magnetic fields.

High detection sensitivity can be obtained by using electron multipliers or microchannel plates.

SIMS can be used to measure surface or bulk constituents, where the technique is named static or dynamic, respectively. Dynamic SIMS measurements, such as on the diamonds studied in this work, use a setup similar to that described above. Static SIMS measurements utilise a pulsed primary ion beam to obtain data.

Chapter 4

General characterisation of single-crystal CVD diamond

4.1 Introduction

Early CVD synthesis of diamond produced polycrystalline films usually of the order of a few tens of micrometers thick, with diameters of a few centimetres. The method of growth, e.g. hot filament, flame-assisted, microwave, and the choice of substrate heavily influenced the observed emission and absorption spectra, by introducing structural and point defects characteristic of the growth conditions.

The polycrystalline nature of the material meant that the distribution of defects in a single sample was usually inhomogeneous (e.g. Lang and Meaden (1991), Kanda *et al* (2003a)). This was due to grains differing in orientation, and impurities being incorporated preferentially in different growth sectors. The impurities incorporated in the synthesised diamonds were found to include elements from the substrate, such as silicon [Ruan *et al* (1991a)]; elements from the walls of the reaction chamber, such as silicon from the quartz windows (e.g. Joeris *et al* (1996)); elements from the filament (in hot filament growth), e.g. tungsten [Gheeraert *et al* (1992)]; and contamination from the atmosphere, by nitrogen, for example.

Optical spectra from these samples showed zero-phonon lines, vibronic bands, and local vibrational modes from many of these impurities. The cathodoluminescence and photoluminescence spectra were also often dominated by an intense broad band, known commonly as band-A. The shape and peak energy of the band varied in diamonds of different types, and also between

natural and synthetic diamonds; a number of different “band-A”s are observed in polycrystalline CVD diamond. Speculation about the nature of these bands is on-going. One band at ~ 2.3 eV, the green band I, has been attributed to recombination within amorphous-carbon phases [Iakoubovskii and Adriaenssens (2000)]. Another broad band at ~ 2.8 eV has been found to originate at dislocations [Yamamoto *et al* (1984)]; possible explanations are that the dislocations (and presumably also grain boundaries) are decorated with donor-acceptor pairs [Kawarada (1990)], or that the band is the strain-broadened vibronic band of a dislocation related defect [Iakoubovskii and Adriaenssens (2000)]. A further, much discussed mechanism is donor-acceptor pair recombination, first proposed by Dean (1965). See Iakoubovskii and Stesmans (2002a) and Collins (1992) for further discussions of band-A phenomena.

Despite the speculation over the mechanisms for these features, the cathodoluminescence spectra of early CVD samples were often dominated by a broad emission band. Additionally, the theoretically sharp zero-phonon lines were usually broadened, and sometimes split, by internal stresses and strains in the lattice (see, for example, Scharwzbach *et al* (1994), Burton *et al* (1995), Kanda *et al* (2003a)). This is due to the presence of grain boundaries, dislocations and other structural defects, and high defect densities (see section 2.2.2.1). It has been found that intrinsic stresses in polycrystalline CVD diamond films increase with decreasing grain size [Schäfer *et al* (1991)]. Extensive broadening of ZPLs sometimes meant that precise features of a spectrum were not resolved; a notable example (important for this work) is the 737 nm doublet. This feature, ascribed to a silicon-related centre, whilst having been observed first in 1980 as a single-broad CL line [Vavilov *et al* (1980)], was not resolved as a doublet until 1994, from cathodoluminescence and photoluminescence measurements of large grain-size polycrystalline CVD diamond [Collins *et al* (1994)]. This was crucial for an understanding of the nature of the centre (see section 6.4.1 for a more in-depth discussion of the history of this centre).

This work has investigated single-crystal CVD synthesised diamonds. Whilst this type of material is not completely free from the impurity contamination issues discussed above, it does offer a number of advantages over the polycrystalline material. First, the cathodoluminescence spectra of the material from Element Six rarely show the band-A emission, indicating a low

dislocation density. This means that emission from point defects, may be investigated without being obscured by a broad emission feature. One of the samples studied in this work was, however, heavily dislocated around the edges of the sample, and hence band-A (at ~ 2.8 eV) CL *was* observed in the dislocated regions.

Second, the ZPLs are usually very narrow (ranging from ~ 0.5 to ~ 1.5 meV, see section 4.3), allowing highly resolved spectra. This suggests lower internal strains than the polycrystalline material; however, the CVD samples occasionally do show evidence of strain in the ZPLs (such as the 532.7 nm centre, section 4.3). Third, the large size of the diamonds produced (of the order of one to six millimetres in this work), and the single-crystal nature, mean that a practically-dimensioned diamond may be oriented to provide a cuboid where a single face corresponds to a lattice direction. This allows uniaxial stress to be applied to a sample in order to study in detail the symmetry properties of defects causing ZPLs.

The cathodoluminescence spectra of the single-crystal diamonds studied in this work show features which occur regularly in different samples. Some of these features have been observed (and characterised) in non-single-crystal CVD and non-CVD diamond. A large number, however, have only been observed in this type of material. Figure 4.1.1 shows a typical cathodoluminescence spectrum of a single-crystal CVD diamond, of the type investigated in this work.

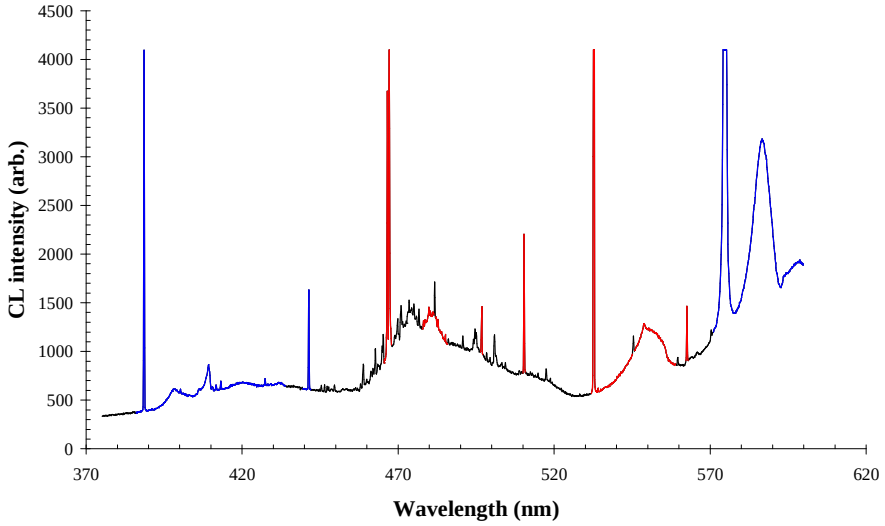

Figure 4.1.1 – Typical cathodoluminescence spectrum of a single-crystal CVD diamond. See text for explanation of the highlighted features. Recorded with the sample at 77 K.

Various features of figure 4.1.1 have been highlighted. The blue regions are those features which have been observed in other types of diamond, and have been well investigated: the ZPL at ~ 389 nm (3.188 eV), and the broader features up to around 430 nm are the ZPL, vibronic band, and local vibrational modes of the 389 nm centre, attributed to a substitutional nitrogen and interstitial carbon complex [Collins and Lawson (1989), and see Zaitsev (2000)]; the ZPL at ~ 441 nm (2.807 eV) is the 441 nm centre, attributed as another substitutional nitrogen and carbon complex [Collins and Lawson (1989)]; the ZPL at 575 nm (2.156 eV) and the band at 586 nm are the ZPL and vibronic band of the neutrally charged nitrogen-vacancy [Mita (1996), and see Collins and Lawson (1989)].

With the exception of the ZPL at 533 nm, all of the other features in the spectrum of figure 4.1.1 have only been observed in single-crystal CVD diamond. The 533 nm ZPL has occasionally been observed in very high purity diamonds grown by HPHT synthesis. A. T. Collins [personal communication (2009)] presented figure 4.1.2 at the 2004 De Beers Diamond Conference, based on spectra recorded in 1998 by Sarah Sharp, a PhD student in the Solid State Physics Group at King's College London. He reported that the 533 nm emission was particularly strong from those regions of the diamond exhibiting free-exciton emission.

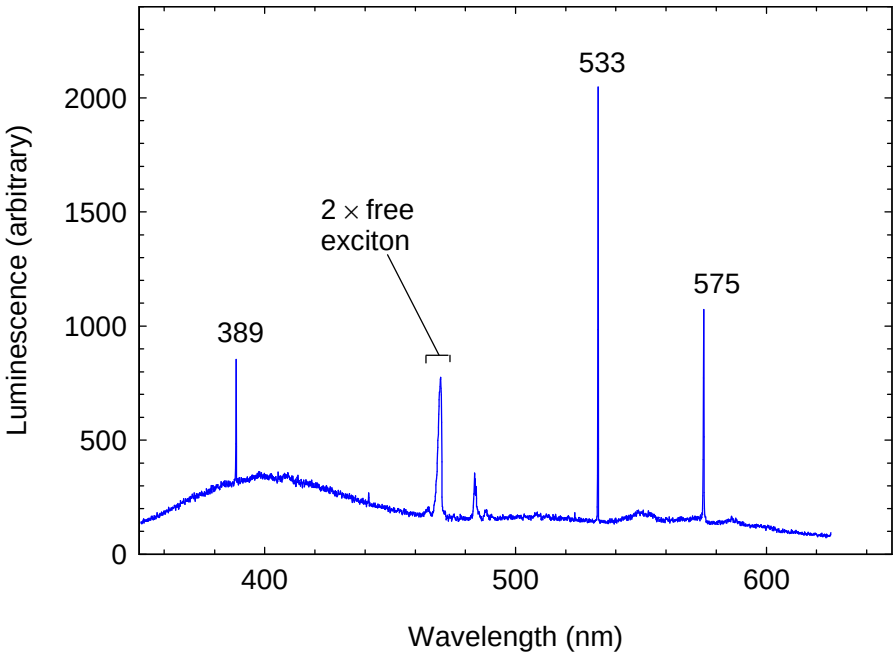

Figure 4.1.2 – Cathodoluminescence spectrum from a high-purity HPHT synthetic diamond recorded with the sample at 77 K. See body text for details.

The features highlighted in red are those which have been investigated in this work. All of the defect centres responsible for the ZPLs (except for the one at 510 nm) have had their symmetry determined by uniaxial stress work. The highlighted bands have been determined to be the vibronic bands associated with some of the highlighted ZPLs. All of the ZPLs have been measured for temperature dependence, and (again, excluding the 510 nm ZPL) been measured for nitrogen-isotope dependence. A number of other features shown in figure 4.1.1, including the band between ~ 460 and 520 nm, are also discussed later in this chapter (sections 4.3 and 4.4).

Two other features, not shown on figure 4.1.1, are occasionally observed in the CL spectra of single-crystal CVD diamond: the 5RL series of lines, and the 737 nm centre. The well-investigated 5RL centre, with a ZPL at 270.5 nm (4.583 eV), has been assigned to a pair of carbon atoms in a <100> split interstitial model [Collins and Spear (1986), and see Collins (1999) for further discussion of the nature of this centre]. The 737 nm (1.6827 eV) centre, as mentioned above, is

a silicon-related defect, and is investigated with uniaxial stress in this work (see section 6.4). Additionally, this type of diamond, and the samples studied in this work often show free-exciton emission in CL spectra.

The absorption spectra of the diamonds studied in this work are generally featureless (except for the lattice and fundamental edge absorption), although one sample (DeB #1) had a brown region which exhibited a number of sharp, yet weak ZPLs in absorption. Being low nitrogen content samples (of the order of a few hundred ppb, see section 4.2) means that the mid-infrared, one-phonon region absorption is featureless, and that the samples can be classified as type IIa. There are, however, a few absorption features at 270 nm, 1344 cm^{-1} (both due to single-substitutional nitrogen), and a cluster of lines around 7300 cm^{-1}, which are discussed in subsequent sections.

All of the spectral data presented in the following sections were recorded with the samples held at liquid nitrogen temperature (~ 77 K, except for some of the silicon-vacancy spectra, which were measured at liquid helium temperatures (~ 40 K)), and all quoted values from optical spectra have been corrected for the wavelength dependence of the monochromators, unless otherwise stated.

4.2 Samples studied

Many diamond samples have been studied in this work, primarily CVD synthesised diamonds, although a couple of HPHT samples have been measured for comparison purposes. In total, ten single-crystal CVD samples grown by Element Six, five single-crystal CVD samples grown by the diamond research group at the University of Paris XIII, one single-crystal CVD film grown by Apollo Diamond Inc., and two HPHT synthesised samples have been investigated. Table 4.2.1 summarises some of the properties of the CVD samples, and Table 4.2.2 summaries those of the HPHT samples.

Sample	Manuf-acturer	Doping	Colouration	N_s content (ppb)	Other comments
DeB #1 S013-02C 0342507-A(i)	Element Six	None	Clear except for brown layer a few hundred micrometers deep on one face	$335 < [N_s] < 173$	
DeB #2 S023-21C 0342504-K(i)	Element Six	None	Clear	384 ± 45	[001] oriented for stress work.
DeB #3 SASC04-10 0442633-B(i)	Element Six	None	Clear	107 ± 12	
DeB #4 A476-151 0171424-B(i)	Element Six	N-15	Clear in the centre, severely blackened along edges due to dislocations		
DeB #5 S010-01A 0171426-B(iii)	Element Six	N-15	Smokey brown colour throughout	NM	
DeB #6 COM-3-59 0586510-F(i)	Element Six	None	Clear	NM	[111] oriented for stress work.
DeB #7 S037-01b 0572207-A(i)	Element Six	Silane (Si-28)	Clear	NM	[001] oriented for stress work; doped with natural abundance Si-28.
DeB #8 S042-11 0572205-A(iii)	Element Six	Silane (Si-28)	Clear	ILC	Doped with natural abundance Si-28.
DeB #9 S042-12 0572205-B(iii)	Element Six	Silane (Si-28)	Clear	ILC	Doped with natural abundance Si-28.
DeB #10 0642741K	Element Six	Si-29	Clear	NM	[111] oriented for stress work; enriched to ~ 90% with Si-29.
Ap4	Apollo	None known	Clear	NM	

Table 4.2.1 – Some properties of the CVD samples studied. N_s means substitutional nitrogen, measured in parts per billion (ppb). *NM* means not measured. *ILC* means immeasurably low concentration. Nitrogen concentrations measured using either the absorption at 270 nm or at 1344 cm^{-1} (see discussion below).

Sample	Manufacturer	Doping	Colouration	N_s content (ppb)	Other comments
M4a	De Beers Diamond Research Lab	None	None	NM	
R944-02(i)	De Beers Diamond Research Lab	N-15	Growth sectors coloured differently due to nitrogen incorporation	NM	Studied previously by Collins and Dahwich (2003); electron-irradiated and annealed.

Table 4.2.2 – Some properties of the HPHT samples studied.

Nitrogen is the dominant impurity in natural and synthetic diamond. Its incorporation in various forms determines the type classification of diamond (see chapter one). Hence, determination of its concentration in diamonds is an important part of characterising a sample.

The determination of the concentration of dispersed, paramagnetic, single-substitutional nitrogen impurities in diamond has been well investigated. The neutrally charged form (N_S^0) of this type of nitrogen impurity, the C-form, gives rise to an optical absorption peak at 1130 cm^{-1} (0.109 eV) [Charette (1961), Dyer *et al* (1965)]. Additionally a broad band at ~ 270 nm (~ 4.592 eV), which shows fine structure when the sample is measured at liquid nitrogen temperature (~ 77 K), is also attributed to N_S^0 [Chrenko *et al* (1971)]. Measuring the electron paramagnetic resonance (EPR) signal attributed to N_S^0, and comparing with the 1130 cm^{-1} and 270 nm absorption features, over many samples, allowed Chrenko *et al* to determine a relationship between the EPR signal and optical features:

$$\left[N_S^0\right] = 25\mu_{1130} = \frac{25}{45}\mu_{270}, \qquad 4.2.1$$

where the [N_S^0] is in ppm (= 1.76×10^{17} cm^{-3} in diamond), μ_{1130} is the absorption coefficient at 1130 cm^{-1}, in units of cm^{-1}, and μ_{270} is the absorption coefficient at 270 nm, in units of cm^{-1}. It is clear that the peak at 270 nm has a greater sensitivity to N_S^0 than the 1130 cm^{-1} peak.

Prior to the work of Chrenko *et al*, Sobolev *et al* (1969) derived a relationship between the [N_S^0] and the peak at 1130 cm^{-1}, where 8 ppm produced an absorption coefficient of 1 cm^{-1} at 1130 cm^{-1}. The discrepancy was resolved, however, by the work of Boyd *et al* (1994), who correlated the [N_S^0] with the absorption coefficient at 1130 cm^{-1} as [N_S^0] = (25 ± 2) μ_{1130}; and Sumiya and Satoh (1996) who correlated the electron spin resonance of N_S^0 with the absorption coefficient at 270 nm as [N_S^0] = 0.56 μ_{270}.

Lawson *et al* (1998) found that the absorption coefficient (in cm^{-1}) of a peak at 1344 cm^{-1} also correlated with the neutral single-substitutional nitrogen

concentration, as $[N_S^0] = 37.5\ \mu_{1344}$. The absorption coefficient at 1344 cm^{-1} is found to be proportional to that at 1130 cm^{-1}, as $\mu_{1344} = 0.572\ \mu_{1130}$. Lawson *et al* additionally found evidence of the presence of N_S^+ impurities, and were able to determine a quantitative relationship between the $[N_S^+]$ and the absorption coefficient (in cm^{-1}) of a peak at 1332 cm^{-1}: $[N_S^+] = (5.5 \pm 1)\ \mu_{1332}$. The authors add the qualification that due to 1332 cm^{-1} being a region of high density of phonon states (1332 cm^{-1} being the maximum phonon frequency in diamond), the absorption at this frequency may also be produced by other defects; hence this relationship is only valid if the absorption peaks at 1046 and 950 cm^{-1} (characteristic of N_S^+) are also present.

4.3 Common optical spectrum features of the CVD diamonds studied

The cathodoluminescence spectra of the single-crystal CVD diamonds studied in this work were introduced in section 4.1, where the optical features previously investigated by other workers, such as the nitrogen-vacancy and interstitial related features, were identified to exist in this material. Most of the other optical features present in CVD samples exist within the visible and near infra-red regions, and all, excluding two ZPLs (the 532.7 nm centre and 737 nm doublet), appear to be unique to CVD synthesised diamond. Figure 4.3.1 shows a cathodoluminescence spectrum with most of the characteristic features of this material (transition energies are given in table 4.3.1).

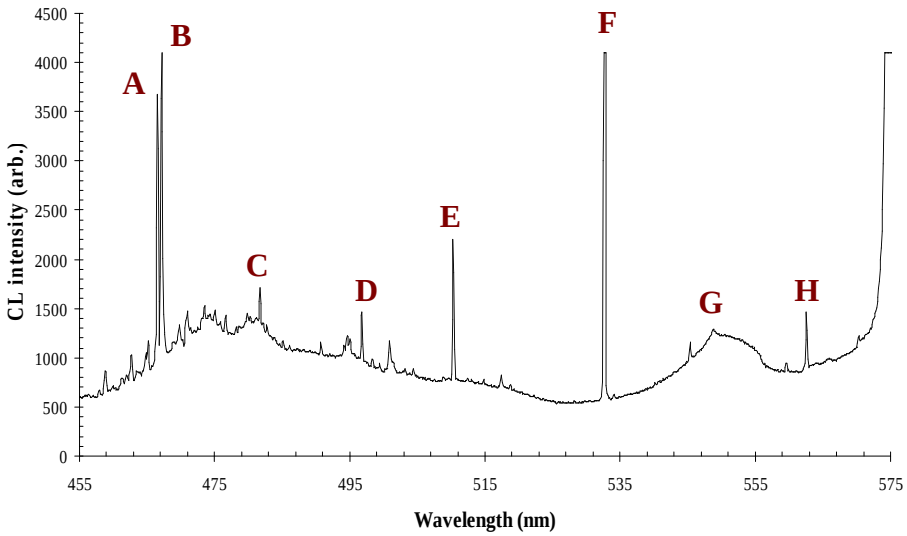

Figure 4.3.1 – Cathodoluminescence spectrum of the optical features characteristic of single-crystal CVD diamond in the visible range. See text for label details. Recorded with the sample at 77 K.

Features of figure 4.3.1 have been highlighted to assist discussion. All of the labelled features, except C and G, are zero-phonon lines. Features C and G have been determined to be the vibronic bands of ZPLs B and F, respectively

(this work, discussed in later sections). (Label C refers to the weak band below the label, not the sharp feature on top of the band.)

All of the ZPLs have been measured for temperature dependence; all of the ZPLs excluding E have been measured for nitrogen-15 isotope dependence and have been measured under uniaxial stress, in order to determine the symmetry of the defect producing the ZPL.

All of the ZPLs, excluding line E, have been observed in single-crystal CVD diamond previously, and identified in the literature; reviews of each ZPL will be presented, along with the data obtained about each, later in this chapter. It has been shown [Tallaire *et al* (2006)] that the features highlighted in figure 4.3.1 are strongly enhanced in intensity by the addition of nitrogen to the gas phase of the growth process, and in undoped samples all of the features, excluding line F, are not present in the CL spectra. This phenomenon applies to the samples grown by University of Paris XIII, but not to the Element Six material, where undoped samples show the features. This has two implications: first, that the features are nitrogen related, either directly, through nitrogen involvement in the defect centres, or indirectly, through other mechanisms; and second, that the Element Six CVD growth chambers are not entirely free from nitrogen. This may be deliberate, however, as it known that the incorporation of a small amount of nitrogen in the gas phase of CVD synthesis produces higher quality material with faster growth rates [Yan and Vohra (1999), Chayahara *et al* (2004), Tallaire *et al* (2006) and references therein].

The peak wavelength, energy, and full width at half maximum (FWHM) of each ZPL highlighted in figure 4.3.1 are listed in table 4.3.1; the values reported are the statistically averaged positions from seven samples; five grown by Element Six, two by the University of Paris XIII. These values will be used throughout this work and should provide reference for other workers as the commonly observed peak positions of these ZPLs in this material (the FWHM, however, will most likely be sample dependent).

ZPL label (corresponding to figure 4.3.1)	Peak wavelength (± 0.05 nm)	Peak energy (± 0.0003 eV)	FWHM (meV)
A	466.65	2.6569	1.36 ± 0.11
B	467.22	2.6536	1.84 ± 0.07
D	496.83	2.4955	1.07 ± 0.09
E	510.36	2.4293	0.94 ± 0.13
F	532.71	2.3274	1.05 ± 0.05
H	562.57	2.2039	0.80 ± 0.04

Table 4.3.1 – Statistically averaged peak wavelength, energy and FWHM of the ZPLs studied in this work.

The ZPLs A and B are spaced very close in energy to one another, and could initially be mistaken for a doublet. However, inspection of the CL spectra from a variety of samples (figure 4.3.2) shows that the lines do not appear with constant relative intensities.

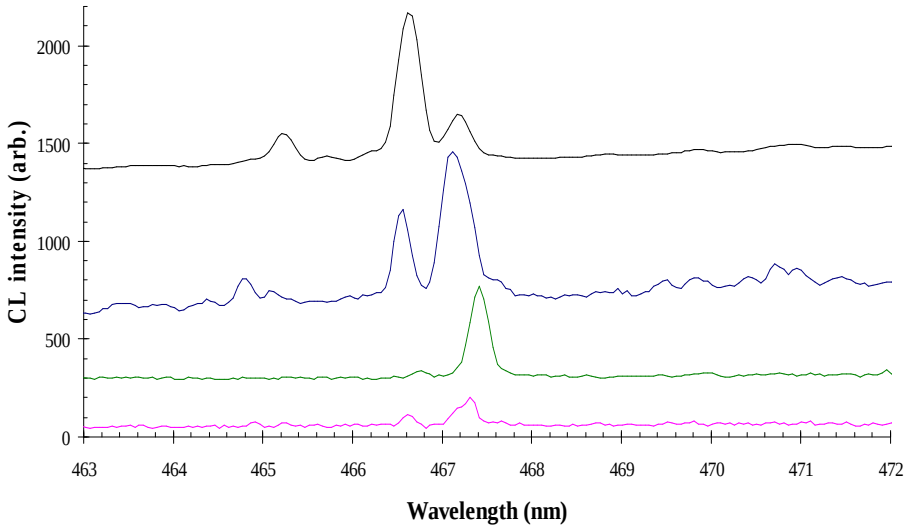

Figure 4.3.2 – Cathodoluminescence spectra of ZPLs A and B (466.6 and 467.2 nm, respectively) in four single-crystal CVD samples. The upper spectrum is from a sample grown by the University of Paris XIII, the lower ones recorded from samples grown by Element Six. Note the non-constant relative intensities. Spectra have been displaced and scaled for clarity. Recorded with the samples at 77 K.

The luminescence from ZPLs A, D and H shows an orientation dependence, and it has been found in this work that the defects responsible for the ZPLs are preferentially oriented within the single-crystal diamonds. This may be a feature of the growth process of this material. This will be discussed in detail in section 5.3.

Line F is considered an important ZPL, as it is observed in CVD synthesised diamonds, both single-crystal and polycrystalline, and it is occasionally seen in HPHT synthesised diamonds; however, it has never been observed in untreated natural diamonds. Hence it is considered a potential spectroscopic marker of synthetic diamonds. The line has been investigated in this work, its temperature and nitrogen dependence measured, and the symmetry of the defect causing the line tentatively determined (section 6.3). Previous workers have debated whether the 532.7 nm ZPL is in fact a doublet (see section 6.3.1); high resolution scans of the ZPL in a variety of high quality single-crystal CVD samples in this work show that the line can be resolved as a single peak (figure 4.3.3a). It can be, and often is, however observed with a “shoulder” (figure 4.3.3b), or slight splitting (with variable splitting energies), which presumably led previous workers to suggest the doublet nature of the line. The fact that it can be resolved as a single narrow peak shows that it is not a doublet; however the frequent observation of splitting with variable energy implies that the line is highly susceptible to internal strains within the crystal, and may even be indicative of the involvement of a vacancy within the centre. The nature of the defect that causes the ZPL at 532.7 nm will be discussed further in section 6.3.3.

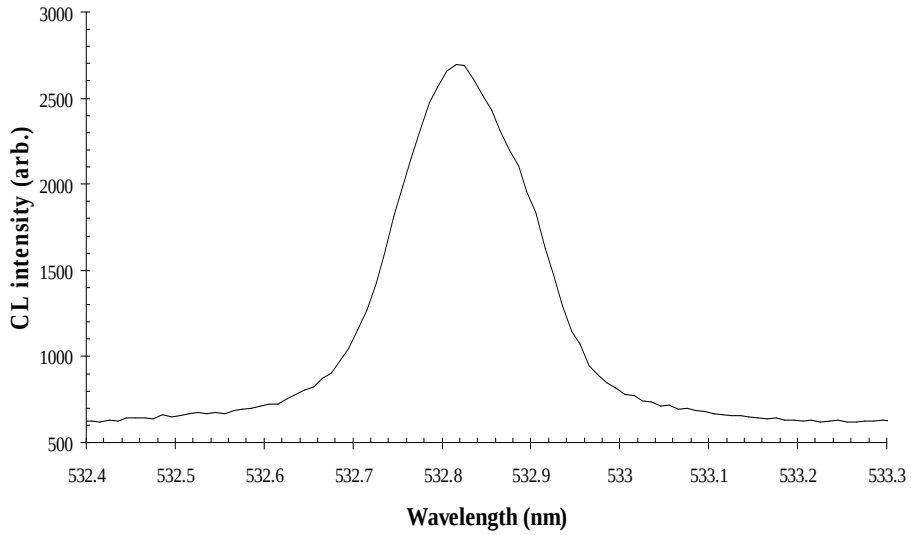

a)

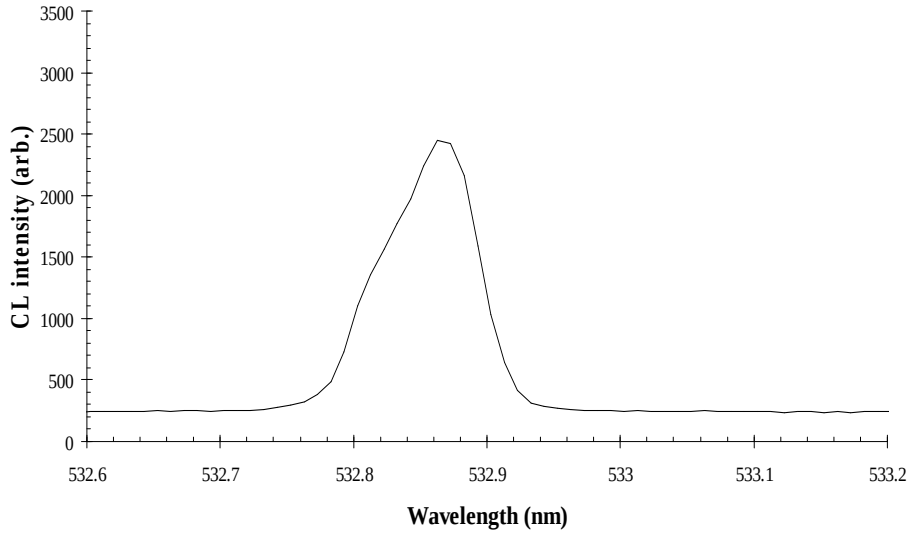

b)

Figure 4.3.3 – High resolution cathodoluminescence scans over line E, the 532.7 nm ZPL. a) the peak shows minimal splitting. b) the peak demonstrates the often-observed shoulder. Recorded with the sample at 77 K.

Along with the optical features A through H which have been studied in this work, a feature just-beyond the visible light region has also been investigated: the 737 nm doublet. This silicon-related feature has been investigated extensively, except for having its symmetry determined experimentally; this task was undertaken in this work. Section 6.4.1 presents a review of the history of this centre, along with experimental results. Here it is included in the summary of defect centres commonly observed in single-crystal

CVD diamond: it can be observed using absorption spectroscopy (figure 4.3.4a) and photoluminescence, but excitation using 40 keV electrons seems relatively inefficient. When the concentration of centres is high enough, however, the 737 nm system can be observed in cathodoluminescence (figure 4.3.4b).

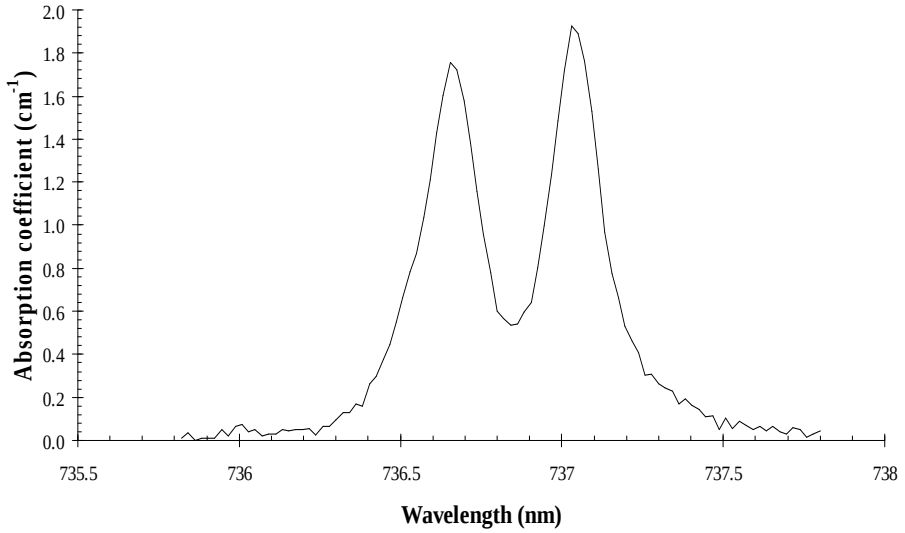

a)

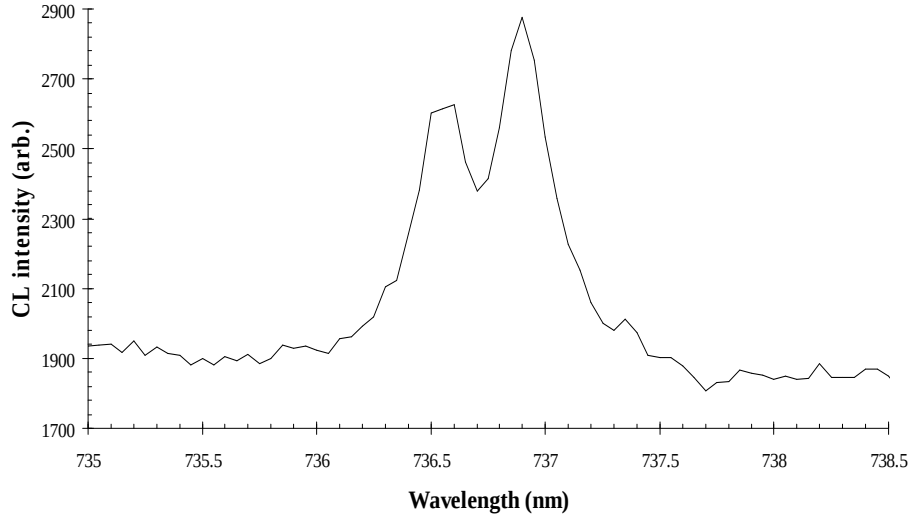

b)

Figure 4.3.4 – Spectra of the 737 nm doublet (at liquid nitrogen temperature) in an irradiated and annealed single-crystal CVD diamond grown with silicon in the gas phase; spectra recorded in a) absorption, and b) cathodoluminescence. Bother spectra recorded with the sample at 77 K.

Along with the ZPLs discussed above, the single-crystal CVD diamonds studied in this work show many minor optical spectrum features, which have not been previously documented. The origins of these features have not been

investigated in further detail in this work, as, generally, they are too weak to subject to the characterisation approaches utilised in this work (temperature dependence, isotope effects, uniaxial stress). Table 4.3.2 presents a summary of the features observed in cathodoluminescence; table 4.3.3 reports the features observed in UV-visible absorption. The summary does not include the 5RL centre cathodoluminescence (ZPL at 270.5 nm (4.583 eV)), or free-exciton recombination luminescence (234.4 nm (5.289 eV)), which are often observed in this material. The features listed in table 4.3.2 are present in all of the "DeB #" samples, except DeB #7, 8, 9 and 10, which were doped with isotopes of silicon. These samples showed only the following features in CL: 737 nm, 575 nm, 532.7 nm 441.2 nm, the 389 nm centre with LVMs, and the 5RL centre. The absorption features exclusive to the brown side of DeB #1 are included in table 4.3.3. References to the known defects centres are omitted here; see section 4.1 for a review of the known defect centres in this material. In many of the CVD samples the concentration of the 736.8 nm centre is too low to produce observable absorption.

Wavelength (nm)	Energy (eV)	Common name / defect (if known)	FWHM (nm)	FWHM (meV)	ZPL or band?
388.4	3.191	389 nm - N & C_I	0.184	1.512	Z
398.0	3.114	Vibronic band of 389 nm	6.203	48.331	b
441.2	2.810	441 nm - N & C_I	0.243	1.552	Z
447.1	2.772		0.187	1.161	Z
466.6	2.657		0.169	0.966	Z
467.2	2.654		0.205	1.167	Z
473.7	2.617		4.539	25.051	b
480.7	2.579	Vibronic band of 467 nm	4.873	26.193	b
496.8	2.495		0.181	0.909	Z
498.3	2.487		0.167	0.833	Z
500.8	2.475		u	-	Z
500.9	2.474		u	-	Z
501.2	2.473		0.221	1.092	Z
501.6	2.471		u	-	Z
502.7	2.466		0.301	1.476	Z
503.9	2.460		0.177	0.865	Z
504.4	2.457		0.159	0.777	Z
508.8	2.436		0.170	0.818	Z
510.3	2.429		0.174	0.829	Z
512.6	2.418		0.216	1.020	Z
514.0	2.412		0.157	0.741	Z
517.4	2.395		0.185	0.860	Z
532.7	2.327	532.7 nm	0.162	0.707	Z
545.4	2.273		0.139	0.580	Z
545.9	2.270		0.157	0.653	Z
551.4	2.248	Vibronic band of 532.7 nm	11.750	48.304	b
559.5	2.215		0.134	0.531	Z
562.6	2.203		0.164	0.645	Z
574.7	2.157	575 nm $(N\text{-}V)^0$	0.254	0.955	Z
587.1	2.111	Vibronic band of 575 nm	6.246	22.455	b
600.0	2.066	Vibronic band of 575 nm	10.380	35.737	b
636.8	1.946	637 nm $(N\text{-}V)^-$	0.191	0.586	Z
777.5	1.594		0.443	0.908	Z
885.9	1.399		0.318	0.503	Z
894.8	1.385		0.404	0.625	Z

Table 4.3.2 – Summary of observed features in the cathodoluminescence spectra of the single-crystal CVD diamonds studied in this work. Error in measurements of ± 0.025 nm, ± 0.108 meV. 'N' means nitrogen, 'C_I' means interstitial carbon, 'V' means vacancy, 'u' means un-measurable, 'Z' means ZPL, 'b' means band. Features highlighted in grey indicate a structured group of lines. Features highlighted in blue have been investigated in this work.

Wavelength (nm)	Energy (eV)	Common name / Defect (if known)	FWHM (nm)	FWHM (meV)	ZPL or band?
270.1	4.589	N_s related peak	u	-	b
271.0	4.573	N_s related peak	0.735	3.643	Z
446.8	2.774		0.195	1.216	
467.6	2.651		0.243	1.380	Z
482.1	2.571		0.430	2.294	
575.0	2.156	575 nm $(N\text{-}V)^0$	0.298	1.119	Z
594.1	2.086		0.733	2.576	
626.6	1.984		0.848	2.694	Z
637.1	1.946	637 nm $(N\text{-}V)^-$	0.188	0.575	Z
736.8	1.682	737 nm doublet	-	-	Z

Table 4.3.3 – Summary of all observed features in the UV-visible absorption spectra of the single-crystal CVD diamonds studied in this work. Error in measurements of ± 0.025 nm, ± 0.108 meV. 'N_s' means substitutional nitrogen, 'N' means nitrogen, 'V' means vacancy, 'u' means un-measurable, 'Z' means ZPL, 'b' means band. The feature highlighted in blue has been investigated in this work. The features highlighted in yellow have only been observed in a brown colouration in sample DeB #1 (see section 4.4). Readings cut off at ~ 800 nm.

The features at 501.2, 508.8, 510.3 (line E), 512.6, 517.4, 532.7 (line F), line F's vibronic band, 562.5 (line H) and 575 nm can all be excited (weakly) by photoluminescence, using a 325 nm HeCd laser (see figure 4.3.5). The 575 and 637 nm centres can be readily excited in PL with a 514.5 nm Argon ion laser.

The 637 nm (1.945 eV) centre, the negatively charged nitrogen-vacancy, has been observed in CL spectra of undoped, untreated, single-crystal CVD synthesised diamond in this work. Previously, observing the centre in CL was only possible using nitrogen-containing diamonds irradiated with high energy ions (see Zaitsev (2001)). The single-crystal CVD synthesised diamonds grown by Element Six show weak CL from this defect – weak relative the neutral nitrogen-vacancy (ZPL at 575 nm, 2.156 eV), which is highly cathodoluminescent efficient in this material. It could be that luminescence from the 575 nm band is being absorbed in the 637 nm centre's absorption band, causing it to produce photoluminescence. The ZPL is observed at 636.90 ± 0.08 nm (1.946 ± 0.002 eV), with a FWHM of 0.598 ± 0.152 meV (values statistically averaged over a number of samples); see figure 4.3.6.

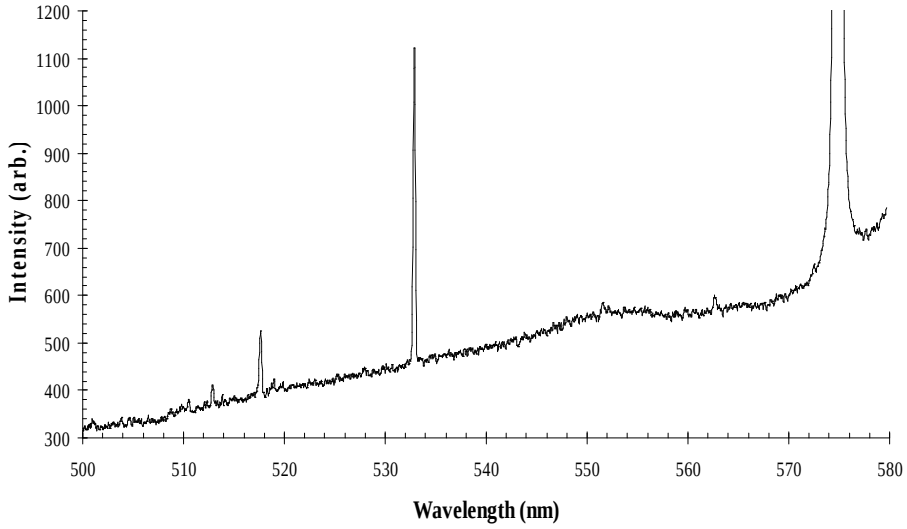

Figure 4.3.5 – Typical photoluminescence spectrum of a single-crystal CVD diamond, excited using a 325 nm HeCd laser, showing weak luminescence from a number of the ZPLs observed in the CL spectra. Recorded with the sample at 77 K.

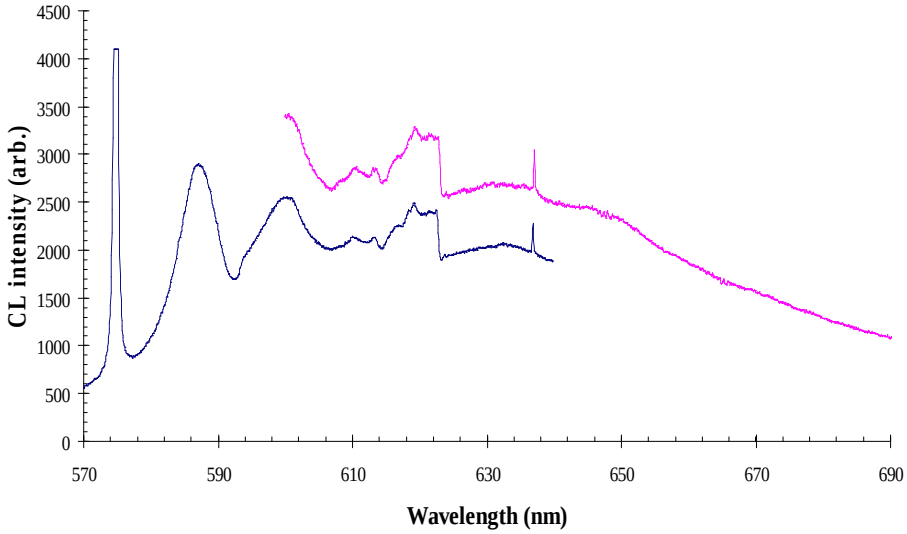

Figure 4.3.6 – Cathodoluminescence spectra of two samples of single-crystal CVD diamond grown by Element Six, showing the 637 nm (1.945 eV) centre, along with the 575 nm (2.156 eV) centre. Recorded with the samples at 77 K.

Finally, a series of weak cathodoluminescence lines which appear frequently in this material were omitted from table 4.3.2. Figure 4.3.7 shows the CL spectrum of these features. They appear distinctly above a broad increase in

luminescence over the range ~ 455 to 485 nm. The wavelengths and energies of the lines are listed in table 4.3.4. Of the many potential mechanisms of production of these features, one possibility is that they are due to donor-acceptor pair recombination (DAPR) considering their energy and presence on top of a broad band. DAPR was suggested to account for the band-A luminescence observed in most types of diamond [Dean (1965)]; a brief discussion of the various "band-A"s observed is given in section 4.1.

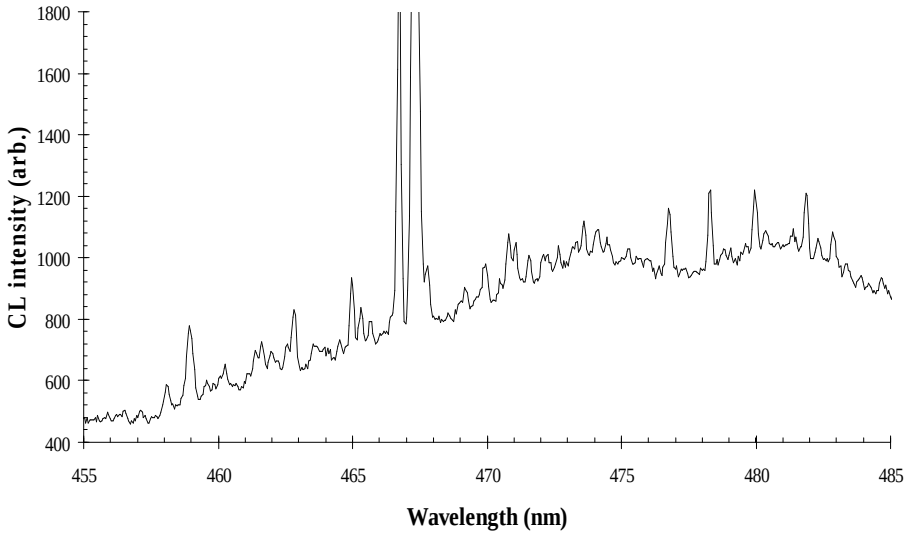

Figure 4.3.7 – Cathodoluminescence spectrum of the series of weak sharp lines between ~ 455 and 485 nm, observed in the single-crystal CVD diamonds studied in this work. The two intense ZPLs present are the 466.6 and 467.2 nm lines. Recorded with the sample at 77 K.

Wavelength (± 0.05 nm)	Energy (± 0.0003 eV)	Normalised intensity
458.06	2.7067	0.34
458.94	2.7015	1.00
459.56	2.6979	0.23
460.20	2.6942	0.17
461.47	2.6867	0.32
461.94	2.6840	0.34
462.55	2.6805	0.36
462.80	2.6790	0.77
463.53	2.6748	0.31
463.92	2.6725	0.21
464.52	2.6691	0.18
464.97	2.6665	0.86

465.31	2.6645	0.50
465.70	2.6623	0.11
468.94	2.6439	0.19
469.25	2.6422	0.18
469.56	2.6404	0.18
469.94	2.6383	0.51
470.46	2.6354	0.18
470.78	2.6336	0.66
471.06	2.6320	0.53
471.54	2.6293	0.36
472.16	2.6259	0.20
472.66	2.6231	0.16
473.26	2.6198	0.13
473.60	2.6179	0.35
474.05	2.6154	0.15
474.48	2.6131	0.22
475.00	2.6102	0.10
475.21	2.6090	0.19
475.94	2.6050	0.20
476.74	2.6007	0.77
477.40	2.5971	0.12
478.28	2.5923	0.64
478.79	2.5895	0.15
479.01	2.5883	0.12
479.62	2.5851	0.12
479.96	2.5832	0.68
480.31	2.5813	0.14
481.36	2.5757	0.29
481.84	2.5732	0.76
482.31	2.5706	0.15
482.86	2.5677	0.25

Table 4.3.4 – List of the wavelength, energy and normalised intensity of each line in the series between ~ 455 and 485 nm in the single-crystal CVD diamonds studied in this work.

This author considers it doubtful that this particular series of lines is due to DAPR for a number of reasons: 1) the small energy range these lines span; 2) the highly structured nature of the broad band luminescence beneath the lines, which appears suggestive of a number of overlapping vibronic bands (indeed, the weak band peaking at ~ 480 nm is shown later in this work to be the vibronic band of the 467.2 nm ZPL); and 3) the lack of reduction of transition intensity to higher energies. However, for consistency, a fit of the energies of these lines to the DAPR equation has been performed. The approach follows that of Dischler *et al* (1994), who performed the analysis on a series of luminescence lines seen in

polycrystalline CVD diamond. The energies of transitions between donor and acceptor pairs are given by the expression:

$$h\nu(r) = E_g - (E_a + E_d) + \left(\frac{e^2}{\varepsilon r}\right) - E_{corr}\,, \qquad 4.3.1$$

where E_g is the energy of the band gap, E_a is the binding energy of the acceptor, E_d is the binding energy of the donor, e is the electronic charge, ε is the dielectric constant, r is the distance between an acceptor and donor, and E_{corr} is an energy term which corrects for large pair separations. Assuming that the acceptor and donor impurities are on substitutional lattice sites, then the separation values, r, are quantised. Further intricacies of the calculation will not be discussed here – the reader is referred to Dischler *et al* (1994). The calculation was performed for this series of luminescence lines listed in table 4.3.4: least-squares fitting the observed line energies to the separation values in the DAPR equation, 4.3.1, yields the expression

$$E_g - (E_a + E_d) = 2.29\,. \qquad 4.3.2$$

Taking the energy of the diamond band gap to be 5.46 eV at 77 K (see Zaitsev (2001)), and assuming the acceptor is substitutional boron, which has a binding energy of 0.37 eV [Collins and Williams (1971)], the binding energy of the donor, E_d, is found to be, from this calculation, 2.80 eV. This is similar to the value of 3.3 eV obtained by Dischler *et al* (1994), but both values are very different to the generally accepted value of 1.7 eV for the ionisation energy of the single substitutional nitrogen donor [Farrer and Vermeulen (1972)].

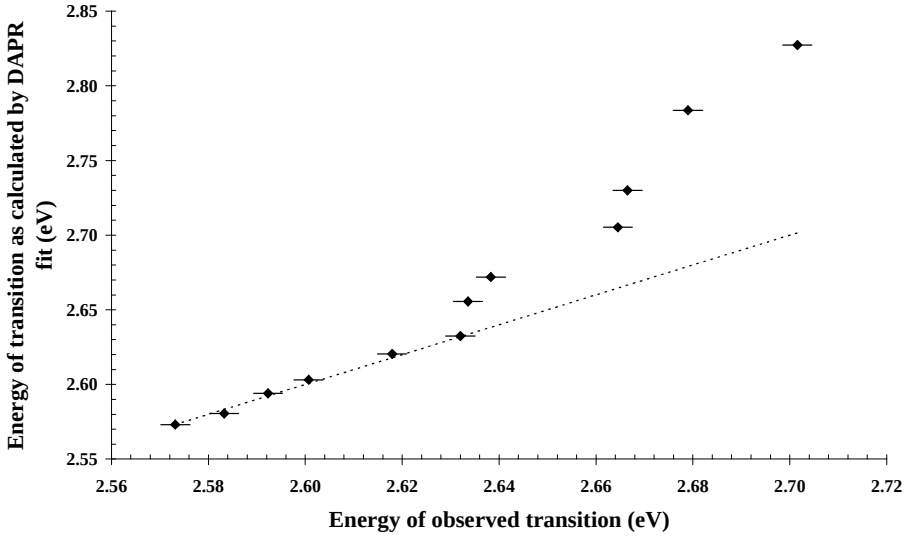

Figure 4.3.8 – Comparison of the energies of the most intense transitions in the 2.56 to 2.71 eV range with the calculated energies as determined by the DAPR model simulation. The dotted line shows a 1:1 ratio with the observed transition energies, in order to highlight the scatter found at higher energy.

Furthermore the fit of the data to equation 4.3.1 (see figure 4.3.8) shows considerable scatter at high energies (larger separation values (r)), and the relative intensities of the lines are not as expected from the calculations carried out by Dischler *et al* (1994). Utilisation of an appropriate E_{corr} may help to reduce the scatter at higher energies; however this would not eradicate the other outstanding issues with this fit. The conclusion then is that DAPR can be excluded from the possible origins of this series of luminescence lines.

4.4 Cathodoluminescence of DeB #1

Sample DeB #1 displays a number of unusual features and hence merits a subsection of its own. The sample is a large, single-crystal CVD synthesised diamond of dimensions 6.325 × 5.343 × 1.735 mm (see figure 4.4.1). It was not intentionally doped during growth, and was provided cut (substrate removed) and polished. The sample is visually clear, and presents a featureless visible-UV absorption spectrum (figure 4.4.2), except for the absorption at the band gap, and a band centred at ~ 270 nm. This band, along with the fine structure visible on top of it at liquid nitrogen temperatures, is due to the presence of neutrally charged single substitutional nitrogen (N_s) impurities [Chrenko *et al* (1971)]. Measurement of this band allows the concentration of N_s in the sample to be estimated as 335 ± 35 ppb.

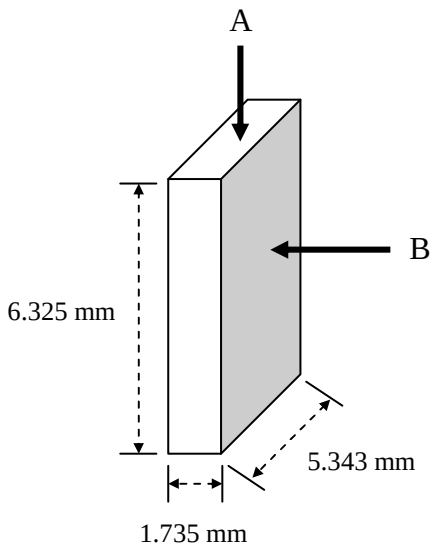

Figure 4.4.1 – A schematic diagram of the DeB #1 sample.

Closer inspection of the sample whilst under the microscope revealed a subtle brown colouration on one of the two larger faces. The colouration can only be observed by looking along an edge of the sample (direction A of figure 4.4.1) and only slightly affects the observed colour of the sample when looking through

the large faces (direction B of figure 4.4.1). The colouration appears to be homogeneous across the sample face. Using a micrometer, an estimate of the depth into the sample bulk is ~ 200 μm at most. It is not known whether this was the substrate or growth side of the sample.

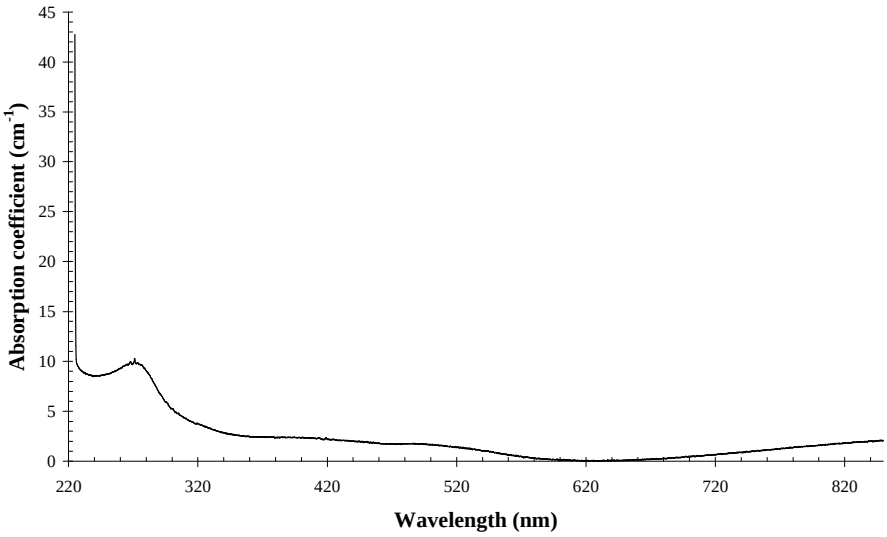

Figure 4.4.2 – Absorption spectrum of the DeB #1 sample, recorded with the sample at 77 K.

A change in observed colour across a single diamond implies a change in the visible absorption spectrum between the regions. This was investigated by masking the brown edge and measuring an absorption spectrum of the clear region, along the length of the sample (direction A of figure 4.4.2) to maximise the quality of the absorption spectrum. Then the clear region was masked, the brown edge unmasked, and an absorption spectrum was recorded along the same axis of the sample. The difference in absorption between the regions is striking (figure 4.4.3), yet not unexpected: the brown region shows strong broad absorption over the blue-green region of the visible spectrum, leaving it relatively transparent to light in the yellow to red region of the visible spectrum. The absorption spectrum of the clear region of the sample is similar to the first absorption spectrum measured on this sample, however that measurement (figure 4.4.2) was made with the beam incident on the large face of the sample (direction B in figure 4.4.1).

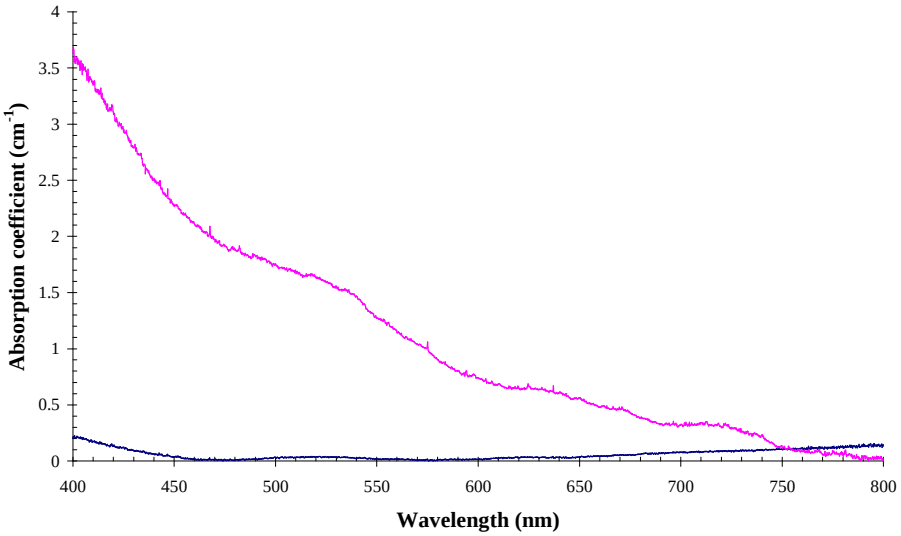

Figure 4.4.3 – Absorption spectra of the DeB #1 sample, at 77 K. The blue spectrum is the absorption measured through the clear region of the sample. The pink spectrum is the absorption measured through the brown region of the sample.

The first absorption measurements made on the sample were recorded using a PerkinElmer Lambda 800 UV-Vis absorption spectrometer. The latter measurements were made on the custom absorption system (see chapter three), as this allowed focusing of the beam on to the narrow brown region.

The spectrum recorded for the brown region appears to be similar to that of brown diamonds; broad step-like absorption increasing towards higher energies (see, for example, De Weerdt and Van Royen (2001), De Weerdt and Collins (2007)). There are a few sharp, yet weak features in the spectrum: 446.8 nm (2.774 eV), 467.6 nm (2.651 eV), 482.1 nm (2.571 eV), 574.9 nm (2.156 eV), 594.1 nm (2.086 eV), 624.6 nm (1.984 eV), 637.1 (1.946 eV). The lines at ~ 575 and 637 nm are the neutral and negatively charged nitrogen-vacancy, respectively [Mita (1996)]. The line at ~ 594 nm is a nitrogen and vacancy related complex (Davies and Nazare (1980), and see Zaitsev (2001) for further references). The other lines have not been previously reported.

This is the first reported measurement of absorption by the neutral and negative nitrogen-vacancy defects in this material. Although the peaks are weak, the concentration of the centres can be determined using the calibration factor [Davies (1999)]. The concentration of $(N\text{-}V)^0$ in the brown region of this material

is calculated as (2.00 ± 0.65) × 10^{15} cm^{-3} (≈ 11 ± 4 ppb); and that of the $(N\text{-}V)^-$ is (0.76 ± 0.25) × 10^{15} cm^{-3} (≈ 4 ± 1 ppb).

As the brown colouration appears to be limited to a region very close to the surface, it is appropriate to investigate it using cathodoluminescence (see chapter three). The electron beam was run at 40 kV for the measurements made in this section, which corresponds to a penetration depth of approximately (0.018 × $(40)^{1.825}$) = 15 μm. Figure 4.4.4 shows comparative composite spectra of the clear and brown sides of DeB #1.

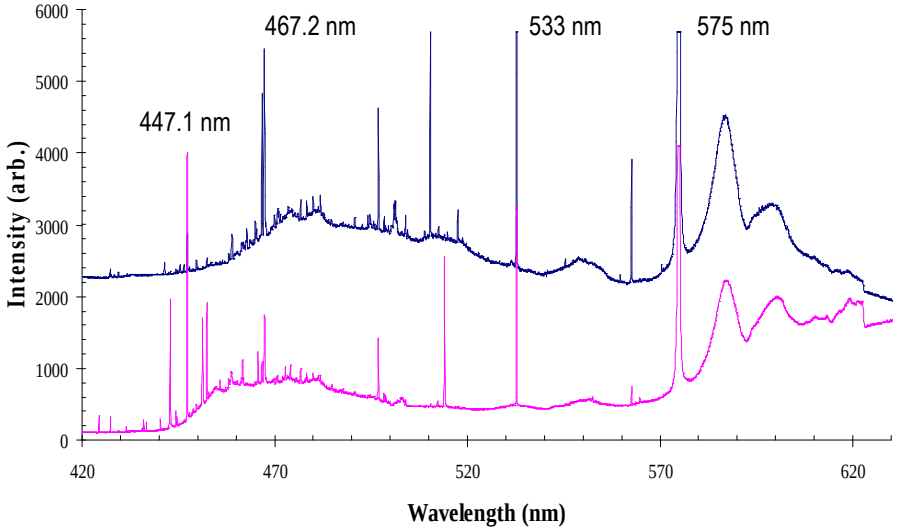

Figure 4.4.4 – Comparative composite cathodoluminescence spectra of the clear (blue, upper spectrum), and brown (pink, lower spectrum) sides of sample DeB #1. Spectra have been displaced and scaled for clarity – relative intensities should not be inferred from this spectrum. All spectra recorded with the sample at 77 K.

There are a few notable differences in the cathodoluminescence (CL) spectra of the brown side of DeB #1. First, the ZPLs at 510.3 and 517.5 nm, present on CL spectra from the clear side, are now very weak (relative to the spectral noise). A new, strong (relative to the noise) emission line is now present at 514.0 nm (2.411 eV). This line has a full width half maximum (FWHM) comparable to the other lines in the emission spectrum: 1.56 Å (0.73 meV). A feature at 514 nm has been previously observed in CL spectra from polycrystalline CVD diamond films [Yacobi *et al* (1991)] and CL from the

{111} sectors of a single-crystal CVD diamond film [Kanda *et al* (2003b)]. These authors did not state the widths of the 514 nm peak in their samples; however estimations from their published spectra suggest that the peaks are substantially broader than the line measured in sample DeB #1.

Second, the broad increase in structured luminescence from the clear side starting at ~ 460 nm and extending to ~ 520 nm, starts at ~ 445 nm in the brown side, and ends around 500 nm. This entire region of luminescence appears to be composed of convoluted vibronic bands associated with a number of ZPLs, as indicated by the highly structured form, and possibly even superimposed on top of a broad band. This region is shown in greater detail in figure 4.4.5.

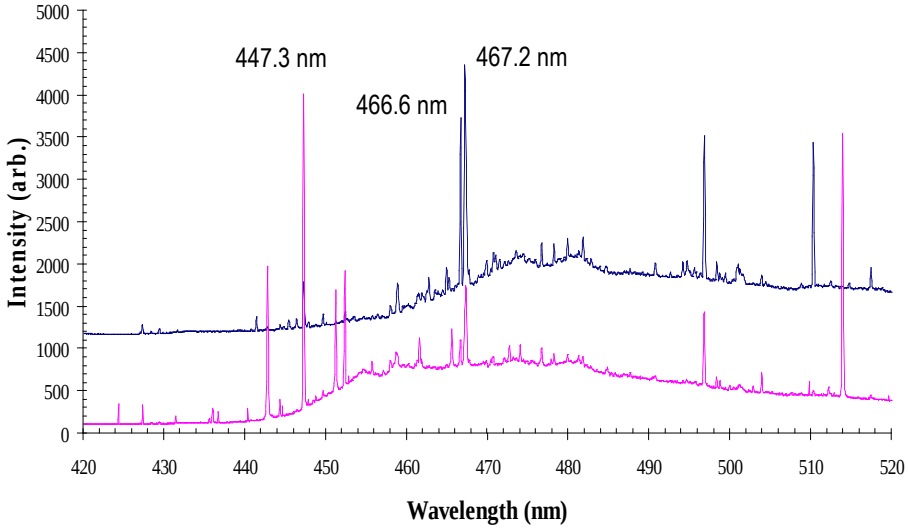

Figure 4.4.5 – Cathodoluminescence spectra of the clear (blue, upper spectrum) and brown (pink, lower spectrum) sides of sample DeB #1. Spectra have been displaced for clarity. These are not composite plots; hence relative intensities may be inferred. Recorded with the sample at 77 K.

The start of the increase of luminescence of the brown side at ~ 445 nm could possibly be explained as the presence of the vibronic band of a ZPL present in the spectra of the brown side, and not of the clear side: a new line is at 442.8 nm (2.799 eV). Zaitsev (2001) reports a feature at 443 nm (2.80 eV) observed in CL spectra of CVD diamond films, however inspection of the references therein suggests that this is unlikely to be the same feature. The first

broad peak of the background luminescence in this region, rising to higher wavelengths, is at ~ 455.9 nm (2.719 eV). This peak may originate from overlapping vibronic bands associated with the four ZPLs between 440 and 455 nm, which are either very weak or absent in the CL spectrum of the clear side. A Gaussian peak centred at 455.9 nm, with a FWHM of 11.2 nm was generated and subtracted from the CL spectrum of the brown side, to leave a modified spectrum which is qualitatively similar to the CL spectrum of the clear side; see figure 4.4.6.

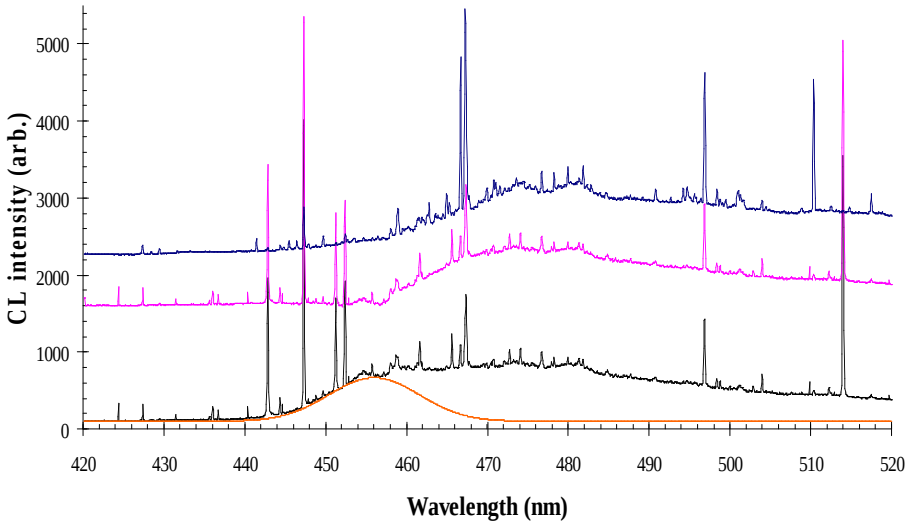

Figure 4.4.6 – Comparative CL spectra showing how a generated Gaussian peak (orange spectrum, superimposed on the lowest, black spectrum – the unmodified CL spectrum of the brown side of DeB #1), can produce a modified spectrum (pink, middle) which appears qualitatively similar to the CL spectrum of the clear side (blue, upper spectrum). Spectra have been displaced vertically for clarity.

Three further strong lines appear in this part of the spectrum of the brown side: 447.3 nm (2.771 eV), 451.2 nm (2.747 eV) and 452.3 nm (2.740 eV). The line at ~ 447 nm is frequently observed in the CL spectra of the samples studied in this work (see sections 4.1 and 4.3), however it is substantially more intense, relative to the peaks at 466.6 and 467.2 nm, in the brown side. The line at 451.2 nm is close to a line reported in Zaitsev (2001) at 451 nm (2.748 eV) in CL from

diamond films; other than the emission line being suppressed by boron doping, no more information is provided. The final line has not been previously reported.

A further difference between the CL spectra of the clear and brown sides will be highlighted. Figure 4.4.7 shows the CL spectrum of the brown side of DeB #1, between 880 to 904 nm. Two sharp features at 886.0 nm (1.399 eV) and 894.8 nm (1.385 eV) are evident, with FWHMs of 2.47 Å (0.39 meV) and 4.02 Å (0.62 meV) respectively. Considering the low intensity of these peaks, relative to the spectral noise, the measurement was repeated and confirmed that these are genuine features.

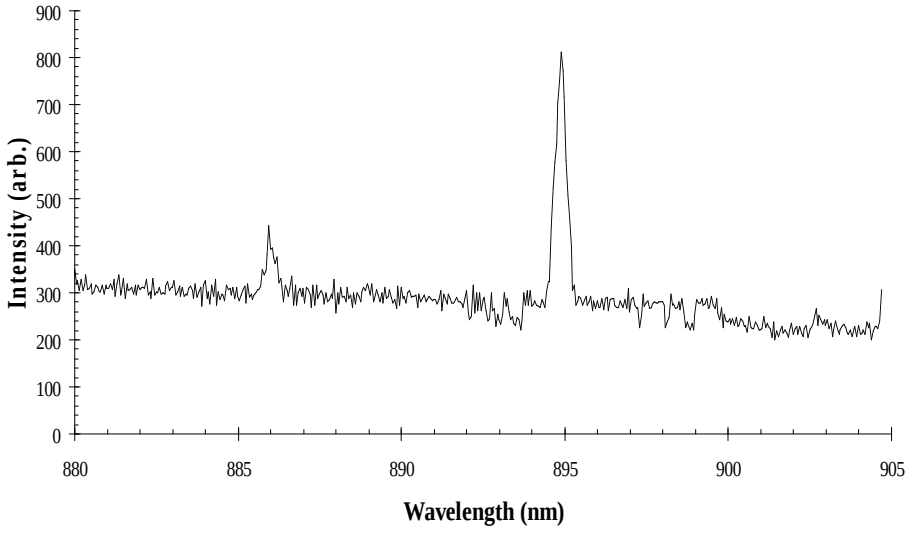

Figure 4.4.7 – Cathodoluminescence spectrum of the brown side of sample DeB #1. Recorded with the sample at 77 K.

None of the features observed exclusively in the brown side of sample DeB #1 was investigated in further detail in this work. Beyond the features discussed above, there was no observed difference in the CL spectra between the clear and brown sides of DeB #1.

One final feature of the CL spectra of sample DeB #1 is worth drawing attention to: a line at 777.5 nm (1.594 eV), with FWHM of 3.20 Å (0.65 meV), is observed in CL spectra of both the clear and brown sides (figure 4.4.8). This feature is close to the reported line at 777.8 nm in Zaitsev (2001) (reported from

Zaitsev's own unpublished data), which is apparently observed in CVD diamond films implanted with B^+ ions and annealed at 1000°C; and in irradiated, undoped CVD diamond films. Sample DeB #1 has undergone neither of these treatments.

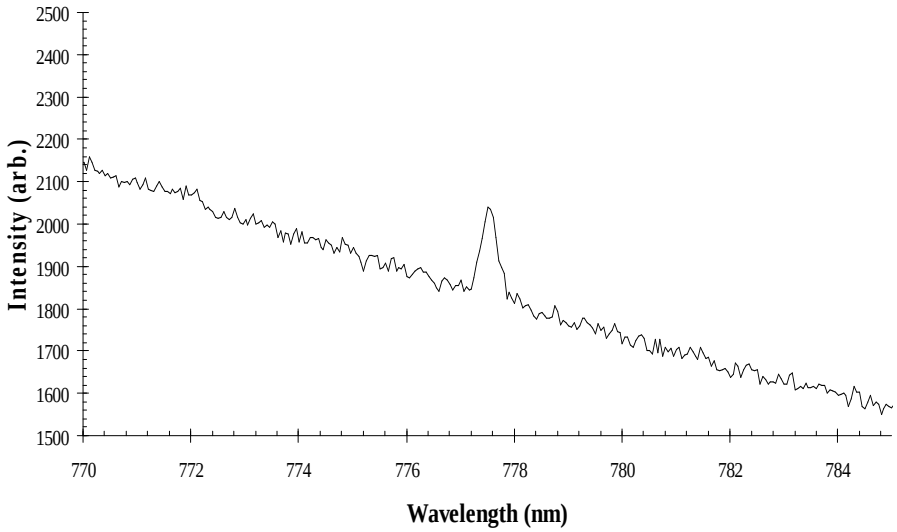

Figure 4.4.8 – Cathodoluminescence spectrum of sample DeB #1. Recorded with the sample at 77 K.

4.5 Cathodoluminescence of Ap4

The single-crystal CVD synthesised sample Ap4, from Apollo Diamond Inc., is a thin sample, ~ 2 mm^2 on the large face, a few hundred microns thick, and is visually clear. This sample presents a cathodoluminescence spectrum different from that of the Element Six and University of Paris XIII single-crystal CVD samples. Ap4 shows a high density of sharp, relatively intense luminescence lines, on top of highly structured broad band luminescence in the visible region (figure 4.5.1). Only a few of the lines can confidently be ascribed to previously reported defect centres. the 574.8 nm (2.156 eV) centre (the neutral nitrogen-vacancy) the 532.7 nm (2.327 eV) centre, and the 389 nm (3.188 eV) and 441 nm (2.808) eV centres. Notably, these are all nitrogen-related centres.

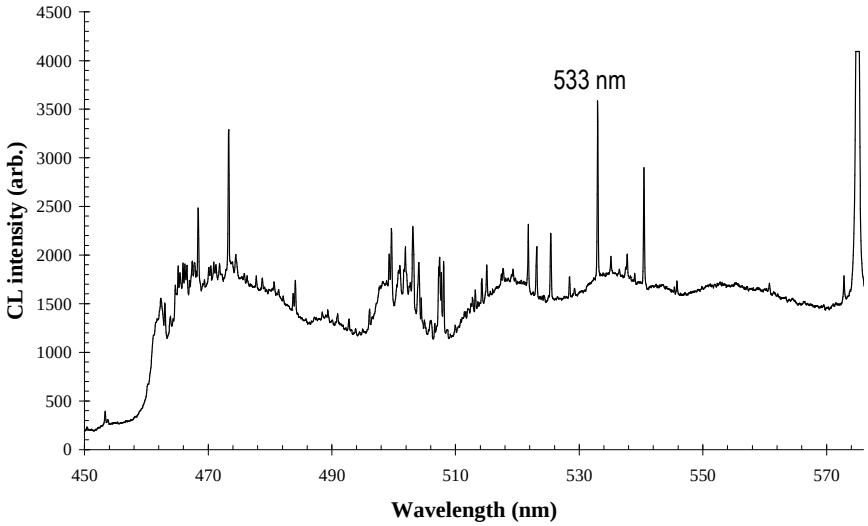

Figure 4.5.1 – Cathodoluminescence spectrum of sample Ap4. Recorded with the sample at 77 K.

The 574.8 nm centre's vibronic band is present along with a very weak 637 nm luminescence line (the negatively charged nitrogen-vacancy), figure 4.5.2.

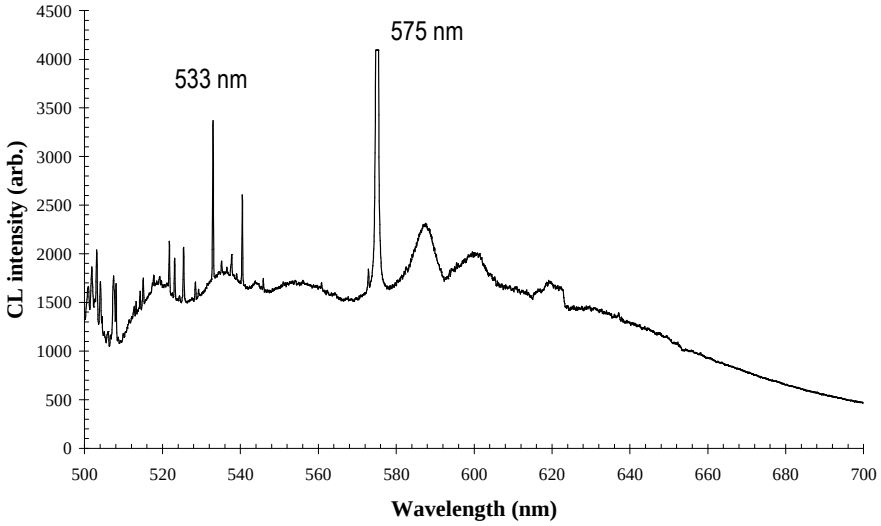

Figure 4.5.2 – Cathodoluminescence spectrum of sample Ap4, showing the 574.8 nm ZPL and vibronic band. Recorded with the sample at 77 K.

The sample is inhomogeneous in terms of defects, as some regions of the sample show relatively strong broad-band luminescence, at ~ 387 nm (~ 3.2 eV), figure 4.5.3; whilst other regions did not show this band, but instead showed intense CL from the 389 nm (3.188 eV) centre, and weak CL from the 441 nm (2.808 eV) centre, figure 4.5.4.

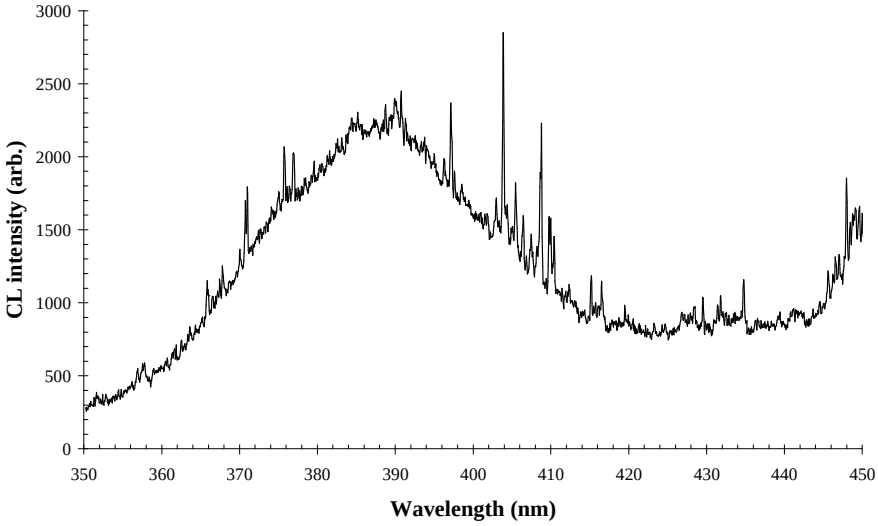

Figure 4.5.3 – Cathodoluminescence spectrum of sample Ap4, showing broad-band luminescence at ~ 387 nm (~ 3.2 eV). Recorded with the sample at 77 K.

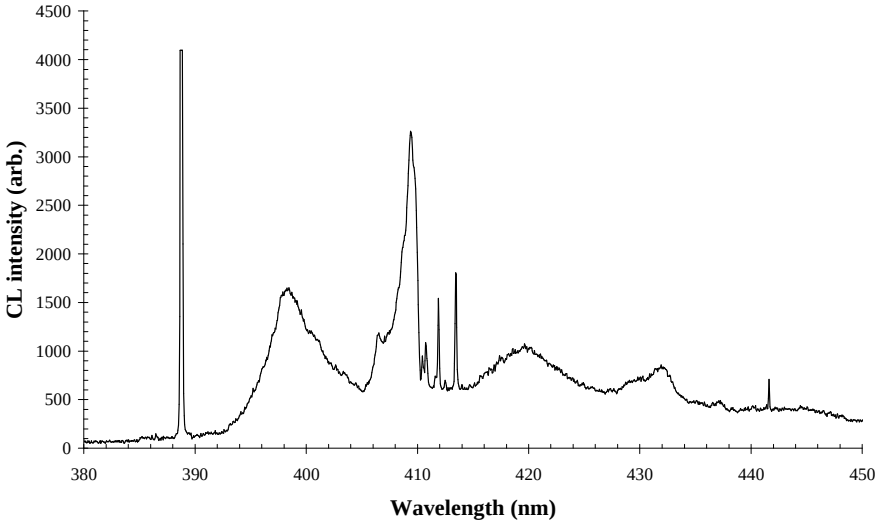

Figure 4.5.4 – Cathodoluminescence spectrum of sample Ap4, showing the 389 nm (3.188 eV) and 441 nm (2.808) eV centres. Recorded with the sample at 77 K.

The CL spectra from sample Ap4 show that it contains a number of the defect centres common to single-crystal CVD material, such as the nitrogen-vacancy centres and interstitial-related centres. The many sharp luminescence lines in the visible region, along with the highly structured band luminescence beneath them, are a wealth of zero-phonon lines and accompanying vibronic bands, from some unknown defects. Details of the growth process of this sample

are unknown, but it is likely that these features are attributable to impurity contamination during growth, or defect incorporation characteristic of the growth process. Notably, however, the electronic transitions of the preferentially oriented defects (466.6 nm (2.6569 eV), 496.8 nm (2.4955 eV) and 562.5 nm (2.2039 eV); see chapter five) were not present in CL spectra of this sample – although polarisation studies were not conducted.

Chapter 5

Preferentially oriented defects

5.1 Introduction

Cathodoluminescence spectra of the single-crystal CVD diamonds studied in this work frequently show ZPLs at 466.6 nm (2.6569 eV), 496.8 nm (2.4955 eV) and 562.5 nm (2.2039 eV) (see figure 5.1.1). The defect centres responsible for these ZPLs demonstrate a preferential orientation within the crystal, the properties of which will be discussed below. These lines have not been observed in absorption spectra, most likely because the concentration of centres is too low. The 562.5 nm ZPL has been observed in photoluminescence using the 325 nm HeCd laser used in this study; the other lines were too weak to study in PL generated by the 325 nm HeCd laser.

Whilst the ZPLs discussed in this section are frequently observed in this material, little information is known about them. They have only been reported a few times in the literature, in cathodoluminescence measurements of CVD diamond. The 496.8 and 562.5 nm ZPLs are identified in a list of lines in Collins *et al* (1989) from CL studies of polycrystalline microwave-CVD diamond.

In separate samples, the ZPLs appear with non-constant relative integrated intensities (figure 5.1.2); this indicates that the transitions which give rise to the observed ZPLs do not originate from a single defect centre. However, it can be seen from figure 5.1.2 that the relative intensities of the lines vary in a similar manner for the ratio of integrated intensities of the 496.8 nm ZPL with the other two lines: both follow the same trend, suggesting a relationship of some kind between the lines, even if they do not originate from the same defect.

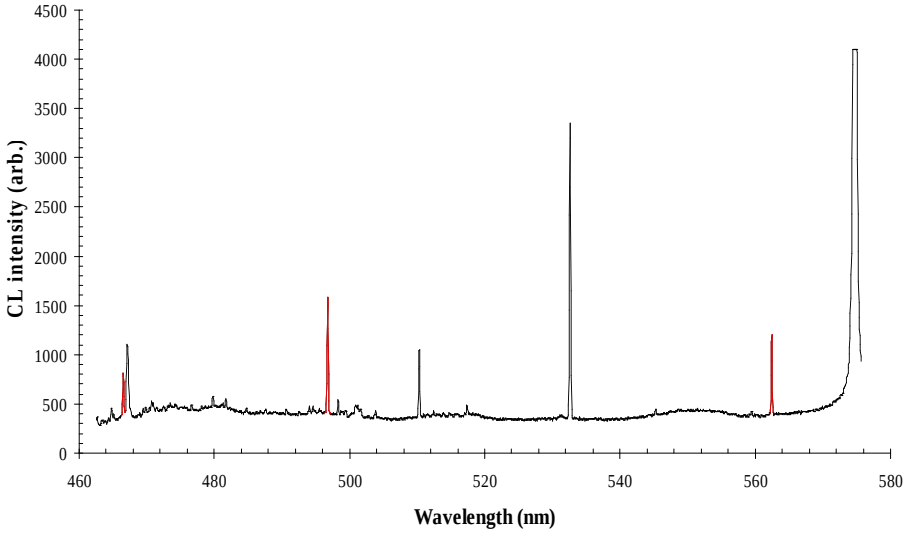

Figure 5.1.1 – Cathodoluminescence spectrum of a single-crystal CVD diamond. Defect centres with zero-phonon lines highlighted in red show preferential orientation. Recorded with the sample at 77 K.

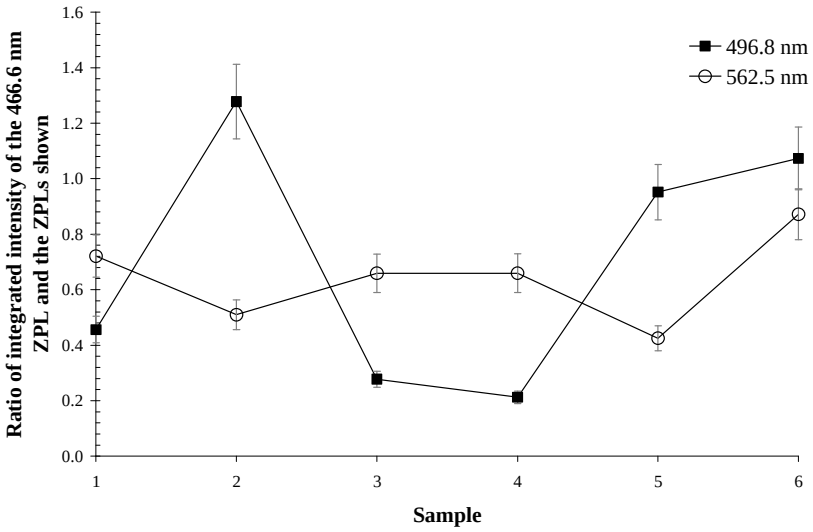

a)

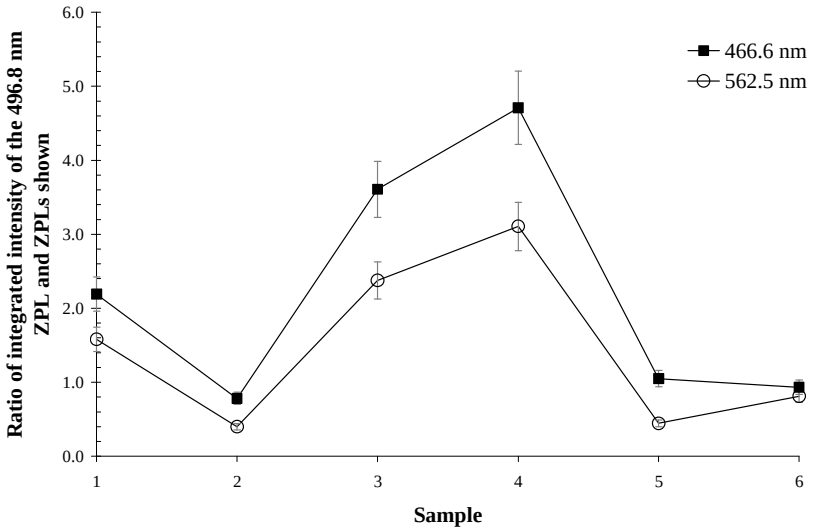

b)

Figure 5.1.2 – Variation across six single-crystal CVD diamonds of the ratio of integrated intensities (in CL) of each of the three ZPLs with respect to the other two. a) is for the 466.6 nm ZPL, and b) is for the 496.8 nm ZPL.

In samples oriented with [001], [110] and [1$\bar{1}$0] crystallographic lattice directions (figure 5.1.3a), the ZPLs appear preferentially depending upon orientation: the ZPLs are observed when a sample is placed in the CL spectrometer with its <001> axis vertical (figure 5.1.3b) and the luminescence is passed through a polariser aligned *perpendicular* to the <001> axis (i.e. a <110> direction); the ZPLs are *not* observed from a sample in a similar setup where the luminescence passes through a polariser aligned *parallel* to the <001> axis. Figure 5.1.4 demonstrates the observed luminescence spectra.

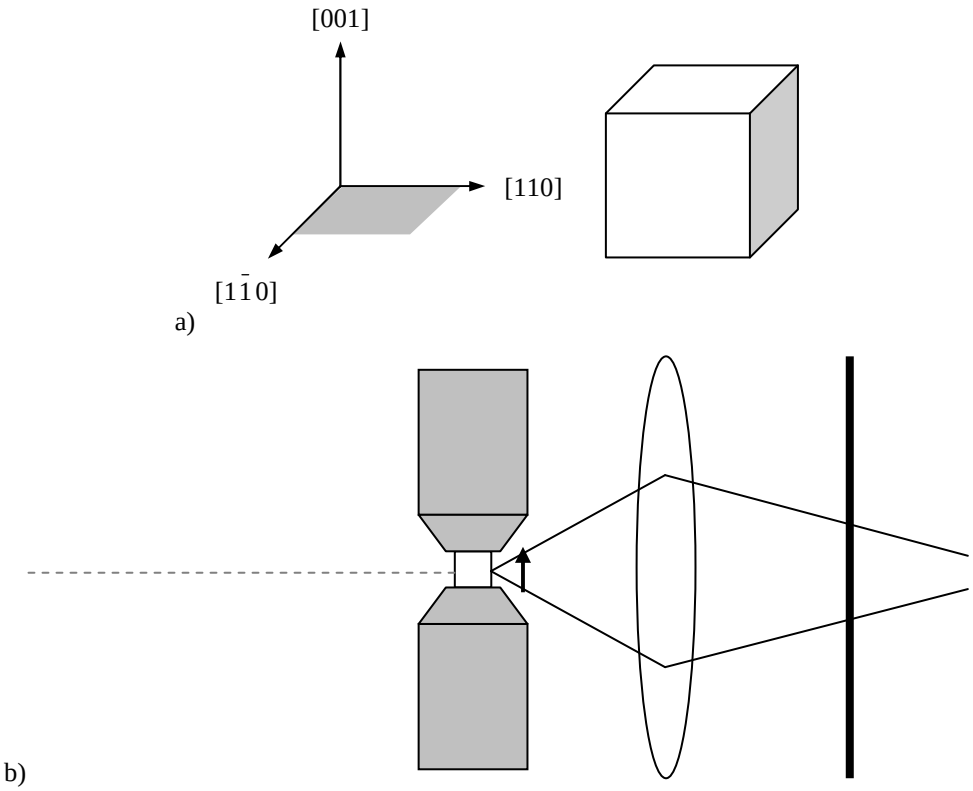

Figure 5.1.3 – a) Representation of the crystallographic axes of an oriented CVD diamond sample. b) Schematic representation of the sample chamber of the cathodoluminescence spectrometer, modified for the incorporation of a uniaxial stress system: the electron-beam (dashed line) is incident on the sample. Luminescence follows the paths indicated through a converging lens and a polariser (thick black line) into the monochromator (not shown). The crystal is initially oriented with its <001> axis parallel to the arrow. The polariser can be aligned parallel to the arrow, or rotated by π / 2 into the page, to align parallel to a <110> axis.

So, in oriented samples, the three ZPLs are not observed in luminescence polarised parallel to the <001> direction; if the defects responsible for the ZPLs were randomly distributed throughout the crystal, it would be expected that the dipoles producing the luminescence would be randomly oriented and there would be equal luminescence intensity in all polarisations. However, the experimental data shows (figure 5.1.4) that this is not the case, which implies that the dipoles are preferentially oriented within the crystal, along the <110> orientations. To check for reproducibility of this phenomenon, the crystals were mounted in the cryostat in a rotated orientation, with a <110> axis vertical: the corresponding luminescence from the ZPLs was only observed, as previously, along <110>

orientations. This qualitatively supports the implication that the defect dipoles are preferentially oriented along the <110> axes.

This conclusion can be verified quantitatively by obtaining the symmetry of the defects responsible for the ZPLs. This has been performed using uniaxial stress spectroscopy, the results of which, and discussion about the nature of the centres are found in the following sections.

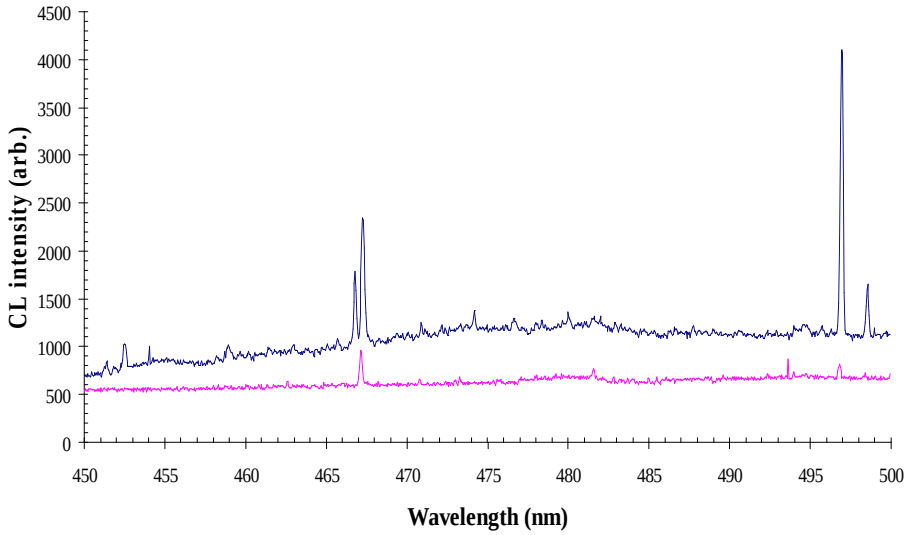

a)

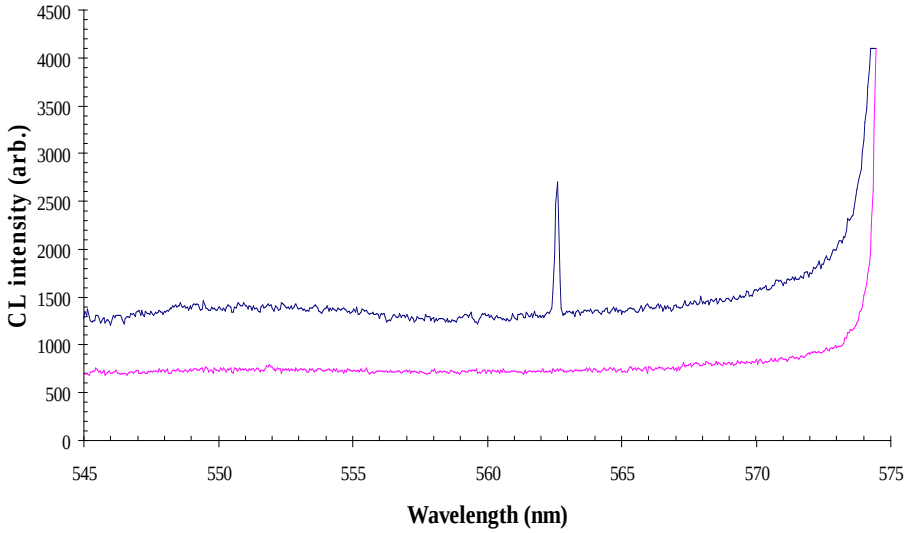

b)

Figure 5.1.4 – Cathodoluminescence spectra of single-crystal CVD diamond oriented with <001> axis vertical; electron beam incident on a <110> face. In a) the upper (blue) spectrum shows the luminescence observed when polarised perpendicular to the <001> direction, i.e. along the <110> direction; the lower (pink) spectrum shows the luminescence observed when the luminescence is polarised parallel to the <001> axis. Note the missing ZPLs at 466.6 and 496.8 nm in the lower spectrum. The spectra in b) have the same experimental parameters as in a). Note the missing ZPL at 562.5 nm in the lower spectrum. Spectra recorded with the sample at 77 K.

Only a small number of point defects have been shown to demonstrate preferential orientation in diamond. The H3 centre (ZPL at 503.4 nm, 2.463 eV) is a vacancy trapped at an A-form nitrogen centre [Davies (1972)], and can be created in type Ia diamonds which have been irradiated and annealed. The centre has been shown to be a <110> electric dipole transition at a rhombic I centre [Davies *et al* (1976)]. This is important for the present work as the symmetries of the preferentially oriented centres in this chapter are shown to be the same as that of the H3 centre, and possess similar structures: the atomic configuration of H3 is $[N\text{-}V\text{-}N]^0$ along <110> directions. The creation of H3 centres via irradiation and annealing of a sample is through trapping of the vacancies during annealing. The centre can also be observed in untreated HPHT synthesised diamond, which is important for the present work, as the centres discussed in this chapter are present in untreated CVD synthesised diamond. A growth mechanism of the H3 centre has been proposed [Dodge (1986)] for layer by layer growth on a (001) plane: single-substitutional nitrogen atoms form A centres along <110>, with

each bonding to three neighbouring carbons. This leaves two excess valence electrons each, which prevents a carbon atom from bonding between the two nitrogen atoms. Therefore a vacancy is left in the next growth layer between the nitrogen pair, forming H3 centres oriented along <110> directions. A similar growth mechanism is proposed in section 5.3 for the formation of the centres studied in this chapter.

Another preferentially oriented impurity-defect in diamond is the 1.40 eV centre, which is observed in absorption and cathodoluminescence of spectra of synthetic diamonds grown using nickel catalysts [Collins, Kanda and Burns (1990)] or in nickel-implanted samples [Collins and Spear (1983), Gippius *et al* (1990)]. The optical spectra consist of a doublet with energies 1.401 and 1.404 eV, along with fine structure at low temperatures (liquid helium), corresponding to the isotopes of nickel. The strong polarisation of the doublet suggests a preferential incorporation of the defect [Collins (1989)], and it has been shown quantitatively that the defect consists of a <111> oriented interstitial nickel impurity atom (possibly positively charged) [Nazaré *et al* (1991)].

The final preferentially oriented defect observed in diamond is a nitrogen-related centre with a ZPL at 490.7 nm (2.526 eV) seen in optical spectra of type IaB diamonds [Collins and Woods (1982), and see Collins *et al* (2000) and Zaitsev (2001)]. The defect has monoclinic I symmetry and appears to decorate slip traces in the crystal, which most likely accounts for the preferential orientation.

5.2 Results

5.2.1 Uniaxial stress measurements

The 466.6, 496.8 and 562.5 nm ZPLs have been investigated in cathodoluminescence whilst under uniaxial stresses. Two untreated, single-crystal CVD diamond samples (DeB #2 and DeB #3) were used, both of which had been cut and polished into cuboids such that the faces corresponded to the crystallographic lattice directions [001], [110] and $[1\,\bar{1}\,0]$ (for the first sample), and [111], $[1\,\bar{1}\,0]$ and $[11\,\bar{2}\,]$ (for the second sample). The faces of the samples onto which the CL beam was incident, and the luminescence exit face, were masked using colloidal carbon with a small aperture etched to expose the centre of the face; this was to avoid the compression gradient along the stress axis. It also prevented the sample faces becoming charged, and minimised beam drift.

Cathodoluminescence was generated using the custom system described in section 3.3, modified to incorporate the stress cell (as in section 5.1). The beam was run at 40 kV and ~ 10 μA, with a chamber vacuum of less than 10^{-5} Torr. The samples were held at liquid nitrogen temperature (~ 77 K) throughout the experiment. Pressure was applied using a manually controlled oil ram with pressure gauge, over the range 0 to 2 GPa. For each of the relevant crystallographic compression directions, <001>, <111> and <110>, luminescence spectra were recorded at intervals between 0 and 2 GPa. For each stress, two spectra were recorded, one where the luminescence was polarised parallel to the stress direction, and one perpendicular to it.

As discussed in the previous section, inspection of the luminescence spectra for the parallel and perpendicular polarisations revealed “missing” components for these three defects, implying a preferential orientation, along <110>. If the defects responsible for the ZPLs were randomly distributed throughout the crystal, it would be expected that the dipoles producing the luminescence would be randomly oriented and there would be equal luminescence intensity in all polarisations. The proposed <110> anisotropy can

be checked against the above statement of equal luminescence intensity in all orientations: the principle of latent anisotropy allows quantification of this by the condition that the intensity of luminescence (or absorption) at zero stress is proportional to the square of the projection of the electric vector of the luminescence on the anisotropic axis (see, for example, Feofilov and Kaplyanskii (1962)). The projection of a given vector *A* on to vector *B* is $\frac{AB}{|A||B|}$. In this case, the anisotropic vector (the dipole) is [110] or [$1\,\bar{1}\,0$], and the electric vectors of the luminescence are [001], [110] and [111] in parallel and perpendicular orientations. Table 5.2.1 lists the theoretical values of the squares of the projections, along with the experimental ZPL integrated intensities of the three centres at zero stress, in the relevant orientations. It can be seen that there is an excellent correspondence between the experimental and theoretical values, which confirms that the dipoles producing the 466.6, 496.8 and 562.5 nm transitions are preferentially oriented along [110] and [$1\,\bar{1}\,0$], rather than being randomly distributed.

Stress direction	**Viewing, E ∥ […]**	**Dipole […]**	**Theoretical (Projection)^2**	**Experimental ZPL relative intensities (∥ : ⊥)**		
				466.6 nm	**496.8 nm**	**562.5 nm**
<001>	001	110	0	0 : 1	0 : 1	0 : 1
		$1\,\bar{1}\,0$	0			
	110	110	1			
		$1\,\bar{1}\,0$	0			
<111>	111	110	2/3	0.67 : 1	0.62 : 1	0.66 : 1
		$1\,\bar{1}\,0$	0			
	$1\,\bar{1}\,0$	110	0			
		$1\,\bar{1}\,0$	1			
<110>	110	110	1	1 : 0.98	1 : 1.09	1 : 0.98
		$1\,\bar{1}\,0$	0			
	001	110	0			
		$1\,\bar{1}\,0$	0			
	$1\,\bar{1}\,0$	110	0			
		$1\,\bar{1}\,0$	1			

Table 5.2.1 – Comparison of theoretical and observed ZPL intensities for the preferentially oriented centres, showing <110> anisotropies.

The symmetry of the centres is determined by fitting the experimental stress-splitting rates to the theoretical shift rates for a proposed symmetry. Inspection of the stress-splitting data for the defects (data points in figures 5.2.1, 5.2.2 and 5.2.3) suggests that the symmetries are rhombic I for the 466.6 and 496.8 nm centres, with <110> dipoles; and monoclinic I or rhombic I for the 562.5 nm centre, with a <110> dipole. All of these have suppressed components to account for the missing transitions in the data. The perturbation to the energy of the ZPL for a rhombic I (A to B) symmetry centre is

$$V = A_1 s_{zz} + A_2 (s_{xx} + s_{yy}) + 2A_3 s_{xy}, \qquad 5.2.1$$

where A_1, A_2 and A_3 are the shift-rate parameters, and the s_{ij} parameters are the components of the stress tensor.

At high stress, the observed stress-splitting spectra for the 466.6 nm centre consisted of one transition in the [001] orientation, two in [111], and two in $[1\,\bar{1}\,0]$. Table 5.2.2 shows the theoretical shift rates and relative intensities of the components of a rhombic I (A to B) centre [Mohammed *et al* (1982)] (these can be calculated as in section 2.5). For this centre, the component with shift-rate A_2 in the **S** ‖ [001] orientation is not observed, nor is the component with shift-rate ½(A_1 + A_2) in the **S** ‖ [110] orientation.

S ‖ [001]		**S ‖ [111]**		**S ‖ [110]**	
Energy	**E ‖ : E⊥**	**Energy**	**E ‖ : E⊥**	**Energy**	**E_{110} : E_{001} : $E_{1\bar{1}0}$**
A_1	0 : 1	⅓ (A_1 + 2A_2 + 2A_3)	4 : 1	A_2 + A_3	1 : 0 : 0
A_2	2 : 1	⅓ (A_1 + 2A_2 – 2A_3)	0 : 3	½ (A_1 + A_2)	1 : 2 : 1
				A_2 – A_3	0 : 0 : 1

Table 5.2.2 – The effects upon the ZPL of a defect centre with rhombic I symmetry undergoing an A ↔ B transition, as observed in absorption or luminescence spectroscopy. The ‘A’ parameters show how the energy of the ZPL components vary under each stress direction, i.e. parallel to the [001], [111] or [110] orientations. The ratios show the relative intensities of the observed components at high stress. After Mohammed *et al* (1982).

	A_1	A_2	A_3	A_4
466.6 nm	-10.10	7.95	8.05	-
496.8 nm	-8.35	2.90	3.00	-
562.5 nm	-3.55	1.20	1.65	0.70
	-3.75	0.95	1.95	-

Table 5.2.3 – Calculated values of the stress-splitting parameters for the preferentially oriented centres. The first set for the 562.5 nm centre are those for the fit to a monoclinic I symmetry, and the second for a rhombic I symmetry. The values are in meV GPa^{-1} with an error of ± 0.30 meV GPa^{-1}.

A least-squares fit of the theoretical shift-rates to the data, using the A_1, A_2 and A_3 parameters as least-squares variables, is shown in figure 5.2.1 (full lines). The good fit to the data is evident, with the stress parameters calculated as in table 5.2.3. Figure 5.2.1 also shows the experimental relative intensities of the ZPL components at high stress, which are found to be equivalent to the theoretical ratios listed in table 5.2.2. The fit, and the relative intensity ratios, confirm that the symmetry of the 466.6 nm centre is rhombic I, with the electronic transition being between singly-degenerate ground and excited states (A to B transition); the dipole is oriented along <110> (a Kaplyanskii π-dipole [Kaplyanskii (1964a, b)]).

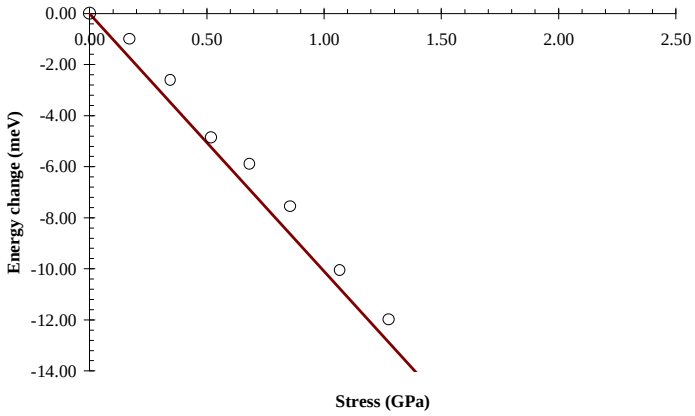

a)

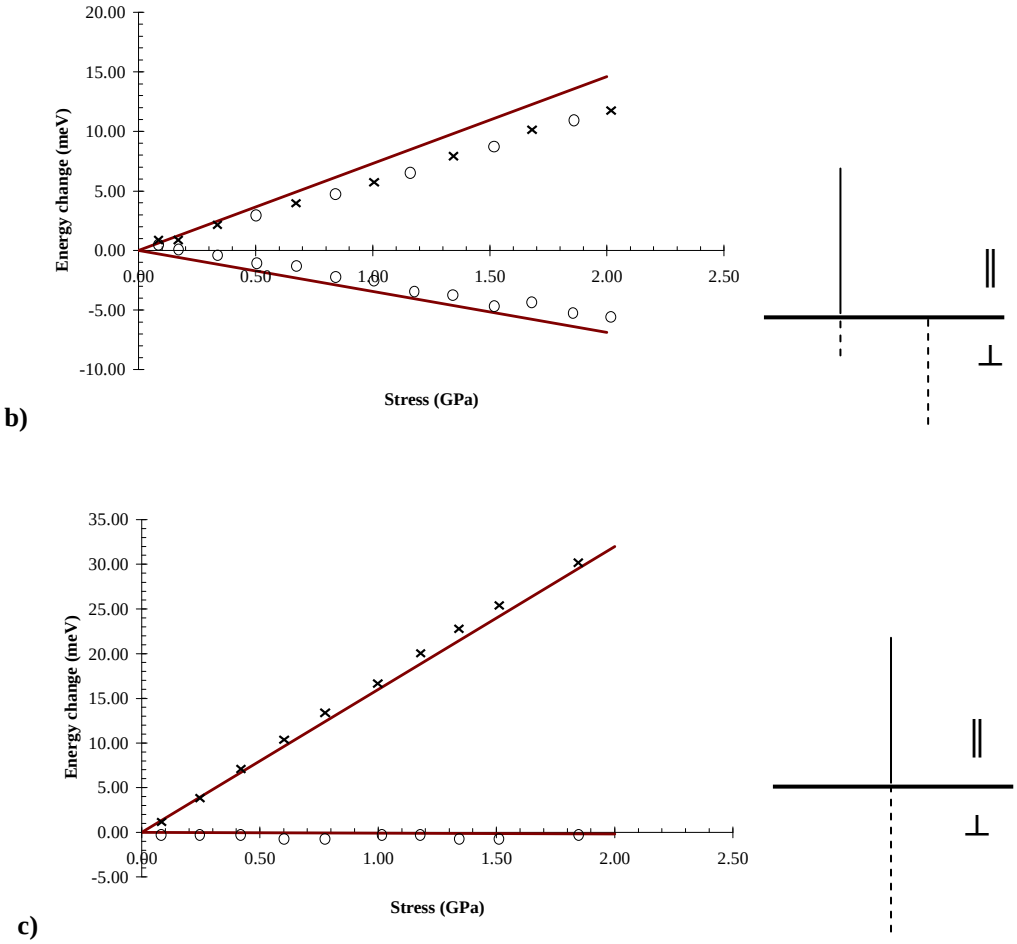

Figure 5.2.1 – Uniaxial stress splitting data for the 466.6 nm (2.656 eV) centre in cathodoluminescence, showing change in energy of ZPL components as a function of applied stress. Data points are experimental results, lines are calculated from the fit to a rhombic I symmetry. a) ZPL under <001> compression (**S**); crosses are for electric vector of luminescence **E** ∥ **S**; unfilled circles are for **E** ⊥ **S**. b) ZPL under <111> compression; crosses are for **E** ∥ **S**; unfilled circles are for **E** ⊥ **S**. c) ZPL under [110] compression; crosses are for **E** ∥ **S** when viewing along; unfilled circles are for **E** ⊥ **S** when viewing along [001], filled circles for **E** ⊥ **S** when viewing along $[1\,\bar{1}\,0]$. Stick diagrams show relative intensities of stress-split ZPL components at maximum recorded stress, with vertical lines above the horizontal line representing **E** ∥ **S**, and vertical lines below representing **E** ⊥ **S**.

For the 496.8 nm ZPL at high stress, the stress-splitting spectra consisted of one transition in the [001] orientation, two in [111], and two in $[1\,\bar{1}\,0]$. This is consistent with a rhombic I (A to B) symmetry centre (table 5.2.2), with suppressed components. For this centre, the component with shift-rate A_1 in the **S** ∥ [001] orientation is not observed, nor is the component with shift-rate ½(A_1 + A_2) in the **S** ∥ [110] orientation.

A least-squares fit of the theoretical shift-rates to the data, using the A_1, A_2 and A_3 parameters as least-squares variables, is shown in figure 5.2.2 (full lines). The excellent fit to the data is evident, using the calculated stress parameters in table 5.2.3. Figure 5.2.2 also shows the experimental relative intensities of the ZPL components at high stress, all of which are found to be equivalent to the theoretical ratios listed in table 5.2.2; except for a missing perpendicular component in the [111] direction (with shift rate ⅓ (A_1 + 2A_2 + 2A_3)). This component is theoretically the lowest intensity of the three predicted for this orientation, and it was not observed in the CL spectra. The reason could be that the peak had broadened and was not obvious beneath other local structure in the spectrum. This doesn't change the quality of the fit, however.

The fit, and the relative intensity ratios, confirm that the symmetry of the 496.8 nm centre is rhombic I, with the electronic transition being between A and B ground and excited states; the dipole oriented along <110>.

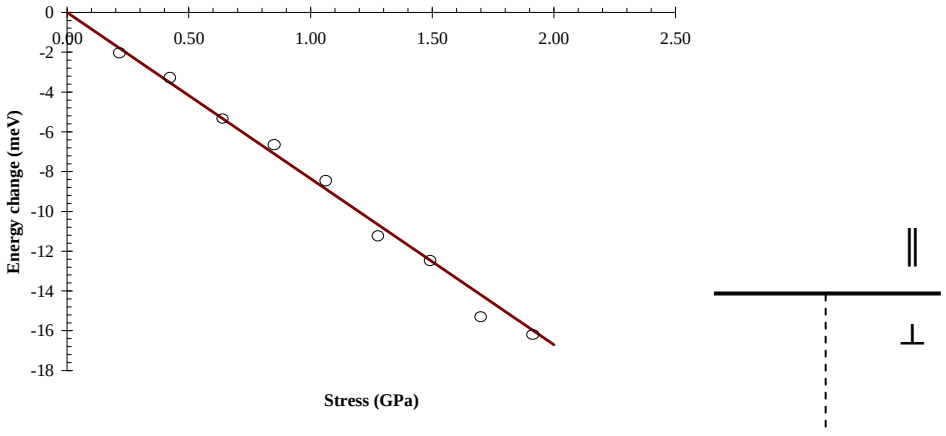

a)

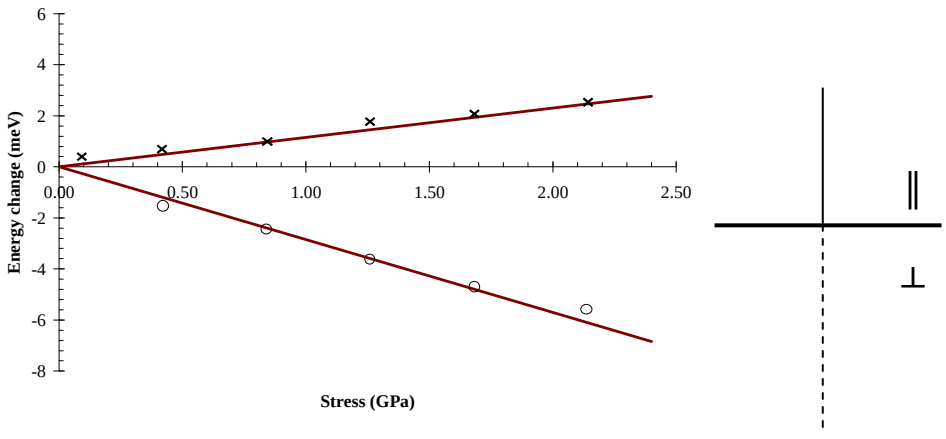

b)

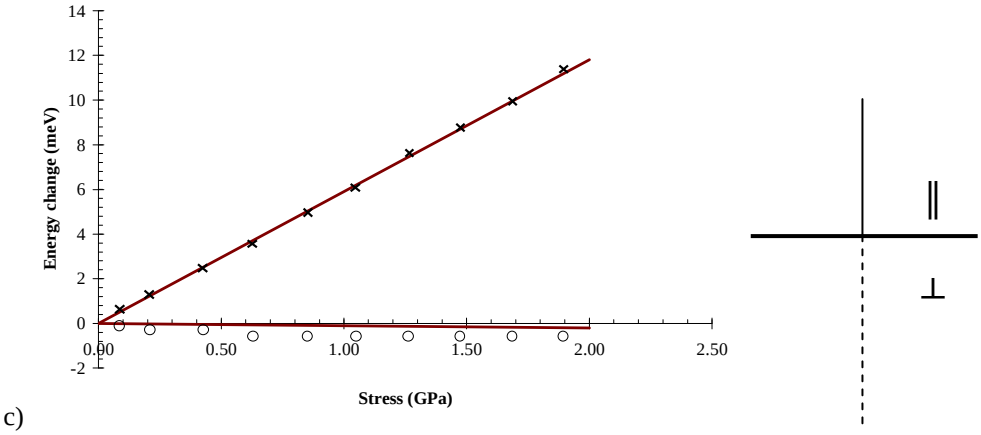

c)

Figure 5.2.2 – Uniaxial stress splitting data for the 496.8 nm (2.495 eV) centre in cathodoluminescence, showing change in energy of ZPL components as a function of applied stress. Data points are experimental results, lines are calculated from the fit to a rhombic I symmetry. a) ZPL under <001> compression (**S**). b) ZPL under <111> compression. c) ZPL under [110] compression. Data point notation as in figure 5.2.1. Stick diagrams show relative intensities of stress-split ZPL components at maximum recorded stress, with vertical lines above the horizontal line representing $\mathbf{E} \| \mathbf{S}$, and vertical lines below representing $\mathbf{E} \perp \mathbf{S}$.

Finally, the observed stress-splitting spectra for the 562.5 nm centre, at high stress, consisted of one transition in the [001] orientation, three in [111], and two in $[1\bar{1}0]$. The theoretical shift rates and relative intensities of the components of a monoclinic I (A'' to A') centre are shown in table 5.2.4. For this centre, the component with shift-rate A_2 in the $\mathbf{S} \| [001]$ orientation is not observed, nor are the components with shift-rates ½ ($A_1 + A_2 - 2A_4$) and ½ ($A_1 + A_2 + 2A_4$) in the $\mathbf{S} \| [110]$ orientation.

S ∥ [001]		S ∥ [111]		S ∥ [110]	
Energy	**E ∥ : E ⊥**	**Energy**	**E ∥ : E ⊥**	**Energy**	**E_{110} : E_{001} : $E_{1\bar{1}0}$**
A_1	0 : 1	⅓ (A_1 + 2A_2 + 2A_3)	8 : 2	A_2 + A_3	2 : 0 : 0
A_2	2 : 1	⅓ (A_1 + 2A_2 – 2A_3 – 4A_4)	0 : 3	½ (A_1 + A_2 – 2A_4)	1 : 2 : 1
		⅓ (A_1 + 2A_2 – 2A_3 + 4A_4)	0 : 3	½ (A_1 + A_2 + 2A_4)	1 : 2 : 1
				A_2 – A_3	0 : 0 : 2

Table 5.2.4 – The effects upon the ZPL of a defect centre with monoclinic I symmetry undergoing an A'' ↔ A' transition, as observed in absorption or luminescence spectroscopy. The 'A' parameters show how the energy of the ZPL components vary under each stress direction, i.e. parallel to the [001], [111] or [110] orientations. The ratios show the relative intensities of the observed components at high stress. After Mohammed *et al* (1982).

A least-squares fit of the theoretical shift-rates to the data, using the A_1, A_2 and A_3 parameters as least-squares variables, is shown in figure 5.2.3 (full lines). Table 5.2.3 presents the calculated stress-parameter values. The fit to the data is very good. Figure 5.2.3 also shows the experimental relative intensities of the ZPL components at high stress, which are found to be consistent with the theoretical ratios listed in table 5.2.2. The fit, the relative intensity ratios, and the missing components confirm that the symmetry of the 562.5 nm centre is monoclinic I, with a <110>-oriented dipole, the electronic transition being between A'' and A' ground and excited states.

Additionally, however, a similarly good fit can be found by fitting to the parameters for a rhombic I symmetry centre with a <110>-oriented dipole; similar to the 466.6 and 496.8 nm centres. A fit to the data using the theoretical expressions for the transitions of a rhombic I symmetry (table 5.2.2), yields values of the stress-splitting parameters (table 5.2.3). The similarities between the parameters for a fit to monoclinic I and to rhombic I symmetry are clear, as are the physical similarities between the symmetries: rhombic I can have a C_{2v} point group, and monoclinic I a C_{1h}. This is suggestive of the 562.5 nm centre being a perturbed rhombic I symmetry centre. The nature of this and the other centres will be discussed further in section 5.3.

Finally, attention is drawn to the high shift-rates of ZPL components in the various orientations of all three ZPLs; high shift-rates identified from uniaxial stress experiments generally indicate the presence of vacancies in the

defect centre [Vavilov (1980)]; for reference, the neutral nitrogen-vacancy centre (at 575 nm) exhibits shift-rates of ~ 6 meV GPa^{-1}.

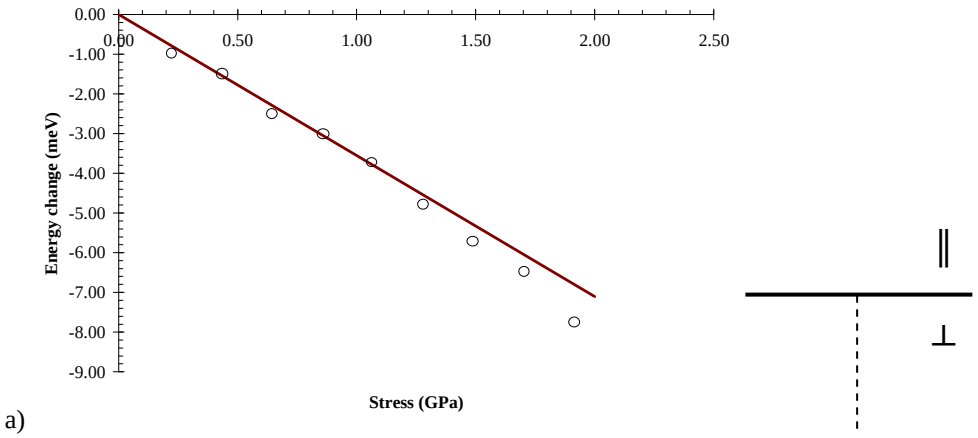

a)

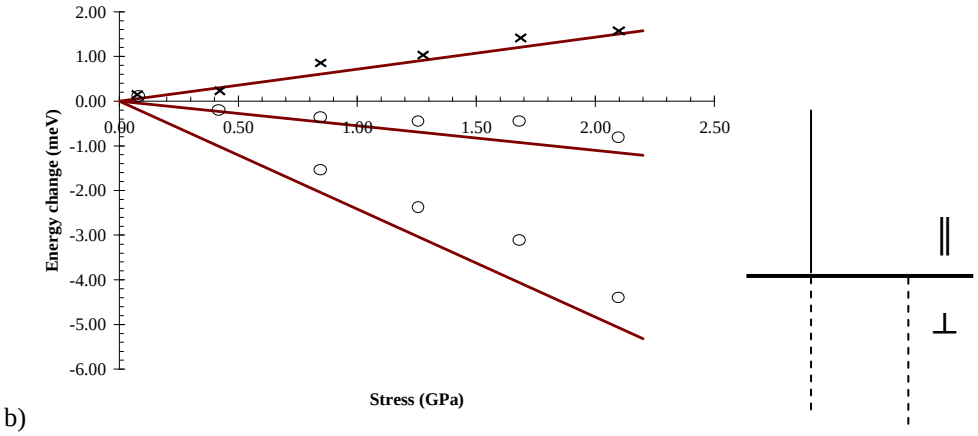

b)

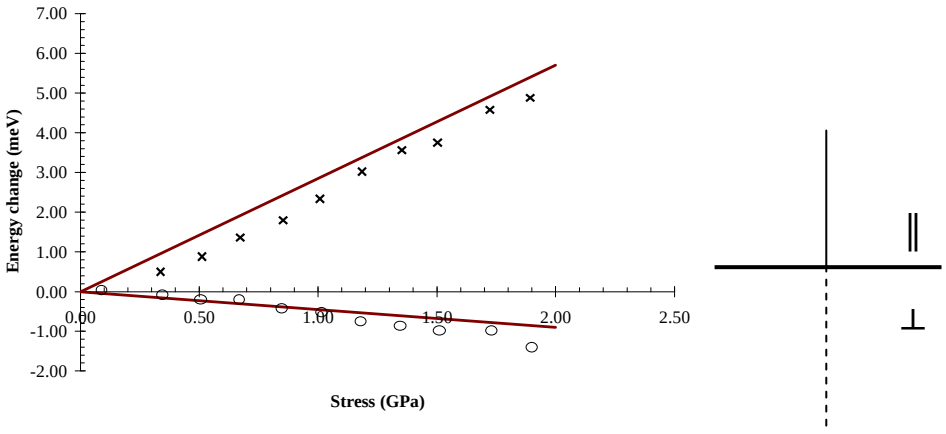

c)

Figure 5.2.3 – Uniaxial stress splitting data for the 562.5 nm (2.204 eV) centre in cathodoluminescence, showing change in energy of ZPL components as a function of applied stress. Data points are experimental results, lines are calculated from the fit to a rhombic I symmetry. a) ZPL under <001> compression (**S**). b) ZPL under <111> compression. c) ZPL under [110] compression. Data point notation as in figure 5.2.1. Stick diagrams show relative intensities of stress-split ZPL components at maximum recorded stress, with vertical lines above the horizontal line representing $\mathbf{E} \parallel \mathbf{S}$, and vertical lines below representing $\mathbf{E} \perp \mathbf{S}$.

5.2.2 Temperature dependence

To further characterise the preferentially oriented centres, the effect of temperature upon the peak intensity, energy and width (FWHM) has been recorded for temperatures between liquid nitrogen temperature (77 K) and room temperature. All of the transitions, however, become immeasurably weak above 200 K. Figures 5.2.4, 5.2.5 and 5.2.6 show the measured temperature dependencies for the 466.6, 496.8 and 562.5 nm centres, respectively.

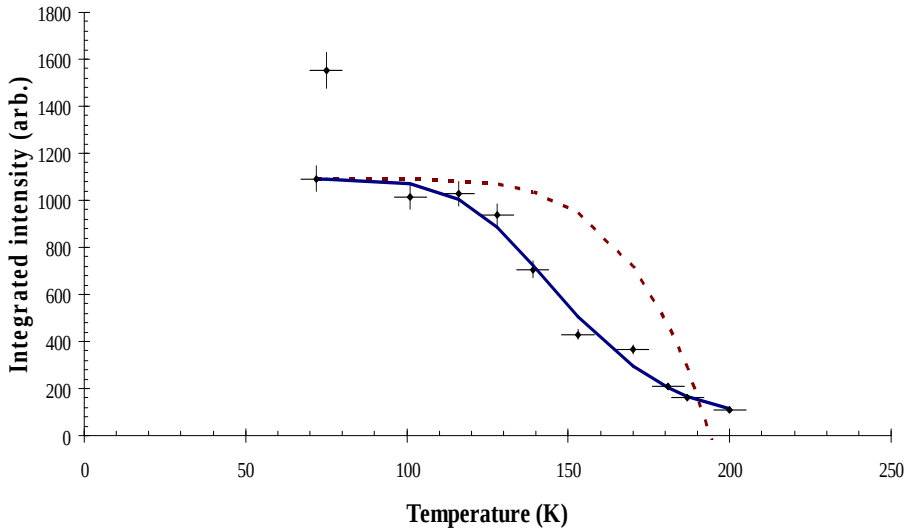

a)

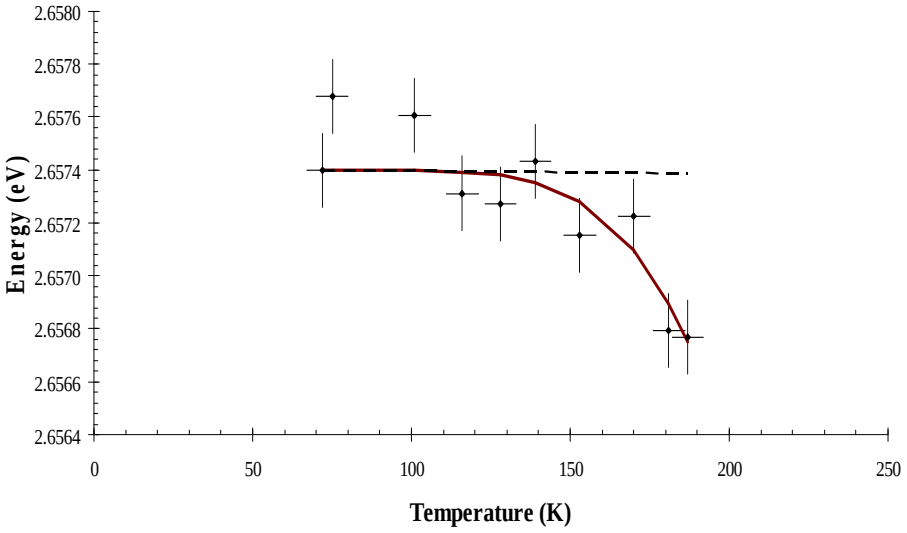

b)

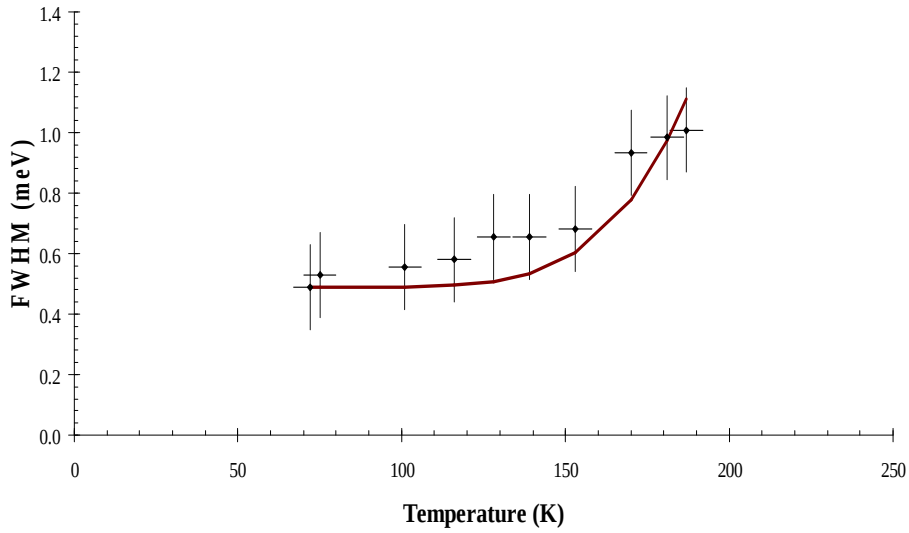

c)

Figure 5.2.4 – Temperature dependence measurements of the 466.6 nm (2.657 eV) ZPL in CVD diamond, recorded in cathodoluminescence. a) shows variation of integrated intensity of the peak with temperature, b) that for the peak energy, and c) that for the FWHM. Data points in all figures are the measured data. Lines through the data are the theoretical fits, see text for details.

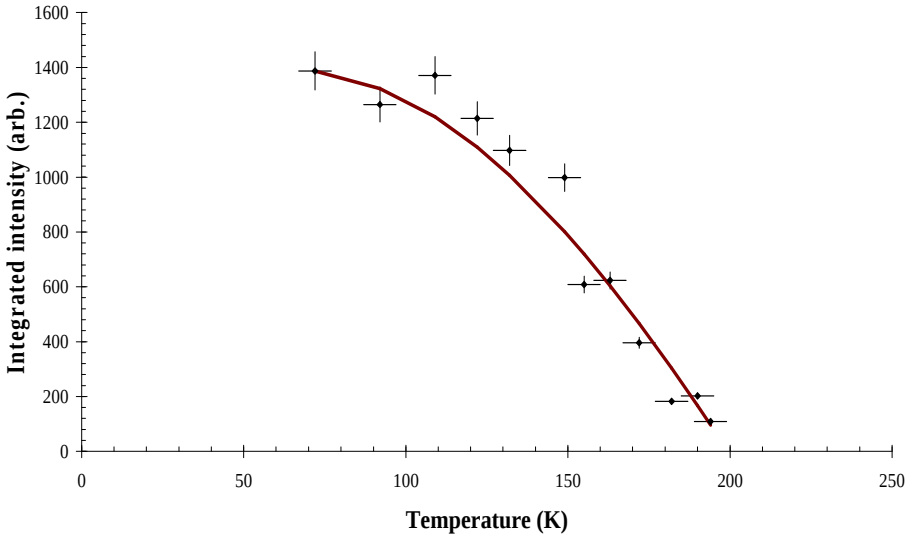

a)

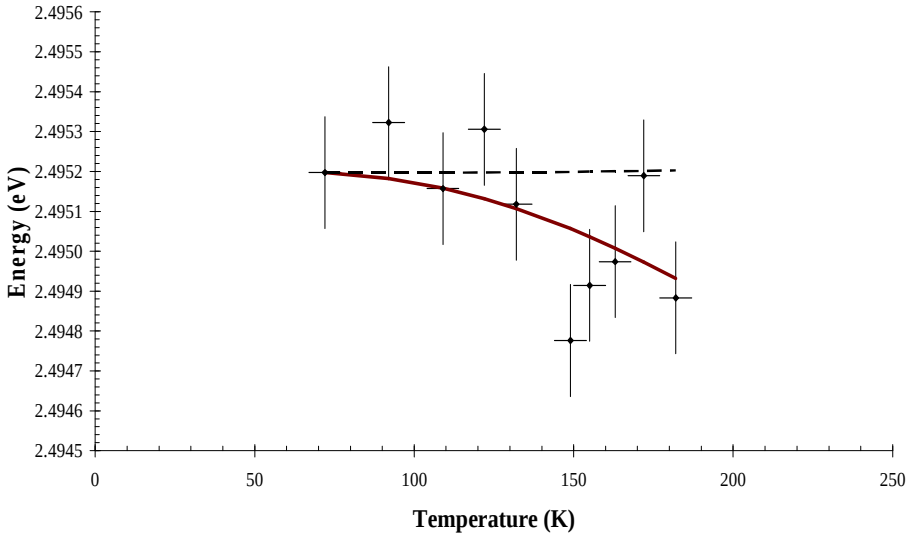

b)

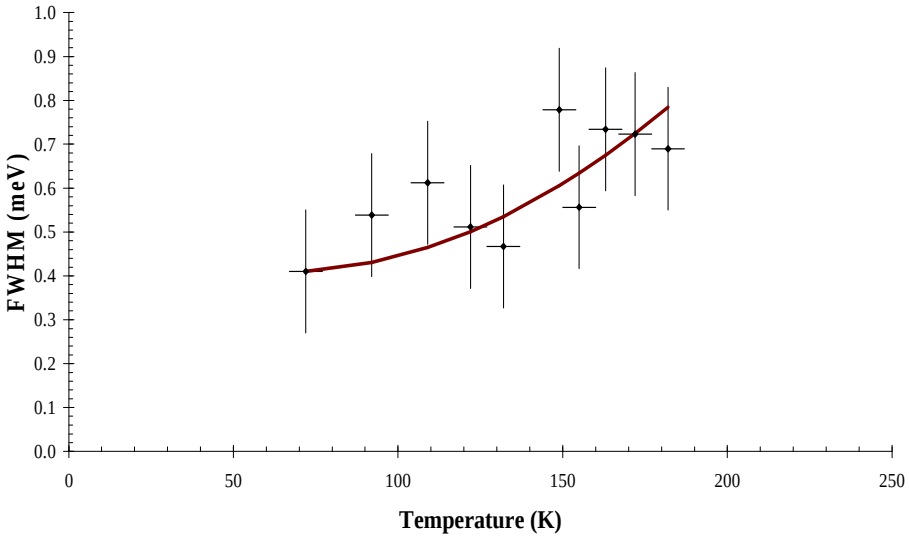

c)

Figure 5.2.5 – Temperature dependence measurements of the 496.8 nm (2.495 eV) ZPL in CVD diamond, recorded in cathodoluminescence. a) shows variation of integrated intensity of the peak with temperature, b) that for the peak energy, and c) that for the FWHM. Data points in all figures are the measured data. Lines through the data are the theoretical fits, see text for details.

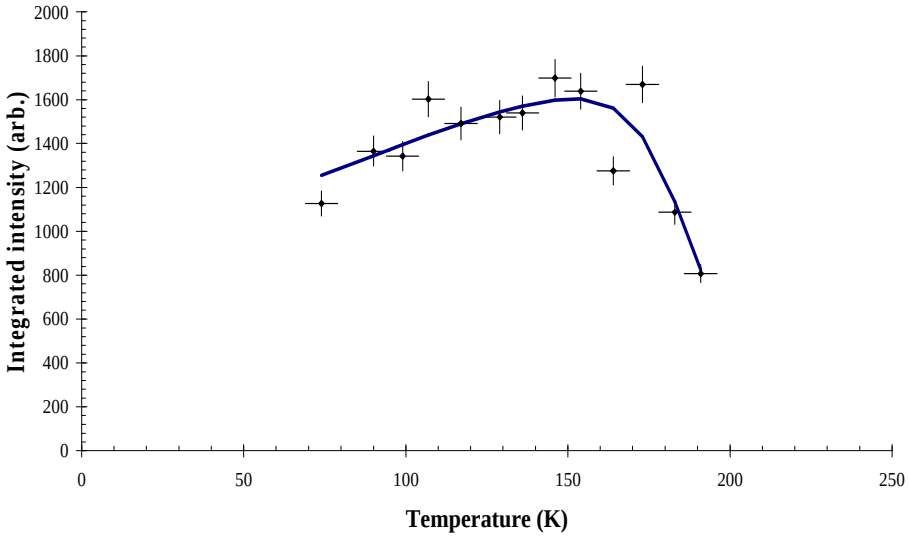
Integrated intensity (arb.)
2000
1800
1600
1400
1200
1000
800
600
400
200
0
0
50
100
150
200
250
Temperature (K)

a)

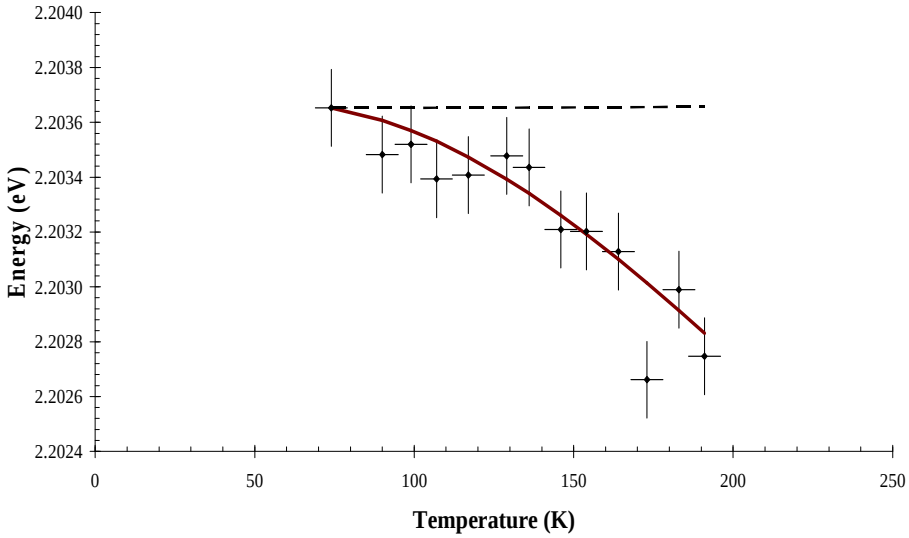
Energy (eV)
2.2040
2.2038
2.2036
2.2034
2.2032
2.2030
2.2028
2.2026
2.2024
0
50
100
150
200
250
Temperature (K)

b)

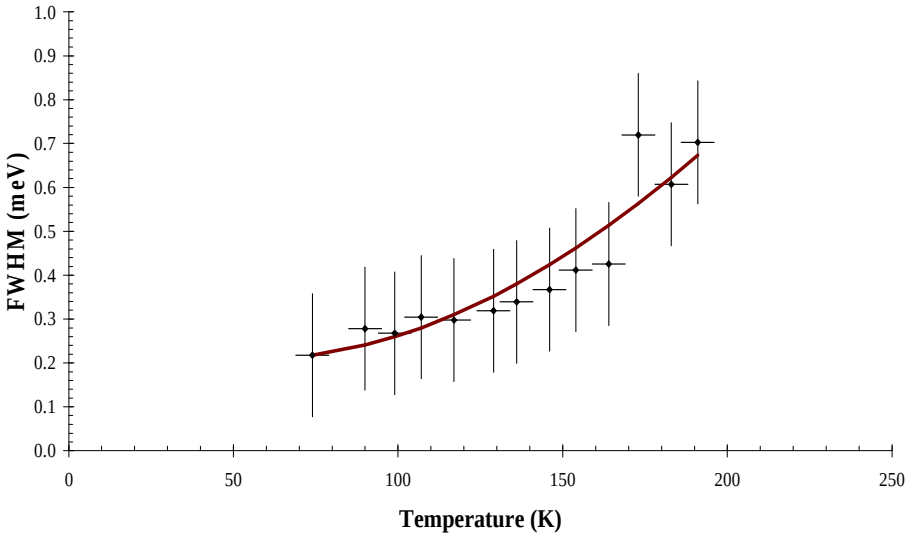

c)

Figure 5.2.6 – Temperature dependence measurements of the 562.5 nm (2.204 eV) ZPL in CVD diamond, recorded in cathodoluminescence. a) shows variation of integrated intensity of the peak with temperature, b) that for the peak energy, and c) that for the FWHM. Data points in all figures are the measured data. Lines through the data are the theoretical fits, see text for details.

Most defect centres in diamond experience single-mode vibronic coupling, so in principle the measured variation of zero-phonon integrated intensity with temperature can be described using the expressions of section 2.2.2.2, the only required parameters being the energy of the dominant phonon, $\hbar\omega$, and the Huang-Rhys factor of the centre. These can usually be determined from the optical spectra of the centre. However, in the case of the 466.6 nm centre, along with a number of the other centres investigated in this work (496.8, 510.3, 562.5 nm), the vibronic band cannot be clearly identified from the optical spectra.

The approach taken in the first instance, to evaluate the variation of ZPL intensity with temperature, has been to estimate the dominant phonon energy at the centre, using the change in peak energy with temperature measurements. The variation of peak energy with temperature originates from the change in vibrational frequencies at the centre, due to quadratic coupling effects, along with the thermal expansion of the lattice (see section 2.2.2.2 for further discussion).

The procedure for estimating the dominant phonon energy from the temperature dependence of the ZPL energy requires calculation of the effect of lattice expansion at the centre, followed by a best-fit determination of the lattice-coupling contribution to the shift, where the variable which determines the fit is the dominant phonon energy. The lattice expansion can be calculated explicitly: the elastic moduli of diamond are known [McSkimmin and Andreatch (1972)]; the coefficient of volume expansion of diamond has been determined, and whilst coarse in interval (see section 2.2.2.2), fitting of a suitable function can allow interpolation of higher resolution data values; the shift rate A of the ZPL under hydrostatic pressure can be determined from the uniaxial stress data, using the perturbation to the ZPL energy under stress for the given symmetry of the point defect.

This technique is demonstrated by measuring the temperature dependence of the ZPL energy for the 575 nm (2.156 eV) neutral nitrogen-vacancy defect. Figure 5.2.7 shows the experimental data recorded for this defect (data points), along with the contribution of the lattice expansion (black dashed line). The lattice expansion is calculated using the perturbation to the ZPL energy under stress for a centre with trigonal symmetry [Hughes and Runciman (1967)]:

$$\begin{aligned} V = {} & A_1\left(s_{xx}+s_{yy}+s_{zz}\right)+A_1'\left(s_{yz}+s_{zx}+s_{xy}\right)+E_X\left(2s_{zz}-s_{xx}-s_{yy}\right) \\ & +\sqrt{3}E_Y\left(s_{xx}-s_{yy}\right)+E_X'\left(2s_{xy}-s_{yz}-s_{zx}\right)+\sqrt{3}E_Y'\left(s_{yz}-s_{zx}\right) \end{aligned}, \qquad 5.2.2$$

where s_{ij} are the components of the stress tensor, and A_1, A'_1, E_X, E'_X, E_Y and E'_Y are the stress parameters determined from uniaxial stress measurements; these are known for the 575 nm centre [Davies (1979b)]. A hydrostatic compression corresponds to a unit stress applied along the s_{xx}, s_{yy} and s_{zz} orientations; other orientations apply shear stresses. This transformation reduces the perturbation to $V = 3A_1$ and hence the shift due to lattice expansion can be determined.

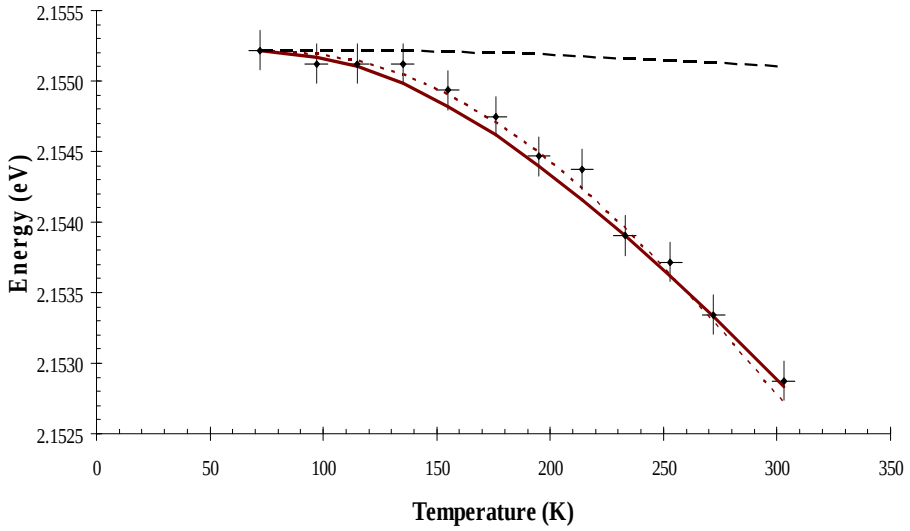

Figure 5.2.7 – Temperature dependence of the peak energy of the 575 nm (2.156 eV) centre in CVD diamond, measured in cathodoluminescence. Data points show measured values, lines show theoretical fits – see text for details.

Allowing for the lattice expansion at the centre (subtracting these values from the measured data), two fits to the temperature dependence data are then performed: the first applies the lattice-coupling contribution (equation 2.2.26) to the shift using the known literature values for the Huang-Rhys factor (S = 3.3) and phonon coupling ($\hbar\omega$ = 46 meV) at the centre; this produces the full line fit to the data in figure 5.2.7. Then, separately, a least-squares fit to the data is performed, using the known Huang-Rhys factor, but with $\hbar\omega$ varied over the full range of allowed phonon energies in diamond (165 meV); this produces the dotted line fit to the data, with the best-fit $\hbar\omega$ = 53.70 ± 0.30 meV.

Within the associated errors of the data, the fit of equation 2.2.24 using the literature values of S and $\hbar\omega$ for the centre is a good match to the data. The alternative, automated fit produces an $\hbar\omega$ value that, whilst ~ 18 % different to the literature value, is a reasonable measure of the phonon coupling at the centre given the possible range of phonon energies in diamond. This conclusion is justified by the application of the technique to provide an $\hbar\omega$ value which is used to produce the theoretical fit to the temperature dependence of the FWHM of the 466.6, 496.8, 510.3 and 562.5 nm centres (see below, and the corresponding sections).

Returning to the 466.6 nm centre, the full line through the data points of figure 5.2.4b (the peak energy variation with temperature) is a fit of equation 2.2.24, allowing for the lattice expansion (dashed line; equation 2.2.26). The shift rate of the ZPL under hydrostatic pressure is determined from the uniaxial stress perturbation of this rhombic I symmetry centre (e.g. Lawson *et al* (1992a)):

$$V = A_1 s_{zz} + A_2 \left(s_{xx} + s_{yy} \right) + 2A_3 s_{xy} . \qquad 5.2.3$$

Here, the final term vanishes as the shear contribution, s_{xy}, is not required for hydrostatic compression. So the perturbation becomes $V = A_1 + 2A_2$, where the stress parameters have been determined (section 5.2.1).

The fit of equation 2.2.24 (full line) to the data in figure 5.2.4b uses a sufficiently low Huang-Rhys factor (S = 0.005, as the vibronic band is not observed) so as to not affect the shape of the fit; and utilises the least-squares method, varying the $\hbar\omega$ value over the full range of phonon energies in diamond, returning $\hbar\omega$ = 122.97 ± 0.30 meV. This value is then used as the dominant phonon energy for the centre in the theoretical fit of the variation of the FWHM with temperature: the FWHM, $\Gamma(T)$, of the ZPL changes with temperature according to

$$\Gamma(T) = d \int_0^{\omega_m} \omega^2 I_1(\omega) n(\omega,T) \left(n(\omega,T) + 1 \right) d\omega , \qquad 5.2.4$$

where d is a constant. Using $\hbar\omega$ = 122.97 meV, the full line fit to the experimental data in figure 5.2.4c is obtained, which within errors can be considered a good fit; this in part justifies the use of the automated fit technique to obtain dominant phonon coupling energies.

Finally, the estimated $\hbar\omega$ value is used to calculate the theoretical fit of equation 2.2.22 to the variation of ZPL integrated intensity with temperature. This fit produces the dashed (red) line in figure 5.2.4a, which is clearly an unsatisfactory fit. It will be seen in the 496.8 nm centre (below), however, that this approach of using a calculated $\hbar\omega$ is not the cause of the poor fit, rather, as is seen below, an additional mechanism taking place at the centre produces the decay in intensity.

An alternative analysis of the change in intensity of a ZPL with temperature, when investigated in cathodoluminescence (rather than absorption), is that utilised by Khong and Collins (1993). Diamond luminescence generated by incident electrons is understood to operate by the production of electron-hole pairs (excitons) within the sample, which are caught at defect centres, resulting in luminescence (see section 3.3). Khong and Collins analysed the temperature dependence of ZPL luminescence by considering the capture of excitons at defects, and the thermally-induced detrapping, to be a competitive process. Under thermal equilibrium between excitons caught at defects and the free excitons, an energy, E, is required to ionise a defect centre. From this, the ZPL integrated intensity, $I_0(T)$, as a function of temperature can be expressed as [Davies (1989)]:

$$I_0(T) = \frac{I_0(0)}{1 + g T^{\frac{3}{2}} \exp\left(\frac{-E}{k_B T}\right)}, \qquad 5.2.5$$

where $I_0(0)$ is the ZPL integrated intensity at zero Kelvin, and $gT^{\frac{3}{2}}$ is the effective density of band continuum states into which the ionisation occurs. The parameters g and E can be treated as variables in a least-squares fit to the experimental data. Fitting to the data in figure 5.2.4a produces the full (blue) line fit, which is in excellent agreement with the data. The values of the parameters of this fit are g = 0.585 ± 0.005 and E = 90.40 ± 0.05 meV. The value of the ionisation energy is in reasonable agreement with the values obtained for other defect centres analysed by Khong and Collins; however, the value for g is significantly different from the values for other defect centres – these are all of the order of ~ 300 to 1000. This corresponds to a density of band continuum states of the order of 10^2 for g from this work, compared with ~ 10^7 for g = 300; this suggests that there is an additional mechanism producing the decay of luminescence intensity with temperature at the defect centre.

Analyses similar to those presented above for the 466.6 nm centre were conducted on the 496.8 nm centre data. A least-squares fit of the peak energy with temperature was performed to estimate the phonon energy at the centre: the

contribution due to lattice expansion was found using equation 2.2.26 (figure 5.2.5b, dashed black line), then the fit to the energy was performed using equations 2.2.24 and 2.2.25, with S = 0.005, and varying over the allowed phonon energies in diamond; the full line through the data points shows this fit. The dominant phonon coupling energy at the 496.8 nm centre is calculated to be $\hbar\omega$ = 39.76 ± 0.30 meV. This value was used to calculate the FWHM change with temperature, using equation 2.2.29 (figure 5.2.5c, full line). Finally, equation 2.2.22 was used to describe the temperature dependence of the integrated intensity of the 496.8 nm ZPL; using the estimated $\hbar\omega$, the full line in figure 5.2.5a was obtained. These results are in excellent agreement with the experimental data, supporting the calculated estimate value of the dominant phonon coupling at the 496.8 nm centre.

The 562.5 nm ZPL peak energy shift with temperature is shown in figure 5.2.6b. The dashed black line shows the contribution of the lattice expansion to the shift. The full red line through the data in figure 5.2.6b shows the least-squares fit to the shift, using $\hbar\omega$ as the fitting variable, with S = 0.005, over the allowed phonon energies in diamond. The fit returns $\hbar\omega$ = 32.84 ± 0.30 meV. This value is used to calculate the variation of the FWHM with temperature, shown as the full line in figure 5.2.6c. The good fit supports the $\hbar\omega$ value estimated from the peak energy shift data.

The change of the 562.5 nm ZPL integrated intensity with temperature shows unusual behaviour, in that it increases as the temperature increases up to ~ 160 K, after which it rapidly decreases. This behaviour cannot be described using the general temperature variation of ZPL intensity defined in section 2.2.2.2, which assumes that the integrated intensity of a ZPL will decrease with increasing temperature, due to the thermal depopulation of the lowest vibrational level in the ground electronic state of the defect. However, the temperature dependence measurements were performed in cathodoluminescence, and hence another analysis approach must be taken.

Khong and Collins (1993) found a similar phenomenon with the 533 nm ZPL in CVD diamond for its temperature dependence in cathodoluminescence. The first approximation is to assume that the traps external to the 562.5 nm centre ionise with a single, lower activation energy, E_t, than the ionisation energy, E, of the 562.5 nm centre. Hence an expression similar to equation 5.2.5

for the ZPL intensity variation with temperature of the 466.6 nm centre can be used [Khong and Collins (1993)]:

$$I_0(T) = \frac{I_0(0)}{(1+f')1+g\,T^{\frac{3}{2}}\exp\left(\frac{-E}{k_B T}\right)}, \qquad 5.2.6$$

where

$$f' = \frac{c}{1+bT^{\frac{3}{2}}\exp\left(\frac{-E_t}{k_B T}\right)}, \qquad 5.2.7$$

where $I_0(0)$ is the ZPL integrated intensity at zero Kelvin, and the parameters g, b, c, E and E_t can be treated as variables in a least-squares fit to the experimental data. Figure 5.2.6a shows the fit obtained (full (blue) line), which is reasonable within the errors. The parameters of the fit, however, do not correlate well with the common range of values calculated by Khong and Collins; E = 269.0 ± 0.5 meV, E_t = -27.0 ± 0.5 meV, g = 4965 ± 5, c = 450 ± 5, b = -0.1 ± 0.05. The values for the activation energy of the 562.5 nm centre, E, and the parameter c, are reasonable, and similar to values found by Khong and Collins. The values of g and b are somewhat different from the expected values. However, the main problem with this fit is the value of the activation energy, E_t, of the traps separate from the 562.5 nm centre: a negative energy value is physically unrealistic for the concept of a charge trap. Further work is clearly necessary to understand the variation of ZPL intensity with temperature for the 562.5 and 466.6 nm lines.

5.2.3 Nitrogen isotope dependences

Additional characterisation of a point defect is identifying the atomic constituents. Isotopic impurity substitution can allow this by showing a change in zero-phonon transition energy if the isotope substituted for in the crystal is present in the defect under inspection. As discussed in section 2.2.2.3, the magnitude and direction of the observed ZPL shift can be predicted from the temperature dependent shift in energy of the ZPL, as the origin of the isotope dependent shift is the change in vibrational frequencies at the centre.

The peak position of the 466.6 nm ZPL was measured in an undoped single-crystal CVD diamond sample, and a nitrogen-15 enriched (during growth) sample; simultaneously measuring over the ZPL and the 470.253 nm calibration line from a neon lamp to obtain the precise position of the peak (see section 3.4 for a description of the experimental design). The measurement was repeated four times using the same samples in order to minimise the errors. The peak was observed to shift by 0.149 ± 0.080 meV to higher energy in the nitrogen-15 enriched sample. Isotope-induced ZPL peak energy shifts in diamond are expected to be of the order of ~ $|0.1|$ meV [Davies (1983), Collins *et al* (1988), and see section 2.2.2.3]; as the observed shift of the 466.6 nm ZPL is comparable to this, it can be concluded that the defect centre which produces the zero-phonon transition at 466.6 nm directly involves nitrogen. A note on the associated error: recording of high-resolution spectra for this ZPL proved difficult due to strain-induced splitting, the presence of the 467.2 nm ZPL and the structured background. As such the error is calculated at over 50 % of the shift value. This is not ideal; and whilst the magnitude of the shift makes it appropriate to conclude isotope involvement, further measurements of the nitrogen isotope-dependence of this ZPL should be made.

The 496.8 nm ZPL appeared immeasurably weak in CL spectra of the nitrogen-15 enriched sample, which prevented measurements from being made, and hence no data on the nitrogen isotope dependency of the centre can be presented.

The 562.5 nm peak was observed to shift by 0.034 ± 0.022 meV to lower energy in the nitrogen-15 enriched sample. This shift is a factor of three less than

that expected for a nitrogen-15 isotope induced shift. The direction of the shift is opposite to that expected for the direction of the temperature dependent shift of the ZPL energy (section 2.2.2.3). These two factors, along with the large associated uncertainty in the measurement, mean that it can be concluded that the defect centre which produces the 562.5 nm ZPL does not directly involve nitrogen.

5.3 Discussion

It has been shown that the luminescence from the 466.6 nm ZPL is an electric dipole transition, originating from a <110> oriented defect centre with rhombic I symmetry. A separate point defect with the same symmetry and dipole properties is responsible for the luminescence transition at 496.8 nm. Both centres have low Huang-Rhys factors, and demonstrate single-mode phonon coupling with dominant energies 122.97 ± 0.30 and 39.76 ± 0.30 meV, respectively. A temperature-dependent luminescence-quenching mechanism takes place at the 466.6 nm centre. Nitrogen isotope measurements of the ZPLs show that the 466.6 nm centre directly involves nitrogen; measurements of the 496.8 nm centre were not possible, however.

The 562.5 nm ZPL has been found to be due to an electric dipole transition at a <110> oriented point defect with either monoclinic I or rhombic I symmetry. The centre demonstrates single-mode coupling to phonons with energy 32.84 ± 0.30 meV; it has a low Huang-Rhys factor. The temperature dependence of the ZPL intensity of the centre demonstrates unusual behaviour, which requires further investigation. Nitrogen isotope measurements of the centre show that it does not directly involve nitrogen. The 562.5 nm centre, along with the two others, exhibits high stress-splitting rates, which is suggestive of the presence of vacancies in the defects.

As noted in section 5.2.1, the 562.5 nm centre's symmetry is either monoclinic I or rhombic I, which means C_{1h} or C_{2v} point groups, respectively. The C_{1h} symbol means that the centre has one reflection plane perpendicular to the rotation axis, and can be rotated by $2\pi/1$ to return to the same configuration. The C_{2v} symbol means that the centre has one reflection plane parallel to the rotation axis, and can be rotated by $2\pi/2$ to return to the same configuration. With a <110> constraint on the orientation, the difference between these two symmetries can be as little as a perturbation to reduce the $2\pi/2$ rotation to $2\pi/1$. It could be that the 562.5 nm centre has monoclinic I symmetry, but is essentially a perturbed rhombic I centre.

The three centres have so far been exclusively observed in CVD-synthesised diamond; and have been observed in this work in material from two different manufacturers. This suggests that the defects are unique to the CVD growth process. Whilst nitrogen is not directly involved in the 466.6 and 562.5 nm centres, increasing the concentration of nitrogen gas for diamond CVD growth increases the luminescence intensity of the three centres [Tallaire *et al* (2006)]. There is no evidence that the centres are directly related, however these findings are indicative of the centres being the result of a characteristic growth mechanism. This conclusion is drawn for the following reasons: the exclusivity of observation of the ZPLs in luminescence spectra of CVD diamond; the preferential orientation of the centres perpendicular to the growth direction (the samples used in this work were grown upwards along [001]); the non-direct influence of nitrogen on the intensity of the ZPLs; and the probable presence of vacancies in the defects.

It is believed that CVD growth of diamond proceeds by the creation and annihilation of vacancies, of various charge states, allowing etching and deposition of atoms on to the growth surface [Bar-Yam and Moustakas (1989), Allers and Mainwood (1998)]. It has been established that increasing the nitrogen concentration in the growth-phase gases can increase the growth rate and improve the macroscopic quality of the crystals produced [Müller-Sebert *et al* (1995), Bohr *et al* (1995), Asmussen *et al* (1999), Tallaire *et al* (2007)]. The reason, it is believed, is that nitrogen-complexes play a number of roles in facilitating the formation of nucleation points at the growth surface [Qi *et al* (2006)], presumably being involved in the creation and destruction of surface vacancies. An implication is that an increase in the growth rate, i.e. more aggressive chemical interaction at the growth surface, may not allow time for the removal of created vacancies before the next atomic layer is deposited. This would create growth-process related complexes, some of which could be stable enough to not dissociate under the high growth temperature. Vacancies deeper in the lattice would migrate with the temperature, and either become caught at traps or annihilate at the surface. The end result of this process would be that the bulk would contain vacancy-complexes of both migration-products and growth-related complexes. Indeed, there is little evidence of isolated vacancies and di-

vacancies being observed optically in the *bulk* of single-crystal CVD diamond (Allers and Mainwood (1998) and this work).

If the three defects discussed here are vacancy-related products of the growth process, then the above situation may explain why these defects are only seen in CVD-synthesised material, and why the increased concentration of nitrogen during growth results in more intense luminescence from these centres. The incorporation of vacancies into the growth surface explains the preferential orientation of these defects, along with the probable direct involvement of vacancies in the centres. A possible growth scheme could be as follows: two vacancies in the (001) plane become "locked" into the lattice (along a <110> vector) by the fast deposition of the next growth layer. This results in the bonding of an atom (carbon, or other) in the lattice site an equal distance between the two vacancies in the next growth layer. The bonded species does not become incorporated into the vacancies' as it is bound to the next atomic layer, as well as the vacancies.

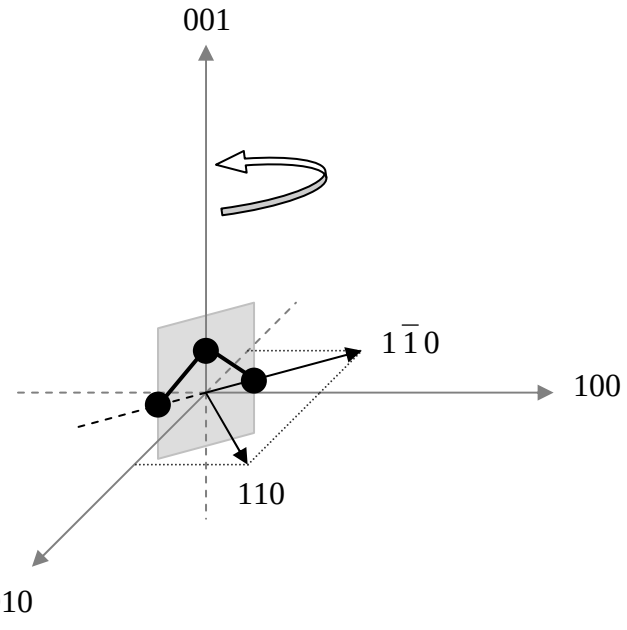

a)

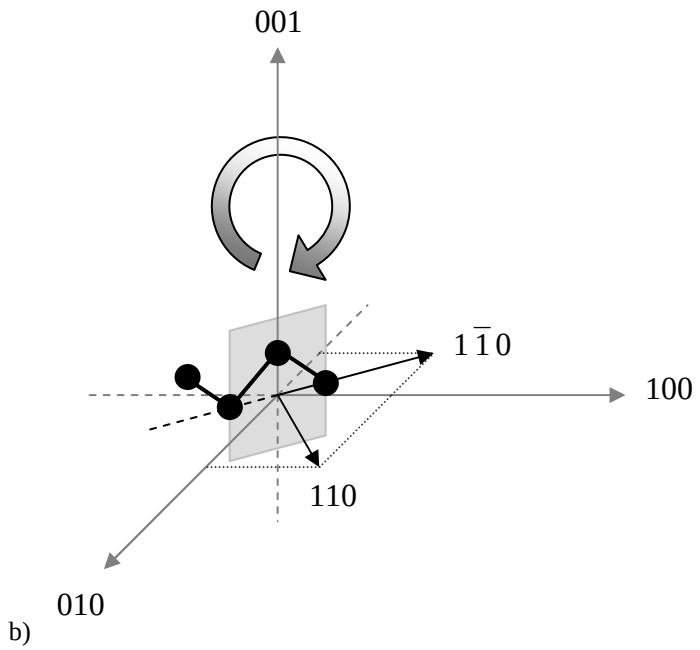

b)

Figure 5.3.1 – a) Schematic diagram of a rhombic I configured molecule, showing the V-X-V configuration. b) Schematic diagram of a monoclinic I configured molecule.

The atomic configuration of these defects is constrained by the symmetry and the preferential orientation. The configurations illustrated in figures 5.3.1a and 5.3.1b are examples of rhombic I and monoclinic I symmetries. For the 466.6 and 496.8 nm centres, symmetry requirements mean generally that the defect species occupying the sites in the plane parallel to the rotation axis can be rotated by $2\pi/2$ into each other, for example an *a-b-c* configuration must consist of *a-b-a*, i.e. the two atoms straddling the rotation axis must be of the same species. Due to the likely presence of vacancies, and regarding the proposed growth mechanism above, it is suggested that the configuration is V-N-V for the 466.6 nm centre, and V-X-V for the 496.8 nm centre, where X is an unknown species.

This proposal can be explored: it could be possible, of course, for any odd number of atomic sites in this configuration to exist. Two possibilities then arise: first, these could consist purely of vacancies; although chains of three to eight vacancies aligned along <110> axes have already been identified [Iakoubovskii and Stesmans (2002b), Hounsome *et al* (2005)]. Second, increasing complexity in the configuration, e.g. V-X-V-X-V cannot be ruled out; however increasing complexity becomes increasingly unlikely considering that the common

temperature of CVD growth (~ 800˚C) means that vacancies are mobile during growth. Finally, the configuration cannot be C-V-C, as this would simply be a vacancy, with tetrahedral symmetry. Hence the most probable configuration is V-X-V. The 466.6 and 496.8 nm centres have been established as distinct point defects (section 5.1) and not transitions from the same centre. Both centres then require different X atoms. For the 466.6 nm centre, N is proposed; for the 496.8 nm centre, another species is required. Given the relative lack of atomic impurity species in this type of material, possible candidates include C and H.

The atomic configuration of the 562.5 nm centre, as discussed, could be that of a perturbed rhombic I symmetry; for example, V-X-V-Y, or Z-V-X-V-Y, where X, Y and Z are all unknown species (not nitrogen) – although the latter is unlikely for the vacancy migration-temperature reason stated above. The constraints are that the symmetry axis passes through X along [001], and that the atoms all lie in the same plane parallel to the rotation axis.

The proposed growth scheme and atomic configurations could be investigated by computational calculations (density functional theory, etc.), and experimentally by thermal annealing experiments, in which the creation and destruction of these centres could be studied; deuterium-doped CVD diamonds could be studied in an attempt to identify if hydrogen is directly involved in the centres.

Chapter 6

Investigation of other defects

6.1 The 467.2 nm ZPL

6.1.1 Introduction

The 467.2 nm (2.653 eV) ZPL is observed in cathodoluminescence of the single-crystal CVD synthesised diamonds studied in this work; in both the Element Six and University of Paris XIII samples. The ZPL has not been observed in photoluminescence, probably because the luminescence is too weak. It has not been observed in absorption measurements of these samples. The ZPL has not been reported previously. The cathodoluminescence spectra of the single-crystal CVD samples used in this work were presented in Tallaire *et al* (2006) and show the line, but the authors do not draw attention to it. The line is not present in the non-nitrogen doped samples of that work, but present after doping; this suggests a nitrogen dependence of some kind. Nitrogen-15 isotope measurements have not been made on the ZPL as the peak frequently appeared split due to strain in the samples.

The following sections identify the vibronic band of this defect, determine the symmetry of the centre, and present temperature dependence measurements of the ZPL, which are shown to be consistent with the Huang-Rhys factor and dominant phonon-coupling energy determined from measurements of the vibronic band. Additionally, it is proposed that the 467.2 nm centre is a perturbed form of the 466.6 nm centre.

6.1.2 Results

6.1.2.1 Uniaxial stress measurements

The symmetry properties of the 467.2 nm (2.653 eV) ZPL have been investigated using cathodoluminescence whilst the diamond sample is under uniaxial stress. Two untreated, single-crystal CVD diamond samples were cut and polished into cuboids, such that the faces corresponded to the crystallographic lattice directions [001], [110] and [$1\bar{1}0$] (for the first sample), and [111], [$1\bar{1}0$] and [$11\bar{2}$] (for the second sample). These were the same two samples used to investigate the preferentially oriented defects. The close proximity in energy of the 467.2 nm ZPL to the 466.6 nm ZPL meant that spectra recorded for the 466.6 nm ZPL whilst the sample was under stress included the splitting and shift of the 467.2 nm ZPL. As such, the experimental details were as discussed in section 5.2.1.

Stress-induced shifts and splitting data of the 467.2 nm ZPL are shown in figure 6.1.1. Stress applied along a <001> axis caused the ZPL to split into two components when the luminescence was polarised perpendicular to the stress direction; only a linear shift of the ZPL was observed when the luminescence was polarised parallel to the stress direction. Luminescence observed when the sample was compressed along a <111> axis showed two components shifting linearly with increasing stress. Under <110> compression, ten distinct components were observed under the various viewing and polarisation directions. All of the components shifted linearly with stress, although a number of them were weak. This is important when considering the symmetry assignment, below.

Comparing the splitting patterns in the three compression orientation to the standard symmetry tables [Mohammed et al (1982), Kaplyanskii (1964a, b)], suggests that the symmetry is rhombic I. The perturbation to the zero-phonon energy and the theoretical shift-rates of the components are listed in section 5.2.1. A least-squares fit of the experimental shift-rates to the theoretical gives the values of the stress-parameters as A_1 = -9.20 ± 0.30 meV GPa^{-1}, A_2 = 6.40 ±

0.30 meV GPa^{-1}, A_3 = 7.8 ± 0.30 meV GPa^{-1}. These values give the theoretical shift-rates shown in figure 6.1.1 (red lines). The fit to the data for the <001> and <111> orientations is good, however that for the <110> orientation is less so. The three theoretical components expected in the <110> stress direction appear as only two in figure 6.1.1 because two of the components have equivalent shift rates.

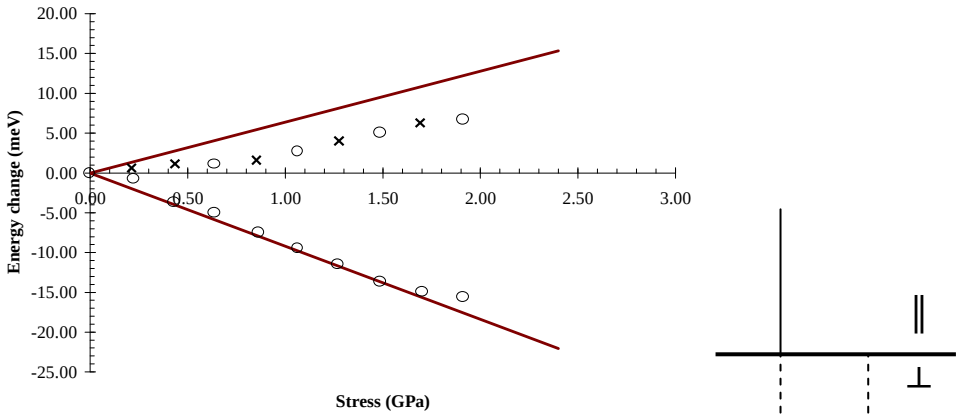

a)

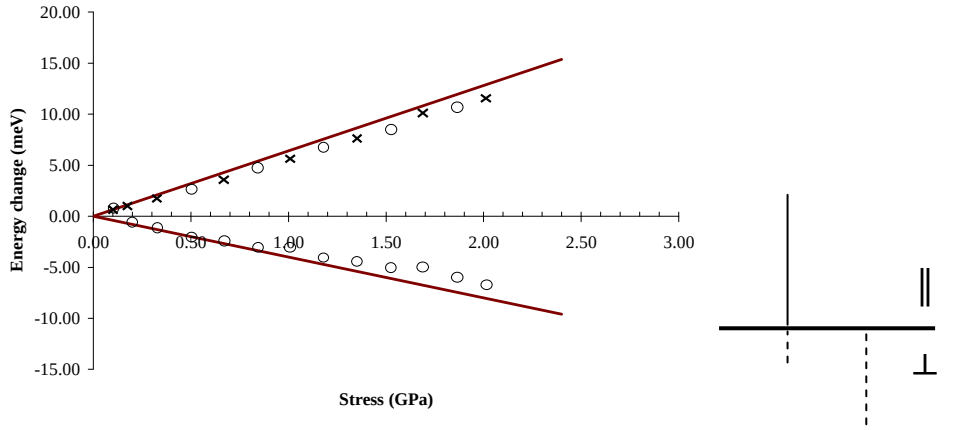

b)

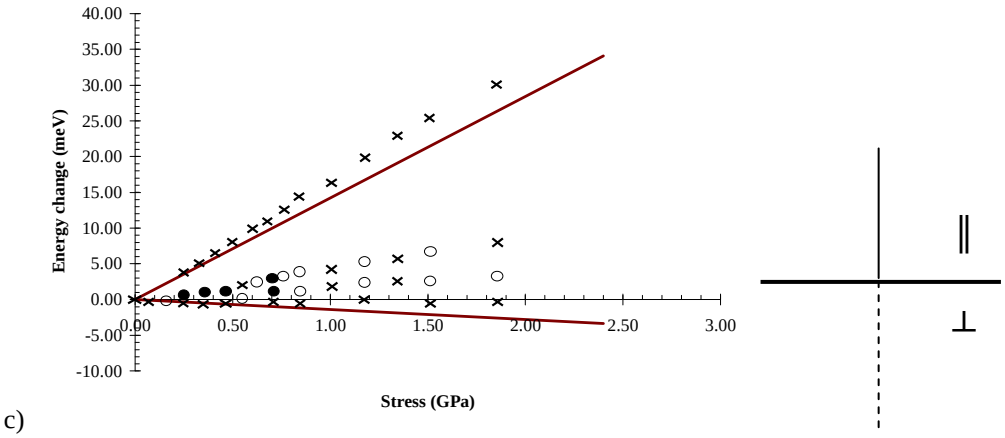

c)

Figure 6.1.1 – Uniaxial stress splitting data for the 467.2 nm (2.653 eV) centre in cathodoluminescence, showing change in energy of ZPL components as a function of applied stress. Data points are experimental results, lines are calculated from the fit to a rhombic I symmetry. a) ZPL under <001> compression (**S**); crosses are for electric vector of luminescence **E** ∥ **S**; unfilled circles are for **E** ⊥ **S**. b) ZPL under <111> compression; crosses are for **E** ∥ **S**; unfilled circles are for **E** ⊥ **S**. c) ZPL under [110] compression; crosses are for **E** ∥ **S** when viewing along; unfilled circles are for **E** ⊥ **S** when viewing along [001], filled circles for **E** ⊥ **S** when viewing along [1 $\bar{1}$ 0]. Stick diagrams show relative intensities of stress-split ZPL components at maximum recorded stress, with vertical lines above the horizontal line representing **E** ∥ **S**, and vertical lines below representing **E** ⊥ **S**.

Figure 6.1.1 also shows the relative intensities of the stress-split components, where a good comparison to theory exists. A reasonable overall fit to an A to B electric dipole transition at a rhombic I symmetry defect centre is found. A discrepancy exists between the experimental and theoretical data for the <110> stress direction, and will be discussed further in section 6.1.3.

Similarly to the preferentially oriented centres, the stress-splitting rates of the ZPL components of this centre are high (up to 14.2 meV GPa^{-1}), which is suggestive of the presence of vacancies in the defect. This provides an insight into the atomic constitution of the centre.

6.1.2.2 Identification of the vibronic band

Observations from a number of CVD diamond samples of the cathodoluminescence spectra of the region around the 467.2 nm ZPL reveals a weak band peaking at ~ 480 nm, in the highly structured region between 455 to 500 nm, which varies in intensity in a similar manner to the 467.2 nm ZPL (figure 6.1.2). This suggests a relationship between the two features. To investigate this further, the integrated intensities of the ZPL and band were measured in a number of samples (from both Element Six and the University of Paris XIII). To measure the intensities, an estimated luminescence background was subtracted; however, this was difficult to determine for the band, as the region is constructed of a number of overlapping vibronic bands of various defects (see section 4.3). Nevertheless, within estimated measuring error, the ratio of the band to ZPL intensity was approximately constant over a range of samples, confirming that the two features are related.

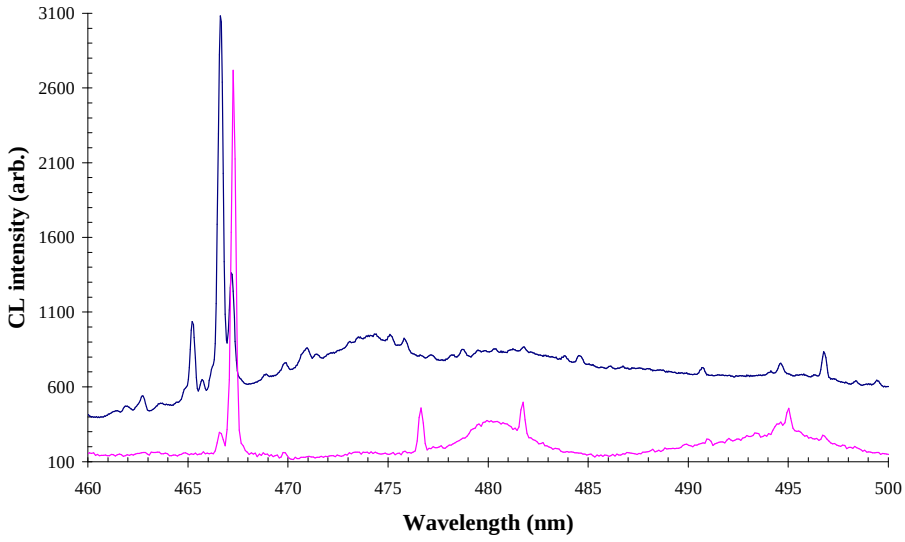

Figure 6.1.2 – Cathodoluminescence spectrum of two single-crystal CVD diamond samples, demonstrating the variation of the 467.2 nm ZPL intensity with that of the band centred at ~ 480 nm.

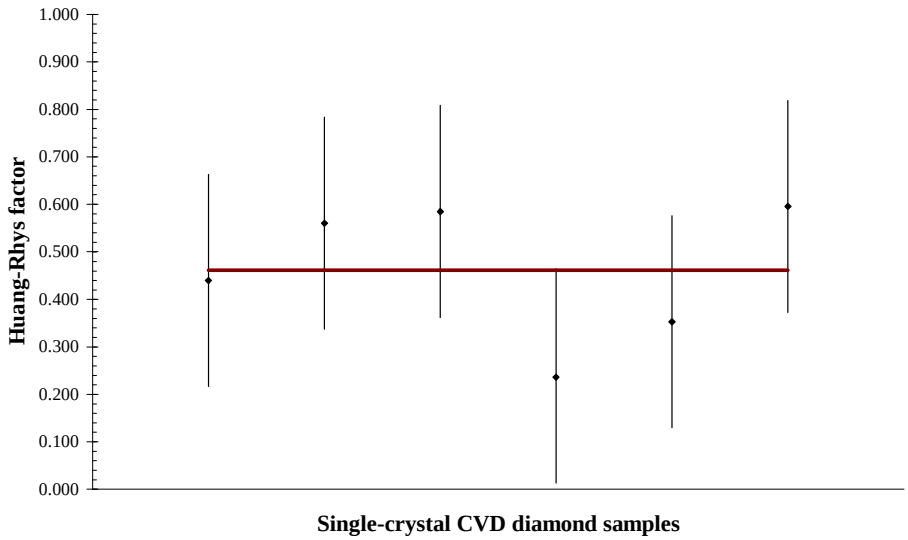

Figure 6.1.3 – Huang-Rhys factor of the 467.2 nm ZPL and band at ~ 480 nm, over a number of samples. Full line is the average of the values.

Figure 6.1.3 shows the natural logarithm of the ratio of the band to ZPL integrated intensity from a number samples. Within errors, this is approximately constant; the full line shows the average value, which when expressed in this form (natural logarithm) is the Huang-Rhys factor (S) of the defect centre responsible for the ZPL and band: $S = 0.46 \pm 0.23$. Assuming that this is the one-phonon band associated with the 467.2 nm ZPL, then at low temperature, and assuming single-mode coupling, it should be possible to describe it by a Gaussian function: figure 6.1.4 shows the fit of a Gaussian peak (full red line) centred at 480.7 nm (2.579 eV), with FWHM of 33.4 nm (18 meV). The background luminescence is likely to be very complex, but it has been assumed to be described by a quadratic function (dashed blue line). This gives the energy of the dominant phonon coupling at the centre as $\hbar\omega = 73.85 \pm 0.25$ meV. These values for the Huang-Rhys factor and phonon coupling energy for this centre are consistent with the temperature dependent energy shift of the ZPL (next section).

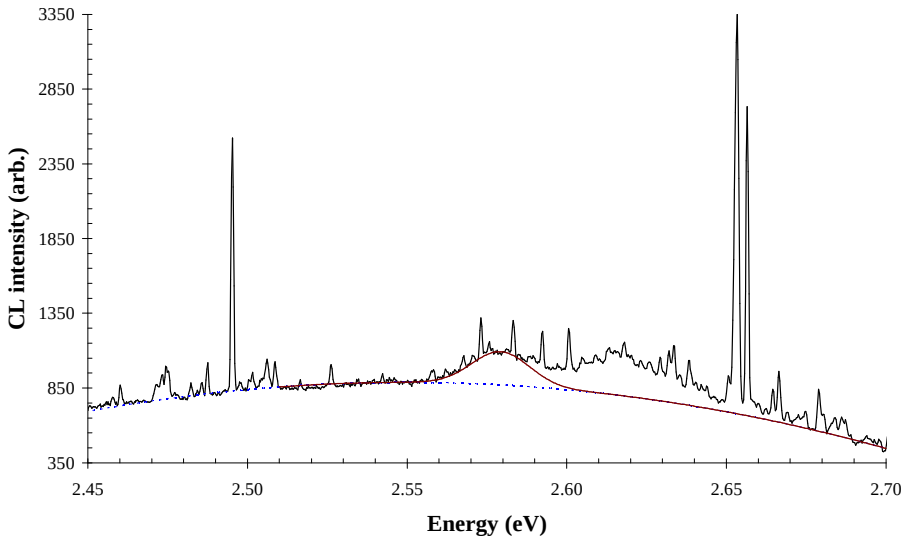

Figure 6.1.4 – Cathodoluminescence spectrum of the 467.2 nm (2.653 eV) ZPL and associated band at 480.7 nm (2.579 eV). Dashed blue line is the assumed background luminescence function, full red line is a Gaussian fitted to the experimental spectrum, centred at 2.579 eV with a FWHM of 18 meV.

6.1.2.3 Temperature dependence

Further characterisation of the 467.2 nm ZPL has been made by measuring the change in energy of the ZPL with temperature. Measurements were taken between 77 K and 190 K, above which the ZPL becomes immeasurably weak. Changes in FWHM of the peak could not be measured accurately, as the peak appeared split due to internal strains; additionally, the intensity of the peak could not be reliably measured as the luminescence background under the ZPL was irregular.

Figure 6.1.5 shows the variation of peak energy with temperature. The black dashed line is the contribution to the shift from the expansion of the lattice (section 5.2.2); the symmetry of the 467.2 nm centre has been determined to be rhombic I (previous section), and so the contribution to the lattice expansion is calculated as equation 2.2.26 using the shift-rate parameters found from the uniaxial stress experiments.

Allowing for the shift of the ZPL due to lattice expansion, the change in peak energy with temperature can be described by equation 2.2.25; this expression requires the Huang-Rhys factor, S, and dominant phonon coupling energy, $\hbar\omega$, of the centre. These were determined in the previous section, S = 0.46 and $\hbar\omega$ = 73.85 meV. Using these values in equation 2.2.25 produces the full line through the data in figure 6.1.5. This good fit is consistent with the assignment of the values of S and $\hbar\omega$ for the defect centre with zero-phonon transition at 467.2 nm.

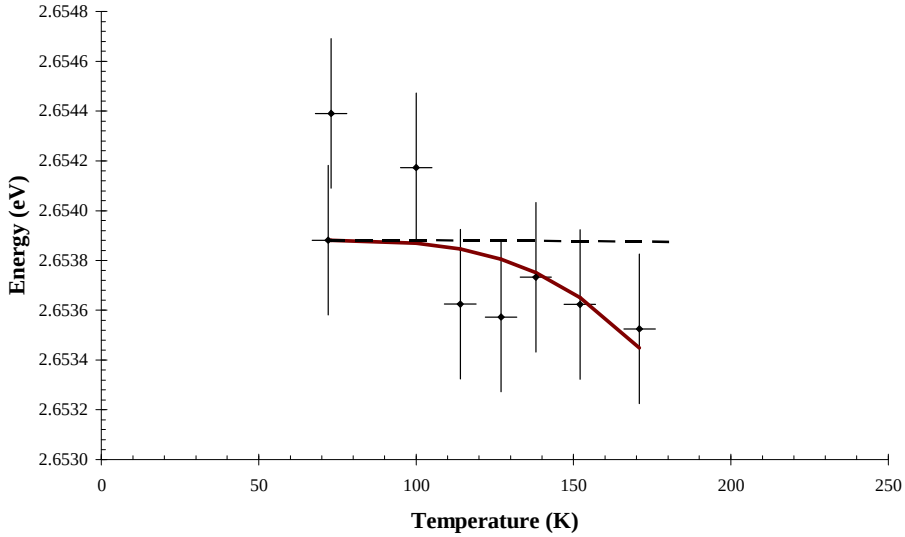

Figure 6.1.5 – Temperature dependence of the peak energy of the 467.2 nm (2.653 eV) ZPL in CVD diamond, recorded in cathodoluminescence. See text for details.

6.1.3 Discussion

The zero-phonon luminescence at 467.2 nm has been determined to originate from an electric dipole transition between A and B states at a defect centre with rhombic I symmetry. The high stress-induced splitting-rates of the ZPL in various orientations are suggestive of the incorporation of at least one vacancy within the centre. The defect centre exhibits single-mode phonon coupling to dominant phonons of energy 73.85 ± 0.25 meV. The Huang-Rhys factor of the centre is determined to be 0.46 ± 0.23. The presence of nitrogen in the centre by analysis of nitrogen-isotope doped samples is inconclusive.

The experimental data for the <110> orientation do not accurately correlate with theory for the lower shift-rate components. The reason for this is, at present, not known; however, as mentioned in section 6.1.2.1, the stress spectra for this orientation produced ten stress-split components – an unusually high number for a moderately high-symmetry defect. Considering the good fits to the theory for the <001> and <111> data, it is plausible that the <110> data were slightly erroneous due to experimental issues: it is known that inhomogeneous stress and misorientation of the crystal can produce misleading results [Davies (1975), Davies *et al* (1976)]. It is not suggested here that the sample was necessarily misoriented, as the <001> orientation measurements from the same sample were acceptable, as were <110> measurements of other defects in the same sample; but rather, that a misalignment during mounting of the sample could produce shear stresses within the sample. Repeat measurements of the orientation did not clarify the situation. However, this author believes that the symmetry assignment is appropriate for the data collected, given the good fit to the <001> and <111> data, and despite the slight difference in experimental and theoretical shift-rates.

The point group of a rhombic I symmetry defect is C_{2v}. This is the same as for the 466.6 nm centre, although in this case the defect is not preferentially oriented. The zero-phonon transition energies of the two defects are very close; the defects have similar symmetries, and comparable values of the stress parameters (see table 6.1.1). Measurements of the integrated intensities of the

ZPLs across different samples do not give a constant ratio, so it is assumed that the two are not transitions from a common centre. The similarities noted above, however, are suggestive of one of the centres being a perturbed form of the other.

	A_1	A_2	A_3
466.6 nm	-10.10	7.95	8.05
467.2 nm	-9.20	6.40	7.80

Table 6.1.1 – Comparison of the stress-parameters for the defects centres with ZPL at 466.6 and 467.2 nm. Stress-parameter values are in meV GPa^{-1}; errors have been omitted for clarity – see the appropriate sections for values.

This situation is comparable to that of the H3 and H4 centres in diamond (503.2 nm (2.463 eV), and 496.2 nm (2.498 eV), respectively). The H3 centre has been determined to be a $(N\text{-}V\text{-}N)^0$ complex with rhombic I symmetry, C_{2v}, with its rotation axis oriented along <001> and reflection plane in {110} [Davies *et al* (1976)], and is formed from an A centre and a vacancy. The H4 centre is considered to be a (3N-V-V-N) complex with monoclinic I symmetry, C_{1h}, with the reflection plane in {110} [Clark and Norris (1970), de Sa and Davies (1977)], and is formed from a B centre and a vacancy. van Wyk and Woods (1976) have determined that the optical (and ESR) properties of the H3 and H4 centres are essentially determined by the dangling bonds into the vacancies of the complexes; the optically-active electronic transitions being between $^1A_1$ and $^1B_1$ singlet states. The implication is that the slight changes in symmetries and transition energies are due to an atomic perturbation. Considering the similarities in symmetry and stress-parameters between the 467.2 and 466.6 nm centres, and the involvement of vacancies, the same may well be true of these defects.

It may be useful to repeat the stress-analysis on a number of further samples to confirm the uniaxial stress results concluded here. Additionally, annealing studies of the 467.2 and 466.6 nm centres may reveal additional information about any possible relationship between the two defects.

6.2 The 510.3 nm ZPL

6.2.1 Introduction

The 510.3 nm (2.429 eV) ZPL is observed in cathodoluminescence of the single-crystal CVD synthesised diamonds studied in this work; in both the Element Six and University of Paris XIII samples. The ZPL can be observed weakly in photoluminescence, with a 325 nm HeCd laser (section 4.3). It has not been observed in absorption measurements of these samples. The ZPL has not been reported previously. Whilst not explicitly reported as being present in Tallaire *et al* (2006), the CL spectra of the nitrogen doped samples do in fact show the line (as the CL data for the Tallaire *et al* work was recorded by this author); the line is not present in the non-nitrogen doped samples, possibly suggesting a nitrogen dependence. However, as is seen from the nitrogen-15 isotope studies of the other ZPLs in this work, which were also present in the nitrogen doped samples, and not in the undoped ones, nitrogen is not directly involved in the defect centres producing the ZPLs. Nitrogen-15 isotope measurements have not been made on the 510.3 nm ZPL as the cathodoluminescence was too weak to measure in the nitrogen-15 enriched samples. Along with this, CL of the ZPL was also too weak to study under uniaxial stress. Thus the symmetry of the centre remains unknown.

The optical spectra over a number of samples do not show any intensity correlation between the 510.3 nm centre and any of the other ZPLs or bands present in the visible region. Hence information on the vibronic coupling at the centre is limited to estimates from the temperature dependence of the ZPL. The first reported temperature dependence measurements of the 510.3 nm ZPL are presented in the next section.

6.2.2 Temperature dependence

The 510.3 nm (2.429 eV) ZPL has been characterised by measuring the effect of temperature upon the integrated intensity, peak energy and FWHM. Figure 6.2.1 shows the recorded data and the theoretical fits made to it. The ZPL becomes immeasurably weak above ~ 180 K.

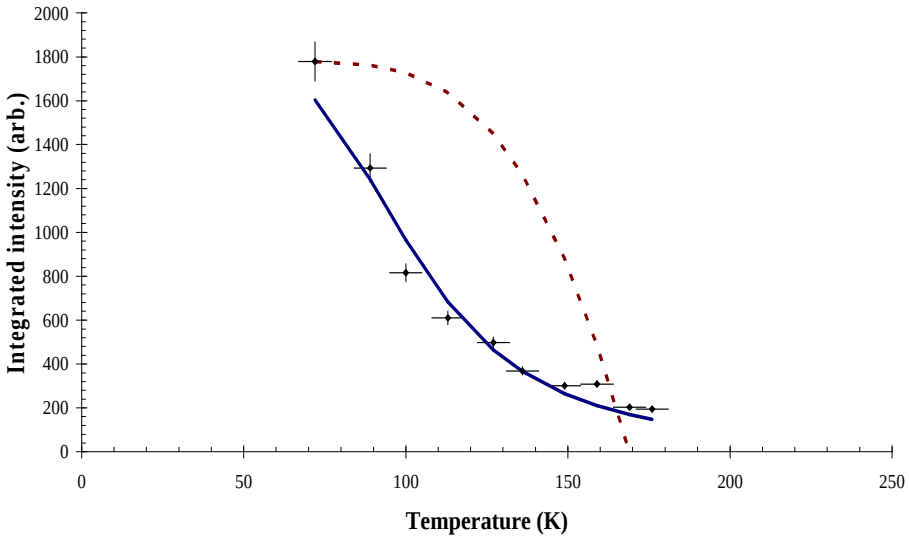

a)

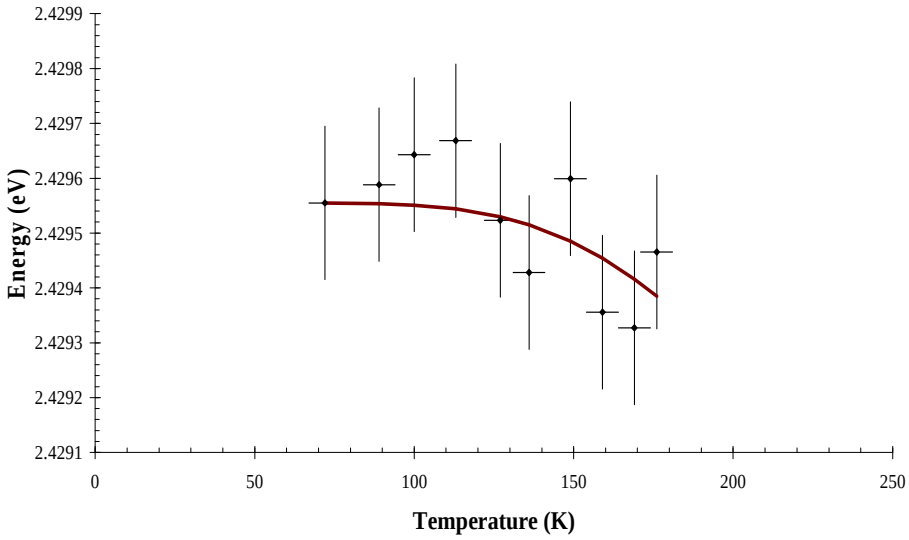

b)

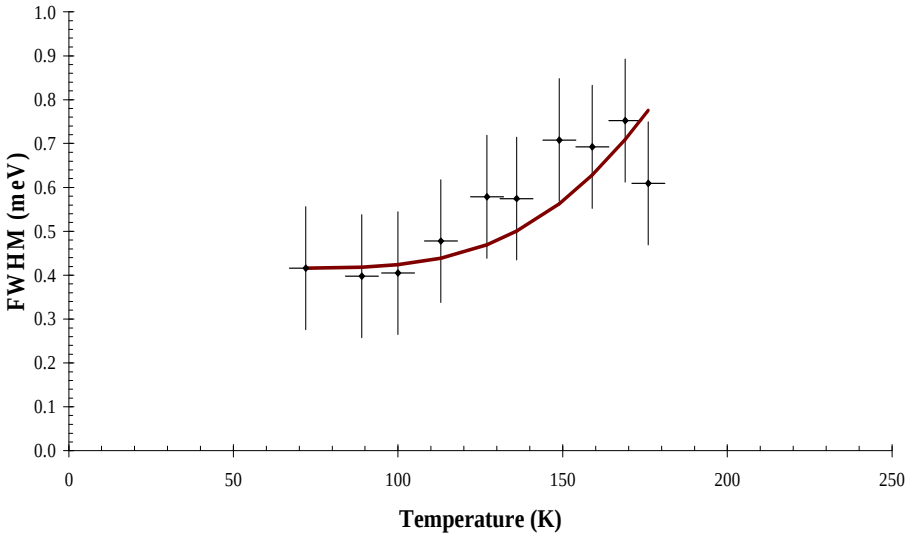

c)

Figure 6.2.1 – Temperature dependence measurements of the 510.3 nm (2.429 eV) ZPL in CVD diamond, recorded in cathodoluminescence. a) shows variation of integrated intensity of the peak with temperature, b) that for the peak energy, and c) that for the FWHM. Data points in all figures are the measured data. Lines through the data are the theoretical fits, see text for details.

The variation of the ZPL integrated intensity, peak energy and FWHM can generally be described using the expressions in section 2.2.2.2. These require the Huang-Rhys factor (S) of, and dominant phonon coupling energy, $\hbar\omega$, at the centre to be known. As with the preferentially oriented centres (section 5.2.2), the vibronic band of the 510.3 nm centre has not been observed in the optical spectra of the samples studied in this work, hence the information required for the theoretical fits is not available. As described in section 5.2.2, the dominant phonon coupling energy can be estimated from a least-squares fit to the peak energy shift with temperature data, using $\hbar\omega$ as the least-squares variable, over the allowed range of phonon energies in diamond (165 meV).

The response of the ZPL under hydrostatic pressure is not known, and cannot be derived from the uniaxial stress parameters, as the ZPL was too weak to measure under uniaxial stress. Hence the lattice expansion contribution cannot be incorporated into the shift of the ZPL. However, as the ZPL becomes immeasurably weak above 200 K, and assuming common values of the stress parameters for ZPLs in diamond (< 10 meV GPa^{-1}), the lattice expansion contribution can be expected to be minimal.

A least-squares fit to the peak energy variation with temperature data, using equation 2.2.24 was performed; the fit is shown as the full line in figure 6.2.1b. This gives $\hbar\omega$ = 73.97 ± 0.30 meV. This value is then used in equation 2.2.29 to describe the variation of the FWHM with temperature; the fit is shown as the full line in figure 6.2.1c. The good fit (within errors) supports the estimated dominant phonon coupling energy at the 510.3 nm centre calculated from the peak energy shift data.

The change in integrated intensity of the ZPL with temperature is shown in figure 6.2.1a. A fit to this data using the estimated $\hbar\omega$ value in equation 2.2.22 produces the dashed (red) line in figure 6.2.1a; this poor fit is not a result of the $\hbar\omega$ value being incorrectly estimated, as it was shown for the 496.8 nm centre (section 5.2.2) that an estimated $\hbar\omega$ value can produce a very successful fit to the temperature dependence of the ZPL intensity. Instead, the same approach as used for the 466.6 nm centre (section 5.2.2) will be used: the temperature dependence measurements were made in cathodoluminescence rather than absorption, and hence an alternative analysis can be performed [Khong and Collins (1993)]. This method assumes that the capture of excitons at defects, and the thermally-induced detrapping, is a competitive process. Equation 5.2.5 has been applied in a least-squares fit to the ZPL integrated intensity data, using E, the activation energy of the 510.3 nm centre, and the parameter g, as least-squares variables. The result of this fit is shown as the full (blue) line through the data in figure 6.2.1a. This fit is parameterised by E = 34.44 ± 0.01 meV and g = 0.046 ± 0.001. The activation energy is similar to the expected activation energy values found by Khong and Collins, however, the value of g is four orders of magnitude lower than anticipated. As with the temperature dependencies of the preferentially oriented centres, it appears that an additional mechanism of luminescence quenching is taking place at the 510.3 nm centre.

6.3 The 532.7 nm ZPL

6.3.1 Introduction

The 532.7 nm (2.327 eV) ZPL frequently appears in PL and CL spectra of polycrystalline and single-crystal CVD synthesised diamonds [Vavilov *et al* (1980), Collins *et al* (1989), Robins *et al* (1989), Kawarada *et al* (1990), Khong and Collins (1993), Kanda *et al* (2003a)], and low nitrogen content HPHT synthesised diamonds. No absorption has been detected. It is not yet reported to have been observed in untreated natural diamonds.

The defect centre which produces the 532.7 nm transition has not yet been fully identified. The centre was determined to contain nitrogen by Vavilov et al (1980), where in that work almost identical luminescence spectra showing the 532.7 and 575 nm (the neutral nitrogen-vacancy) lines were produced both by samples grown with nitrogen, and natural type IIa samples implanted with nitrogen. The authors suggested that the 532.7 nm centre might also involve one or more vacancies in order to explain the broadening of the line in thick (~ 30 μm) polycrystalline samples with large internal stresses (~ 1.4 GPa).

Further investigation has identified a number of characteristics of the centre: whilst the 532.7 nm transition is frequently observed with the 575 nm line, Kanda *et al* (2003a) suggested it has a different symmetry than that of the 575 nm centre after investigations into grain-boundary stress-splitting of luminescence lines in polycrystalline samples; the 532.7 nm line persists up to at least 1800^{o}C and 6 GPa (in polycrystalline samples at least) (Kanda *et al* (2003a) again); Kanda *et al* (2003b) found that the centre producing the 532.7 nm line is probably formed in the {100} growth layer; Khong and Collins (1993) measured the temperature dependence of the 533 nm line and found that it follows the same form as that for the “band-A” emission.

Two major questions regarding the nature of the 532.7 nm centre have been raised in the literature. The first is whether the centre is boron related; the

second is whether the ZPL is composed of two superimposed peaks. The boron related query will be discussed first.

The boron related nature of the centre was first suggested by Ruan *et al* (1992) after CVD samples grown with added boron in incremental concentrations were characterised by cathodoluminescence. It was observed that as the boron concentration increased, the "band-A" emission at 2.83 eV decreased in intensity, whilst a band at 2.32 eV appeared with increasing intensity, with the 532.7 nm line on top of this band (which also increased in intensity). The results of Ruan *et al* (1992) were supported by Gheeraert *et al* (1994), in so much as the decrease in intensity of the "band-A" (at 2.9 eV here) was accompanied by an increase in intensity of a band appearing at 2.4 eV, as the boron concentration increases. Correspondingly the 532.7 nm line increases in intensity as the 2.4 eV band intensity increases.

According to Kawarada *et al* (1990), boron impurities in diamond do indeed produce a luminescence band centred in the range 2.3 – 2.4 eV, with a corresponding decrease in intensity of the "band-A" emission. However, the authors of that work make no mention of the 532.7 nm line being present in any of their un-doped or boron doped samples. This present work has not investigated the possible boron-related nature of the 532.7 nm centre, and it will not be discussed further.

It has been reported a number of times that the 532.7 nm luminescence line occurs as a doublet [Collins *et al* (1989), Ruan *et al* (1991b), Burton *et al* (1995), Zaitsev (2001)]. Zaitsev lists the centre as consisting of two peaks at 530.8 and 533.8 nm. The doublet form was observed by Ruan *et al* (1991b) in polycrystalline samples, where the singlet form is explained as an observed single broad line, which is in fact due to the superposition of the two separate lines. This was suggested after annealing studies, where before annealing, two peaks were observed at 532.1 and 534.4 nm, and once annealed to 1350^{o}C, one broad peak is seen at 532.57 nm.

Kanda *et al* (2003a) suggested that the apparent doublet form could be due to two different defects, as mapped cathodoluminescence spectra (of single-crystal samples) produce different spatial distributions and peak widths depending on orientation: for {111}, the line is more intense, has a greater width,

and is present with the “band-A”; for {100}, there is no “band-A”, and the line is accompanied by its own broad band.

The final piece of evidence for two independent luminescence sources around 532.7 nm comes from the results of Khong *et al* (1994), who although did not directly observe a doublet form of the 532.7 nm line, found two luminescence decay times: the sharp 532.7 nm peak has a decay time of 9.6 ± 0.8 ns, while a broad band underlying the sharp peak has 1.0 ± 0.1 μs. It is also mentioned that the decay time of the broad band has a similar decay rate to a line at 2.48 eV (500 nm).

Whilst the doublet nature of the ZPL has been under discussion, a pertinent comment may be made: an observed doublet in a diamond luminescence spectrum could be due to (primarily) one of two causes, first, internal strains on a susceptible defect centre (such as a vacancy-related centre) can potentially cause a splitting of orientationally degenerate energy levels resulting in broadened or doublet lines; alternatively two independent defect centres with very similar transition energies can produce overlapping peaks. Isotopes can also result in multiple transitions being observed from a single defect centre, although this is unlikely for this centre, considering the magnitude of the splitting, the ratio of the peak intensities, and knowledge of the isotopes of common impurity centres in diamond (primarily nitrogen, boron and silicon).

It is established in this work that the single-crystal diamonds studied in this work can show the 532.7 nm ZPL with negligible splitting in one region of the sample, and with considerable splitting in another (particularly in dislocated areas, where three convoluted peaks can be seen). See sections 4.3 and 2.1.3 for example spectra. This unambiguously determines that the ZPL is not a doublet.

Uniaxial stress-analysis (in the following section) indicates that the 532.7 nm centre involves at least one vacancy, which explains the strain-induced splitting of the peak in dislocated regions of the samples. Indeed, the early CVD diamond material was polycrystalline in nature, which has been established to be readily susceptible to strain effects (see section 4.1). The observation of Ruan *et al* (1991b) that the ZPL becomes less split after annealing may be understood by considering that annealing removes sources of strain in the lattice, such as point defects (via migration, combination, dissociation etc). Less strain on the defect

would hence improve the bi-Lorentzian (if not Gaussian) nature of the ZPL (see section 2.2.2.1).

6.3.2 Results

6.3.2.1 Uniaxial stress measurements

The defect which produces the 532.7 nm (2.327 eV) ZPL has been investigated using cathodoluminescence whilst the diamond sample is under uniaxial stress. Two untreated, single-crystal CVD diamond samples – the same two as used for the previous defects investigated under uniaxial stress – were cut and polished into cuboids, such that the faces corresponded to the crystallographic lattice directions [001], [110] and $[1\,\bar{1}\,0]$ (for the first sample), and [111], $[1\,\bar{1}\,0]$ and $[11\,\bar{2}]$ (for the second sample). Cathodoluminescence was generated using a 40 keV electron beam, run at ~ 10 μA. The samples were held at liquid nitrogen temperature. The other experimental details were as discussed in section 5.2.1.

Cathodoluminescence of the 532.7 nm ZPL whilst under uniaxial stress showed that it splits and shifts in all three compression directions (figure 6.3.1). In the [001] stress direction, the ZPL split into three components: two when the luminescence was perpendicular to the stress direction and one when parallel; these resolved to two overall components. In [111], it split into a total of five over both luminescence polarisations; these resolved to three. Under <110> compression the splitting was very complex, showing a total of 11 components in the various stress and polarisation orientations. It is estimated that these resolve to four stress-split components.

Comparing these components to the theoretical combinations in the standard symmetry tables [Mohammed et al (1982), Kaplyanskii (1964a, b)] suggests that the symmetry is monoclinic I. The perturbation to the zero-phonon energy and the theoretical shift-rates of the components of a monoclinic I symmetry centre are given in section 5.2.1. A least-squares fit of the theoretical shift-rates to the experimental data gives the values of the stress-parameters as A_1 = 7.64 ± 0.30 meV GPa^{-1}, A_2 = -4.30 ± 0.30 meV GPa^{-1}, A_3 = 1.51 ± 0.30 meV GPa^{-1}, and A_4 = 1.03 ± 0.30 meV GPa^{-1}. Putting these values into the theoretical stress-splitting rate equations in table 5.2.4 of section 5.2.1 yields the theoretical

change in energy with stress of the components, shown as the (red) lines in figure 6.3.1.

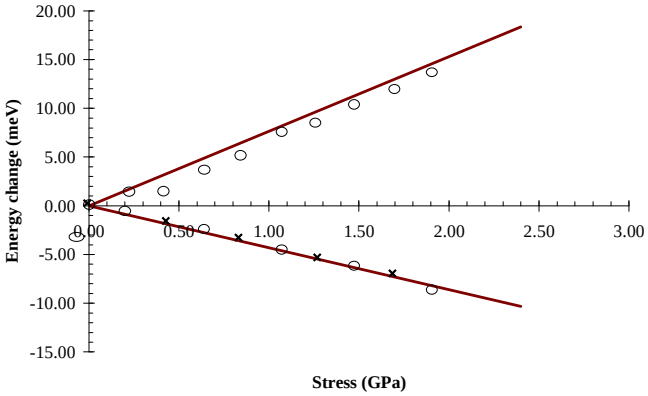

a)

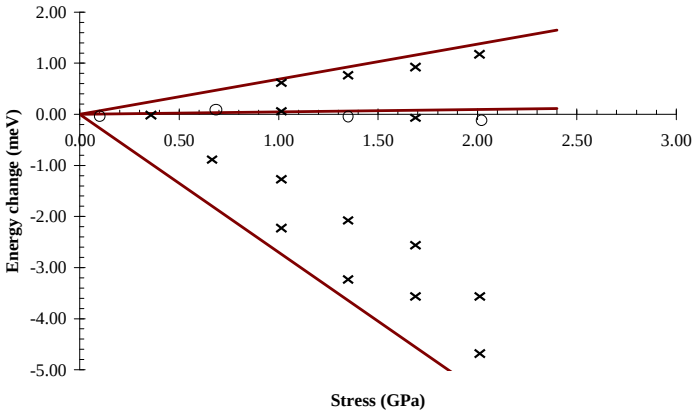

b)

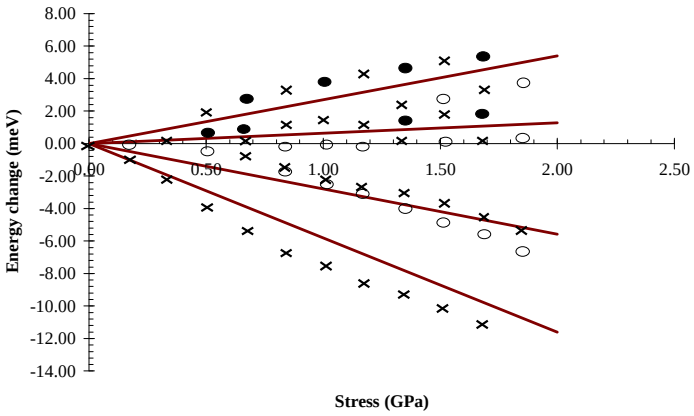

c)

Figure 6.3.1 – Uniaxial stress splitting data for the 532.7 nm (2.327 eV) centre in cathodoluminescence, showing change in energy of ZPL components as a function of applied stress. Data points are experimental results, lines are calculated from the fit to a rhombic I symmetry. a) ZPL under <001> compression (**S**); crosses are for electric vector of luminescence **E** ∥ **S**; unfilled circles are for **E** ⊥ **S**. b) ZPL under <111> compression; crosses are for **E** ∥ **S**; unfilled circles are for **E** ⊥ **S**. c) ZPL under [110] compression; crosses are for **E** ∥ **S** when viewing along; unfilled circles are for **E** ⊥ **S** when viewing along [001], filled circles for **E** ⊥ **S** when viewing along [1 $\bar{1}$ 0]. Stick diagrams show relative intensities of stress-split ZPL components at maximum recorded stress, with vertical lines above the horizontal line representing **E** ∥ **S**, and vertical lines below representing **E** ⊥ **S**.

The fit of the theoretical splitting-rates to the data is reasonable, which initially supports the assignment of a monoclinic I symmetry to the defect. However, the relative intensities of the components do not all match the theoretically predicted intensities: for components under <001> and <110> the agreement is reasonable, but for <111> there is predicted to be only one component in the parallel polarisation and three in the perpendicular – the data shows the inverse of this, with the relative intensity of the perpendicular component being ~ 21 : 1 relative to the weakest parallel component. The reason for this is discrepancy is unknown, despite checks of the validity of the data. This casts doubt on the quantitatively correct assignment of the symmetry, although, qualitatively the splitting pattern of the ZPL appears to fit that of a monoclinic I symmetry centre.

Alternatively, it is possible to fit a rhombic I symmetry splitting pattern to the data, although this is also a flawed fit as the experimental relative transition intensities do not correlate with the theoretical values. This centre proved a

particularly difficult ZPL to investigate using uniaxial stress as the observed line at zero stress split into numerous superimposed components when under [110] stress. This contrasts with the relatively simple splitting patterns observed under [001] and [111] stresses. It would be appropriate to repeat the measurements on a large selection of different samples in order to hopefully observe a reproducible set of splitting patterns.

Finally, as with the previous ZPLs studied under uniaxial stress in this work, the high stress-splitting rates (~ 7.6 meV GPa^{-1} at most) of this centre suggest the involvement of at least one vacancy in the defect.

6.3.2.2 Identification of the vibronic band

Cathodoluminescence spectra of the region around the 532.7 nm ZPL frequently show a weak (relative to the 532.7 nm ZPL) broad band centred at ~ 549 nm, with FWHM of ~ 10.1 ± 0.4 nm (44.5 ± 1.5 meV). The band peaks at 548.85 ± 0.07 nm, which places it at 68.26 ± 0.20 meV below the 532.7 nm (2.327 eV) ZPL. Figure 6.3.2 shows a typical CL spectrum of the region, and a spectrum of the ZPL and band only.

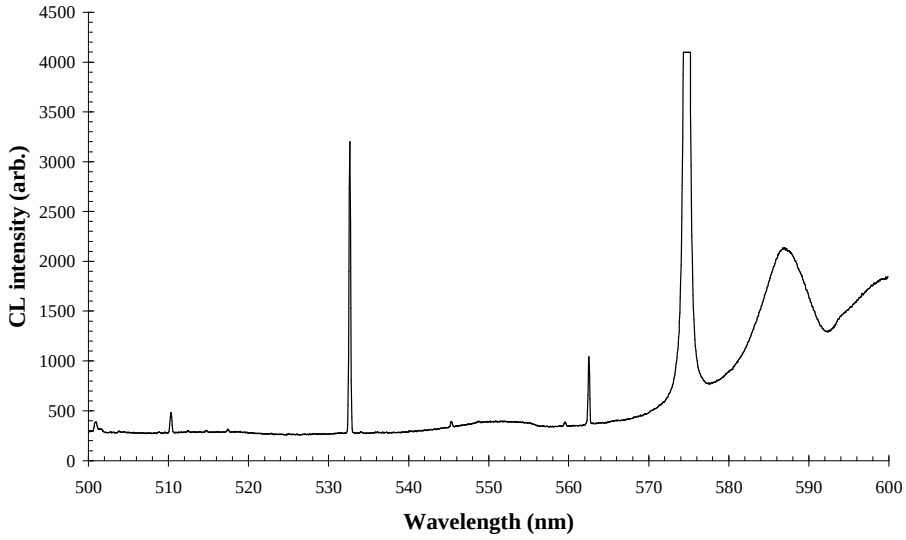

a)

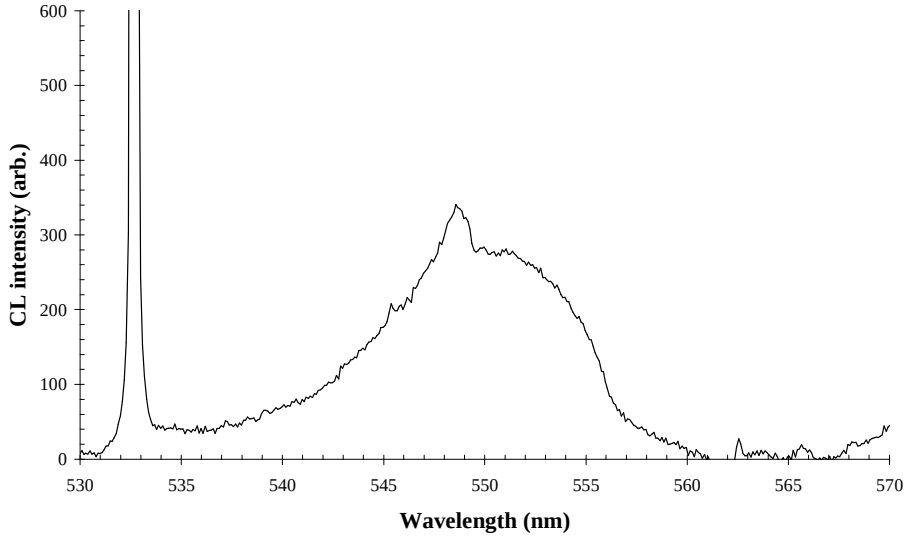

b)

Figure 6.3.2 – Typical cathodoluminescence spectrum of a single-crystal CVD diamond, showing the 532.7 nm ZPL and the weak band at ~ 549 nm; a) broad scan of the local region, b) the ZPL and band, corrected for background luminescence.

The presence of the band at lower energy than the 532.7 nm ZPL, along with the observation over a number of samples of the intensity of the band varying in a similar manner to the ZPL, suggests that it could be the one-phonon band of the 532.7 nm ZPL. To investigate this, the intensity of the band, and the integrated intensity of the ZPL were measured over a number of samples, from both Element Six and the University of Paris XIII: the intensity ratio of the band to the ZPL was found to be approximately constant, within experimental uncertainty (figure 6.3.3). This, at the least, confirms that the band at ~ 549 nm is related to the 532.7 nm ZPL.

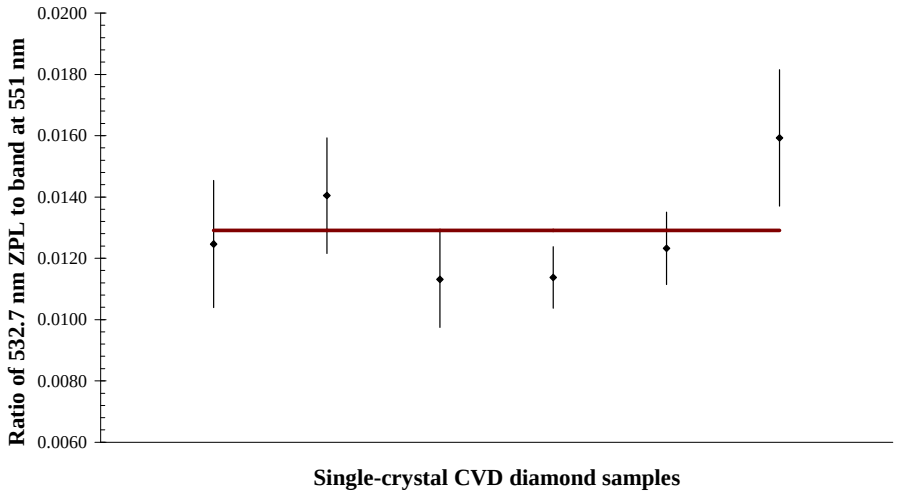

Figure 6.3.3 – Intensity ratio of the band at ~ 549 nm to the 532.7 nm ZPL, measured over six samples. Data points are recorded data, full line is the average ratio.

Assuming single-mode phonon coupling at the centre, if this is the one-phonon band, then the energy of the dominant phonon coupling to the defect is the energy separation of the peak of the one-phonon band and the ZPL, which was defined above: 68.26 ± 0.20 meV (this value is statistically averaged over a number of samples). Further characterisation of the centre is to determine the Huang-Rhys factor, which is defined as the natural logarithm of the ratio of the integrated intensities of the vibronic band to ZPL (section 2.2.1). The intensities were measured by subtracting an estimated quadratic-form background luminescence from the data; however in many samples, the background was difficult to estimate accurately. Additionally, the strict definition of the Huang-Rhys factor requires that the integrated intensity of the vibronic band be measured over the *entire* phonon range in diamond (up to 165 meV); due to other luminescence features being present within 165 meV of the 532.7 nm ZPL (including the 575 nm ZPL), and the varying luminescence background, the intensity was measured on the one-phonon band only. It should be noted here that it is the intensity of the maxima of the band which is used, rather than the integrated intensity, due to the difficulty in estimating the background luminescence. Consequently the defect centre producing the 532.7 nm ZPL has an estimated Huang-Rhys factor of ~ 0.76 ± 0.30.

Inspection of the optical spectra (figure 6.3.2b) shows that the band at ~ 550 nm is asymmetric, possesses moderate structure and cannot be described by a Gaussian peak like many one-phonon bands in diamond can. The narrow feature on top of the band is most likely a genuine feature of the band, rather than another weak feature unrelated to the centre; this is suggested because it is still present when the only features in the CL spectra are the 532.7 nm and 575 nm centres.

The band shape has not been investigated further in this work. Temperature dependence measurements of the 532.7 nm ZPL, detailed in the next section, support the calculated phonon coupling energy and the suggestion that this is the one-phonon band.

6.3.2.3 Temperature and nitrogen isotope dependence

Along with the determination of the symmetry of the defect producing the 532.7 nm ZPL, and the identification of the vibronic band, further characterisation can be made by measuring the temperature dependence of the ZPL. The variations of peak energy, FWHM and integrated intensity of a ZPL can be expressed by the equations in section 2.2.2.2. Along with information required to calculate the peak energy shift with temperature, the expressions of section 2.2.2.2 require knowledge of the Huang-Rhys factor (S) and dominant phonon coupling energy, $\hbar\omega$, at the centre; these were determined in the previous section with identification of the one-phonon band. Measurements of the temperature dependence of the ZPL will provide additional confirmation of the values of S and $\hbar\omega$.

Figure 6.3.4 shows the temperature dependencies measured for the 532.7 nm ZPL. The data for the variation of the FWHM with temperature are not presented, as the ZPL (as is often found (section 4.3)), appeared slightly split at most temperatures; hence FWHM data would be unreliable.

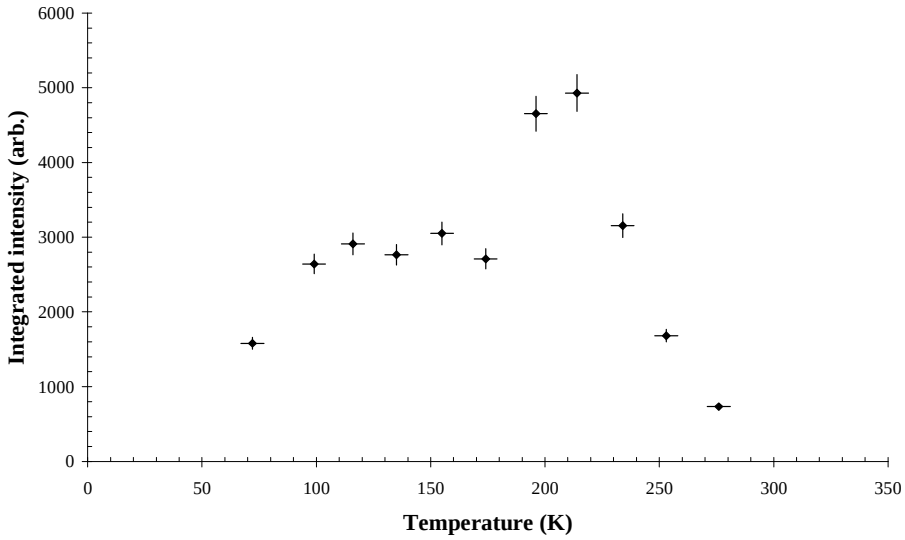

a)

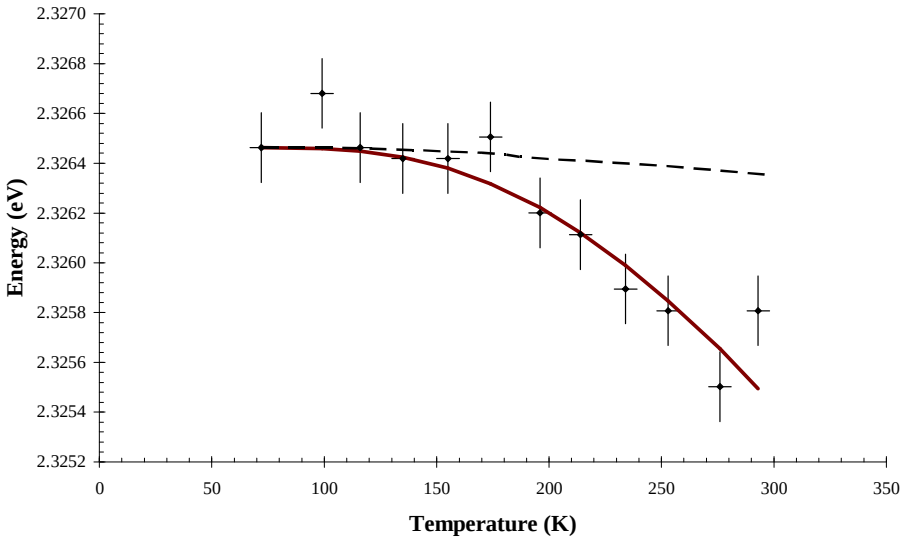

b)

Figure 6.3.4 – Temperature dependence measurements of the 532.7 nm (2.327 eV) ZPL in CVD diamond, recorded in cathodoluminescence. a) shows variation of integrated intensity of the peak with temperature, and b) that for the peak energy. Line through the peak energy data is the theoretical fit, see text for details.

The black dashed line in figure 6.3.4b is the calculated contribution to the shift due to lattice expansion. It is calculated in the same way as that for the 562.5 nm ZPL (section 5.2.2). Allowing for this, the shift in peak energy of the ZPL with increasing temperature is defined by equation 2.2.25. Using this, with the values determined in the previous section, S = 0.76 and $\hbar\omega$ = 68.26 meV, produces the full line through the data points in figure 6.3.4b. This is in good agreement with the experimental data, and supports the measured value for the Huang-Rhys factor and phonon coupling energy. It is noted here, however, that the measured Huang-Rhys factor has a large uncertainty, as discussed in the previous section, and as such should be stated as S = 0.76 ± 0.30.

The temperature variation of the integrated intensity of the ZPL (figure 6.3.4a) is similar to that of the 562.5 nm centre, in that it initially increases with increasing temperature, and then rapidly decreases at higher temperatures. The temperature dependence of the 532.7 nm ZPL has been studied previously by Khong and Collins (1993) in cathodoluminescence. The qualitative form of the intensity of the ZPL varying with temperature is the same as the previous measurements, and so has not been investigated further.

Vavilov *et al* (1980) suggested that the 532.7 nm centre is nitrogen related. To investigate this, two high-quality single crystal CVD diamonds, one grown with normal gas constituents, the other grown in a nitrogen-15 enriched atmosphere, have been studied using cathodoluminescence. If the 532.7 nm centre directly involves nitrogen, then a shift in energy of the ZPL should be observed, as described in section 2.2.2.3.

Cathodoluminescence of the two samples was measured by slowly scanning over the 532.7 nm ZPL and the 534.109 nm line from a neon calibration lamp, at high resolution and with narrow monochromator slits (set-up as described in section 3.4). As the shift in energy of a ZPL due to isotopic changes is expected to be small (~ $|0.1|$ meV (section 2.2.2.3)), the experiment was repeated four times using each sample, in order to minimise the error in the measurements. It was found that the 532.7 nm ZPL shifts by 0.20 ± 0.05 meV to higher energy in the nitrogen-15 enriched sample. This confirms that the centre directly involves at least one nitrogen atom.

6.3.3 Discussion

The 532.7 nm (2.327 eV) ZPL qualitatively demonstrates the stress-splitting pattern of the zero-phonon transition associated with a monoclinic I symmetry defect centre. The centre shows single-phonon coupling to dominant phonons of energy 68.26 ± 0.20 meV, with a Huang-Rhys factor of ~ 0.76 ± 0.30, determined from temperature dependence and spectral measurements. The centre has been shown to directly involve nitrogen due to a measured isotope-induced shift in the energy of the ZPL. Additionally, the uniaxial stress data suggest the involvement of at least one vacancy within the centre.

Debate in the literature (section 6.3.1) about the doublet nature of the ZPL has been resolved by observations of a single, unsplit ZPL in high quality single-crystal CVD diamond samples; it can be concluded that the 532.7 nm ZPL is an isolated electronic transition from a single point defect. Previous worker's observations of splitting are probably due to strains on the defect in dislocated or polycrystalline samples.

It would be useful to further investigate the uniaxial stress-splitting of the ZPL in an attempt to quantitatively assign a symmetry to the centre.

6.4 The 736.8 nm ZPL – the silicon-vacancy

6.4.1 Introduction

The 736.8 nm (1.682 eV) centre has been well investigated. It has been established to directly involve silicon and a vacancy, although the precise atomic configuration has not yet been experimentally verified. The ZPL consists of a doublet centred at 736.80 ± 0.05 nm at liquid nitrogen temperature [Collins *et al* (1994)]; at liquid helium temperature it appears as a set of twelve lines [Clark *et al* (1995)], with the most intense pair centred at 737 ± 0.05 nm (1.6822 ± 0.0003 eV). The peak separation is 3.96 ± 0.05 nm (0.9 ± 0.3 meV) at liquid nitrogen temperature. It is observed in absorption, photoluminescence and cathodoluminescence spectra of synthetic diamonds grown by CVD (microwave and hot filament methods), and HPHT synthesis [Sternschulte *et al* (1994), Sittas *et al* (1996), Lin *et al* (1996), Sharda *et al* (1998a)]. The only way it is observed in natural diamonds is after a sample has been implanted with silicon ions. It was once thought to have been observed in some natural type I diamonds [Solin (1972)], but the luminescence in that work is probably due to the GR1 defect (neutral vacancy, 741.1 nm (1.673 eV)).

The centre was first reported by Vavilov *et al* (1980), who observed a single luminescence line at 736 nm (1.684 eV) in diamond crystals grown by CVD under low pressures and temperatures. They conducted a study of silicon-ion implanted natural diamonds and found that a luminescence line appeared at 736 nm. They attributed this to a defect containing two interstitial silicon atoms. They calculated that the internal stresses of their diamond films were ~ 1.4 GPa, and as such observed a broadening of the 575 and 533 nm lines, attributed to the presence of vacancies. This led to the suggestion that the 736 nm centre does not involve a vacancy as the observed line was not significantly broadened. Additional work showed that the 736 nm centre persists up to at least 1400^{o}C annealing.

Ruan *et al* (1991a) suggested that the 737 nm centre is due to silicon, and is incorporated into the synthetic diamond primarily through the use of silicon substrates. This was concluded from inspection of the intensity of the single 737 nm luminescence line of diamonds grown on silicon substrates, and those grown on tungsten ones. The tungsten substrate-grown diamonds showed 737 nm luminescence more than an order of magnitude weaker than that of the silicon substrate-grown samples. Their work implies that the weakly present 737 nm centre in the tungsten substrate-grown diamonds is due to silicon incorporation from the quartz windows of the reactor.

Vlasov and Ralchenko (2004) presented evidence to support the suggestion by Ruan *et al* (1991a) that a silicon substrate was the primary source of the silicon related impurity, although they also noted that a homoepitaxial sample grown by the hot-filament method also produced the 737 nm luminescence – this was attributed to contamination by silicon from the filament. Additionally, the authors conducted an integrated-peak intensity vs. sample depth study of the single 737 nm line, and found that the silicon impurity concentration was greatest closest to the (silicon) substrate, and decreases smoothly over a depth of ~ 60 µm.

Initially there was speculation that the single 737 nm ZPL may be due to one of the zero-phonon components of the GR1 defect, because under stress the GR1 luminescence line shifts to higher energy – close to 1.682 eV, i.e. internal crystal stress could induce the shift. Collins, Kamo and Sato (1990) showed by comparative spectra of the vibronic bands of the two defects that their origins are separate, even though their ZPLs are at similar energies. Additionally, Ruan *et al* (1991a) noted that the 737 nm centre must be due to an independent defect for the following reasons: the GR1 centre anneals out at 800^{o}C [Collins (1978a)], whereas the 737 nm luminescence line persists up to at least 1350^{o}C; the linewidths of the single 737 nm luminescence line were from 4 to 10 meV depending on the sample, whereas the stress shifted component of the GR1 centre would have been much wider due to inhomogeneous splitting.

Collins, Kamo and Sato (1990) implanted ^{29}Si ions into synthetic and natural diamonds of varying nitrogen concentration. The samples with the highest single-substitutional nitrogen concentration showed the most intense 737 nm luminescence, whilst the ones with the lowest nitrogen concentrations

produced the weakest 737 nm luminescence. This implies that silicon is certainly involved in the defect, with nitrogen playing a direct or indirect part in the luminescence of the defect when the sample is excited under cathodoluminescence.

Annealing studies of as-grown and electron irradiated CVD diamond films suggested that the 737 nm centre is due to silicon and a vacancy: Clark and Dickerson (1991) observed a significant increase in the integrated luminescence intensity of the 737 nm peak after annealing at 700^{o}C, followed by a decrease in intensity after annealing at 900^{o}C; because the vacancy is mobile at 700^{o}C in diamond, this implies that the centre involves one or more vacancies. The authors explain the decrease in intensity at 900^{o}C by suggesting that self-interstitials are released at this temperature. Photoluminescence of a diamond film implanted with ^{28}Si ions, which previously showed no 737 nm emission, displayed a 737 nm peak after implantation – suggesting the presence of silicon in the centre. The authors made a significant suggestion about the nature of the defect centre: a single-substitutional silicon atom in the lattice would not be expected to produce electronic transitions within the forbidden energy gap; but the presence of a vacancy on a neighbouring lattice site would produce emission and absorption at an energy close to that of the neutral vacancy (GR1, 1.673 eV). Additionally, an annealing study in this paper showed a correlation between integrated intensities of the 1.682 eV (737 nm) luminescence line and three nearby lines, 1.618 eV, 1.558 eV, and 1.527 eV. A further line which was always present at 1.639 eV did not correlate with the 1.68 eV.

An important development of the understanding of this centre was made by Collins *et al* (1994), who repeated the annealing measurements of Clark and Dickerson (1991) in absorption; their results agreed with Clark and Dickerson's with the indication that the 737 nm centre involved a vacancy. Collins *et al* (1994)'s measurement of the ZPL in large-grain polycrystalline CVD samples showed it to be a doublet for the first time. Low temperature measurements at 1.7 K in the same work suggested the doublet structure arose from a split excited state.

The symmetry of the 737 nm centre has yet to be determined, although some uniaxial stress work has been undertaken [Sternschulte *et al* (1994)] on the (100) orientation of CVD diamond films showing 737 nm luminescence. Their

work did not conclude a symmetry due to the physical dimensions of the films limiting them to only the (100) axis to apply stress along. Nevertheless, this did produce a number of important results about the centre: the electronic transitions of the defect appear to originate from both a doubly degenerate ground and excited state – which partly explains the many (four major) zero-phonon lines often observed by many separate authors in luminescence spectra of unstressed samples; the defect is apparently (in their samples at least) under intrinsic internal stress, due to the large atomic radius of the silicon atom(s) involved. This conclusion was drawn from the stress splitting data which gives a zero stress splitting location of all the ZPL peaks at a stress of ~ -0.06 GPa. The authors suggested the aforementioned internal overpressure to explain this (assuming that the uniaxial stress adds linearly to the internal stress).

In a paper extending their previous work, Sternschulte *et al* (1995) performed Zeeman measurements on the 737 nm centre. Their work was quantitatively inconclusive, although the relative simplicity of the splitting data for the (magnetic field parallel to the) (111) orientation suggests a preferential (100) oriented symmetry axis of the defect, e.g. a tetragonal or lower symmetry.

Clark *et al* (1995) investigated HPHT synthesised diamond in photoluminescence and absorption at liquid helium temperatures and found that each component of the 737 nm doublet resolved into two, which led to a proposed four level transition scheme of doubly degenerate ground and excited states. Furthermore, fine structure was resolved along with the four main components, the ratio of intensities of which correlated with the ratio of naturally abundant silicon isotopes. This unambiguously demonstrated the presence of one silicon atom in the centre.

A number of atomic models of the defect which produces the 737 nm doublet have been suggested. The leading one is that of Goss *et al* (1996), who used cluster model *ab initio* calculations of a diamond cell with a silicon-vacancy defect present: they found that the defect relaxes to an atomic arrangement of the silicon between a split vacancy, with a trigonal (D_{3d}) symmetry, possibly in a negative charge state. They also found that the defect has two doubly degenerate states, which is in agreement with the doubly degenerate ground and excited states from the work of Clark *et al* (1995) and Sternschulte *et al* (1994). Moliver

(2003) modelled the silicon vacancy using another simulation method, and also concluded a D_{3d} point group for the defect.

An alternative model is that proposed by Gorokhovsky *et al* (1995): a quasi-molecular Si_2 cluster oriented along the (111) axis. This is based upon their observation of a luminescence peak at 767 nm, which has a vibrational energy of 515 cm^{-1}, leading to comparisons between the transverse-optical mode in crystalline silicon (522 cm^{-1}), Si-Si bond in amorphous SiC (508 cm^{-1}), and the vibration of the free cluster Si_2 (509 cm^{-1}). The (111) orientation of the defect is explained by the high activity of the *L* point phonons in the luminescence spectra. Additionally, the authors used a tunable Ti-sapphire laser at 737.3 nm to excite photoluminescence, and were able to observe additional luminescence of (what they identified as) phonon replicas at 756, 767, 797 and 814 nm.

Much additional experimental information has been discovered about the centre, as discussed in the following paragraphs: CVD diamond films doped with boron (at 500 ppm) showed no 737 nm luminescence from positron lifetime investigations [Dannefaer *et al* (1993)]. The authors attribute this to boron doping removing the vacancies present in diamond. This supports previous results that vacancies are involved in the 737 nm centre. However, an alternative explanation is that, if the 737 nm defect is a Si-V centre in the negative charge state, as now believed [Goss *et al* (2007)], doping with boron would reduce the concentration of such centres (due to charge transfer), perhaps to zero.

The radiative efficiency of the 737 nm luminescence line in plasma-assisted CVD diamond grown on a silicon substrate was estimated to be greater than 80% [Bilodeau *et al* (1993)]. This is in contrast to the radiative efficiency of the GR1 centre which was estimated to be less than 2% [Davies *et al* (1987)]. Bilodeau *et al* (1993) also mention that they have detected absorption at 737 nm using calorimetric transmission spectroscopy.

Turukhim *et al* (1996) measured the photoluminescence lifetime of the 737 nm centre to consist of a biexponential decay, with time constants of 55 ps and 950 ps. The quantum yield was measured to be 0.05.

A defect centre with an emission line at 1.68 eV was observed in hot-filament CVD diamond films by Lin *et al* (1996). The authors state that their reactor and substrate were silicon free, which, along with the poorly resolved spectra of the 1.68 eV emission, caused them to conclude that this emission is not

the same as the 1.682 eV (737 nm) silicon related defect. This may have implications on other 1.68 eV emission observations, such as Freitas *et al* (1990), as noted by Lin *et al* and Clark *et al* (1995).

Sharda *et al* (1998b) concluded that the incorporation of silicon into diamond films grown by microwave-plasma CVD (indicated by 737 nm luminescence) is from the formation of volatile Si-H at the silicon substrate surface. This conclusion was drawn from the correlation between the intensity of the 737 nm luminescence and the microwave power density.

An investigation by Joeris *et al* (1996) gives a mechanism for the incorporation of silicon into CVD diamond via reaction of hydrogen and the quartz reactor walls. This study revealed a correlation between the 737 nm peak area and the concentration of atomic hydrogen in the plasma gas.

A wealth of evidence has shown that the 737 nm (1.682 eV) centre involves silicon and a vacancy. Experimental and computational results conclude a doubly degenerate ground and excited state for the defect. The symmetry is computationally predicted to be trigonal (D_{3d}). Experimental measurements of the behaviour of the zero-phonon doublet under uniaxial stress have been undertaken in this work to investigate the symmetry of the defect.

6.4.2 Results

6.4.2.1 Annealing behaviour

The annealing behaviour of the 737 nm doublet was investigated in order to support work undertaken by previous workers [Clark *et al* (1995), Collins *et al* (1994), Clark and Dickerson (1991)]. Isochronal annealing took place on a single-crystal CVD diamond, which had previously been irradiated with 5×10^{18} cm^{-2} 2-MeV electrons. The sample was annealed from 400ºC to 900ºC at intervals of 100ºC, with a time period of one hour at each temperature. Absorption spectra were collected before the study and after each anneal, allowing the decay of the GR1 and growth of the 737 nm doublet to be observed.

It was assumed that the absorption peaks were on top of a background, which was subtracted before the integrated intensities of the peaks were measured. Figure 6.4.1 shows the integrated absorption of the GR1 and 737 nm doublet as a function of annealing temperature. It can be seen that GR1 peak starts to decay in intensity after the 600ºC anneal as the neutral vacancy becomes mobile and either combines with other defects, annihilates with self-interstitials or moves to the sample surface. After annealing at 1000ºC absorption due to the neutral vacancy had almost completely disappeared.

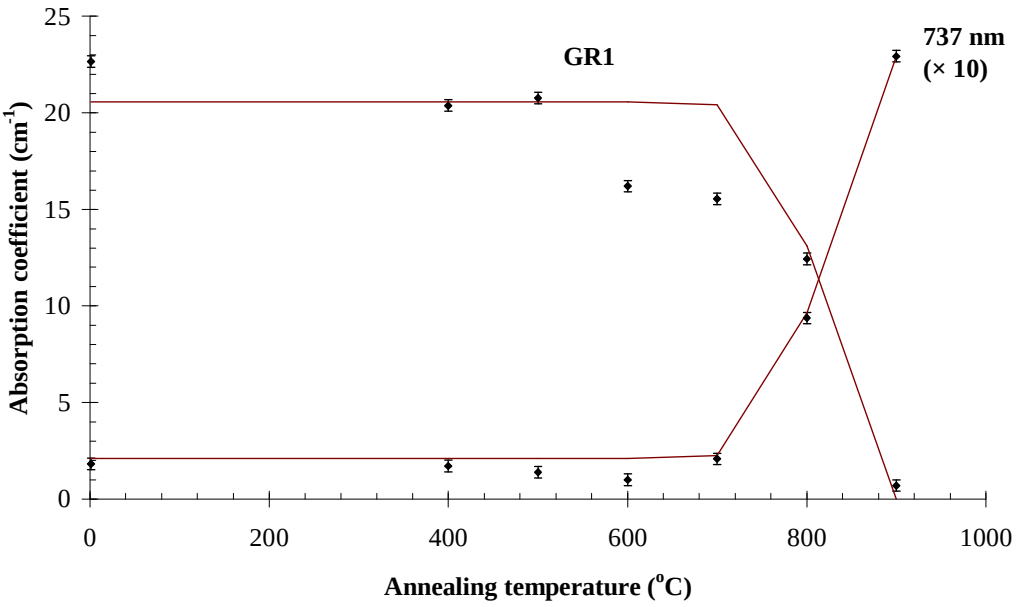

Figure 6.4.1 – Integrated intensities of the GR1 and 737 nm ZPLs after each annealing stage (data points). Lines show the theoretical change in absorption after each stage (see text). Data and fit for the 737 nm doublet are scaled by a factor of ten for clarity.

In particular, the decay in GR1 intensity between 500ºC and 600ºC is non-linear and due to annihilation of GR1 with interstitials and vacancies: Allers *et al* (1998) found that the GR1 intensity in type IIa diamond drops by ~ 15% in 400 minutes during isothermal annealing measurements at 460ºC. Kiflawi *et al* (2007) found the intensity lost to be sample dependent. After 700ºC the absorption intensity of the 737 nm doublet, the silicon-vacancy, increases rapidly. Conducting these measurements in absorption allows a quantitative change in intensity to be recorded: after the 900ºC anneal the 737 nm doublet had increased in intensity by a factor of 12.9 ± 2.3, whilst the GR1 had reduced by a factor of 32.3 ± 3.2. Any absorption of the silicon-vacancy complex before annealing at 700ºC is due to any centres present in the as-grown or irradiated diamond; after this and at subsequently higher annealing temperatures, the increase in absorption can be attributed to migrating vacancies being captured by the 737 nm centre's precursor impurity. Indeed, it was observed that all other irradiation-induced defect centres in this sample which were seen in visible-UV absorption measurements had annealed out by 900ºC, whereas the 737 nm doublet persisted. This suggests that the 737 nm centre's precursor impurity, in

this type IIa CVD sample, was the dominant optically active trap for migrating vacancies. Quantitatively, the loss of 22.0 meV cm^{-1} of GR1 in absorption gives a loss of (~ 1.9 ± 0.5) × 10^{17} cm^{-3} vacancies [Davies (1999)]. Therefore, at most, this concentration of silicon-vacancy centres has been created.

Along with the integrated intensities of the GR1 and 737 nm doublet, Figure 6.4.1 shows the theoretical change in absorption intensity after each annealing stage. This was calculated for the GR1 using the expressions in section 2.4.2. The probability of a vacancy being caught at a trap is given by

$$P = \left(\frac{\nu}{n_j}\right)\exp\left(\frac{-E}{kT}\right), \qquad 7.4.2.1.\mathbf{1}$$

where, the symbols are as defined in section 2.4.2. The number of jumps made before a vacancy is trapped, n_j, can be defined as the inverse of the concentration of traps, C. The values of the parameters used to produce the line through the GR1 data in figure 6.4.1, are the hopping frequency in diamond, ν = 10^{13} Hz, the activation energy of the vacancy, E = 2 eV, and C = 4.9 × 10^{-5} ≈ 22 ppm. The value used for the activation energy of the vacancy is at the boundary of the experimentally established value: 2.3 ± 0.3 [Davies *et al* (1992)]. The concentration of traps in this case is the initial concentration of silicon-vacancy centres. This is the first calibration of the concentration of the silicon-vacancy centre in diamond: assuming that all of the vacancies are trapped at the 737 nm centre's precursor impurity, then (using the GR1 calibration factor from Davies (1999)) $A_{737\ nm}$ = (2.2 ± 0.3) × 10^{-17} [Si-V], where the absorption coefficient is in meV cm^{-1}, and the Si-V concentration is in cm^{-3}.

The line through the 737 nm data in figure 6.4.1 was calculated by subtracting the intensity of GR1 at each annealing stage from the intensity before annealing, and scaling to the maximum intensity of the 737 nm doublet. The excellent fit to the data shows how the vacancies mobilised by the annealing are caught at the 737 nm precursor impurity.

6.4.2.2 Liquid helium temperature absorption

Clark *et al* (1995) determined that the 736.8 nm doublet was due to a silicon-related defect by measuring the photoluminescence spectrum while the sample was at liquid helium temperature. This resolved 12 components, which, it was concluded could be separated into three sets of four lines; each group of four corresponded to four transitions between two doubly degenerate states of a silicon defect, with the three sets shifted in energy and varying in intensity. Clark *et al* measured the integrated intensity ratios of the three sets of lines and found that they corresponded to the ratio of the three dominant isotopes of silicon; 28, 29 and 30.

Current diamond growth methods allow high quality, single-crystal, doped diamonds to be synthesised. As such, it is appropriate to support Clark *et al*'s work by repeating their investigation in absorption on both a natural-abundance Si-28 sample, and a Si-29 enriched sample.

The natural-abundance silicon sample is the same one used for the annealing study described in the previous section: it was grown with silane in the gas phase, electron irradiated, and annealed isochronally over 400 to 1000˚C, for an hour at each stage. This substantially increased the 736.8 nm doublet absorption intensity. The Si-29 enriched sample was synthesised with silane in the gas phase, which produced a ^{28}Si : ^{29}Si enrichment ratio of approximately 1 : 8 (estimated from EPR measurements). Liquid nitrogen temperature measurements were conducted on the custom absorption system described in section 3.1. Liquid helium temperature (LHT) measurements were conducted on a Bruker IFS 66 infrared spectrometer (see section 3.1), using a custom flow cryostat and an Oxford Instruments flow pump for cooling; adjusting the flow rate allowed temperatures between ~ 4 K and 40 K to be reached. For the rest of this section, the 736.8 nm doublet will be referred to by its energy, 1.6827 eV, in order to be consistent with previous workers.

Absorption measurements at LHT were performed on the two samples. The change in absorption spectrum of the 1.6827 eV centre between liquid nitrogen (77 K) and liquid helium (less than 40 K) temperature can be seen in

figure 6.4.2 for the natural abundance Si-28 sample. At LHT the central position of the transition shifts to lower energy by ~ 0.50 ± 0.08 meV. The four main components of the transition are resolved, along with satellite structure from the silicon isotopes.

LHT absorption measurements of the Si-29 enriched sample distinctly show the change in relative intensity of the twelve transitions of the centre in favour of the components assigned to transitions from Si-29 centres (see figure 6.4.3). This confirms that the satellite structure of the centre in this material is indeed due to the isotopes of silicon. Relative to the transition energies of the Si-28 data, a small shift to lower energy of 0.067 ± 0.018 meV for each component is detected for the Si-29 data. This is probably due to a slight difference of sample temperature during measurement of the data.

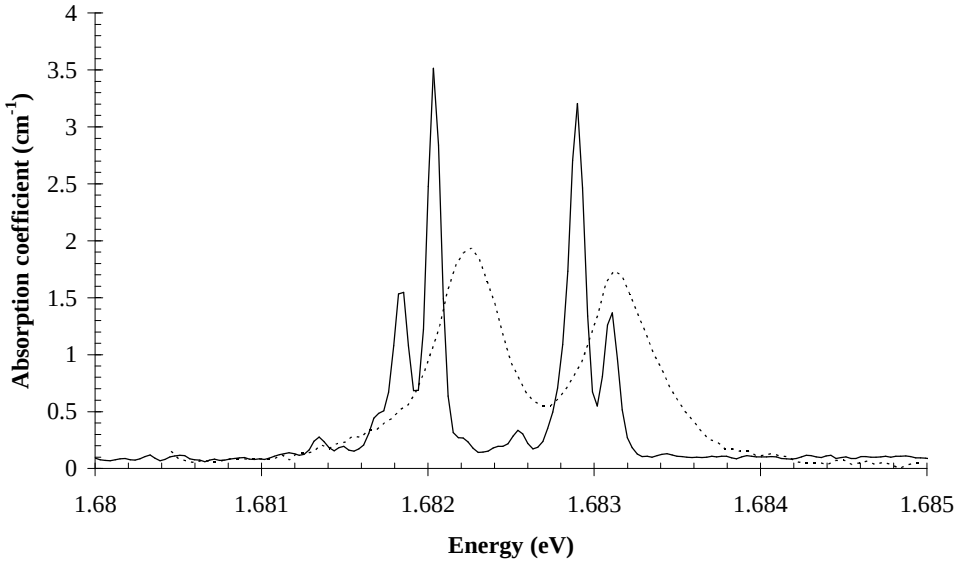

Figure 6.4.2 – Comparison of absorption of the 1.6827 eV centre at liquid nitrogen temperature (77 K, dotted spectrum) and at liquid helium temperature (less than 40 K, full line spectrum, displaced vertically).

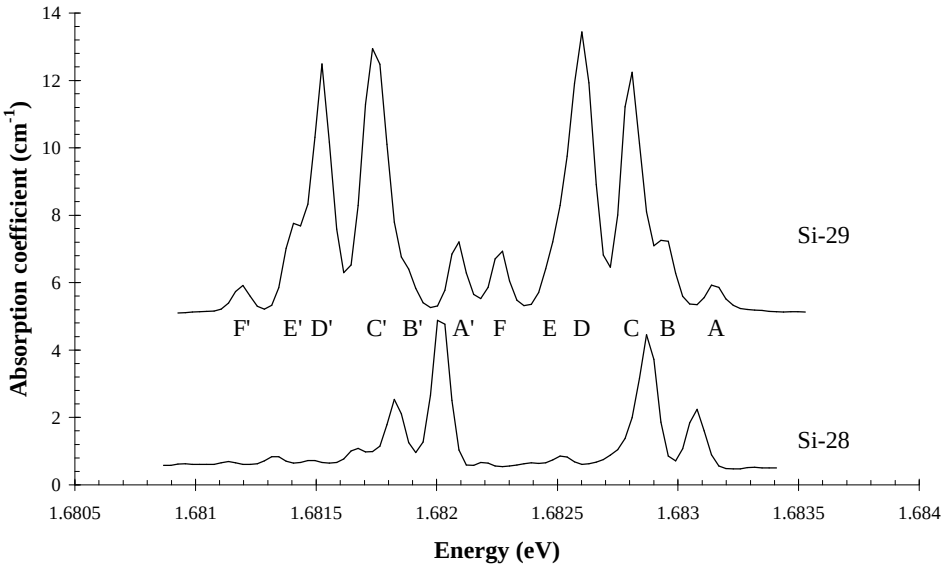

Figure 6.4.3 – Absorption spectra of the 1.6827 eV centre at liquid helium temperature in a natural abundance silicon-28 sample, after irradiation and annealing (lower spectrum, scaled by a factor of three), and a silicon-29 enriched sample (upper spectrum). Spectra are displaced vertically for clarity. Peak labels as Clark *et al* (1995).

For both the Si-28 and Si-29 data an absorption spectrum has been generated using bi-Lorentzian lineshapes (see section 2.2.2.1). These take the form $I(\upsilon) = a\ [\ b + (\upsilon - \upsilon_0)^2\ ]^{-2}$, where a scales the height of the peak, b determines the width, and υ_0 is the peak position. The b parameter is related to the full width half maximum, Γ, by $b = \Gamma^2\ [2\sqrt{}\ (\sqrt{2} - 1)]^{-2}$. The simulated spectrum for the Si-28 data (figure 6.4.4) was generated using a measured Γ of 0.079 meV, with the relative intensities of the peaks being set to the ratio of the natural abundance of the isotopes of silicon, 0.922 : 0.046 : 0.030 for 28 : 29 : 30. The positions of the peaks were determined by using the energy shift of the isotopes from the experimental data: it was found that for each nuclear mass added, the four line transition scheme shifted to lower energy by 0.344 ± 0.018 meV. The good fit of the generated spectrum to the data confirms the work of Clark *et al* (1995).

The simulated spectrum for the Si-29 data (figure 6.4.5) was generated using a measured Γ of 0.090 meV, with the relative intensities of the peaks this time being determined by fitting to the experimental data. The ratio of the isotopes were found to be 0.137 : 0.748 : 0.114 for silicon 28 : 29 : 30. The

measured 0.137 : 0.748 ratio is in excellent agreement with the EPR estimated ^{28}Si : ^{29}Si enrichment ratio of 1 : 8.

The positions of the peaks were determined from the experimental data, the decrease in energy per additional nuclear mass being 0.344 ± 0.016 meV. Figure 6.4.6 shows the component bi-Lorentzian peaks which are convoluted to form the complete spectrum. The various line patterns of the peaks identify the different silicon isotope contributions: the full line components are for Si-28 transitions, the dashed line components are for Si-29 transitions, and the dotted components are for Si-30 components. This demonstrates how the four component system is shifted to lower energy for each additional nuclear mass.

An important consequence of the success of the natural abundance Si-28 fit to the experimental data, is that a deconvolution of the 1.6827 eV centre in samples with silicon isotope enrichment allows the concentration of the isotopes present in the sample to be determined, as for the Si-29 sample. If the absorption coefficient of the centre were large, then this approach would only be valid in absorption spectroscopy, as luminescence measurements have the risk of providing misleading results due to self-absorption at the centres.

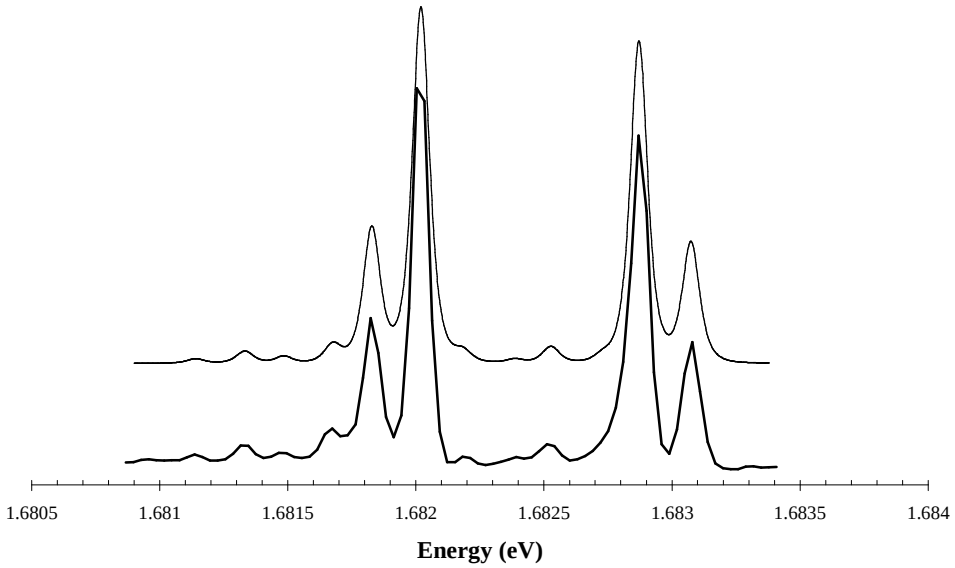

Figure 6.4.4 – Absorption spectrum of the 1.6827 eV centre at liquid helium temperature in a natural abundance silicon-28 sample, after irradiation and annealing (lower spectrum), and a generated absorption spectrum using bi-Lorentzians (upper spectrum). Spectra have been displaced vertically for clarity.

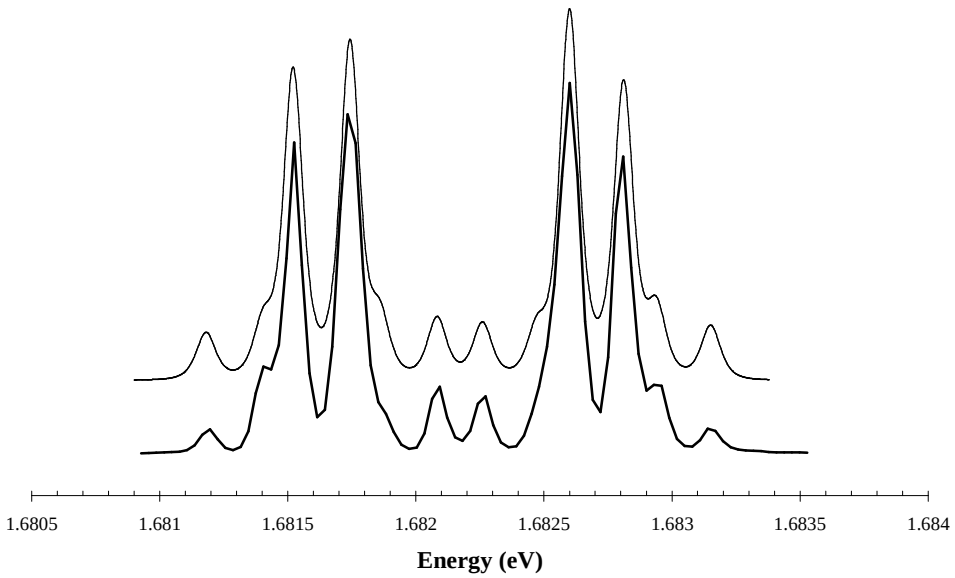

Figure 6.4.5 – Absorption spectrum of the 1.6827 eV centre at liquid helium temperature in a silicon-29 enriched sample (lower spectrum), and a generated absorption spectrum using bi-Lorentzians (upper spectrum). Spectra have been displaced vertically for clarity.

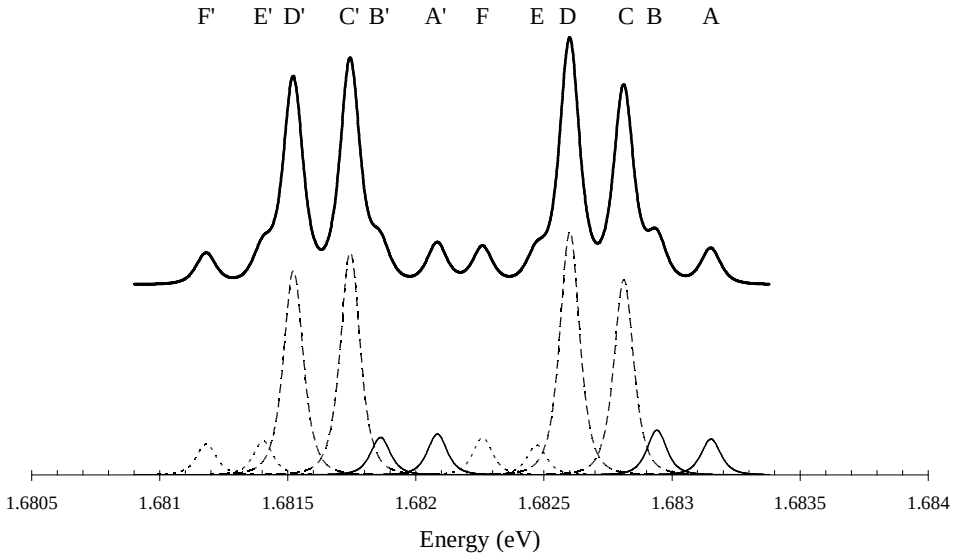

Figure 6.4.6 – Generated spectrum for the Si-29 enriched 1.6827 eV absorption system. The lower bi-Lorentzian peaks show the component transitions, and the upper spectrum shows the convolution of these. See text for identification of component patterns. Peak labels as Clark *et al* (1995).

6.4.2.3 Uniaxial stress measurements

In order to address the lack of information about the symmetry of the defect which produces the 736.8 nm (1.682 eV) ZPL doublet, uniaxial stress measurements were conducted. Two single-crystal CVD diamonds, cut and polished into cuboids, were investigated using absorption spectroscopy whilst the crystals were under uniaxial stress. One of the samples was doped with silane, irradiated with 5×10^{18} cm^{-2} 2 MeV electrons, and annealed at 1000°C for one hour in order to increase the absorption intensity of the doublet; the other sample was grown with a substantial gas-phase silane concentration, which resulted in a usable 737 nm doublet absorption intensity without the need for treatment.

Two sets of measurements were made: one with the samples held at liquid nitrogen temperature (LNT); and another with the sample at liquid helium temperature (LHT). The approach in the first case was to resolve the zero-phonon doublet, but not the fine structure present at LHT. For the second case, uniaxial stress effects on the fine structure were investigated. All of the readings were made using the Bruker IFS 66 absorption spectrometer. For the LNT measurements, uniaxial stress was applied to the two crystals by compressing opposing faces of the cuboids, in the [001], [111] and <110> orientations, using a push-rod with the force applied by a controllable gas pressure. For the LHT measurements, experimental constraints meant that readings were taken with the sample under [001] compression only. The sample was mounted in an Oxford Instruments liquid-helium flow-cryostat. The temperature of the sample was between 4 and 40 K; the temperature controlled by the flow-rate of the liquid helium. For both LNT and LHT measurements, absorption spectra were recorded, with the light polarised parallel and perpendicular to the stress direction, for a series of applied stresses between 0 and 2 GPa.

For the LNT measurements, compressing the sample along [001] caused each component of the doublet to shift non-linearly with stress; no splitting was observed in either polarisation, although this resulted in three independent stress-split components. Compressing along [111] caused each component of the doublet to split in both polarisations, two of which shifted non-linearly; there

were four independent stress-split components overall. Compressing along <110> caused the doublet to split into nine components in total, although these resolved to five independent components; two of which shifted non-linearly with stress. The change in energy of the components under each stress direction is shown as data points in figure 6.4.7; the lines through the data are guides (not theoretical fits).

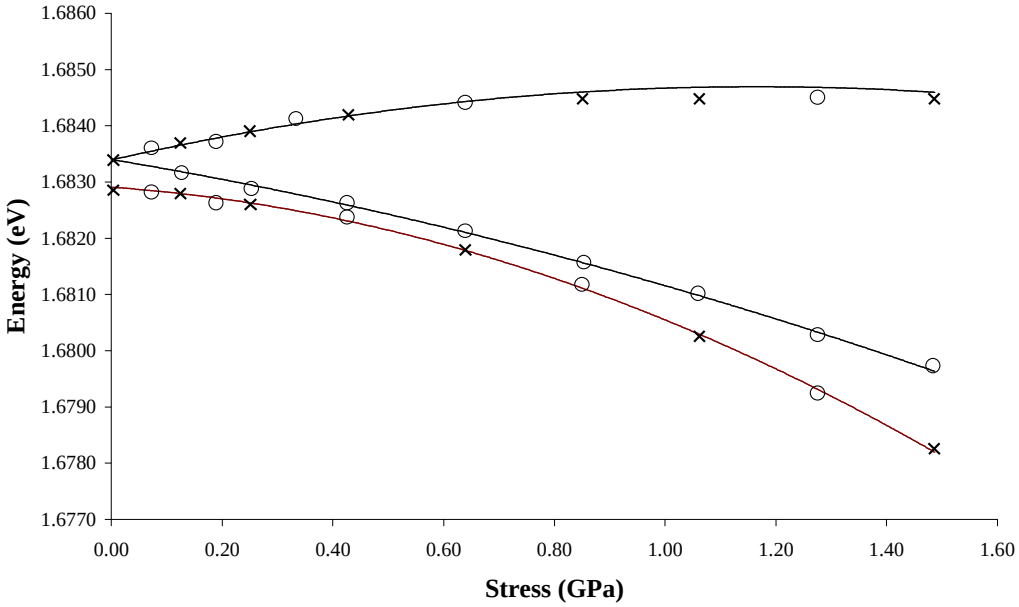

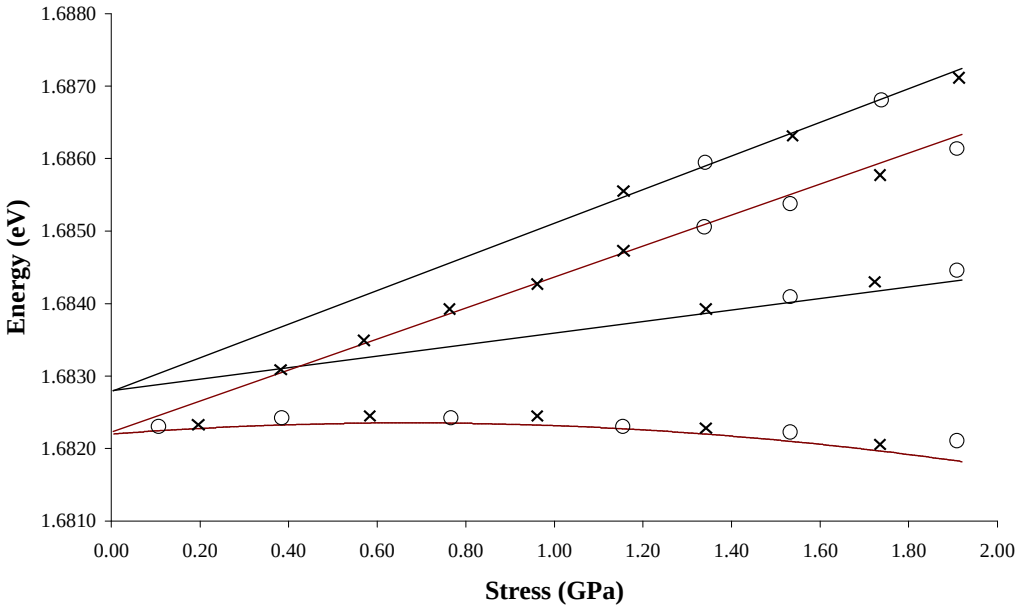

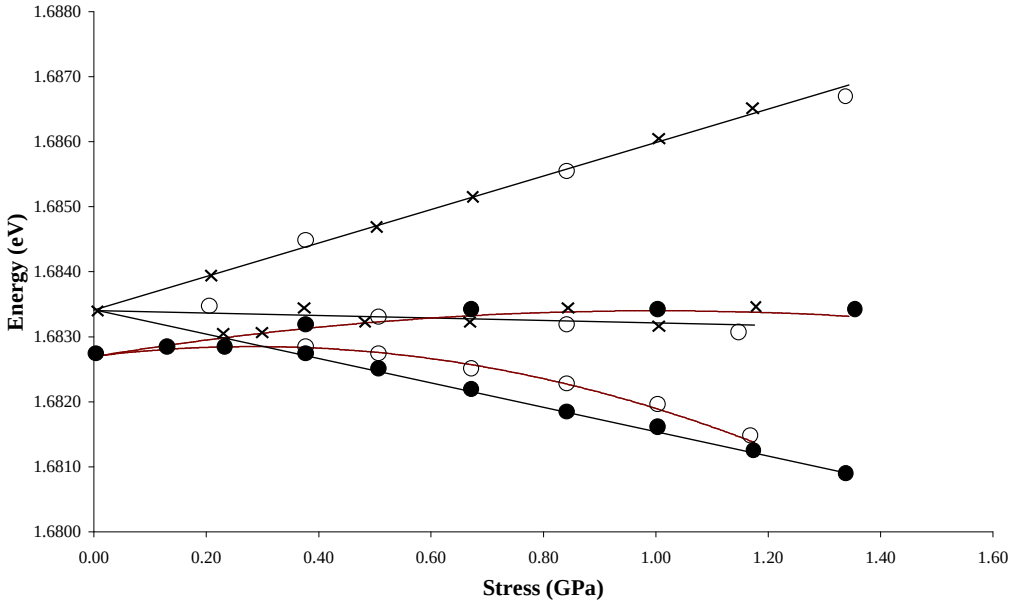

Figure 6.4.7 – Uniaxial stress splitting data for the 736.8 nm (1.682 eV) centre in absorption, at LNT, showing change in energy of ZPL components as a function of applied stress. Data points are experimental results, lines are guides (not theoretical fits). a) ZPL under <001> compression (**S**); crosses are for electric vector of luminescence $\mathbf{E} \parallel \mathbf{S}$; unfilled circles are for $\mathbf{E} \perp \mathbf{S}$. b) ZPL under <111> compression; crosses are for $\mathbf{E} \parallel \mathbf{S}$; unfilled circles are for $\mathbf{E} \perp \mathbf{S}$. c) ZPL under [110] compression; crosses are for $\mathbf{E} \parallel \mathbf{S}$ when viewing along; unfilled circles are for $\mathbf{E} \perp \mathbf{S}$ when viewing along [001], filled circles for $\mathbf{E} \perp \mathbf{S}$ when viewing along $[1\ \bar{1}\ 0]$.

In addition to the non-linear splitting, the components of the doublet show complicated relative intensity changes as stress is applied. Figure 6.4.8 shows the response under [001] compression: the integrated intensity of the higher energy component decreases rapidly as the stress increases; the integrated intensity of the lower energy component increases slightly. At zero stress the ratio of the integrated intensities of the high to low energy components is 1.24, and at 1.5 GPa it increases to 18.72; a factor of 15 increase. Similar responses of the doublet are found in the other stress directions.

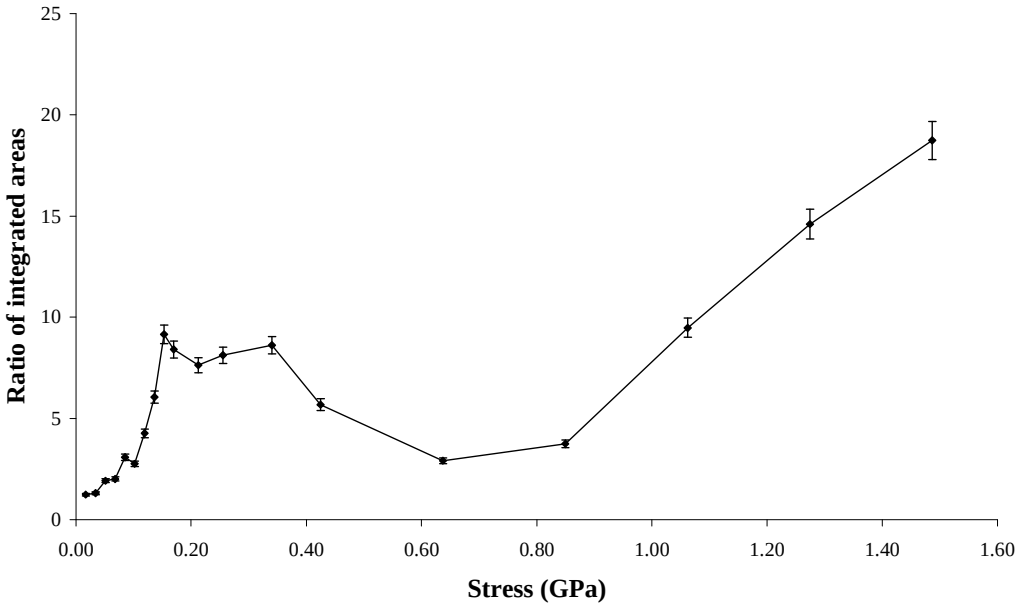

Figure 6.4.8 – Variation of relative intensity of the components of the 737 nm doublet, as a function of stress.

The non-linear shift rates of the components would ordinarily mean that there is an additional energy level interacting with one of the levels of the defect. The interaction causes a Coulomb repulsion, changing the energy of the transition from / to that state, supplemental to the shift caused by the compression of the lattice. The implication would be that there is a dynamic Jahn-Teller (J-T) distortion taking place at the centre (see section 2.5). A dynamic J-T effect can also cause intensity changes in zero-phonon components [Longuet-Higgins *et al* (1958)]. However, a J-T effect is not proposed as the origins of these effects, as further insight is gained by studying the stress-response of the components of the ZPL at LHT.

As discussed in section 6.4.2.2, the doublet resolves into 12 components at LHT: three groups of four transitions, one for each isotope of silicon. Following the stress-splitting of the four most intense components is appropriate to gain an understanding of the centre, as the splitting pattern will be the same for each isotope. Figure 6.4.9a shows a series of spectra demonstrating the response of the lines to increasing stress. It can be seen that each of the four main components splits into two, except for the highest energy component, which appears to remain unsplit. Figure 6.4.9b shows that the shift-rates of the

components are linear with the applied stress, contrary to the observations made at LNT. Additionally, intensity changes of the components at LHT are negligible; again contrary to the finding at LNT. The unusual results of uniaxial stress measurements at LNT can be explained by considering the components of the doublet at LNT as the envelope of the components at LHT: as the LHT components split with stress the intensity of the envelope changes, and the differing shift-rates of the LHT components cause the envelopes to appear to split and shift non-linearly. These results will be discussed further in the next section.

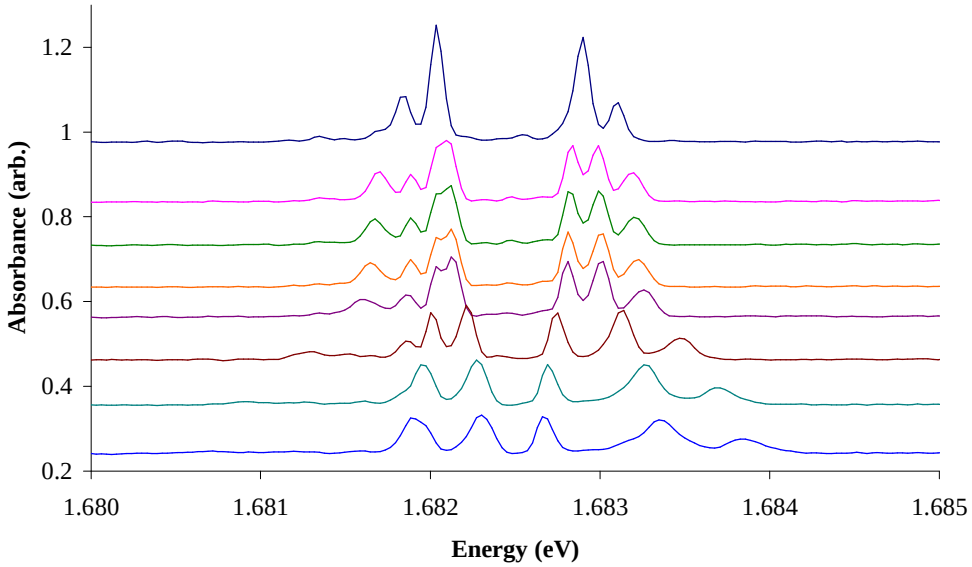

a)

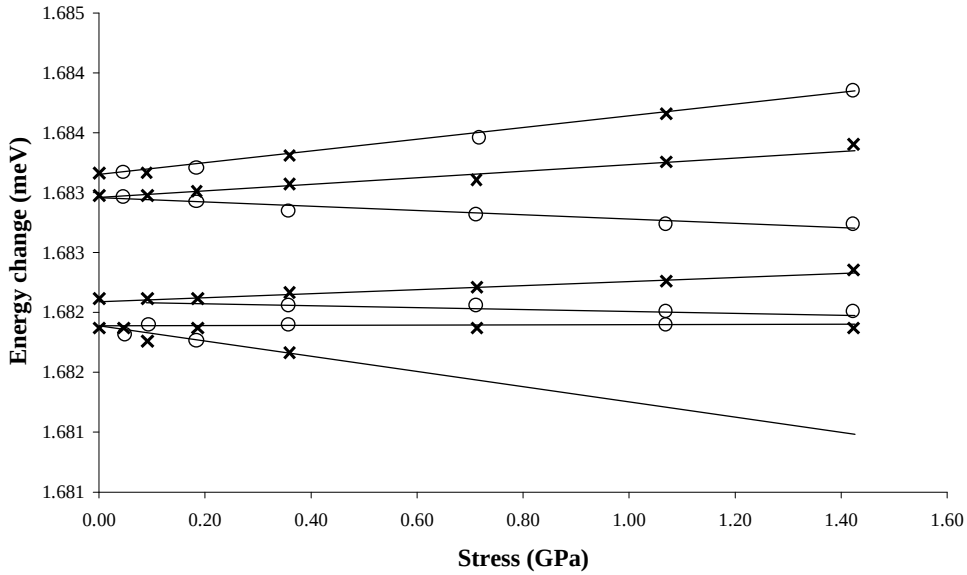

b)

Figure 6.4.9 – Uniaxial stress effects on the 736.8 nm (1.682 eV) doublet at liquid helium temperature, under [001] compression (data taken in absorption). a) Splitting pattern observed for stress from 0 GPa (top spectrum) to 1.4 GPa (lower spectrum) (not a linear selection of stresses). b) Change in energy of the components as a function of stress. Crosses are for electric vector, **E** parallel to the stress direction, **S**; open circles are for $\mathbf{E}^{\perp}\mathbf{S}$. Lines are guides (not theoretical fits).

6.4.3 Discussion

Low temperature investigations of the 736.8 nm (1.6827 eV) doublet have taken place. Liquid helium temperature (LHT) optical absorption measurements of a single-crystal CVD diamond, enriched with silicon-29, unambiguously confirm previous worker's [Clark *et al* (1995), and see section 6.4.1] assignments of silicon in the centre. This is due to the observation of a correlation between absorption intensity in the transitions ascribed to silicon-29 and 28, and the EPR-estimated silicon-29 to 28 concentration ratio. A useful consequence of this is that the silicon-29 to 28 concentration ratio in a sample may be estimated from LHT absorption measurements of the centre.

An isochronal annealing study of the centre has taken place, which has allowed the first calibration factor for the centre to be estimated as $A_{737\ nm} = (2.2 \pm 0.3) \times 10^{-17}$ [Si-V], where the absorption coefficient is in meV cm^{-1}, and the Si-V concentration is in cm^{-3}.

It has been shown that it is inadequate to record uniaxial stress spectra at liquid nitrogen temperature (LNT), as the lack of fine structure results in an inaccurate representation of the effects of stress on the defect. The short study in this work has shown that it is technically possible to make uniaxial stress measurements at LHT and to follow the shift and splitting behaviour of the major zero-phonon components of the centre.

Calculations by Goss *et al* (1996) predict a Jahn-Teller (J-T) distortion taking place at the centre. Experimentally, this would correspond to a dynamic J-T effect seen in the uniaxial stress splitting of the components of the ZPL: evidenced by non-linear shift-rates. This was observed in the LNT measurements, but subsequently shown to be an artefact. The preliminary uniaxial stress measurements at LHT show linear splitting-rates of the components. This does not strictly eliminate the possibility of observing J-T effects at the centre, as a full uniaxial stress investigation may demonstrate. Comparison with the uniaxial stress data of the 1.40 eV interstitial-nickel centre is drawn (see Nazaré *et al* (1991)).

6.5 Nitrogen-isotope-induced energy shifts of various ZPLs

A number of well-studied ZPLs in diamond have been established to directly involve nitrogen in the defect centres which produce them. The conclusion of nitrogen involvement for some of them, whilst not in doubt, has been through indirect measurements. In particular, the 389, 575, 594 and 637 nm centres. High resolution optical measurements of the ZPLs of these defects have been conducted on undoped synthetic HPHT and CVD samples, and nitrogen-15 doped samples, in order to obtain a direct measurement of the presence of nitrogen via an energy shift of the ZPL.

Some of the properties of these centres were introduced in chapter four, but they will be discussed further here. The 389 nm centre has been established to be a substitutional nitrogen and interstitial carbon complex [Collins and Lawson (1989)]. That work, and other investigations [Collins and Woods (1987), Collins *et al* (1988)], studied the effects of carbon and nitrogen isotopes on the vibronic band and local-vibrational modes of the 389 nm centre, but didn't measure the effect on the energy of the ZPL. However, Gippius *et al* (1982) did record an energy shift of the 389 nm ZPL in nitrogen-15 ion-implanted natural diamonds of 0.2 meV to higher energy. That work demonstrated a curious dependence of the isotope-induced shift of the ZPL on the annealing of the sample, which was attributed to the location of the 389 nm centres in disordered regions of the sample. It would be useful to obtain a quantitative confirmation of the isotope-induced ZPL energy shift in samples where disorder is not a result of creation of the centres; i.e. in non-ion-implanted nitrogen-15 doped single-crystal samples.

The 575 and 637 nm centres have been established as the nitrogen-vacancy complex by the irradiation and annealing of type Ib diamonds, which primarily contain single-substitutional nitrogen. The creation of vacancies by irradiation, and trapping of those vacancies at single-nitrogen centres during annealing forms the complex [Davies and Hamer (1976)]. The neutral form of the centre has a ZPL at 575 nm, and the negative charge state has a ZPL at 637 nm. The relationship between the 575 and 637 nm centres was confidently

established by Mita (1996) from neutron irradiation experiments. Collins and Lawson (1989) showed that it is a vacancy, rather than an interstitial, trapped at a single nitrogen atom for the 575 nm centre, by studying the strain response of the ZPL width; and the lack of local-vibrational modes supports this. Collins *et al* (1987) studied the effects of nitrogen isotope substitution on the 575 and 637 nm vibronic bands, although they did not measure the effect on the ZPL.

The 594 nm centre is a nitrogen and vacancy-related complex, which shows a ZPL and band in optical absorption measurement of irradiated, high nitrogen-concentration diamonds [Dugdale (1953), Davies and Nazaré (1980)]. The nitrogen isotopic dependence of the 594 nm ZPL has not yet been reported.

In the present work, two nitrogen-15 doped synthetic samples were studied: one single-crystal HPHT diamond, which had been previously electron irradiated and subsequently annealed, and one single-crystal CVD diamond. The use of single-crystal samples allows the line-widths to be as narrow as possible. The spectral data from these were compared to undoped HPHT and CVD samples. The samples were investigated in absorption and cathodoluminescence, at liquid nitrogen temperature, with in-line calibration of the transition energies using calibration lamps (neon and mercury); see chapter three for the experimental setups.

High resolution spectra were recorded over the four ZPLs discussed above. Table 6.5.1 shows the shifts observed. The values are the differences between the energies measured in the nitrogen-15 doped samples and the undoped samples. It was explained in section 2.2.2.3 that ZPL shifts due to isotopic changes in defect centres are expected to be of the order of ~ $|0.1|$ meV. It can be seen that all of the measured ZPLs show a nitrogen isotope-induced energy shift of a similar magnitude to that predicted; this provides the first unambiguous evidence that the 575, 594 and 637 nm centres directly involve nitrogen.

	389 nm	575 nm	594 nm	637 nm
ZPL energy shift (meV)	0.164 ± 0.060	0.229 ± 0.037	-0.098 ± 0.037	0.187 ± 0.037

Table 6.5.1 – ZPL energy shifts of various centres in nitrogen-15 doped samples. Values are the differences between the ZPL energies measured in the nitrogen-15 doped samples and the undoped samples.

The direction of the shift of ZPL energy in isotopic substitution, where heavier isotopes are used, is expected to be to higher energy, assuming that the temperature dependent shift of the ZPL energy is to lower energy (section 2.2.2.3). Temperature dependent energy shifts of the 389, 575 and 637 nm ZPLs have been shown to be to lower energy (Davies and Hamer (1976), this work (section 5.2.2), and Hizhnyakov *et al* (2003), respectively). The nitrogen isotope-induced shift of the 594 nm ZPL, however, is to lower energy; Davies (1974a) reports that the 594 nm ZPL does not show a temperature dependent shift. This means that the shape of the vibrational potentials in the excited and ground electronic states of the defect are the same; so the sum in equation 2.2.34 will be unity, and therefore the shift of the ZPL will be to lower energy upon increasing the isotopic mass.

Chapter 7

Conclusions and further work

Optical data on single-crystal CVD diamonds have been collected and analysed in order to provide a comprehensive optical characterisation of point defects in this material. The major features of cathodoluminescence, absorption and photoluminescence spectra have been systematically inspected, with additional experimental techniques employed to probe the properties of the defects further: uniaxial stress, temperature dependence, isotopic substitution, and annealing. The results have been analysed within the framework of establish theory.

A full list of ZPLs and bands observed in the cathodoluminescence spectra of the material is presented for the first time. A number of weak ZPLs have been recorded in the absorption spectra of one of the samples, which has allowed the first measurement of the concentration of nitrogen-vacancy defects in the material: $[(\text{N-V})^0] = 11 \pm 4$ ppb, $[(\text{N-V})^-] = 4 \pm 1$ ppb. The concentration of single-substitutional nitrogen is found to be of the order of a few hundred ppb. Annealing of the samples has allowed a calibration factor of the silicon-vacancy centre (737 nm, 1.682 eV) to be determined: $A_{737\ \text{nm}} = (2.2 \pm 0.3) \times 10^{-17}$ [Si-V], where the absorption coefficient, A, is in meV cm^{-1}, and the Si-V concentration is in cm^{-3}.

High-resolution measurements of ZPLs in nitrogen-15 enriched CVD and HPHT samples have been made. This has unambiguously confirmed existing research conclusions that nitrogen is directly involved in the defects with zero-phonon transitions at 389, 575, 594 and 637 nm. Liquid helium temperature measurements of a silicon-29 enriched CVD diamond quantitatively confirm previous research ascribing the fine structure of the 737 nm system to the isotopes of silicon.

Three defect centres with ZPLs at 466.6, 496.8 and 562.5 nm have been found to demonstrate preferential orientation within the lattice. The defects are shown to have rhombic I, rhombic I and either monoclinic I or rhombic I symmetries, respectively; all aligned with dipoles along <110> axes. Isotope measurements show nitrogen to be directly involved in the 466.6 nm centre, and *not* directly involved in the 562.5 nm centre. Atomic configurations of the three centres are suggested to be of the form V-X-V oriented along <110> directions, where V is a vacancy, and X is an atomic species. The three centres are proposed to be products of the CVD growth process, with a tentative incorporation mechanism proposed. The temperature dependences of the ZPLs have been recorded, with proposed phonon-coupling energies determined from the data.

The 532.7 nm ZPL, a transition frequently observed in this material, has been investigated. Uniaxial stress measurements have qualitatively found the defect to posses monoclinic I symmetry; with isotope measurements showing that the centre directly involves nitrogen. The vibronic band of the centre has been identified, with the Huang-Rhys factor and phonon-coupling energy measured (see table 7.1). The temperature dependence of the ZPL has been recorded. Careful measurements of the ZPL show it to *not* be a doublet transition, as was stated by previous researchers.

A further prominent ZPL in the CL spectra of this material at 467.2 nm has been found to originate from a rhombic I symmetry defect. The vibronic band of the centre has been identified, and the temperature dependence of the ZPL measured. The Huang-Rhys factor and phonon-coupling energy have been found. The centre shows similarities to the 466.6 nm centre, and it is proposed that the defect producing the transition at 467.2 nm is a perturbed form of that defect.

The silicon-vacancy centre (ZPL at 736.8 nm, 1.682 eV) has been investigated using uniaxial stress perturbations. It is shown that it is technically possible to perform uniaxial stress measurements on the centre at liquid helium temperature; and that this is preferable to liquid nitrogen temperature measurements, as these produce misleading results.

Table 7.1 summarises the properties of the centres investigated in this work.

ZPL wavelength (± 0.05 nm)	ZPL energy (± 0.0003 eV)	Symmetry	Huang-Rhys factor	Phonon coupling energy (meV)	Direct nitrogen involvement?
466.65	2.6569	Rhombic I	< 0.1	53.7 ± 10	*Yes*
467.22	2.6536	*Rhombic I*	0.46 ± 0.23	73.85 ± 0.25	-
496.83	2.4955	Rhombic I	< 0.1	39.7 ± 10	-
510.36	2.4293	-	< 0.1	73.9 ± 10	-
532.71	2.3274	*Qualitatively monoclinic I*	0.76 ± 0.30	68.26 ± 0.25	Yes
562.57	2.2039	Monoclinic I or Rhombic I	< 0.1	32.8 ± 10	No

Table 7.1 – Summary of the properties the ZPLs investigated in this work. Italicised properties are tentative.

Taking the work forward, it would be useful to have a better understanding of the nature of the preferentially oriented centres, their formation in the lattice, and the roles nitrogen, and potentially hydrogen, play. Computational calculations may assist by simulating growth environments; a rigorous study of the effects of gas-phase nitrogen and hydrogen concentrations; annealing of the centres to investigate any relationships between the centres; deuterium enriched samples to probe isotope-induced ZPL shifts. Additionally, it would be desirable to obtain nitrogen-isotope measurements of the 466.6 nm ZPL with a lower associated error, to confirm the conclusion drawn here.

The tentative symmetry assignments of the 532.7 nm and 467.2 nm centres could be clarified by repeating uniaxial stress measurements on a number of different samples. Studying a large number of samples would be useful to confirm the proposed identification of the vibronic band of the 532.7 nm centre; along with any investigation into the origin of the structure observed on top of the band.

A full uniaxial stress study of the silicon vacancy centre is due; this should be conducted with the samples at liquid helium temperatures, and as the linewidths at these temperatures are ~ 0.1 meV or less, using a highly stable spectrometer with a high resolving power would be required.

Finally, considering the frequent presence of the 389 nm centre in this high-quality material, it would be appropriate to conduct uniaxial stress measurements on the ZPL in an attempt to obtain the symmetry of the centre.

Chapter 8

References

Allers, L., Collins, A. T., and Hiscock, J. (1998). *Diamond and Related Materials*. **7**, 228

Allers, L., and Mainwood, A. (1998). *Diamond and Related Materials*. **7**, 261

Asmussen, J., Mossbrucker, J., Khatami, S., Huang, W. S., Wright, B., and Ayres, V. (1999). *Diamond and Related Materials*. **8**, 220

Bachmann, P. K., and Wiechert, D. U. (1992). *Diamond and Related Materials*. **1**, 422

Bar-Yam, T., and Moustakas, T. D. (1989). *Nature*. **342**, 786

Benndorf, C., Schmidt, I., and Joeris, P. (1996). *Physica Status Solidi (a).* **154** (1), 5

Bilodeau, T. G., Doverspike, K., and Strom, U. (1993). *Diamond and Related Materials*. **2**, 699

Birks, J. B. (1970). *Photophysics of Aromatic Molecules*, Wiley-Interscience

Blank, V. D., Kuznetsov, M. S., Nosukhin, S. A., Terentiev, S. A., and Denisov, V. N., (2007). *Diamond and Related Materials*. **16**, 800

Bohr, S., Haubner, R., and Lux, B. (1995). *Applied Physics Letters*. **68** (8), 1075

Boyd, S. R., Kiflawi, I., and Woods, G. S., (1994). *Philosophical Magazine B.* **69**, 1149

Burns, R. C., Cvetkovic, V., Dodge, C. N., Evans, D. J. F., Rooney, M-L. T., Spear, P. M., and Welbourn, C. M., (1990). *Journal of Crystal Growth.* **104**, 257

Burton, N. C., Steeds, J. W., Meaden, G. M., Shreter, Y. G., and Butler, J. E. (1995). *Diamond and Related Materials*. **4**, 1222

Campbell, B., Choudhury, W., Mainwood, A., Newton, M., and Davies G. (2002). *Nuclear Instruments and Methods in Physics Research A*. **476**, 680

Charette, J. J., (1961). *Journal of Chemical Physics*. **35**, 1906

Chayahara, A., Mokuno, Y., Horino, Y., Takasu, Y., Kato, Y., Yoshikawa, H., Fujimori, N. (2004). *Diamond Related Materials*. **13**, 1954.

Chrenko, R. M, Tuft, R. E., and Strong, H. M. (1977). *Nature*. **270**, 141

Chrenko, R. M., Strong, H. M., and Tuft, R. E., (1971). *Philosophical Magazine*. **23**, 313

Clark C. D. *et al*, *Phys. Rev. B*, **51** (23), 16681-16688 (1995)

Clark, C. D., and Dickerson, C. B. (1991). *Surface and Coatings Technology*. **47**, 336
Clark, C. D., and Norris, C. A. (1970). *Journal of Physics C: Solid State Physics*. **3**, 651
Clark, C. D., and Walker, J., (1973). *Proceedings of the Royal Society of London Series A*. **334**, 241
Clark, C. D., Ditchburn, R. W., and Dyer, H. B. (1956a). *Proceedings of the Royal Society of London, Series A*. **234** (1198), 363
Clark, C. D., Ditchburn, R. W., and Dyer, H. B. (1956b). *Proceedings of the Royal Society of London, Series A*. **237** (1208), 75
Clark, C. D., Kanda, H., Kiflawi, I., and Sittas, G. (1995). *Physical Review B*. **51** (23), 16681
Collins A. T., Allers, L., Wort, C. J. H., and Scarsbrook, G. A. (1994). *Diamond and Related Materials*. **3**, 932
Collins, A. T. (1978a). In *Defects and Radiation Effects in Semiconductors*. Institute of Physics Conference Series, No. 46, pp. 327-333. (Institute of Physics, Bristol, London, 1979)
Collins, A. T. (1978b). *Journal of Physics C*. **11**, 1957
Collins, A. T. (1982). *Journal of Gemmology*. **18**, 37
Collins, A. T. (1989). *Journal of Physics: Condensed Matter*. **1**, 439
Collins, A. T. (1992). *Diamond and Related Materials*. **1**, 457
Collins, A. T. (1992). *Diamond and Related Materials*. **1**, 457
Collins, A. T. (1998). *Diamond and Related Materials*. **7**, 1257
Collins, A. T. (1999). *Diamond and Related Materials*. **8**, 1455
Collins, A. T. (2002). *Journal of Physics: Condensed Matter*. **14**, 3743
Collins, A. T., Allers, L., Wort, C. J. H., and Scarsbrook, G. A., (1994). *Diamond and Related Materials*, **3**, 932
Collins, A. T., and Dahwich, A. (2003). *Journal of Physics: Condensed Matter*. **15**, L591
Collins, A. T., and Lawson, S. C. (1989). *Journal of Physics: Condensed Matter*. **1**, 6929
Collins, A. T., and Rafique, S., (1979). *Proceedings of the Royal Society of London Series A*. **367** (1728), 81
Collins, A. T., and Spear, P. M. (1983). *Journal of Physics C: Solid State Physics*. **16**, 963
Collins, A. T., and Spear, P. M., (1986). *Journal of Physics C: Solid State Physics*. **19**, 6845
Collins, A. T., and Williams, A. W. S. (1971). *Journal of Physics C: Solid State Physics*. **4**, 1789
Collins, A. T., and Woods, G. S. (1982). *Philosophical Magazine, B*. **45**, 385
Collins, A. T., and Woods, G. S. (1987). *Journal of Physics C: Solid State Physics*. **20**, L797
Collins, A. T., Connor, A., Cheng-Han Ly, Shareef, A., and Spear, P. M. (2005). *Journal of Applied Physics*. **97**, 083517

Collins, A. T., Davies, G., Kanda, H., and Woods, G. S. (1988). *Journal of Physics C: Solid State Physics*. **21**, 1363
Collins, A. T., Kamo, M., and Sato, Y. (1989). *Journal of Physics D: Applied Physics*. **22**, 1402
Collins, A. T., Kamo, M., and Sato, Y. (1990). *Journal of Materials Research*. **5** (11), 2507
Collins, A. T., Kanda, H., and Burns, R. C. (1990). *Philosophical Magazine B*. **61**,797
Collins, A. T., Kanda, H., and Kitawaki, H. (2000). *Diamond and Related Materials*. **9**, 113
Collins, A. T., Stanley, M., and Woods, G. S. (1987). *Journal of Physics D: Applied Physics*. **20**, 969
Collins, A. T., Woad, P. J., Woods, G. S., and Kanda, H. (1993). *Diamond and Related Materials*. **2**, 136
Collins, R. J., and Fan, H. Y. (1954). *Physical Review*, **93** (4), 674

Dannefaer, S., Bretagnon, T., Kerr, D. (1993). *Diamond and Related Materials*. **2**, 1479
Davies, G. (1970). *Journal of Physics C: Solid State Physics*. **3**, 2474

Davies, G. (1970). *Journal of Physics C: Solid State Physics*. **3**, 2474

Davies, G. (1971). *Journal of Physics D: Applied Physics*. **4**, 1340

Davies, G. (1972). *Journal of Physics C: Solid State Physics*. **5**, 2534

Davies, G. (1974a). *Journal of Physics C: Solid State Physics*. **7**, 3797

Davies, G. (1974b). *Proceedings of the Royal Society, Series A*. **336** (1607), 507
Davies, G. (1975). *Journal of Physics C: Solid State Physics*. **8**, 2448

Davies, G. (1977). *Nature*. **269**, 498

Davies, G. (1979a). In "*The Properties of Diamond*" (Field, J. E. editor). Chapter 5, page 165. Academic Press, London.
Davies, G. (1979b). *Journal of Physics C: Solid State Physics*. **12**, 2551

Davies, G. (1979c). *Solid State Communications*. **32**, 745

Davies, G. (1981). *Reports on Progress in Physics*. **44**, 787

Davies, G. (1983). *De Beers XXth Diamond Conference*. Unpublished.

Davies, G. (1989). *Physics Reports*. **176**, 83

Davies, G. (1999). In: *Identification of Defects in Semiconductors, Volume 51B (Semiconductors and Semimetals)*, p. 1
Davies, G., and Crossfield, M. (1973). Journal of Physics C: Solid State Phys. **6**, L104
Davies, G., and Hamer, M. F. (1976). *Proceedings of the Royal Society of London, Series A*. **348** (1653), 285
Davies, G., and Nazaré, M. H. (1980). *Journal of Physics C: Solid State Physics*. **13**, 4127

Davies, G., Lawson, S. C., Collins, A. T., Mainwood, A., and Sharp, S. J. (1992). *Physical Review B*. **46** (20), 13157
Davies, G., Nazaré, M. H., and Hamer, M. F. (1976). *Proceedings of the Royal Society of London, A*. **351**, 245
Davies, G., Thomaz, M. F., Nazare, M. H., Martin, M. M., and Shaw, D. (1987). *Journal of Physics C:Solid State Physics*. **20**, L13
de Sa, E. S., and Davies, G. (1977). *Proceedings of the Royal Society A*. **357**, 231
De Weerdt, F., and Collins, A. T., (2007). *Diamond and Related Materials*, **16**, 512
De Weerdt, F., and Van Royen, J., (2001). *Diamond and Related Materials*. **10**, 474
Dean, P. J., (1965). *Physical Review*. **139**, A588

Dischler, B., Rothemund, W., Maier, K., Wild, C., Biebl, H., and Koidl, P. (1994). *Diamond & Related Materials*. **3**, 825
Dodge, C. N. (1986). *PhD Thesis*. University of Reading, UK

Dugdale, R. A. (1953). *British Journal of Applied Physics*. **4**, 334

Dyer, H. B., and de Preez, L. (1965). *Journal of Chemical Physics*. **42**, 1898

Dyer, H. B., Raal, F. A., du Preez, L., and Loubser, J. H. N., (1965). *Philosophical Magazine*. **11**, 763
Elliot, R. J., and Gibson, A. F. (1976). *Solid State Physics*, The Macmillan Press Ltd., London
Evans, T. and Z, Qi. (1982). *Proceedings of the Royal Society of London A*. **381** (1780). 159
Farrer, R. G., and Vermeulen, L. A. (1972). *Journal of Physics C: Solid State Physics*. **5**, 2762
Feofilov, P. P., and Kaplyanskii, A. A. (1962). *Uspekhi Fizicheskikh Nauk*. **76** (2), 201
Field, J. (ed.), (1992). *The Properties of Natural and Synthetic Diamond*. Academic Press, London
Fletcher, R. C. and Brown W. L. (1953). *Physical Review*. **92** (3), 585

Freitas, J. A., Butler, J. E., and Strom, U. (1990). *Journal of Materials Research*. **5** (11), 2502
Gattinoni, C., (2007). Personal communication.

Gheeraert, E., Deneuville, A., Brunel, M., and Oberlin, J. C. (1992). Diamond and Related Materials. **1**, 504
Gheeraert, E., Fontaine, F., Deneuville, A., Khong, Y. L., Collins, A. T. (1994). *Diamond and Related Materials*, **3**, 737
Gippius, A. A., Vavilov, V. S., Zaitsev, A. M., and Zhakupbekov, B. S. (1983). *Physica, B*. **116**, 187
Gippius, A. A., Zaitsev, A. A., and Vavilov, V. S. (1982). *Soviet Physics Semiconductors*. **16**, 256
Gorokhovsky, A. A., Turukhin, A. V., Alfano, R. R., and Phillips, W. (1995). *Applied Physics Letters*. **66** (1), 43
Goss, J. P., Briddon, P. R., and Shaw, M. J. (2007). *Physical Review B*. **76**, 075204

Goss, J. P., Jones, R.. Breuer, S. J., Briddon, P. R., and Öberg, S. (1996). *Physical Review Letters*. **77** (14), 3041
Harlow, G. E. (1998). *The Nature of Diamonds*, Cambridge University Press. ISBN: 0521629357
Hizhnyakov, V., Boltrushko, V., Kaasika, H., and Sildos, I. (2003). *Journal of Chemical Physics*. **119** (12), 6290
Hounsome, L. S., Jones, R., Martineau, P. M., Shaw, M. J., Briddon, P. R., Öberg, S., Blumenau, A. T., and Fujita, N. (2005). *Physica Status Solidi (a)*. **202** (11), 2182
Hughes, A. E., and Runciman, W. A. (1967). *Proceedings of the Physical Society*. **90**, 827
Hunt, D. C, Twitchen, W. D., Newton, M. E., Baker, J. M, Anthony, T. R., Banholzer, W. F., and Vagarali, S. S. (2000). *Physical Review B.* **61**, 3863
Iakoubovskii, K., and Adriaenssens, G. J., (2000). *Physical Review B.* **61**, 10174
Iakoubovskii, K., and Stesmans, A. (2002a). *Journal of Physics: Condensed Matter*. **14**, R467
Iakoubovskii, K., and Stesmans, A. (2002b). *Physical Review B.* **66**, 045406
Isberg, J., Hammersberg, J., Johansson, E., Wikström, T., Twitchen, D. J., Whitehead, A. J., Coe, S. E., and Scarsbrook, G. A., (2002). *Science*. **297**, 1670
Joeris, P., Schmidt, I., and Benndorf, C. (1996). *Diamond and Related Materials*. **5**, 603
Joshi, A. W. (1973). *Elements of group theory for physicists*, published by Wiley Eastern Private Limited, New Delhi. Chaper 5. ISBN: 0852264402
Kanda, H., Watanabe, K., Eun, K. Y., and Lee, J. K. (2003a). *Diamond and Related Materials*. **12**, 1760
Kanda, H., Watanabe, K., Koizumi, S., and Teraji, T., (2003b). *Diamond and Related Materials*, **12**, 20
Kaplyanskii, A. A. (1964a). *Optics and Spectroscopy*. **16**, 329
Kaplyanskii, A. A. (1964b). *Optics and Spectroscopy*. **16**, 557
Kawarada, H., Yokota, Y., Mori, Y., Nishimura, K., and Hiraki, A. (1990). Journal of Applied Physics. **67** (2), 983
Khong, Y. L., and Collins, A. T. (1993). *Diamond and Related Materials*. **2**, 1
Khong, Y. L., Collins, A. T., and Allers, L. (1994). *Diamond and Related Materials.* **3** (7), 1023
Kiflawi, I., Collins, A. T., Iakoubovskii, K., and Fisher, D. (2007). *Journal of Physics: Condensed Matter*. **19**, 046216
Kiflawi, I., Mainwood, A., Kanda, H., and Fisher, D. (1996). *Physical Review B*. **45**, 1436
Kittel, C. (1986). *Introduction to Solid State Physics*, sixth edition, John Wiley & Sons, Inc., New York
Koike, J., Parkin, D. M., and Mitchell, T. E. (1992). Applied Physics Letters. **60**, 1450
Krishnan, R. S., (1946). *Proceedings of the Indian Academy of Science A*. **24**,

Lang, A. R., and Meaden, G. M., (1991). *Journal of Crystal Growth*. **108**, 53

Lawson, S. C., and Kanda, H. (1993). *Diamond and Related Materials*. **2**, 130

Lawson, S. C., Davies, G., Collins, A. T., and Mainwood, A. (1992a). *Journal of Physics: Condensed Matter*. **4**, 3439

Lawson, S. C., Davies, G., Collins, A. T., and Mainwood, A. (1992b). *Journal of Physics: Condensed Matter*. **4**, L125

Lawson, S. C., Fisher, D., Hunt, D. C., and Newton, M. E. (1998). *Journal of Physics: Condensed Matter*. **10**, 6171

Lax, M., and Burstein, E. (1955). *Physical Review*, **97** (1), 39

Lax, M., Hu, P., and Narayanamurti, V. (1981). *Physical Review B*. **23**, 3095

Leamy, H. J. (1982). *Journal of Applied Physics*. **53**, R51

Lin, L.-T.S., *et al*, (1996). *Diamond and Related Materials*. **5**, 1236

Litvinov, V. V., Petukh, A. N., and Pokotilo, Yu. M. (2000), *Journal of Applied Spectroscopy*, **67** (2), 384

Longuet-Higgins, H. C., Opik, U., Pryce, M. H. L., and Sacks, R. A. (1958). *Proceedings of the Royal Society of London, Series A*. **244** (1236), 1

Lowther, J. E. (1978). *Journal of Physics C*. **11**, L373

McSkimmin, H. J., and Andreatch, P., (1972). *Journal of Applied Physics*. **43** (7), 2944

Mita, Y. (1996). *Physical Review B*. **53**, 11360

Mita, Y., Nisida, Y., Suito, K., Onodera, A., and Yazu, S. (1990). *Journal of Physics: Condensed Matter*. **2**, 8567

Mita, Y., Ohno, Y., Adachi, Y., Kanehara, H., and Nisida, Y. (1993). *Diamond and Related Materials*. **2**, 768

Mohammed, K., Davies, G., and Collins, A. T., (1982). *Journal of Physics C: Solid State Physics*. **15**, 2779

Moliver, S. S. (2003). *Technical Physics*. **48 (**11), 1449

Mott, N. F. and Gurney, R. W. (1940). *Electronic Processes in Ionic Crystals*. Oxford University Press, London

Muller-Sebert, W., Worner, E., Fuchs, F., Wild, C., and Koidl, P. (1995). *Applied Physics Letters*. **68** (6), 759

Nadolinny, V. A., Yelisseyev, A. P., Yuryeva, O. P., Feygelson, B. N. (1997). *Applied Magnetic Resonance*. **12** (4), 543

Nazaré, M. H., Neves, A. J., and Davies, G. (1991). *Physical Review B*. **43** (17), 14196

Newton, M. E., and Baker, J. M. (1991). *Journal of Physics: Condensed Matter*. **3**, 3605

Pankove, J. I. (1971). *Optical Processes in Semiconductors*, Dover Publications Inc., New York

Pearson, K. (1916). Philosophical *Transactions of the Royal Society of London, Series A (1896-1934)*. **216**, 429

Qi, X.-G., Chen, Z.-S., and Xu, H. (2006). *Surface and Coatings Technology*, **200**, 5268

Raal, F. A., (1958). *Proceedings of the Physical Society*. **71**, 846

Robins, L. H., Cook, L. P., Farabaugh, E. N., and Feldman, A. (1989). Physical Review B. **39** (18), 13367

Ruan, J., Choyke, W. J., and Partlow, W. D. (1991a). *Applied Physics Letters*. **58** (3), 295

Ruan, J., Choyke, W. J., and Partlow, W. D. (1991b). *Journal of Applied Physics*. **69** (9), 6632

Ruan, J., Kobashi, K., and Choyke, W. J. (1992). *Applied Physics Letters*. **60** (25), 3138

Runciman, W. A. (1965). *Proceedings of the Physical Society*. **86**, 629

Schäfer, L., Jiang, X., and Klages, C.-P., in Tzeng, Y., Yoshikawa, M., Murakawa, M., and Feldman, A., (eds.), (1991). *Applications of Diamond and Related Materials*. Elsevier, Amsterdam, p. 121

Schwarzbach, D., Haubner, R., and Lux, B., (1994). *Diamond and Related Materials*. **3**, 757

Sharda, T., *et al*, (1998a). *Diamond and Related Materials*. **7**, 250-254

Sharda, T., Vaidya, A., Misra D. S., *et al*, (1998b). *Journal of Applied Physics*. **83** (2), 1120

Sittas, G., Kanda, H., Kiflawi, I., and Spear, P.M. (1996). *Diamond and Related Materials*. **5**, 866

Sobolev, E. V., Litvin, Yu. A., Samsonenko, N. D., Il'in, V. E., Lenskaya, S. V., and Butuzov, V. P., (1969). *Soviet Physics Solid State*. **10**, 1789

Solin, S. A. (1972). *Physics Letters A*. **38** (2), 101

Steeds, J. W., Davis, T. J., Charles, S. J., Hayes, J. M, and Butler, J. E. (1999). *Diamond and Related Materials*. **8**, 1847

Sternschulte, H., *et al*, (1994). *Physical Review B*. **50** (19), 14554

Sternschulte, H., *et al*, (1995). *Diamond and Related Materials*. **4**, 1189

Stoneham, A. M. (1969). *Reviews of Modern Physics*. **41** (1), 82

Sumiya, H., and Satoh, S., (1996). *Diamond and Related Materials*. **5**, 1359

Tallaire, A., Collins, A. T., Charles, D., Achard, J., Sussmann, R., Gicquel, A., Newton, M. E., Edmonds, A. M., and Cruddace, R. J. (2006). *Diamond & Related Materials*. **15**, 1700

Turukhin, A. V., *et al*, (1996). *Physical Review B*. **54** (23), 16448

Twitchen, D. J., Newton, M. E., Baker, J. M., Tucker, O. D., Anthony, T. R., and Banholzer, W. F. (1999a). *Physical Review B*. **59**, 12900

Twitchen, D. W., Hunt, D. C., Wade, C., Newton, M. E., Baker, J. M., Anthony, T. R., and Banholzer, W. F. (1999b). *Physica B*. 273 - 274, 644

van Wyk, J. A., and Woods, G. S. (1995). *Journal of Physics: Condensed Matter*. **7**, 5901

Vavilov, V.S., Gippius, A. A., Zaitsev, A. M., Deryagin, B. V., Spitsyn, B. V., and Aleksenko, A. E. (1980). *Soviet Physics Semiconductors*. **14** (19), 1078

Vlasov, I. I., and Ralchenko, V. G. (2004). *Defect and Diffusion Forum*. Vols

226-228, 61

Warren, J. L., Yarnell, J. L., Dolling, G., and Cowley, R. A. (1967). *Physical Review*, **158**, 805

Wotherspoon, A., Steeds, J., Coleman, P., Wolverson, D., Davies, J., Lawson, S., and Butler, J. (2002). Diamond and Related Materials. 11, 692

Woods, G. S. (1986). *Proceedings of the Royal Society A*. **407**, 219

Woods, G. S., and Collins, A. T. (1982). *Journal of Physics C*. **15**, L949

Yacobi, B. G., and Holt, D. B. (1986). *Journal of Applied Physics*. **59**, R1

Yacobi, B. G., Badzian, A. R., and Badzian, T., (1991). *Journal of Applied Physics*, **69** (3), 1643

Yamamoto, N., Spence, J. C. H., and Fathy, D., (1984). *Philosophical Magazine B*. **49**, 609

Yan, C., and Vohra, Y. (1999). *Diamond Related Materials*. **8**, 2022

Yu, P. Y., and Cardona, M. (2001). *Fundamentals of Semiconductors*, third edition, Springer-Verlag, Berlin, Heidelberg

Zaitsev, A. M. (2000). *Physical Review B*. **61** (19), 12909

Zaitsev, A. M. (2001). *Optical Properties of Diamond: A Data Handbook*, Springer-Verlag Berlin and Heidelberg